

2016-01-01

Materials Characterization of Deposits on Starboard (Inboard) Elevon Actuator Shaft Recovered from Space Shuttle Columbia

Mayra Contreras

University of Texas at El Paso, mjcontreras@miners.utep.edu

Follow this and additional works at: https://digitalcommons.utep.edu/open_etd



Part of the [Materials Science and Engineering Commons](#), and the [Mechanics of Materials Commons](#)

Recommended Citation

Contreras, Mayra, "Materials Characterization of Deposits on Starboard (Inboard) Elevon Actuator Shaft Recovered from Space Shuttle Columbia" (2016). *Open Access Theses & Dissertations*. 627.
https://digitalcommons.utep.edu/open_etd/627

This is brought to you for free and open access by DigitalCommons@UTEP. It has been accepted for inclusion in Open Access Theses & Dissertations by an authorized administrator of DigitalCommons@UTEP. For more information, please contact lweber@utep.edu.

MATERIALS CHARACTERIZATION OF DEPOSITS ON STARBOARD
(INBOARD) ELEVON ACTUATOR SHAFT RECOVERED FROM SPACE
SHUTTLE *COLUMBIA*

MAYRA J. CONTRERAS
Doctoral Program in Materials Science and Engineering

APPROVED:

Stephen W. Stafford, Ph.D., Chair

Anupama B. Kaul, Ph.D.

Peter Golding, Ph.D.

Aaron Velasco, Ph.D.

Charles Ambler, Ph.D.
Dean of the Graduate School

Copyright ©

by

Mayra Contreras

2016

DEDICATION

Dedicated to my family, friends, and UTEP Upward Bound staff.

MATERIALS CHARACTERIZATION OF DEPOSITS ON STARBORD (INBOARD)
ELEVON ACTUATOR SHAFT RECOVERED FROM SPACE SHUTTLE *COLUMBIA*

by

MAYRA J. CONTRERAS
B.S. in Metallurgical and Materials Engineering

DISSERTATION

Presented to the Faculty of the Graduate School of
The University of Texas at El Paso
in Partial Fulfillment
of the Requirements
for the Degree of

DOCTOR OF PHILOSOPHY

Materials Science and Engineering
THE UNIVERSITY OF TEXAS AT EL PASO
December 2016

ACKNOWLEDGEMENTS

I would like to thank my doctoral advisor Dr. Stephen W. Stafford who gave me the opportunity to conduct research under his guidance. It has been a pleasure working with Dr. Stafford and learning from him as well. I would also like to thank Dr. John “Danny” Olivas and Darren Cone who lead CASSMAR and have provided the funding needed to conduct this research. I am also thankful to all the members of the CASSMAR research team for their help throughout the research. Special thanks to HSA and staff for allowing me to use their services when needed. NASA’s *Columbia* Research and Preservation Office approved a loan to The University of Texas at El Paso which allowed for research on *Columbia* debris to be performed at the university. This study would not have been possible if it wasn’t for them providing the samples and would also like to thank them for approving this research.

I would also like to thank the Department of Metallurgical and Materials Engineering faculty for all the knowledge gained from each one of them throughout my college education which has prepared me well for my future career. I would also like to thank the students that make up the department which made my college experience a wonderful one. During my educational journey, I have made forever lasting friendships. I would like to thank all my friends, those that I have known for many years, those living out of state, and fairly new friends, all which have had a great impact during my college career. I am truly grateful to have you all be part of my life. Thank you for all the unforgettable memories, the smiles, the laughter, for giving me the best advice, and brightening my days. Finally, I would like to thank my family for all their support, understanding, infinite love, and believing in my potential to accomplish my goals.

ABSTRACT

With the new era of space exploration upon us and the Orion spacecraft currently being tested, which would replace the Space Shuttle as the orbiter that will transport humans into space once again, safety assurance is the main component for a successful mission. Aerospace materials have always played a big role when it comes to safety assurance. Having the knowledge of what materials are suitable to keep using when designing the future spacecraft that will take humans to Mars is fundamental in order to be confident that the vehicle and all that comprises it will function as envisioned. Expanding the knowledge and obtaining a better understanding on how space materials behave in extreme environments like outer space is crucial when space safety and mission assurance is the goal to accomplish. The *Challenger* and *Columbia* accidents are reminders that advancement in materials science plays an important role for the success of space exploration. While the debris from *Challenger* were buried in the abandoned Minuteman silos, *Columbia* debris has been stored in a room at the Vertical Assembly Building for the scientific community to conduct research on it with the goal of improving the designs of new spacecraft. One of the artifacts recovered from *Columbia* and loaned to the university to conduct scientific research on was the starboard (inboard) elevon actuator. This hydraulic powered component contains a shaft that displayed a significant amount of molten metal deposited onto it. Doing a thorough materials characterization on the deposit as well as the base metal will allow for information such as identification of deposits to be known, any thermal alterations that occurred to the base metal, and possibly, temperatures reached by surrounding metal as well as the base metal of the shaft. Since the hydraulic system that contains the shaft powers the orbiter's aerosurfaces, the movement of the elevons throughout the breakup might be an area that can be closely investigated and may lead to new trajectory data.

TABLE OF CONTENTS

ACKNOWLEDGEMENTS.....	v
ABSTRACT	vi
TABLE OF CONTENTS	vii
LIST OF TABLES.....	x
LIST OF FIGURES	xi
LIST OF ILLUSTRATIONS	xvi
CHAPTER 1: INTRODUCTION.....	1
1.1 BREAKUP OF <i>COLUMBIA</i> DURING RE-ENTRY	3
1.2 ELEVON ACTUATORS AND STRUCTURE	5
1.3 LITERATURE REVIEW	7
1.3.1 17-4 PH STAINLESS STEEL.....	8
1.3.2 ALUMINUM 2024.....	10
1.3.3 TYPE 304 CRES STAINLESS STEEL	12
1.3.4 INCONEL 718.....	14
1.3.5 TI- 6AL- 4V.....	15
1.4 PROJECT DISCRIPTION.....	17
CHAPTER 2: EXPERIMENTAL PROCEDURES	19
2.1 METHODOLOGY	19
2.2 NON-DESTRUCTIVE EVALUATION	20
2.2.1 AS-RECEIVED PHOTOGRAPHY AND VISUAL EXAMINATION.....	20
2.2.2 3-DIMENSIONAL MODELING.....	21
2.2.3 DIMENSIONAL ANALYSIS.....	22
2.2.4 ELEMENTAL ANALYSIS	23
2.3 SECTIONING	24
2.3.1 PRIMARY SECTIONING	24
2.3.2 SECONDARY SECTIONING	26
2.3.3 ADDITIONAL SECTIONING	27
2.4 MICROSCOPY	28
2.4.1 SCANNING ELECTRON MICROSCOPY.....	28
2.4.2 X-RAY DIFFRACTION	29

2.4.3	OPTICAL MICROSCOPY	29
CHAPTER 3: NON-DESTRUCTIVE AND SECTIONING RESULTS.....		31
3.1	NON-DESTRUCTIVE EVALUATION	32
3.1.1	AS-RECEIVED PHOTOGRAPHY AND VISUAL EXAMINATION.....	32
3.1.2	3-DIMENSIONAL ANALYSIS	37
3.1.3	DIMENSIONAL ANALYSIS.....	39
3.1.4	ELEMENTAL ANALYSIS.....	41
3.2	SECTIONING	45
3.2.1	AREA 1	48
3.2.2	AREA 2	48
3.2.3	AREA 3	49
3.2.4	AREA 4	50
3.3	SUMMARY.....	51
CHAPTER 4: MICROSCOPY RESULTS.....		52
4.1	SCANNING ELECTRON MICROSCOPY ANALYSIS	53
4.1.1	AREA 1	53
4.1.1.1	SURFACE ANALYSIS	54
4.1.1.2	CROSS-SECTIONAL ANALYSIS	60
4.1.2	AREA 2	70
4.1.2.1	SURFACE ANALYSIS.....	71
4.1.2.2	CROSS-SECTIONAL ANALYSIS	74
4.1.3	AREA 3	77
4.1.3.1	SURFACE ANALYSIS.....	79
4.1.3.2	CROSS-SECTIONAL ANALYSIS	85
4.1.4	AREA 4	88
4.1.4.1	SURFACE ANALYSIS.....	91
4.1.4.2	CROSS-SECTIONAL ANALYSIS	96
4.2	X-RAY DIFFRACTION	104
4.2.1	AREA 1	104
4.2.2	AREA 2	105
4.2.3	AREA 3	107
4.2.4	AREA 4	110
4.3	OPTICAL MICROSCOPY	113
4.3.1	AREA 1	113

4.3.2 AREA 2	115
4.3.3 AREA 3	116
4.3.4 AREA 4	119
4.4 SUMMARY.....	126
CHAPTER 5: DISCUSSION	127
5.1 SURFACE ANALYSIS DISCUSSION	127
5.2 CROSS-SECTIONAL ANALYSIS DISCUSSION.....	134
5.3 OPTICAL MICROSCOPY DISCUSSION.....	138
5.4 SUMMARY.....	143
CHAPTER 6: CONCLUSIONS	145
6.1 OVERVIEW	145
6.2 FOLLOW ON WORK.....	149
REFERENCES	152
VITA.....	156

LIST OF TABLES

TABLE 1.1: ELEMENTAL COMPSITION OF 17-4 PH STAINLESS STEEL.	9
TABLE 1.2: ELEMENTAL COMPOSITION OF COMPONENTS SURROUNDING HYDRAULIC SYSTEM	16
TABLE 1.3: PROPERTIES OF MATERIALS SURROUNDING HYDRAULIC SYSTEM ...	17
TABLE 3.1: MEASURMENTS CORRESPONDING TO DIAMETER OF SHAFT.....	40
TABLE 3.2: DIMENSIONS OF ACTUATOR SHAFT.	41
TABLE 3.3: RESULTS FOR XRF CONDUCTED ON PORT-SIDE OF SHAFT.....	43
TABLE 3.4: RESULTS FOR XRF CONDUCTED ON STARBOARD-SIDE OF SHAFT.....	45
TABLE 4.1: ELEMENTAL COMPOSITION OF DEPOSIT LAYERS ON CROSS-SECTION (CS) FOR AREA 1	63
TABLE 4.2: ELEMENTAL COMPOSITION OF CS DEPOSITS IN THREADED REGION IN AREA 1.	70

LIST OF FIGURES

FIGURE 1.1: ELEVON POSITION IN RELATION TO SPACE SHUTTLE.....	3
FIGURE 1.2: STARBOARD-SIDE OF ACTUATOR SHAFT.....	18
FIGURE 2.1: PRIMARY SECTIONING PLAN	25
FIGURE 2.2: SECONDARY SECTIONING PLAN.....	27
FIGURE 2.3: ADDITIONAL SECTIONING PLAN	28
FIGURE 3.1: AS-RECEIVED PHOTOGRAPHY OF STARBOARD (INBOARD) ELEVON ACTUATOR.....	33
FIGURE 3.2: ELECTRICAL CONTROL MODULE AND LOCKING NUT.	34
FIGURE 3.3: AS-RECEIVED PHOTOGRAPHY OF PORT-SIDE OF SHAFT.	35
FIGURE 3.4: AS-RECEIVED PHOTOGRAPHY OF STARBOARD-SIDE OF SHAFT	36
FIGURE 3.5: 3-D MODEL OF A PORTION OF ELEVON ACTUATOR	37
FIGURE 3.6: 3-D MODEL OF PORT AND STARBOARD-SIDE OF SHAFT	38
FIGURE 3.7: VISUAL REPRESENTATION OF POSITIONS OF CLOCK IN REFERENCE TO THE SHAFT.....	39
FIGURE 3.8: GRID OVERLAY USED FOR XRF OF PORT AND STARBOARD-SIDE OF SHAFT WITH COLOR COORDINATING RESULTS.....	45
FIGURE 3.9: RESULTS FOR PRIMARY SECTIONING.	46
FIGURE 3.10: RESULTS FOR SECONDARY SECTIONING OF STARBOARD-SIDE OF SHAFT.....	47
FIGURE 3.11: RESULTS FOR ADDITIONAL SECTIONING CONDUCTED ON STARBOARD-SIDE OF SHAFT	49
FIGURE 4.1: KEYANCE- AREA 1 SAMPLE.....	54
FIGURE 4.2: SEM- TOP SURFACE IN AREA 1	55
FIGURE 4.3: EDS- AREA 1 SURFACE ANALYSIS.	56
FIGURE 4.4: SEM- AREA I SURFACE ANALYSIS OF THREADED SIDE.....	58
FIGURE 4.5: EDS- SURFACE RESULTS FOR THREADED SIDE	59

FIGURE 4.6: KEYENCE- CS VIEW OF AREA 1 THREADED SIDE AND ELEMENTAL COMPOSITION OF BASE METAL.....	60
FIGURE 4.7: SEM- CS OF AFT-FACING SIDE IN AREA 1	61
FIGURE 4.8: EDS- CS OF AFT-FACING SIDE IN AREA 1	65
FIGURE 4.9: SEM- CS OF THREADED SIDE IN AREA 1.....	67
FIGURE 4.10: EDS- CS OF THREADED SIDE IN AREA 1.	68
FIGURE 4.11: KEYENCE- AREA 2 SAMPLE	71
FIGURE 4.12: EDS- BASE MATERIAL AND COATING ON SHAFT	71
FIGURE 4.13: SEM- AREA 2 SURFACE ANALYSIS.....	72
FIGURE 4.14: EDS- AREA 2 SURFACE SPECTRA.	73
FIGURE 4.15: SEM- CS VIEW OF AREA 2	75
FIGURE 4.16: EDS- CS VIEW FOR AREA 2.....	76
FIGURE 4.17: KEYENCE- AREA 3 SAMPLE A3.1	77
FIGURE 4.18: KEYENCE- AREA 3 SAMPLE A3.2	78
FIGURE 4.19: KEYANCE- AREA 3 SAMPLE A3.3.....	78
FIGURE 4.20: SEM- A3.1 SURFACE ANALYSIS	79
FIGURE 4.21: EDS- A3.1 SURFACE SPECTRA.	81
FIGURE 4.22: SEM- A3.2 SURFACE ANALYSIS	82
FIGURE 4.23: EDS- A3.2 SURFACE SPECTRA	83
FIGURE 4.24: SEM- A3.3 SURFACE ANALYSIS	84
FIGURE 4.25: EDS- A3.3 SURFACE SPECTRA	85
FIGURE 4.26: SEM/EDS-CS VIEW OF A3.1	85
FIGURE 4.27: SEM- CS VIEW OF A3.2	86
FIGURE 4.28: EDS-CS VIEW OF A3.2	87

FIGURE 4.29: SEM/EDS- CS VIEW OF A3.3 .	88
FIGURE 4.30: KEYENCE- ARE 4 SAMPLE A4.1 .	89
FIGURE 4.31: KEYENCE- AREA 4 SAMPLE A4.2 .	90
FIGURE 4.32: KEYENCE- AREA 4 SAMPLE A4.3 .	90
FIGURE 4.33: SEM- A4.1 SURFACE ANALYSIS.....	92
FIGURE 4.34: EDS- A4.1 SURFACE SPECTRA .	93
FIGURE 4.35: SEM- A4.2 SURFACE ANALYSIS.....	93
FIGURE 4.36: EDS- A4.2 SURFACE SPECTRA.	94
FIGURE 4.37: SEM- A4.3 SURFACE SPECTRA.....	95
FIGURE 4.38: EDS- A4.3 SURFACE SPECTRA.	95
FIGURE 4.39: SEM- CS VIEW OF A4.1.....	97
FIGURE 4.40: EDS- CS VIEW OF A4.1	98
FIGURE 4.41: SEM- CS VIEW OF A4.2	99
FIGURE 4.42: EDS- CS VIEW OF A4.2	101
FIGURE 4.43: SEM- CS VIEW OF A4.3	102
FIGURE 4.44: EDS- CS VIEW OF A4.3	103
FIGURE 4.45: XRD SPECTRA OF AREA 1.....	105
FIGURE 4.46: XRD SPECTRA OF AREA 2 DEPOSIT-FREE AREA.	106
FIGURE 4.47: XRD SPECTRA OF AREA 2 DEPOSIT LINES.....	106
FIGURE 4.48: XRD SPECTRA OF AREA 3 SAMPLE A3.1 R1.	107
FIGURE 4.49: XRD SPECTRA OF AREA 3 SAMPLE A3.1 R2.	108
FIGURE 4.50: XRD SPECTRA OF AREA 3 SAMPLE A3.2 R1	109
FIGURE 4.51: XRD SPECTRA OF AREA 3 SAMPLE A3.2 R2	109
FIGURE 4.52: XRD SPECTRA OF AREA 3 SAMPLE A3.3	110

FIGURE 4.53: XRD SPECTRA OF AREA 4 SAMPLE A4.1.	111
FIGURE 4.54: XRD SPECTRA OF AREA 4 SAMPLE A4.2 R1	111
FIGURE 4.55: XRD SPECTRA OF AREA 4 SAMPLE A4.2 R2.	112
FIGURE 4.56: XRD SPECTRA OF AREA 4 SAMPLE A4.3.	112
FIGURE 4.57: OPTICAL MICROGRAPHS OF AREA 1 AFT-FACING SAMPLE.	114
FIGURE 4.58: OPTICAL MICROGRAPHS OF AREA 1 THREADED SAMPLE.....	115
FIGURE 4.59: OPTICAL MICROGRAPHS OF AREA 2.	116
FIGURE 4.60: OPTICAL MICROGRAPHS OF AREA 3 SAMPLE A3.1.	117
FIGURE 4.61: OPTICAL MICROGRAPHS OF AREA 3 SAMPLE A3.2.	118
FIGURE 4.62: OPTICAL MICROGRAPHS OF AREA 3 SAMPLE A3.3	119
FIGURE 4.63: OPTICAL MICROGRAPHS OF AREA 4 SAMPLE A4.1	120
FIGURE 4.64: KEYENCE- AREA 4 SAMPLE A4.2 CROSS-SECTIONAL VIEW.....	121
FIGURE 4.65: OPTICAL MICROGRAPHS OF AREA 4 SAMPLE A4.2.	122
FIGURE 4.66: MICROSTRUCTURAL CHANGES OF AREA 4 SAMPLE A4.2.....	123
FIGURE 4.67: OPTICAL MICROGRAPHS OF AREA 4 SAMPLE A4.3.	124
FIGURE 4.68: MICROSTRUCTURAL CHANGES OF AREA 4 SAMPLE A4.3	124
FIGURE 5.1: ELECTRICAL JUNCTION BOX COMPARISON	128
FIGURE 5.2: TITANIUM HONEYCOMB SANDWICH PANELS.....	130
FIGURE 5.3: LOCKING NUT AND CLEVIS PIN COMPARISON.	131
FIGURE 5.4: TITANIUM RUB STRIPS.....	132
FIGURE 5.5: INCONEL 718 STRUTS.	133
FIGURE 5.6: SURROUNDING COMPONENTS OF ACTUATOR SHAFT	137
FIGURE 5.7: MICROSTRUCTURAL COMPARISON OF H925 CONDITION.....	139
FIGURE 5.8: MICROSTRUCTURAL COMPARISON OF H1150 CONDITION.....	142

FIGURE 5.9: MICROSTRUCTURAL COMPARISON OF H1075 CONDITION	143
---	-----

LIST OF INLLUSTRATIONS

ILLUSTRATION 1.1: ELEVON ACTUATOR SUPPORT STRUCTURE..... 6

ILLUSTRATION 1.2: ELEVON CONSTRUCTUION 7

ILLUSTRATION 3.1: TOP VIEW OF FLIGHT CONTROL SYSTEM HYDRAULIC
ACTUATOR.....41

CHAPTER 1: INTRODUCTION

As the Space Shuttle Program came to an end in 2011, several commercial entities have moved forward on building new spacecraft that will once again take astronauts from American soil to the International Space Station (ISS) to continue the ongoing research performed on site or simply transport ordinary people above the Earth's atmosphere to experience the magnificent view of Earth from outer space. With this new era of commercial human spaceflight and space exploration, it is necessary that research in materials science continues to advance for the safety of the astronauts and America citizens while going to space. Even though spaceflight is still young and a lot is left to explore, accidents have occurred and lives have been lost while attempting to discover the unknown. During the past few years, no human losses have occurred but several major accidents that involve the loss of rockets, equipment, science experiments, and supplies that add up to millions of dollars have been lost. Most recently, on June 28, 2015, a Space X rocket, Falcon 9, which was an unmanned mission and its purpose to resupply the ISS, exploded minutes after launch due to a strut failure in the liquid oxygen tank. The Falcon 9 rocket was the third attempt to resupply the space station, before this accident, two others occurred within that year. One April 28, 2015, the Russian Progress failed to complete its mission when there was an abnormal separation of the supply ship from the launch vehicle and led to an uncontrolled spin of the spacecraft that ended burning up in Earth's atmosphere. The first attempt of three within the year to resupply the ISS was with the Antares rocket by Orbital Sciences. This rocket also exploded seconds after liftoff on October 28, 2014 due to an AJ26 engine failure and discontinued the use of this main engine after the accident. With advancing technology, failures should not happen as often as they have been nowadays.

In 2013, the Center for the Advancement of Space Safety and Mission Assurance Research (CASSMAR) was established at the University of Texas at El Paso (UTEP), its main mission, working towards conducting risk reduction research that can help reduce the possibility of these types of events from occurring. Now that commercial human spaceflight is coming closer to reality, the safety of these

human beings is the priority and to accomplish that, being able to rely on the vehicle that will take ordinary citizens up into space is a major step. Having the certainty that the spacecraft that will be carrying human lives was designed and tested in every possible way and knowing that the materials and technology used to build are the best and latest will reduce the risk of accidents. One of CASSMAR's ongoing projects consists of analyzing Space Shuttle *Columbia* debris to obtain information on how several materials systems react to the re-entry environment which were never intended to encounter. Since there are still a lot of aerospace materials currently being used to build new spacecraft that have been used for decades and the start of manned missions, it is important that research on these same materials continue to make sure they are still suitable to use in future spacecraft. Knowledge gained will contribute to the safety of future spaceflight, whether it involves well trained astronauts or regular citizens trying to get a closer look at outer space.

The research that will be conducted involves the starboard (inboard) elevon actuator shaft which would be located at the right side of the trailing edge of the wing in a space shuttle (Figure 1.1). The actuator shaft on this component shows a significant amount of deposits and indications of possibly three unique deposition events. A small section of the elevon hydraulic assembly housing also contains deposits and will be examined. To identify the deposits that have adhered to the actuator shaft and housing material, a thorough materials characterization on four specific areas was conducted. It is important that the areas examined are compared to each other since the texture of the deposits differentiate with position along the shaft. This can provide important information such as how many depositions occurred throughout the event, make it possible to trace the deposits to their source on the vehicle, and provide correlation of the deposits' locations to the elevon position during re-entry. Data on thermal alterations occurring on the elevon actuator shaft, if any, will also be investigated during this study since this component was never intended to be directly exposed to the re-entry environment.

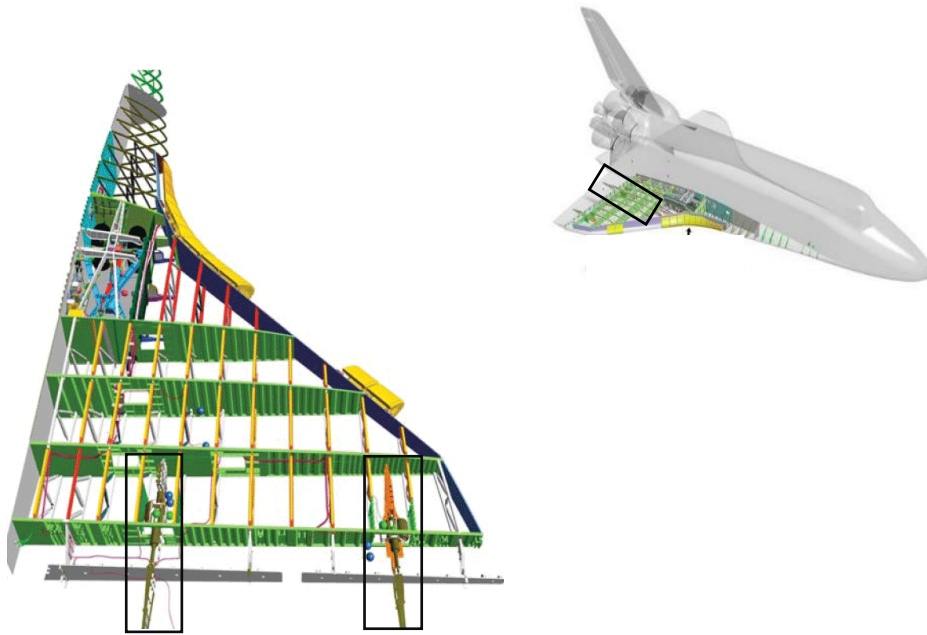


Figure 1.1 Left. Right wing showing starboard outboard and inboard elevon actuators. **Top Right.** Location of starboard (inboard) elevon actuator with respect to space shuttle. Images [10]

1.1 BREAKUP OF *COLUMBIA* DURING RE-ENTRY

On January 16, 2003, the Space Shuttle *Columbia* launched from Cape Canaveral at the Kennedy Space Center (KSC). Seven astronauts on a 16-day microgravity mission ready to conduct approximately 80 experiments that would help better understand Earth's atmosphere and ozone layers as well as studies on how the human body reacts when it experiences zero gravity were on board *Columbia* [1]. On February 1, 2003 as the Space Shuttle *Columbia* returned from its mission, an unexpected tragedy occurred. As *Columbia* entered back into the Earth's atmosphere, a breach in the Thermal Protection System (TPS) on the leading edge of the left wing caused superheated plasma to penetrate through, which in turn compromised the structural integrity of the space shuttle. The breach had occurred 81.9 seconds into the launch when a piece of foam from the external tank struck the leading edge of the left wing [2]. As *Columbia* and the crew were preparing to return home, the severity of the foam hitting the Reinforced Carbon Carbon (RCC) panels went unnoticed until 16 minutes before landing and resulted in the catastrophic breakup of the orbiter and the tragic loss of the seven astronauts aboard. During the debris

recovery process conducted by NASA's Columbia Accident Investigation Board, more than 83,900 pieces were found in areas around east Texas and western Louisiana which only made up 38 percent of the shuttle's dry weight [2] [3].

Even though analysis of several debris pieces has been performed, most of the information that was obtained belonged to components recovered from the forward fuselage or the port side of the leading edge of the wing where the breach occurred in hope of understanding the root cause of the accident. Components that were analyzed looked at materials like titanium, aluminum, glass shards, RCC panels, and insulation tiles. After the accident, impact testing was conducted on fiberglass panels to reconstruct the event that took place after *Columbia* launched from KSC. A 48.2 centimeters (cm) (19") by 29.2cm (11.5") by 14cm (5.5") block of foam with a density of 34.4kg/m^3 (2.4lb/ft^3), at a 30° angle, struck the RCC panels at a velocity of 853 kilometers per hour (530 miles per hour) [4]. This caused a hole of about 40.6cm (16") by 43.2cm (17") which was consistent with the findings from the *Columbia* investigation. Doing a failure analysis on a RCC composite material concluded that the RCC leading edge failed by erosion due to the extreme temperatures that it was exposed to and stress conditions that allowed for cracking to occur during break up [3][5]. Research was also done on glass fragments belonging to the windowpanes where three distinct layers were discovered in the alumino-silicate glass matrix. These TiO_2 layers consisted of equi-dimensional subhedral TiO_2 crystals, a layer of elongated TiO_2 with acicular mullite crystals, and a metallic aluminum porous layer [6]. The presence of titanium was surprising to find in this area and further research was conducted on Ti-6Al-4V and its ability to combust in oxygen enriched environments. An arc-jet facility was used to simulate the re-entry environment where Ti-6Al-4V coupons were tested and three different classifications were established depending on the material's response to this test. Material passivation was Class I, ignition and initiation of melting with unstained combustion being Class II, and Class III is defined as ignition with sustained combustion [7]. Clearly, this test showed

that in re-entry conditions, titanium may ignite, combust, and serve as an accelerant of other material's systems.

Although this is a wide range of materials that have been investigated, research being done on how materials react in the re-entry environment is still scarce. The recovery of the space shuttle debris is of great importance because the knowledge that can be obtained from it can be of tremendous value. These pieces are one of a kind since they experienced re-entry conditions. They are not pieces which have gone through re-entry simulations where the conditions are not the same as the ones reached in extreme environments like outer space. Since there have not been many space accidents where debris has reached the ground and been recovered, Columbia debris provides an opportunity to learn of the different conditions these materials were exposed to. A massive amount of knowledge can be discovered in the recovered debris once an extensive, in-depth analysis is conducted.

1.2 ELEVON ACTUATORS AND STRUCTURE

In a space shuttle, there are four elevon actuators that are located at the trailing edge of the wings. An inboard and outboard elevon actuator can be found in each rear portion of the wings. The inboard elevon actuators will be closest to the main propulsion engines, while the outboard elevon actuators are located further out at each terminal of the wings as seen in Figure 1.1. A side view of the elevon including the hydraulic system where the actuator shaft can be seen is shown in Illustration 1.1. The function of these components was to control the movement of the space shuttle during atmospheric flight. The elevons would cause a pitching force when they were moved in the same direction making the nose go up or down. When the elevons were moved in different orientations, this would cause a rolling motion and would make the wings move up or down. The elevons had three hinges apiece that supported them and would respond to the movement given by the flight control system hydraulic actuators where the elevons were attached. Each elevon would deflect 40 degrees up and 25 degrees down with 5 degrees overtravel as seen in Illustration 1.2 [8].

The elevons themselves were constructed of aluminum multiribs and beams and had aluminum honeycomb skins which were well suited for the type of environment that was seen in that region. The

aluminum alloy used for these structures was Al 2024 among other 2000 series Al alloys. In the surrounding areas where the elevons were located, there were panels made of Inconel 718 and titanium honeycomb sandwich construction, which provided a closeout of the wing-to-elevon opening. The wings rod assembly were also made of Inconel 718. In the upper leading edge of the elevons, there were titanium rub strips made also of titanium honeycomb construction which offered the sealing surface area for the elevon seal panels [9]. Some of the exposed areas on the elevons were covered with reusable surface insulation TPS materials but excluded the elevon seal panels. Type 304 CRES stainless steel was also used for the actuating mechanism, locking nut and clevis among other inserts. Construction of the elevons can be seen in Illustration 1.2.

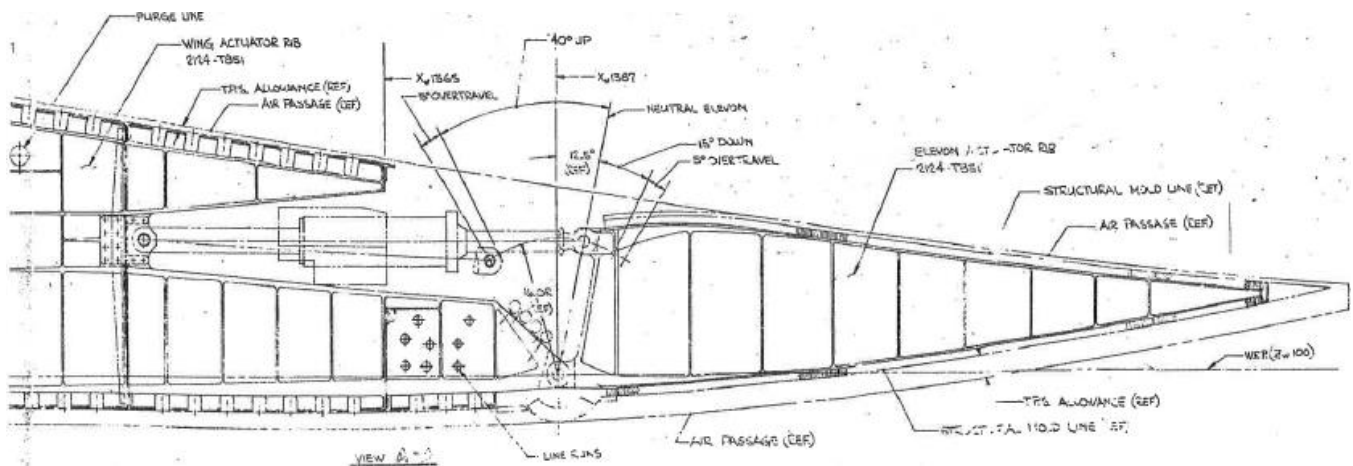


Illustration 1.1 Side view of the elevon actuator support structure including the hydraulic system which contains the actuator shaft. Illustration provided by NASA.

A motion and thermal analysis was performed by the Spacecraft Crew Survival Integration Investigating Team where it was concluded that the hydraulic pressure to the aerosurfaces was completely lost due to the breach that occurred on the port-side RCC panels which caused the aerosurfaces to float and the orbiter went into an uncontrolled pitch-up. This occurred near Dallas, Texas right after fault messages were received concerning the landing gear doors and the flight control system bypass valves closed, which would indicate failure of the aerosurface actuators [9]. At that time, the vehicle was no longer in a controlled glide and the ballistic number was constantly changing during re-entry.

Investigating the starboard (inboard) elevon actuator shaft which was one of the components recovered from the Space Shuttle Columbia can reveal valuable knowledge on the motion of the elevon

during and/or after the break up as well as the behavior of several material systems when they encountered extreme thermal conditions during re-entry. This research will consist of looking at the starboard-side of the actuator shaft which is made up of a 17-4 precipitation hardening (PH) stainless steel material where deposits with unique textures can be seen throughout the shaft, which was characterized.

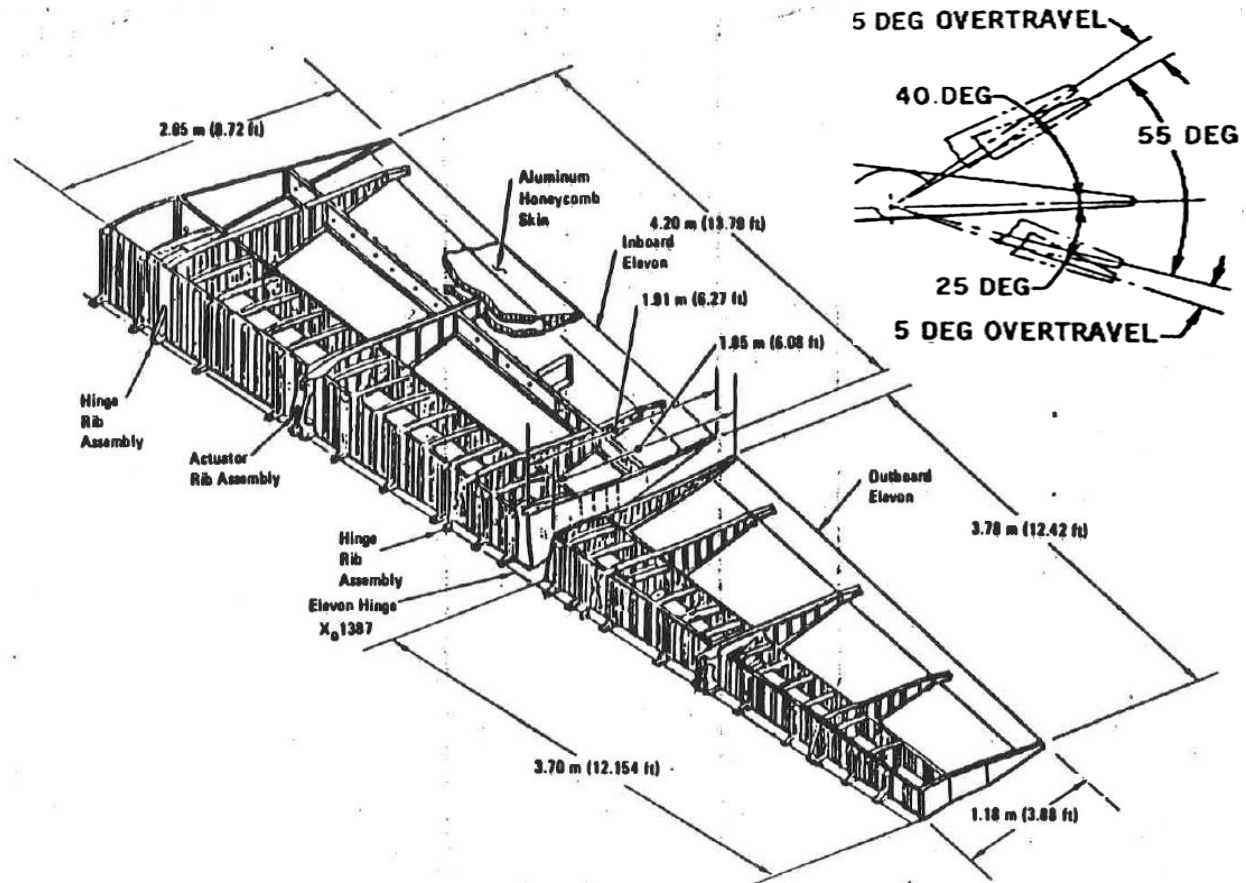


Illustration 1.2 Construction of elevon along with dimensions is shown as well as the maximum deflections reached by the elevon. Illustration provided by NASA.

1.3 LITERATURE REVIEW

Metallic deposits found on the shaft came from surrounding areas which consisted of components made up of materials such as 17-4 PH stainless steel as well as Type 304 CRES stainless steel. Al 2024 was among the most widely used aluminum alloy on the wing structure and is expected to be present on the shaft's deposits in large quantities. Degradation of other materials such as Inconel 718 and titanium which surrounded the area, most likely occurred and could have deposited themselves onto the shaft. Since evidence of erosion on the actuator shaft was observed, microstructural behavior of the 17-4 PH stainless

steel was researched. Due to extremely high temperatures reached, changes in the materials occurred and comprehending the effects will provide information that can help determine the deposition process that took place on the shaft. It is essential to understand these materials systems that were near the shaft to characterize the metallic deposits.

1.3.1 17-4 PH STAINLESS STEEL

The starboard elevon actuator shaft recovered from the *Columbia* debris is made up of a 17-4 precipitation hardening stainless steel. This type of steel, also known as Type 630 is a chromium-nickel-copper martensitic stainless steel. Its composition consists of 17 wt. % chromium (Cr), 4 wt. % nickel (Ni), and 4 wt. % copper (Cu) which will precipitate during heat treatment, hardening the material and increasing its strength by introducing strain to the lattice. It will also contain austenite-stabilizing elements such as carbon, manganese, and nitrogen with additions of niobium and titanium which will help prevent the formation of chromium carbides by forming other precipitates which will contribute to the strength of the material. It is widely used as a structural material or parts in aerospace, chemical processing components, biomedical hand tools, in the gas and oil industry, and in power plant applications. This martensitic stainless steel is used in these applications because it provides an excellent combination of high strength, outstanding corrosion and oxidation resistance, and good mechanical properties at elevated temperature [11]. The properties of a 17-4 PH stainless steel can range depending on the type of heat treatment and the application it will be used for, but it is typically solution treated around 1040°C to 1065°C (1900°F - 1950°F), cooled to room temperature, and aged between 480°C and 620°C (900°F-1150°F) usually for about 4 hours, and air cooled once again to attain the maximum strength and corrosion resistance [11-13]. The actuator shaft has an H925 condition which requires the stainless steel to be solution treated at 1038°C (1900°F), air cooled below 32°C (90°F), and aged at 496°C (925°F) for four hours before being air cooled once again [12].

Typical mechanical properties for a 17-4 PH stainless steel would have an ultimate tensile strength (UTS) ranging from 1103MPa (160ksi) and 1448MPa (210ksi), a yield strength of 896MPa (130ksi) up to 1379MPa (200ksi), and a Rockwell hardness C (HRC) scale in the range of 33 to 45 [12]. The Rockwell hardness value for an H925 treatment is at Rc43 hardness and will have a UTS of 1379MPa (200ksi) and

a yield strength of 1345MPa (195ksi). The typical mechanical properties and composition of a 17-4 PH stainless steel is shown in Table 1.1, along with the composition of the actuator shaft [12]. This type of stainless steel will reach its melting point at a temperature of 1404°C (2560°F) but the optimal operating condition for the 17-4 PH stainless steel shaft is roughly 316°C (600°F). Since the actuator shaft is coated with chromium, the operating temperatures increases to 400°C (752°F) [14]. Though hard chromium plating will increase the operating temperature of the stainless steel, it will start softening at temperatures between 260°C (500°F) and 280°C (536°F), which will decrease the hardness of the chromium coating. At 700°C (1292°F), the chromium plating will completely soften and will have the hardness value of the base metal [15]. The coating will remain solid up until the melting temperature of chromium at 1907°C (3465°F). Hard chrome, also called industrial chrome is used to reduce friction and resists wear. For this reason, it tends to be very hard, usually having hardness values between 63 and 70 HRC, but will also depend on the hardness of the base metal [16]. The chromium deposits range from 0.25µm to 1,000µm in thickness depending on the application. Thinner layers are used in components which require high wear or corrosion resistance whereas thicker layers will be applied to components that have already been damaged or need to be salvaged and repaired.

Table 1.1 Elemental composition of 17-4 precipitation hardening stainless steel, condition A along with the actual elemental composition of the actuator shaft. Mechanical properties are also available in the table. [12]

<i>Wt. %</i>	<i>C</i>	<i>Cr</i>	<i>Cu</i>	<i>Fe</i>	<i>Mn</i>	<i>Nb + Ta</i>	<i>Ni</i>	<i>P</i>	<i>Si</i>	<i>S</i>
<i>Avg.</i>	≤ 0.07	15.0-17.5	3.0-5.0	70.0–80.0	≤ 1.0	0.15-0.45	3.0-5.0	≤ 0.40	≤1.0	≤ 0.30
<i>Actual</i>	-----	16.14	3.06	72.6	0.72	0.34	4.88	-----	1.55	-----
<i>Mech.Prop.</i>	<i>Tensile Strength Yield</i>		1345 MPa		<i>Ultimate Tensile Strength</i>		1379 MPa		<i>HRC</i>	43

Being a martensitic stainless steel, its microstructure will be mostly an austenitic structure but as it is being cooled to room temperature the microstructure will transform from austenite to martensite as the martensite start (M_s) temperature is reached and will stop transforming once the martensite finish (M_f) temperature is obtained. The M_s and M_f temperatures will depend on the carbon content of the steel and will only start the martensitic transformation if there are sufficiently high cooling rates. As carbon content increases, the M_s and M_f temperatures will be lowered due to carbide formation. This transformation is an

athermal transformation and can also be called diffusionless since the arrangement of atoms do not occur by diffusion, instead it happens by shear displacement in small distances and in a quick, ordered manner [13]. Retained austenite will be present in most occasions during the transformation since martensite will expand and will pressurize the austenite making it impossible to go through the martensite transformation and hence, retained. The pressurized austenite will exist as small island grains among martensite. The expansion of martensite during the process will change the face-centered cubic structure of austenite to a body-centered tetragonal structure of martensite. The growth of martensite and change in crystal structure leads to a less densely packed structure that hardens the stainless steel.

Formation of delta-ferrite (δ -ferrite) stringers is common to see on a 17- 4 PH stainless steel. Elements that compose this material must be carefully balanced in order to prevent the formation of harmful amounts of δ -ferrite stringers. Delta-ferrite stringers are usually present throughout the material in amounts of 5-10 volume wt. % and are caused by an imbalance in the equivalent of the Cr-Ni ratios; an increase in the Cr content will decrease the temperature formation of the δ -ferrite [17-19]. These δ -ferrite stringers will appear in the microstructure as long, thin, discontinuous, off-white outlined phase running parallel to each other depending on the samples' orientation. The appearance of martensite in the microstructure will also depend on a specific element, carbon. With increasing carbon content, the martensite, which is a metastable phase, will look finer and will change from a lath morphology to a plate morphology [13]. An increase in carbon will also lead to higher amounts of retained austenite but will not be detrimental to the material. The percentage of a 17-4 PH stainless steel will be less than 0.6 wt. % C which makes martensite have a lath morphology. Martensite laths will appear as needle-like morphology with different orientations. Higher than 1.0 wt. % C will result in martensite having a plate morphology and a mixture of both laths and plates will occur if the carbon content is between 0.6 wt. % and 1.0 wt. %. Due to martensite being a metastable phase, high temperature will cause martensite to decompose into ferrite and cementite leading to tempered martensite. In this state, the cementite also called a carbide phase will have tiny, coarse particles instead of a plate morphology. Having tempered martensite will increase the strength of the material and make it more ductile [13].

1.3.2 ALUMINUM 2024

Aluminum alloy was used in most of the shuttle's structure where Al 2024 was the material of choice for the wing actuator and elevon rib panels structures, a part of which were attached to the hydraulic actuator system when it was recovered after the breakup of *Columbia*. Other nearby components to the shaft that were also Al 2024 were elevon hinges and seal panels. Aluminum 2024 is widely used on aerospace applications due to its high strength-to-weight ratio. Besides having high strength, it has good machinability and weldability though it can only be welded through friction welding, since Al is susceptible to solidification cracking [20]. Another well-known property of Al 2024 is its excellent fatigue resistance which is an essential quality to possess in the aerospace industry. This type of aluminum contains about 94 wt. % Al, 4 wt. % Cu, and 1 wt. % magnesium (Mg) where Cu is the primary alloying element [21]. Copper, for the same reason that is added to 17-4 PH stainless steel, is the major alloying element in Al 2024 since it will increase the strength of Al by facilitating precipitation hardening but will also lower other properties such as corrosion resistance and ductility [22]. Since Al 2024 has relatively low corrosion resistance, much of the time, this alloy will be anodized or clad to increase its corrosion resistance. Anodizing will consist of integrating aluminum oxide with the underlying aluminum substrate and provides a durable finish that will not peel off or chip [23]. Cladding of aluminum, Alclad, is done by using Al 1230, a high purity aluminum which applies a thin coating to the aluminum alloy to protect against corrosive environments but can be costly and adds weight to the structure [24].

One of the major disadvantages of this alloy is the low melting temperature at 500°C (935°F). The maximum operating temperature for this alloy would be at 400°C (752°F). With re-entry temperatures reaching as high as 1649°C (3000°F) these structural components would be the first ones in the surrounding areas to exhibit some type of degradation. As mentioned, the Al alloy tends to have a high strength-to-weight ratio with its density at 2.78g/cc (0.1lb/in³) and a tensile yield strength at 324MPa (47ksi). The UTS for Al 2024 is 469 MPa (68ksi) and a hardness of 75 HRB [21]. These mechanical properties will vary depending on the heat treatment of the Al alloy. A typical Al 2024 will be annealed between 399°C (750°F) and 427°C (800°F) for two hours and will then be slowly furnace cooled. Around the actuator, Al 2024 T62, T8511 and O condition were utilized. Having an O temper designation means that the aluminum was not heat treated and remains in the annealed condition which is the softest

condition. A T62 designation would mean that the alloy was solution treated and later artificially aged to obtain the highest strength by precipitation of metastable phases. Al 2024 T8511 will go through a solution heat treatment, will then be stretched to relieve stresses, and will finally be artificially aged [25]. The strength of Al 2024 can be achieved to as high as 520MPa (75ksi) depending on the temper chosen [26]. The temperatures will also be dependent on the user and the properties they want to obtain but solution treatments are usually carried out at temperatures close to 500°C (932°F) and water quenched, then it will be artificially aged at temperatures between 160°C (320°F) and 190°C (375°F) followed by air cooling.

The microstructure of high strength aluminum alloys, which included this 2000 series Al alloy, is complex to define since they will depend heavily on the heat treatment, processing, and deformation condition. In addition, they will have a combination of both equilibrium and non-equilibrium phases leading to properties being dependent on temperature [26]. This type of Al has a heterogeneous microstructure since it has alloying elements which will contribute to the high strength-to-weight ratio. Typically, an Al 2024 microstructure will consist of fine equiaxed grains with intermetallic particles, dispersoids, constituents, and impurity particles along with crystalline defects. The equiaxed grains will usually elongate depending on the processing it has gone through. Several changes can be seen in wrought alloy sheets for example. In wrought Al sheets, there will be a gradient in grain size and particles found on it as well as a fine microstructure which can vary in the precipitation of these particles when compared to the bulk. These constituent particles are made up of impurity elements such as Fe, Mn, and Si and are formed during solidification, forming insoluble compounds, which later will breakup and align due to the rolling and extrusion processes [26]. These same constituents can also be found in clusters which are made up of intermetallic compounds and will contribute to pitting on the microstructure due to their electrochemical behavior. These alloying elements will cause the formation of intermetallic particles which have a compositional variation making it difficult to characterize them. Several intermetallic particles that can be found on Al 2024 are $Al_{12}CuMg$, Al_7Cu_2Fe , $(Mn, Fe)_3SiAl_{12}$, and $Al_7Mn_3Cu_2$ which is a dispersoid [26].

1.3.3 TYPE 304 CRES STAINLESS STEEL

The Type 304 CRES steel was used on several components surrounding the hydraulic system of the elevon such as inserts in the actuating mechanism. The stainless steel is designated as CRES which stands for Corrosion RESistant steel. Due to this grade of stainless steel being so versatile, it is utilized more than any other stainless steel. Since it has a low cost and well-rounded mechanical properties, chemistry, and machinability, it is widely used on the aerospace, automotive, and construction industries. Type 304 CRES steel is non-magnetic and has an austenitic microstructure with low carbon content which minimizes the precipitation of carbides especially during welding giving it good weldability characteristics. It has excellent drawing and forming properties and can be used for high temperature applications as well. This grade of steel has a chemical composition of 18 wt. % Cr, 8 wt. % Ni, 2 wt. % Mn and approximately 66-74 wt. % Fe. Chromium is added to improve its corrosion resistance and nickel and manganese will act as austenite stabilizers. Its UTS is at 621MPa (90ksi) and a tensile yield strength of 290MPa (42ksi) making it a strong material but still has a low strength-to-weight ratio since steel is about 66% heavier than aluminum alloys used in the aerospace industry [27]. Type 304 stainless steel has a Rockwell hardness value of 80 on the B scale and its melting range is between 1399°C (2550°F) and 1454°C (2650°F). During solidification, the Type 304 stainless steel will undergo a ferritic mode of solidification where upon heating, the austenite will transform into delta-ferrite until it reaches its melting point [28]. Being a stainless steel, it will have great oxidation resistance and can be exposed to operating temperatures of around 899°C (1650°F) before encountering early stages of scaling.

Unlike Al 2024 and 17-4 PH stainless steel, Type 304 steel cannot be hardened by heat treatment. It is annealed by heating it to temperatures between 1038°C (1900°F) and 1121°C (2050°F) and will then be rapidly cooled. This is an austenitic stainless steel with a face-center cubic structure making the structure very ductile and tough at elevated temperature but can cause precipitation of carbides if exposed continuously. This is due to carbon having a thermodynamic affinity to chromium which forms chromium carbides, Cr_{23}C_6 , when carbon is supersaturated in austenite. Carbon and chromium will then segregate to form precipitates at the grain boundaries when temperatures are just below 850°C (1562°F). Precipitation will occur at the grain boundaries since they are excellent nucleation sites and diffusion will occur faster at these sites than in the bulk [29]. Intergranular attack is caused due to the formation of these carbides at

the grain boundaries, which will deplete the grain boundaries of chromium leading to sensitization. Sensitization will then lead to intergranular corrosion since chromium is the major alloying element that makes the steel corrosion resistant. Another microstructural change that can be encountered in austenitic stainless steels is sigma phase which is a chromium-iron intermetallic and grain growth [30]. Sigma phase and grain growth as well as the chromium carbides will form at elevated temperatures over long periods of time and will have negative effects on the components. As the volume fraction of sigma phase increases due to high concentrations of Cr in austenitic steels, the higher the grain growth will occur.

1.3.4 INCONEL 718

Inconel 718 which would be found on wing spanner beams and the rod assembly on the wing structure of the Space Shuttle *Columbia* is an austenitic, nickel-based superalloy. It is composed of 55 wt. % Ni, 20 wt. % Cr, 5 wt. % Nb and Ta, 3 wt. % Mo, and less than 1 wt. % of elements such as Ti, Al, C, Mg, Si, and Cu. It is considered a superalloy for its excellent corrosion and oxidation resistant properties at elevated temperatures in components that are constantly under high pressure. When Inconel is under extreme heat, it will form an adherent, thick, passivation oxide layer which is very stable and does not allow for oxidation to continue at elevated temperatures. The passivation layer that forms on the Inconel 718 is NiCr_2O_4 , a combination of nickel and chromium oxides [31]. The addition of elements such as calcium, silicon, zirconium, or cerium in small amounts will improve the oxidation resistant in the nickel-chromium superalloys. Aside from these properties, the precipitation hardenable alloy will have great creep-rupture properties and extremely high tensile strength at temperatures as high as 704°C (1300°F) [32]. The extraordinary creep-rupture property at high temperatures is due to gamma double prime (γ''), an intermetallic compound, Ni_3Nb , which forms small cubic crystals, hindering creep and slip [33]. The intermetallic phase will act as barrier to dislocation motion.

To obtain the optimal tensile and fatigue strength as well as creep-rupture properties, Inconel 718 will be subjected to the following precipitation hardening heat treatment. The superalloy will be solution annealed at temperatures ranging from 927°C to 1010°C (1700°F - 1850°F) for an hour and then rapidly cooled in water. Following annealing, Inconel will then go through the precipitation hardenable process. Temperatures will increase up to 718°C (1325°F) for 8 hours before it is furnace cooled, dropping the

temperature 38° C (100°F) per hour down to 621°C (1150°F) and held there for an additional 8 hours following air cooling [32]. The ultimate tensile strength at 649°C (1200°F) will be approximately 1103MPa (160ksi) and its yield strength will be 979MPa (142ksi). The rupture strength will be 593MPa (86ksi) at 1000 hours. At room temperature, the tensile strength will increase to 1207MPa (175ksi) for yield strength and 1447MPa (210ksi) for the ultimate tensile strength [33]. Fatigue strength will be at its highest with this treatment accompanied with fine grain size. By subjecting Inconel to this heat treatment, Inconel 718 can operate in temperatures as low as -252°C (-423°F) up to 704°C (1300°F) without exhibiting any signs of oxidation or creep. Inconel 718 will reach its melting point at 1336°C (2437°F).

Inconel 718 is known for having a great weldability, a property that other gamma prime superalloys that contain high Al/Ti ratios cannot obtain. This is accomplished by lowering the Al/Ti ratio and adding Nb so that gamma prime constituents, $\text{Ni}_3(\text{Al}, \text{Ti})$, do not form as quickly but instead γ'' forms. The formation of Ni_3Nb will help avoid post weld cracking but the addition of Nb will also encourage solidification cracking in the heat-affected zone. The formation of solidification products such as laves phase/gamma eutectic, which have a low melting point, will retain liquid that is enriched in Nb, Si, and Ti between the dendritic structures which will lead to solidification cracking [33-34]. By carefully controlling the alloying elements, Inconel 718 has become the most used superalloy in the aerospace industry since it has excellent properties at elevated temperatures.

1.3.5 TI- 6AL- 4V

Titanium was used in the wing and elevon construction on areas such as the seal panels and rub strips. These components had a honeycomb sandwich construction and would separate the wing and elevon section and were also used on the top surfaces of the elevon to seal the area of the panels. The titanium alloy used on these two components was composed of 90 wt. % Ti, 6 wt. % Al, and 4 wt. % vanadium (V) and is commonly known as Ti-6Al-4V or Grade 5 alloy. It is a two phase, metastable, titanium alloy where Al is the alpha stabilizer and V will be the beta stabilizer. Since this alloy will go through an alpha/beta phase transformation, several microstructures can be obtained depending on the processing method it goes through, heat treatment, and the required properties for a specific application. The alpha phase can have elongated plates if the material has been worked or may have equiaxed globular

grains if the materials were worked excessively since recrystallization will occur. The beta phase will also have different morphology and can transform into martensite or Widmanstätten plates but will show as an intergranular formation in the matrix [35]. These types of changes in morphology on the alpha and beta phase will depend on the cooling rates that they experience.

Ti-6Al-4V is usually used in the annealed condition which requires heating the metal at 1038°C (1900°F) between half an hour and 2 hours before it is furnace or air cooled [36]. In the annealed condition, titanium will obtain the highest tensile and fatigue strength as well as hardness values. The additions of Al and V as the alloying elements allows this alloy to have great tensile strength and toughness at temperatures up to 427°C (800°F) aside from being light weight which makes it a very desirable material to use in aerospace applications. The UTS for this alpha-beta alloy is approximately 950MPa (138ksi) and the yield strength is 880MPa (128ksi) [37]. Ti-6Al-4V will have a fracture toughness of 75MPa-m^{1/2} (68ksi-in^{1/2}) and a fatigue strength of 510MPa (74ksi). Typical hardness values for Ti-6Al-4V are between Rockwell C 30 and 34 and have a melting range of 1604°C (2920°F) and 1660°C (3020°F).

Table 1.2 Chemical composition of surrounding components near the elevon actuator shaft.

<i>Wt. %</i>	<i>Al</i>	<i>Cr</i>	<i>Cu</i>	<i>Fe</i>	<i>Mg</i>	<i>Mn</i>	<i>Mo</i>	<i>Nb+Ta</i>	<i>Ni</i>	<i>Ti</i>	<i>V</i>
<i>Al 2024</i>	94	---	3.8	0.5	1.2	0.3	---	---	---	0.15	---
<i>Type 304 SS</i>	---	18	---	72	---	2.0	---	---	8.0	---	---
<i>Inconel 718</i>	0.8	20	---	14	---	.35	3.0	5.5	55	1.0	---
<i>Ti-6Al-4V</i>	6.0	---	---	---	---	---	---	---	---	90	4.0

This titanium alloy will immediately form an oxide layer when exposed to oxygen or water which makes it have an excellent resistance to corrosive environments especially in seawater. The oxide film will form spontaneously and in a continuous manner making it very adherent and stable. Few conditions will compromise the oxide layer such as reducing acids or dry chlorine gas [38]. Problems can be encountered if titanium is used in questionable conditions promoting stress-corrosion cracking and hydrogen embrittlement. Environments that will lead to these degradation mechanisms could be the use of chlorides, phosphoric acids, and hydrofluoric and hydrochloric acids. Hydrocarbons will lead to the breakdown of the protective layer and corrosion will attack the Ti-6Al-V4. In the Space Shuttle *Columbia* investigations that have been conducted, Ti-6Al-4V was known to ignite and combust well below the melting temperature when tested in oxygen rich environments [39]. Due to the harsh re-entry

environments, the microstructures of samples tested changed as it went through oxidation, ignition, and combustion stages. There is a possibility that titanium components that were in the surrounding areas of the hydraulic system had the same response as these samples tested in the arc jet facilities before being deposited onto the shaft.

Table 1.3 Properties for materials surrounding hydraulic elevon actuator shaft.

<i>Properties</i>	<i>Solidus (°C)</i>	<i>Liquidus (°C)</i>	<i>Operating Temp. (°C)</i>	<i>UTS (MPa)</i>	<i>TYS (MPa)</i>	<i>HRB</i>
<i>Al 2024</i>	500	638	400	469	324	75
<i>Type 304 SS</i>	1399	1454	899	621	290	80
<i>Inconel 718</i>	1260	1336	704	1103	979	36
<i>Ti-6Al-4V</i>	1604	1660	427	950	880	32

1.4 PROJECT DESCRIPTION

Research on materials characterization of the deposits found throughout the starboard (inboard) elevon actuator shaft was proposed in order to have a better understanding of the different material systems' behavior in re-entry environment as well as thermal conditions that are experienced in this harsh environment (Figure 1.2). A thorough evaluation of four different sections on the starboard-side of the actuator shaft was be conducted and finding several deposition layers, thermal alterations, and the ability to correlate the depositions with the elevon position. These observations were expected since the four areas that were examined do have different textures and thicknesses which may imply unique depositions throughout the event. By characterizing these deposits, new information on the behavior of several materials can possibly be known and help determine if these material systems are suitable to keep using in future spacecraft design.

To conduct a detailed analysis of the shaft, non-destructive evaluation (NDE) and the use of analytical instrumentation were be used in this research. Noting the state of the *Columbia* debris upon arrival was a highly emphasized requirement from the National Aeronautics and Space Administration (NASA); this requirement was satisfied by taking sufficient photographic documentation. Once relevant NDE techniques are exhausted, sectioning proceeded to continue analyzing the deposits found on the

shaft. Analytical instrumentation such as light microscopy, scanning electron microscopy with energy dispersive x-ray spectroscopy, x-ray diffraction, and transmission electron microscopy will be used to do elemental analysis and possibly identifying the exposure temperatures.



Figure 1.2 Starboard-side of starboard (inboard) elevon actuator shaft showing significant amounts of deposits.

Microscopically analyzing these deposits, looking at the different layers, if any, noting the thermal alterations that occurred, possibly figuring out the temperatures that were reached as they were being deposited is research that will help future generations of engineers decide what materials can be safely utilized in space on future spacecraft. Since there was evidence found in the elevon actuator that the orbiter rotated 180°, directionality on how the material got deposited onto the shaft will be analyzed in this investigation as well. Data obtained from this study can help verify if the vehicle did in fact fly backwards at some point throughout the catastrophic event. Analyzing these results will provide valuable knowledge on different material systems, how they behave in the re-entry environment, and possibly the position of the elevon at different times throughout the breakup.

CHAPTER 2: EXPERIMENTAL PROCEDURES

Characterization of the starboard-side of the shaft will require several steps to achieve. As mentioned earlier, there will be two phase: a non-destructive evaluation phase and the other involves optical microscopy. Materials characterization will be the focus in this project since it is a fundamental process that will support any information that was obtained by visually or hypothesized. Without materials characterization, validating the materials properties, structure, and its behavior is practically impossible. The scientific understanding of materials science would be unknown if microscopy and spectroscopy was not applied. These techniques are needed to examine the deposits and the base material of the shaft, providing answers to questions being asked in this project. Identifying the elemental composition of the deposits and noticing how they got deposited on the shaft, their flow trajectory or any particles that were embedded in the material will be possible by conducting materials characterization. The different techniques that will be used in this research will be explained in this chapter.

2.1 METHODOLOGY

The first phase of this project will consist of NDE where information such as the as-received state of the elevon actuator was documented. This will be accomplished by taking high-definition photography and noting any important details seen on the actuator and its surrounding areas as it is being inspected visually. Other techniques that was employed to forever capture the details found on the actuator shaft will be 3-dimensional modeling using commercial available software. Besides documenting the physical state of the shaft, dimensional analysis as well as elemental composition of the surface deposits was done. Non-destructively, the diameter of the shaft can be calculated and an estimated thickness of the deposits found on the surface of the shaft. Also, an x-ray fluorescence portable detector was used to get the representative composition of the elements present on the surface of the shaft.

The second phase of the project will include sectioning of the shaft as well as looking at the samples at a microscopic level. A sectioning plan specifying where the shaft would be sectioned will be

provided and the areas of interest will be identified by carefully analyzing the information that has been compiled at this point in the research. Metallography will take place after all sectioning and surface analysis is completed in order to look at the cross-sectional view of the deposits. Characterization of deposits and base material will be performed using x-ray diffraction (XRD) and scanning electron microscopy (SEM) with energy dispersive x-ray spectroscopy (EDS) capabilities. Optical microscopy will also be used for characterization. Using this methodology will lead to a thorough materials characterization of the actuator shaft.

2.2 NON-DESTRUCTIVE EVALUATION

The NDE methods that were performed were as-received photography, visual examination using high-definition photography, 3-dimensional modeling, dimensional analysis, and preliminary elemental analysis. The details and information that were obtained from NDE were essential to the research since the surface of deposits were examined more closely. Referencing back to information obtained from NDE will be necessary once sectioning of the component is permitted since it will assist in selecting the areas where samples will be taken from for further examination.

2.2.1 AS-RECEIVED PHOTOGRAPHY AND VISUAL EXAMINATION

Coming from the Space Shuttle *Columbia* and being a component that was loaned to UTEP by NASA's *Columbia* Research and Preservation Office, documentation in every aspect of the starboard elevon actuator shaft was crucial. By taking photographs of the starboard (inboard) elevon actuator shaft, documentation of the component in its original state upon its arrival at UTEP was accomplished. Photographs will be captured by using a Sony Alpha NEX-5T digital camera with 16.1 mega pixels and an ASP-C sensor which produced a high-quality image. The component was staged by adding a solid blue background that worked as a backdrop and eliminated any background distractions so that it solely captured the detail in the shaft. A dimensional reference will also be used while photography was performed. During the as-received photography stage, visual examination of the actuator shaft was also

conducted. Close attention to every detail was the focus, while visually examining the starboard (inboard) elevon actuator as a whole, noting details such as color, surface texture, solidification of deposits, directionality, and any unusual markings were noted. With the information acquired by doing a visual examination, different areas of interest were identified to do a more in-depth analysis of each section. It was of great importance that the as-received photography and visual examination were conducted since these two techniques can forever capture evidence that may no longer be present once sectioning of the actuator was performed.

2.2.2 3-DIMENSIONAL MODELING

Another procedure that was considered for this research was using a 3-dimensional software that would construct the shaft and apply its texture to it as well, providing an additional way to preserve the *Columbia* debris prior to sectioning. 3-dimensional (3-D) modeling of the shaft was performed on specific regions of the actuator using a software called PhotoModeler Scanner. To make the 3-D model, photography of the actuator at different angles were taken using the same Sony NEX-5T camera used for the as-received photography. For a model to be built, the photographs must be taken in a way that there is an overlap between photographs and that the component was not moved while this process was completed. These were important procedures that needed to be followed since the software used the background of each photograph as reference points to automatically match features of the overlapping photos. The number of photographs taken ranged from 100-400 depending on the different angles that were chosen and how much was overlapped in each photograph. Once the photographs were uploaded to the software it produced a dense point cloud from photographs of textured surfaces to build a 3-D model of the object photographed. Since the elevon actuator was a very large component, and the location where it was stored were not optimal, there was limited space access to all surfaces of the component. Only a portion of the starboard elevon actuator and shaft were modeled and an animation of the 3-D model was also produced.

2.2.3 DIMENSIONAL ANALYSIS

Getting dimensional references was something that was done and was as important to this research as the photographic documentation since this was a component coming from a catastrophic event and the dimensional changes to the component might have occurred. The construction of the elevon was made by Lockheed Martin decades ago and NASA was not able to obtain many drawings belonging to the elevon actuator and the components that make it up, which made it necessary to obtain measurements before proceeding to sectioning. Dimensions of the total length of the component that was received as well as dimensions of the shaft itself were obtained since drawings on the elevon debris were very limited. Measurements of the shaft also included the average diameter of the shaft with and without deposits so that calculations can be made to approximate the thickness of the deposits found along the shaft.

To obtain dimensional analysis of the diameter of the shaft, a digital caliber was used. Two measurements were made relevant to their respective positions of the clock face. 12 o'clock was defined with respect to the nut located in the center of the housing, next to the electrical junction box. The first measurement was taken at the 12 o'clock and 6 o'clock positions and the second measurement at 3 o'clock and 9 o'clock. These measurements occurred in intervals of 10 millimeters. The measurements were taken at a certain distance with respect to the actuator length, starting from the location where the shaft connects to the housing.

Even though there is not much information on the construction of the elevons or the materials used on it, NASA did provide information on the elevon deflection at several points throughout the breakup of the space shuttle. The calculations provided an estimate of the elevon's angles at different distances belonging to the three unique indications found on the shaft which were mentioned earlier. Included with this information were dimensions of the hydraulic system that contained the actuator shaft which will be discussed later.

2.2.4 ELEMENTAL ANALYSIS

The final NDE method that was used to investigate the actuator shaft while preserving its original state was elemental analysis. This was accomplished by using a handheld Olympus INNOV-X Delta x-ray fluorescence (XRF) analyzer that contains a 40kV miniature x-ray tube and a Silicon Drift Detector. With this device, preliminary results of elements present on the surface of the shaft were identified and their corresponding amounts quantified. Though using the XRF analyzer might be a fast and accurate way of getting a materials composition, there were a few limitations when it came to using it. One of these limitations was the depth that the x-rays can penetrate through the material. In general, this depended on the elements present at the surface and where they were in the energy spectrum. The higher up in the energy spectrum, the greater the depth at which the x-rays were be able to penetrate in the sample [40]. For lighter elements, the depth of penetration would only be the surface while, heavier ones might penetrate up to a centimeter. Most of these devices are not able to accurately measure the elemental composition of elements with an atomic number less than 12 [41]. The thickness of the material also played a role in how accurately the elements present could be quantified; thinner samples were affected differently than bulkier ones. Another limitation was the spot size that could be analyzed, for the INNOV-X Delta XRF, it was supplied with a standard 10mm diameter analysis spot, which could be changed to a collimated 3mm diameter spot size for smaller areas to be analyzed. Both spot sizes were be used in this analysis.

When conducting elemental analysis on areas that were reachable, a survey grid overlay was established on the actuator rod surface to facilitate documentation. This allowed for the exact location where the XRF was used along the shaft to be easily identified since there was a numbering system on the grid. The elemental composition of all the areas that were analyzed including the areas of interest were documented in an excel spread sheet for whenever referencing was needed. Because the XRF was limited to detecting surface elemental composition, results obtained in this analysis might vary once elemental

analysis of the cross-sectional areas was performed, but elements with greater amounts detected were present in both analyses.

2.3 SECTIONING

The as-received starboard elevon actuator debris that was recovered from the *Columbia* accident was a very large component since it contained a portion of the wing actuator rib. Since this was the case, mechanical disassembly at the forward attachment of the actuator was necessary to get significantly more access to the actuator shaft. By doing this, the wing actuator rib, which also had the elevon rib attached to it and together were part of the structural components of the space shuttle, were separated from the hydraulic system making the piece significantly smaller and manageable for sectioning. With this accomplished, sectioning of the shaft occurred in three different stages, preliminary sectioning, secondary sectioning, and additional sectioning. In order to isolate the shaft from the actuator, a water jet cutter was used to prevent any thermal alterations that might have occurred if another type of equipment was used. This type of equipment was not available at the university, but the equipment was available in El Paso. As emphasized before, NASA recognizes the value of the *Columbia* debris and had loaned these components for research with the condition that conservation of the piece would be preserved as much as possible. With this request, the research done on the shaft would only concentrate on the starboard-side of the elevon actuator shaft. The other half will be conserved for any other research that might be necessary at a future time.

2.3.1 PRIMARY SECTIONING

After mechanically disassembling the wing actuator rib from the hydraulic system, sectioning of the shaft proceeded. It was necessary to cut the shaft off the hydraulic system since there was no possible way available that would allow for manual disassembly. A water jet cutter at a local machine shop made three primary cuts, which are shown by the yellow dashed lines in Figure 2.1. Figure 2.1 indicates the location of where sectioning was done and indicates the order at which each cut were executed. Cuts 1

and 2 were transverse cuts, while Cut 3 was an axial cut that ran along the 12 o'clock reference used for dimensional analysis.



Figure 2.1 Primary sectioning plan shown in the 12 o'clock view (top view). Numbering indicates how sectioning would proceed and the yellow dashed lines indicate the location where sectioning was done along the shaft.

By using the water jet, it provided a better precision with the absence of any heat induced changes in the microstructure. The water jet that was used to cut through the actuator uses a mixture of water and an abrasive slurry at very high velocity and pressure. Water, along with an aluminum oxide abrasive were ejected out of the nozzle and onto the component, which was submerged in a bath of water to deliver the cutting action without any heat affect.

The precision of the cut depended on the nozzle size being used and due to this being a high-pressure stream of water, minimal loss of deposits along the cutting lines was expected to occur. With this in mind, precautions on not eliminating areas of interest had been considered when choosing where the three primary cuts were done. Since water was used in the sectioning process, and this is a ferrous material, corrosion might have become an issue if the proper steps were not taken. To prevent corrosion or any consequent damage from occurring after the three primary cuts are completed, parts were rinsed with water followed by a bath of isopropanol and then blown dried to eliminate all moisture and prevent corrosion from occurring in the future. Note that the starboard-side of the shaft was the focus of the project

and was the only piece that was not stored in crates. This side of the elevon actuator shaft was then sectioned again to provide the samples for the research.

Cut 1 which was a transverse cut was located at the end of the shaft where it connects with the clevis and locking nut as shown in Figure 2.1. This cut was necessary since disassembly of the locking nut and clevis from the shaft was not successful when attempted. The locking nut and clevis was not further analyzed and was stored after sectioning was completed and the component had been blown dry after isopropanol was applied. The next cut that was made was Cut 2, which is located directly next to the hydraulic assembly. The cut was made where the threaded area began completely through the shaft. At this point, the shaft was freed from the actuator and the third cut followed. Cut 3 was an axial split at the 12 o'clock reference that sectioned the shaft in half resulting in the port and starboard-sides of the shaft. This third cut also isolated the piece of housing from the hydraulic assembly which was Area 1 and would be part of this research.

2.3.2 SECONDARY SECTIONING

Once the shaft was liberated from the hydraulic system, secondary sectioning took place to section the starboard-side of the shaft into smaller sections where areas of interest were identified, but additional sectioning was needed to obtain the sample pieces used for research. At this point, since it was only one side of the shaft that was sectioned and was very manageable to work with, an abrasive cut-off saw was used to do all the remaining cuts. The water jet cutter was not considered for secondary cutting since the resulting pieces would be small in size and the stream of water had the potential of disrupting the areas of interest. The cut-off saw that was used for any sectioning from this point on is a Buehler AbrasiMet 250 Abrasive Cutter and the blade used was a 22.9cm (9") Al_2O_3 wheel with Rockwell hardness scale C (HRC) that ranges between 35 and 50. This type of blade is used for medium hard steels and is suitable for a 17-4 PH stainless steel. Secondary sectioning of the shaft included five transversal cuts which provided the four areas of interest. These cuts were Cuts 4 to 8 and are depicted by the yellow dash lines in Figure 2.2.

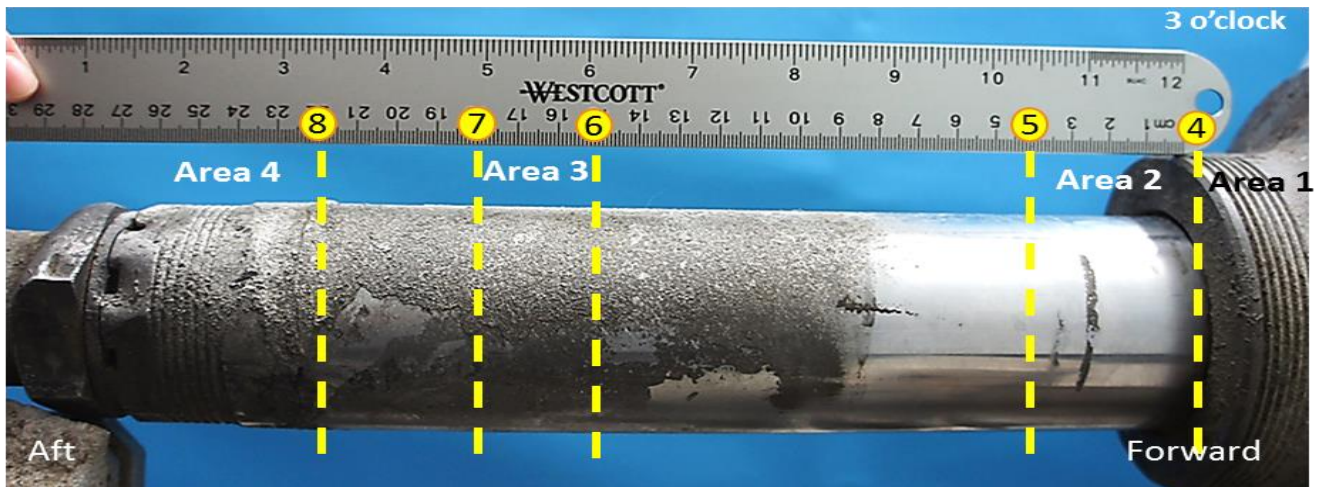


Figure 2.2 Plan showing secondary sectioning. Cuts 4 through 8 as shown by the yellow dashed lines.

Cut 4 and 5 were transverse cuts that provided samples for Area 2, which contains the three deposit lines. Since these two cuts were close to the deposit lines, they were made in a way that they were a safe distance away from the deposit lines. Cut 6 and Cut 7 were also transverse cuts that provided samples for Area 3 where deposits cover most of the section. The final transverse cut was Cut 8 and provided Area 4, which had a much thicker layer of deposit and by visually examining this region, it seems to have reached higher temperatures than other regions of the shaft. From these four areas, additional sectioning followed to obtain several samples from each region that could be examined microscopically.

2.3.3 ADDITIONAL SECTIONING

Additional sectioning was necessary in all four areas of interest in order to obtain small sample pieces that could be accommodated in all the equipment used to analyze the deposits found on the shaft. These cuts were done with the same cut-off saw used for secondary sectioning and also used the same type of blade. An additional cut were made in Area 1, one axial cut and one transverse cut were made in Area 2, two additional axial cuts were made in Area 3, and two axial cuts and one transverse cut were also made in Area 4. The additional sectioning resulted in a total of ten samples that were analyzed under the microscopes. The sectioning plans for the additional cuts, which are shown as red dashed lines, can be seen in Figure 2.3. After sectioning was completed, all the samples were cleaned using a Barnson 1510

Ultrasonic Cleaner. The basket was filled with water and the samples were each placed in a beaker with methanol for 20 minutes to get rid of any buildup that might have occurred during sectioning or while debris was dislodged from impacting the earth.

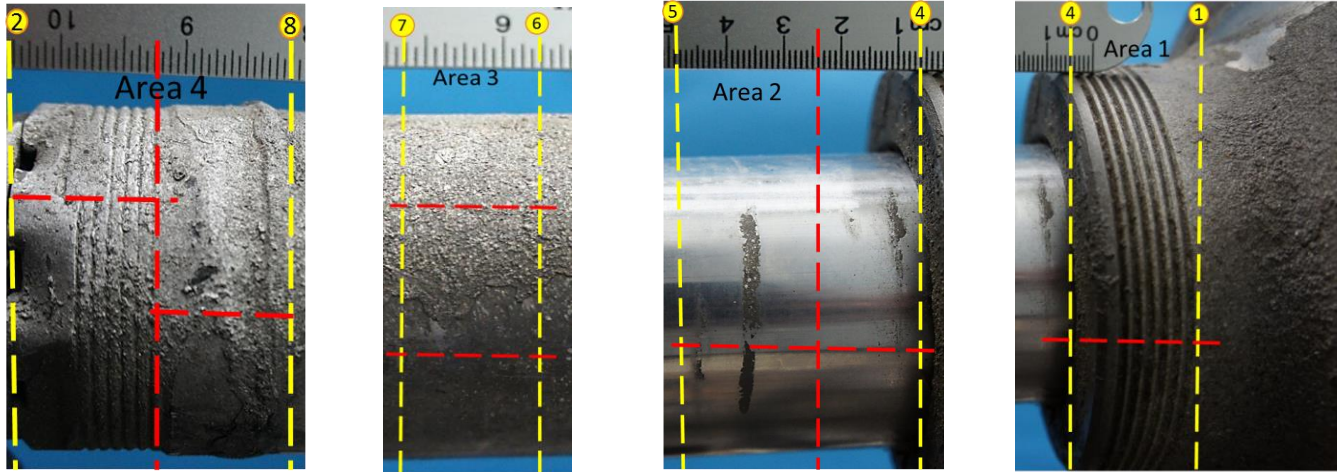


Figure 2.3 Plan showing additional sectioning in each the four areas of interest which are shown by the red dashed lines.

2.4 MICROSCOPY

To perform a detailed material characterization of the starboard elevon actuator shaft, the following instrumentation was utilized. Characterization of the deposits and base material were performed using x-ray diffraction and scanning electron microscopy with energy dispersive x-ray spectroscopy capabilities. The Keyence and optical microscopes helped characterize the surface and sub-surface of the areas within deposits. The analysis consisted of a surface analysis, which using the SEM with EDS capabilities, followed by an x-ray diffraction study. After the surface morphology of each sample was examined, a cross-sectional analysis was performed. Using these instruments allowed further understanding how the materials that surrounded the elevon actuator behaved during re-entry.

2.4.1 SCANNING ELECTRON MICROSCOPY

Surface analysis as well as cross-sectional analysis was conducted on samples belonging to the four different areas on the shaft. Surface analysis was done first and once that was completed, along with XRD, the metallography prepared cross-sectional samples were then analyzed under the SEM. The SEM

was essential to this study because it provided information about the surface morphology and any layers that were deposited on the shaft. It was helpful in determining the order of the different depositions present on the actuator rod. Looking at the morphology that was present in each sample revealed information on how the solidification occurred and if the layers being deposited were uniform throughout. The SEM with EDS capabilities provided information about the composition of the deposits and the elements present in the layers. Elemental data obtained from the surface and cross-section was then be compared to each other and differences will be discussed.

The instrument that used in this research was be a Hitachi S-4800 field emission SEM with EDS. The accelerating voltage used was between 15kV and 20kV and images of the surface and cross-sectional views were taken at different magnifications. Elemental analysis was obtained with EDS on spots that were of interest due to their distinct morphology and texture throughout each sample. Copper tape was used when necessary to decrease the charging of electrons and allow the charge build up to dissipate via the sample holder.

2.4.2 X-RAY DIFFRACTION

Results of chemical composition on samples that were analyzed with the aid of energy dispersive x-ray spectroscopy, were compared to the results of x-ray diffraction, which verified the results or brought attention to any discrepancies. XRF provided information on the crystal structure, which could possibly aid in the identification of the different compounds that were deposited onto the shaft. Considering these deposits most likely to include different material systems, it was essential to make sure that all the information that can be obtained from XRF be examined thoroughly. This analysis was carried out on the Bruker D8 Discover using a scan rate of 5° per minute and measuring angle 2-theta from 20° to 120°.

2.4.3 OPTICAL MICROSCOPY

Once surface analysis was performed for all the samples, metallography was the next step to take in order to prepare the samples for optical microscopy and SEM analysis. The cross-sectional views of

the samples were taken for a closer look at the microstructure of the base material. Samples were first ultrasonically cleaned with a methanol solution, once again using the same method used after sectioning and were then be cold mounted. Mounting the samples was done by using an epoxy resin and hardener, five parts to one by weight, respectively. Once samples were cured, grinding and polishing of the samples followed to make the surface of the specimen to be as flat, smooth, reflective, and scratch free as possible. A Buehler MetaServ 250 grinder-polisher wheel was used at a speed of 300 rpm. Samples were ground using silicon carbide abrasive paper with increasing fineness. Grit sizes of 80 up to 1200 were used and the samples were then polished with a polishing cloth using diamond suspension media. The diamond suspension media used varied in size from 6 μ m to 0.05 μ m. After samples were polished, they were chemically etched with Kalling's No.2 reagent. This etchant consisted of 5g of CuCl₂, 100ml of HCl, and 100ml of ethanol and was suitable for the 17-4 PH stainless steel shaft.

After the specimens were prepared for optical light microscopy, characterization of the surface and sub-surface of the areas with deposits was performed. Analyzing the microstructure of the samples and being able to notice any microstructural alterations revealed how these materials behaved and estimates of the probable temperatures reached. Phases or constituents present, inclusions, and documentation on the depth and morphology of the deposits were identified during this stage. The equipment used for this study was a Zeiss Observer.D1m optical microscope and micrographs of the microstructure as well as the deposits were taken at different magnifications.

CHAPTER 3: NON-DESTRUCTIVE AND SECTIONING RESULTS

The first phase of the project consisted on documenting the original state of the elevon actuator where the techniques used would avoid any type of destructive methods that could potentially hinder the physical state of the component. The results of the applicable techniques used on the shaft, which include as-received photography, 3-dimensional modeling, dimensional analysis, and elemental composition of deposits on the surface of the shaft will be discussed. Details on textured surfaces, color, and location of such descriptions will be provided and will ultimately help identify the areas where sample were taken for further examine. The elemental composition done on the surfaces of the shaft was also be essential in the process of choosing where the shaft was sectioned and samples captured. Being that there are different material systems that surround the shaft, many elements were detected but expectations were that there were elements that were present in greater concentrations than others. The same major elements detected by the XRF were expected to show on the results obtained later when different characterization techniques were used and would serve to verify preliminary results. The final images of the 3-dimensional model that were obtained from photographs also served to illicit physical attributes of the deposits. Data collected at this stage was preliminary since analysis of the component non-destructively and results were only pertinent to the surface. Nonetheless, NDE was very helpful when analyzing all the information obtained at the end of the study.

Once the first stage of the research concluded, sectioning of the shaft took place. Sectioning had to be carefully considered since NASA allowed for only minimal sectioning of the shaft where conserving intact pieces was the major goal. The pieces that would not be used for the research were safely put away and preserved for possible research in the future. Sectioning occurred in three different stages which lead to samples suitable for microscopic analysis. Results after sectioning the shaft will be shown and the reasoning for sectioning in that manner will be discussed.

3.1 NON-DESTRUCTIVE EVALUATION

Four non-destructive techniques were performed on the elevon actuator and techniques were chosen according to the condition of the received component and the equipment available at the university. These four techniques, as aforementioned, were as-received photography, modeling the actuator shaft in three dimensions, recording dimensions of the shaft, and using the XRF to survey the surface of the deposits found on the shaft for their elemental composition. Note that even though these techniques were going to be applied to most of the component, the main area of interest is the starboard-side of the actuator shaft.

3.1.1 AS-RECEIVED PHOTOGRAPHY AND VISUAL EXAMINATION

As-received photography and visual examination alongside was done first to document the state of the elevon actuator shaft upon its arrival. Figure 3.1 shows the as-received photography of the starboard (inboard) elevon actuator as a whole, where the position of the elevon actuator shaft in relation to the whole component is pointed out by an orange box. As shown in Figure 3.1, attached to the actuator at the forward attachment is a large piece of airframe. The airframe attached to the flight control system hydraulic actuator, which is part of the wing actuator rib assembly from a conventional aluminum alloy. Looking at the rib assembly attached, hot tearing occurred at the forward end of the rib all throughout the edge as well as the top portion of the rib where four attachments are protruding. Hot tearing most likely occurred as the wings were breaking off from the main body. Besides the sharp edges that were seen along the forward edge where it detached from the rest of the wing assembly, it sustained minimal damage in the surrounding areas. A brown coloration with oily texture covers regions of the component which can be contributed to hydraulic fluid which probably came out of the actuator as it made its way to the ground. In the aft portion of the attached rib assembly, mechanical damage was noticed just below the location of the shaft. Heavy deposits cover the region as well and evidence of erosion which could also be seen in this region. Also, noted in this area, portions of the aluminum alloy were covered in dry mud and grassy

plants as well as corrosion products and oxidation in other areas which most likely occurred as a result of sitting in the swampy areas of north Texas and western Louisiana while the recovery team found it and brought it to the Kennedy Space Center in Florida.

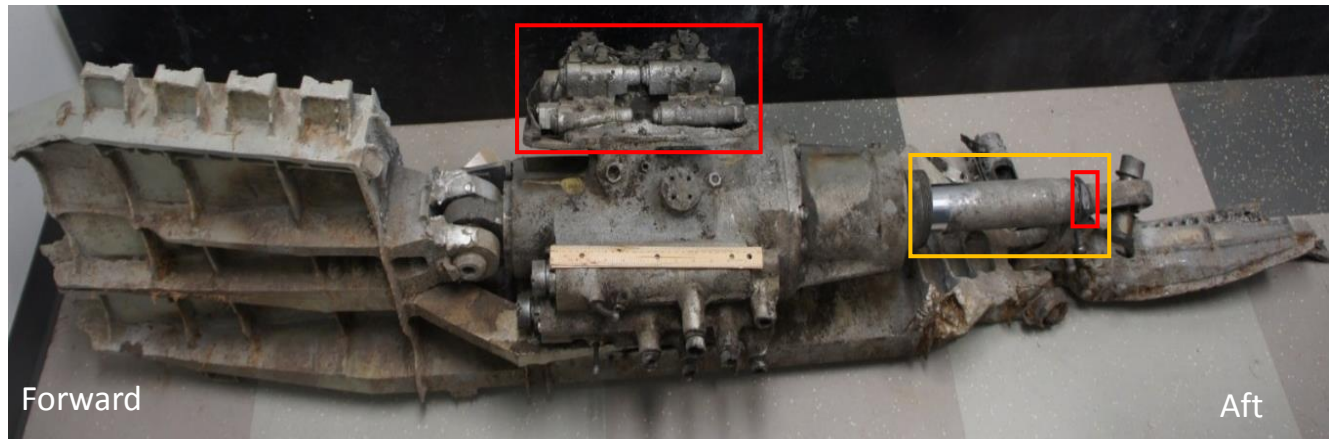


Figure 3.1 Starboard (inboard) elevon actuator. Orange box indicates location of elevon actuator shaft and red boxes show position of electrical junction box and locking nut where possible evidence of reverse flow occurred.

Now examining the hydraulic actuator, the presence of hydraulic fluid residue was evident throughout the component, particularly in the region closest to the shaft. On the port side, several hose connections were eroded away showing a few of them having possible flow directionality. Flow of superheated plasma seemed to be going from aft to forwards, showing some connections deteriorated more from the back portion than the front of them. This caused the cylindrical connections to have a slant opening to them. Other regions in the hydraulic actuator showed accumulations of metallic deposits especially located in the forward area of the actuator. These deposits were not very tightly adhered to the base metal and could easily flake off. Small components that protruded out of the hydraulic actuator also exhibited signs that they reached elevated temperatures, sufficiently high enough to cause them to melt at some point in time.

While continuing with visual examination of the actuator, there were two additional locations where possible signs of reverse flow could be observed. Evidence of what seemed to be the existence of reverse flow were seen in the electrical control module as well as in the locking nut of the actuator shaft; these are indicated in Figure 3.1 by the red boxes. The electrical control model or electrical junction box,

showed the housing material that used to protect this area was almost completely gone except for a small portion of the housing which remained intact at the bottom forward corner (Figure 3.2 Left). The bolts that held the housing in place showed erosion in most of the aft portion and negligible damage in the forward region. The components comprising the electrical junction box that were exposed had deposits on their surfaces and erosion could also be seen in several components, once again showing greater damage occurring on the aft region of the box. This could be a possible indication that the direction of flow was going from aft to forward instead of the usual direction of flow that the shuttle would see, forward to aft. Looking at the locking nut in Figure 3.2 (Right), it is clear that erosion occurred in this area where the direction of flow once again was from aft to forward. The image shows significant material loss, sufficient enough that the straight edges of the nut cannot be distinguished and the color of the nut is no longer shiny but dull and the texture is coarse. With different pieces of hardware showing possible evidence of reverse flow, it could be assumed that the vehicle rotated 180° at some point during the re-entry where the nose of the shuttle was traveling backwards.

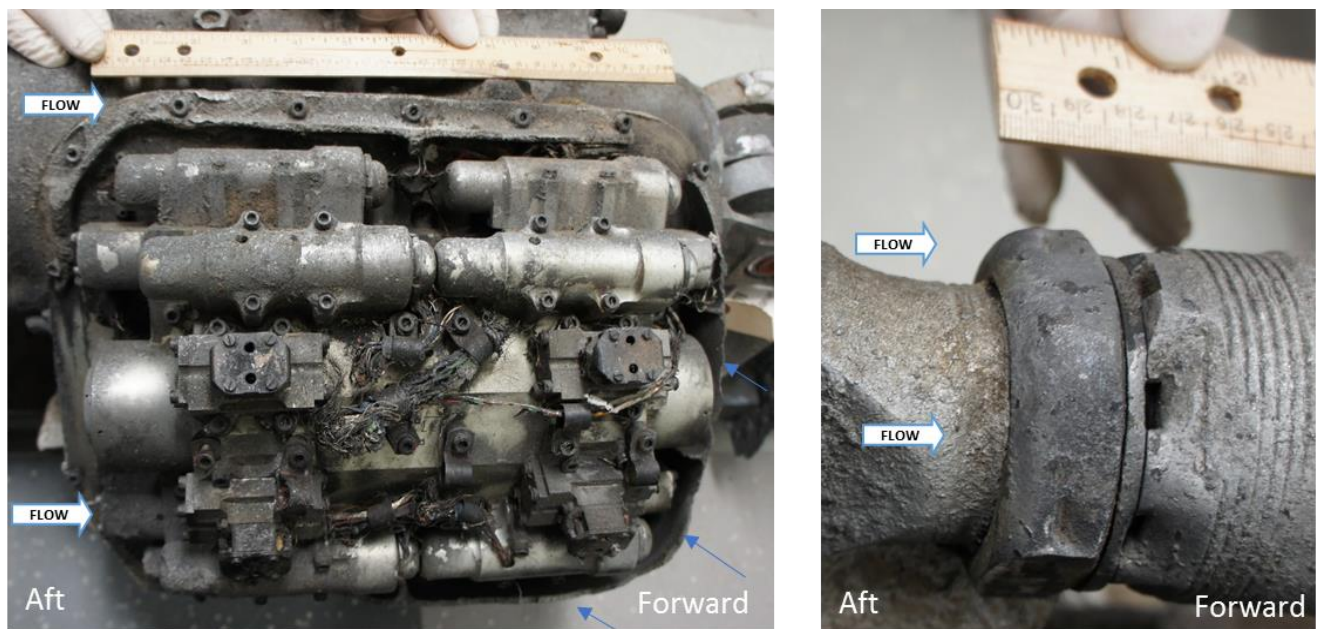


Figure 3.2 Left. Electrical control module with housing component mostly gone. **Right.** Locking nut of elevon actuator shaft showing erosion. White arrows indicate suspected direction of flow.



Figure 3.3 Port-side of starboard (inboard) elevon actuator shaft showing three different zones.

In Figure 3.3, a detailed photograph of the port-side of the starboard (inboard) elevon actuator shaft is shown. Visual examination revealed that for the port-side of the inboard starboard elevon actuator shaft there was a deposit-free zone located next to the housing. This deposit-free zone measured a few centimeters and had a plane, smooth, reflective surface. Adjacent to this section, there was a multi-directional spatter deposit zone, which extended through most of the shaft and the transition between these two areas was well defined by a straight vertical line. In this area, deposits seemed to transition from light to heavier deposits from top to bottom and from forward to aft. Also, the multi-directional streaks varied in length while other regions had a granular texture. One thing to note is that the underside of the shaft did not have many depositions. This might be a result of the shaft being shielded by part of the attached elevon actuator rib. Before reaching the end of the shaft, a heavy deposit zone was also identified. Here, thickness increased drastically when compared to the rest of the deposits. Near the end of the shaft, part of the locking nut can be seen where one of the faceted sides deteriorated and the loss of material was evident.

Figure 3.4 shows the starboard-side of the elevon actuator where the same deposit-free zone seen on the port-side can be seen with the exception that this shiny area is significantly larger. The deposit-free zone on the starboard-side was nearly double the size of the one seen on the port-side. A difference that can be noted when the deposit-free zone is compared to the port-side is that the starboard-side has three

distinctive deposit lines close to the housing of the hydraulic actuator. These deposit lines are running in a vertical direction and have a darker color than the deposits found on other areas. These deposits, even though they are linear along the edges, the lines are not continuous and deposits do not seem to have been deposited uniformly. There are regions where deposits appear to be thicker than other regions. The first deposit line is the closest to the housing and the deposit line further to the left is the third deposit line. The first deposit line is composed of a thicker and wider deposit on the top portion and then starts to diminish as it progresses to the bottom. The second deposit line contains the most molten metal. It appears to be the widest and longest of all three deposit lines as well as the one having a more uniform deposition when compared to the other deposit lines. The debris found here was also discontinuous at some point and there were several tiny spots where the deposit flaked off. The final deposition found on this area, the line closest to the deposit area, had debris on the surface that looks as if it was fading from right to the left. There were a lot of discontinuities seen in the third deposit line and only a small area where the deposition was substantial.



Figure 3.4 Starboard-side of starboard (inboard) elevon actuator shaft pointing out several areas of interest along the shaft.

Adjacent to this area, where the deposit zone begins, the texture of the deposits were very different to the ones found on the port-side; here, the deposits had a spray-like texture whereas in the port-side they were multi-directional spatter deposits. Another observation noted in this section was that portions of the

deposits have chipped off exposing a thin layer of deposit. This same thin layer of deposit was seen mostly in the middle section at the bottom of the shaft and had a smooth dark colored surface. In this region, there were small areas where the shiny base metal surface could be seen and no deposits seem to have adhered to those areas. The spray-like deposit, almost granular, seems to have adhered well to the base metal and looked evenly deposited throughout this area. Next to this area, where the heavy deposit zone was seen in the port-side, appeared to have a thermally eroded zone. Material loss was apparent in this region since the diameter of the shaft seemed to decrease across a length of a couple of centimeters. Observed in this area were thicker deposits found on either side of the depression where probable erosion occurred. In the threaded region at the end of the shaft, there were several threads located at the top of the shaft that were completely eroded away as if they were never there. These were some of the things that were identified while taking as-received photography and conducting visual examination on the starboard (inboard) elevon actuator, particularly on the actuator shaft.

3.1.2 3-DIMENSIONAL MODELING



Figure 3.5 3-D model of portion of the starboard view of the starboard (inboard) elevon actuator rib and shaft. White areas are incomplete regions in the model.

Following visual examination and high definition photography, 3-dimensional modeling was done, again, with the intention of keeping a record of the original state and dimensions of the component since the artifact was of high importance. The software used to achieve the 3-D model of the component was PhotoModeler Scanner. Photography of the shaft at different angles and at every visible spot were taken in order to capture the texture, shape, and position of the shaft. Since the elevon actuator received was a very large component and the location where it was kept was limited to a very confined space, access to all surfaces of the component was not possible and only a portion of the starboard elevon actuator rib and shaft were modeled (Figure 3.5).

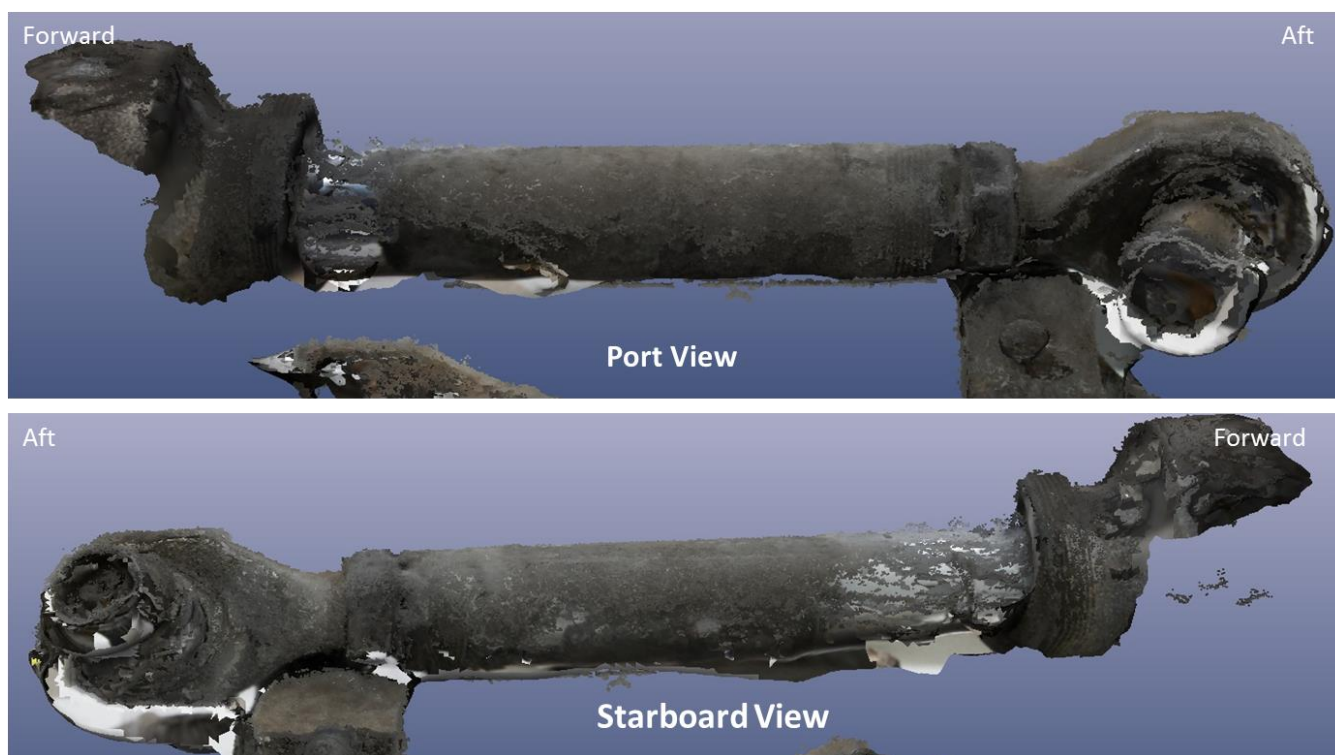


Figure 3.6 Top. 3-D model port-side of starboard elevon actuator shaft. **Bottom.** 3-D model of starboard-side of starboard elevon actuator shaft.

A 3-D model was obtained of the elevon actuator shaft since it is the focus of this research and is shown in Figure 3.6. An animation of the 3-D model was also made. Looking at Figures 3.5 and 3.6, several regions in the 3-D model were not completed due to the lack of photographs taken in those specific regions. Again, this is the result of having a limited space to take the photographs needed and not being

able to capture all the angles to complete the model correctly. Most of these regions were located on the bottom region belonging to the airframe and incomplete areas on the shaft were also located on the lower area of the shaft and regions of the clevis. These incomplete areas in the model are shown by the white regions. The model showed the deposits having a darker color which was distinguishable when compared to the base metal. Overall, the 3-D modeling of the shaft helped document several details found on it and the animated video will forever capture the shape and size of the elevon actuator.

3.1.3 DIMENSIONAL ANALYSIS

Dimensional analysis was done on the shaft before sectioning since no type of dimensional documentation was provided upon receiving the elevon actuator. This type of analysis would be helpful to note any differences seen in the port and starboard side of the shaft as well as obtaining a rough estimate of the diameter of the shaft with and without deposits which in turn would allow for the thickness of the deposits along the shaft to be estimated. A digital caliper was used to take several measurements of the diameter of the shaft. These measurements were taken at the 12 o'clock and 6 o'clock position and at 3 o'clock and 9 o'clock as explained earlier and their position in the shaft are referenced in Figure 3.7.

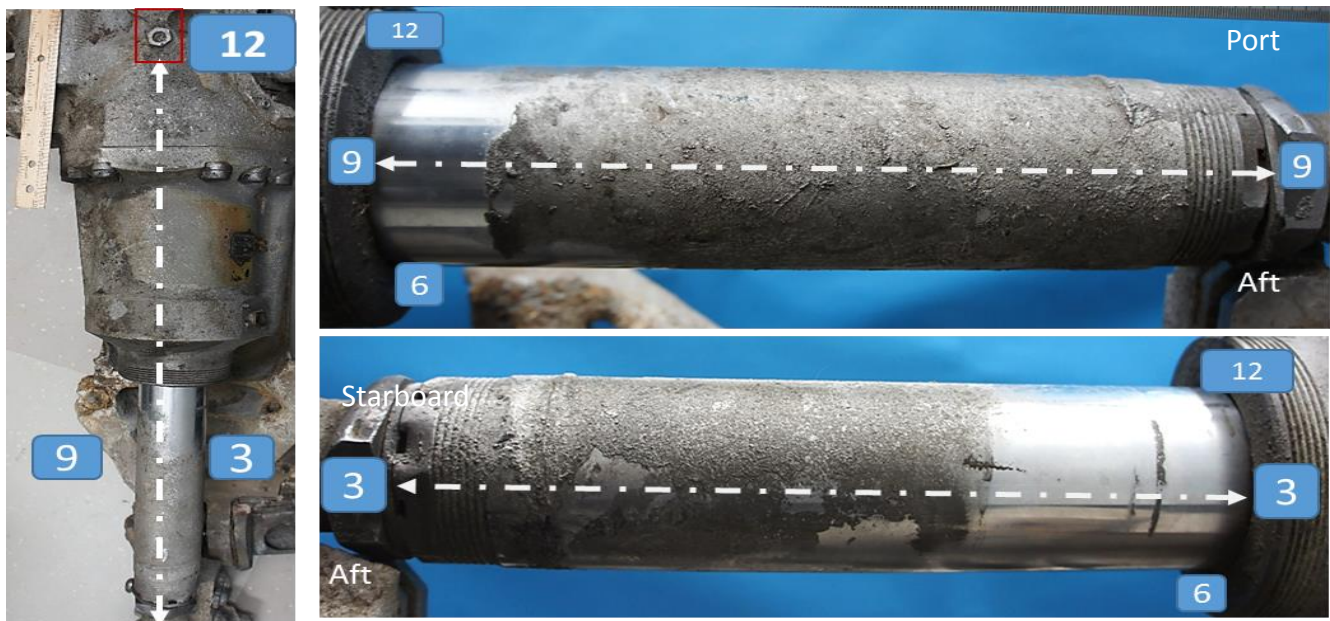


Figure 3.7 Left. 12 o'clock is defined by the nut as shown by the red box. **Top Right.** Port side of elevon actuator shaft showing the 9 o'clock position. **Bottom Right.** Starboard side of elevon actuator shaft showing the 3 o'clock position.

Using the positions of the clock to reference the positions where measurements of the diameter of the shaft were taken, the average diameter was 6.334cm (2.49”) and the average diameter of the shaft with deposits was 6.355cm (2.50”). Several measurements, but not all that were taken are included in Table 3.1 and a general trend was observed when looking at the average diameter of the shaft with deposits. As the diameter is measured from forward to aft, the diameter tends to increase in thickness, meaning that the debris deposited onto the shaft is increasing as it reaches the end of the shaft. The average thickness of deposits found along the rod was approximately 0.011cm (0.004”) and the maximum thickness of deposits found along the shaft was calculated to be 0.066cm (0.026”) which was located before the thermally eroded area pointed out in Figure 3.4.

Table 3.1 Several measurements taken with a digital caliper of the diameter of the actuator shaft at different positions relevant to the clock face.

<i>Position (cm)</i>	<i>1</i>	<i>3</i>	<i>4</i>	<i>5</i>	<i>6</i>	<i>7</i>	<i>17</i>	<i>20</i>	<i>21</i>	<i>22</i>	<i>23</i>
<i>12-6</i>	6.335	6.338	6.343	6.337	6.337	6.339	6.348	6.350	6.358	6.378	6.450
<i>3-9</i>	6.332	6.337	6.347	6.341	3.342	6.345	6.372	6.360	6.359	6.351	6.484
<i>Average Diameter</i>	6.334	6.338	6.345	6.339	6.340	6.342	6.360	6.355	6.359	6.365	6.467

The total length of the visible shaft was 26.2cm (10.3”) long and the visible deposit-free zone for the port-side measured approximately 3.5cm (1.38”) and 7.5cm (2.95”) for the starboard-side. When measuring the length of the deposit zone which covered the rest of the shaft after the deposit-free zone, the port-side was covered in deposits for a length of approximately 22.7cm (8.94”) and the starboard-side covered a smaller area, only 18.7cm (7.36”) in length. Table 3.2 shows all average measurements taken of the starboard elevon actuator shaft. Since the deposit-free zone differs in length for both the port and starboard-side, with the port-side having a shorter deposit-free zone and a longer deposit region, it is probable that the port-side was shielded longer than the starboard-side throughout the duration of the breakup of the shuttle. The final measurements that were taken of the component received included the length of the elevon actuator rib that was attached to the control flight system hydraulic actuator and the hydraulic actuator itself. The total length of the starboard (inboard) elevon actuator that was recovered

from the Space Shuttle *Columbia* measured approximately 2.33 meters (7.64') long. The hydraulic actuator measured 72.54cm (28.56") in length, excluding the shaft since the total length of the whole component will depend on the position of the elevon. Illustration 3.1 shows the length of the flight control system hydraulic actuator.

Table 3.2 Average results for several measurements taken of the shaft including length, diameter, and deposits.

<i>Total Length of Shaft</i>	<i>Original Diameter</i>	<i>Diameter with Deposits</i>
26.2cm	3.5cm	7.5cm
<i>1st Deposit Line</i>	Length ≈ 1.9cm	Width ≈ 0.015cm
<i>2nd Deposit Line</i>	Length ≈ 4.2cm	Width ≈ 0.025cm
<i>3rd Deposit Line</i>	Length ≈ 1.1cm	Width ≈ 0.010cm
<i>Deposit Free Zone</i>	Port ≈ 3.5cm	Starboard ≈ 7.5cm
<i>Deposit Zone</i>	Port ≈ 22.7cm	Starboard ≈ 18.7cm

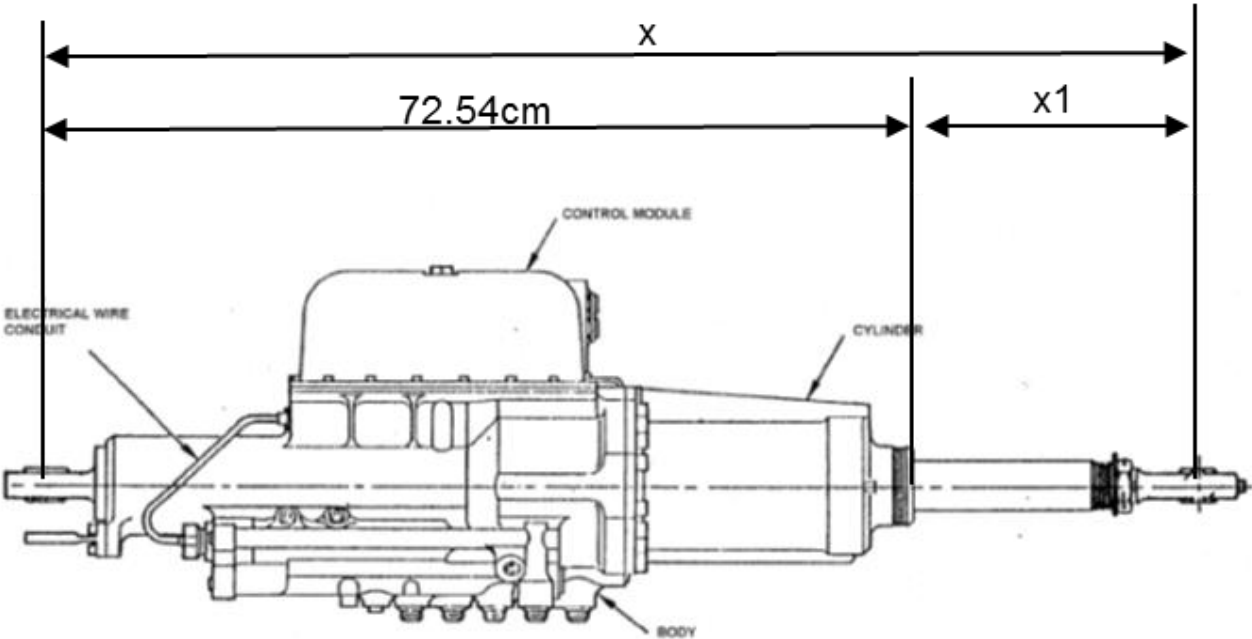


Illustration 3.1 Top view of the hydraulic system that makes part of the elevon structure. X presents total length of component depending on elevon position. Illustration provided by NASA.

3.1.4 ELEMENTAL ANALYSIS

Using an Olympus INNOV-X Delta portable XRF on areas of interest, preliminary elemental analysis on the surface was obtained. The results received back from the portable analyzer shows a list of elements that were being detected at the surface in the area analyzed. The results usually contained a few

elements but only the elements with the greatest amounts detected were relevant to the discussion. The first area that was analyzed was the deposit-free zone. In this area chromium (Cr) was the element that was detected in greater amounts and was concluded that the actuator shaft was electroplated with Cr since results showed it to be approximately 98 weight percent (wt. %) Cr. Another reason for assuming that this was a Cr coated shaft is that hard chrome is usually used as a coating when friction and wear are a concern. Hard chrome is used to reduce friction which will increase the lifespan of the component since its durability is increased by having good wear resistance and abrasion endurance. Other areas that where Cr was found in large amounts was in the bottom region of the shaft where very thin layers of deposits were present. Since these were sections where minimal deposits were found, the XRF was mostly detecting the chromium coating. This is one of the limitations that was encountered when working with the XRF and a reason why these results are preliminary and will be verified by another type of elemental analysis. When analyzing the deposit lines, the spot size was changed from a 10mm to a 3mm diameter to get a more accurate reading of the thin deposit lines. Results from the XRF for the deposit lines showed that there was approximately 49 wt. % aluminum (Al) and 50 wt. % Cr. In this specific area, Cr was detected since the rod is plated with Cr and the 3mm spot size was wider than the deposit lines which still detected regions of the chromium plated base metal.

Moving on to the deposit zone which is covered by re-solidified metal, five elements were predominating this section. These elements were iron (Fe), copper (Cu), nickel (Ni), titanium (Ti), and aluminum (Al). The port-side was analyzed first and results showed that at the beginning of the deposits the most common element found was Cr. As mentioned before while doing visual examination, areas at the start of the deposit zone had a very thin layer of deposit present which in turn, resulted in XRF readings mostly showing the presence of Cr, again coming from the coating on the shaft. Aluminum was also detected in this region but was in concentrations of approximately 15 wt. %.

As XRF was being done in the middle section of the deposit zone, the presence of other main elements were detected. Results continued to show high concentrations of Cr, approximately 52 wt. % and the remaining elements detected were Al, Fe, Cu, and Ni. From these elements, excluding Cr, the middle section mostly contained Al with compositions ranging from 20 to 25 wt. %. Lesser amounts of Cu, Fe, and Ni were also present and ranged from 6-9 wt. %. XRF results belonging to the area which is closest to the end of the shaft also contained the same elements found in the middle section but with greater concentrations. An additional element that was identified as being at the surface of this region was Ti. In this region Cr decreased dramatically to 8 wt. % and Al became the main element found on the surface. Al increased about 10% from one area to another as well as Ni and Fe which spiked up to 20 wt. % and 25 wt. %, respectively. Approximately 5 wt. % Cu was detected which remained the same as in the middle section. Around 6 wt. % Ti was present in this region, while insignificant amounts were detected in the middle sections of the shaft.

Table 3.3 Results of several XRF readings obtained from the port-side of the elevon actuator shaft. The position of where they were taken as well as the general area on the shaft with average results for each of these zones are also represented.

<i>Element Wt. % Position</i>	<i>Deposit-Free Zone</i>				<i>Deposit Zone (Middle)</i>					<i>Deposit Zone (End)</i>				
	25	37	49	Avg.	28	30	42	53	Avg.	33	45	49	57	Avg.
<i>Al</i>	-----	-----	-----	-----	26.7	19.8	22.4	21.7	22.7	35.7	26.2	38.5	33.6	33.5
<i>Cr</i>	98.6	97.4	98.4	98.1	50.9	52.9	46.0	56.9	51.7	11.3	7.82	6.11	8.26	8.37
<i>Fe</i>	-----	-----	-----	-----	7.54	6.60	10.4	9.12	8.42	20.6	30.3	28.2	24.3	25.9
<i>Cu</i>	0.21	0.43	-----	0.21	7.88	9.73	8.98	5.02	7.88	8.9	2.10	3.81	4.81	4.9
<i>Ni</i>	-----	-----	-----	-----	4.35	7.18	6.81	4.36	5.68	15.3	26.7	20.98	19.9	20.7
<i>Ti</i>	-----	-----	-----	-----	-----	-----	1.13	0.23	0.34	4.14	4.59	1.71	7.30	5.91

The XRF results done on areas of the shaft including the deposit-free zone and deposit zone for the port-side are shown in Table 3.3. The table contains several readings that are numbered which corresponded to the position on the overlay grid used during the elemental analysis. Note that only the

major elements are shown in Table 3.3 and elements that were found in amounts less than 1 wt. % were excluded from the table. These minor elements were magnesium, manganese, sulfur, phosphorus, niobium, molybdenum, vanadium, and cobalt. Figure 3.8 shows the numbered overlay grid on the shaft which helped identify the relative position of where the reading was done.

The results for the starboard-side are similar to the port-side but do show a decrease in composition for several elements present. Chromium was detected on the deposit-free zone in concentrations of about 98 wt. % once again and does not include the readings performed on the deposit lines. Proceeding to the deposit zone, on the spray-like deposits, Al was the predominating element with almost 55 wt. % of Al present, followed by 22 wt. % Cr. Fe, Cu, Ni, and Ti all were detected and contained approximately 4 wt. % of each of these elements except for Ti which was present in amounts of 1 wt. %. In the area where deposits were denser, similar amounts of Al were found on the surface with about 49 wt. % and a much higher Fe composition at 18 wt. %. The change in Fe composition may be due to the locking nut which is mostly made of a Fe composition and was adjacent to the area examined. Other elements found in amounts smaller than 3 wt. % on this area were Ti and Cu. Silicon (Si) was an element that was seen in the starboard-side of the shaft more than on the port-side. Cr and Ni were present in this region with 10 wt. % Cr and approximately 8 wt. % Ni. Composition for Si ranged from 7-9 wt. % throughout the deposit zone of the starboard-side of the shaft while its presence was negligible on the port-side.

Table 3.4 shows several of the XRF readings taken on the starboard-side of the elevon actuator shaft. Figure 3.8 is a representation of the three different areas where trends were seen on the port and starboard-sides. The purple section represents the area where Cr was dominant. The yellow sections in the middle where the deposit zone begins, major elements like Fe, Cu, and Ni were detected but Al and Cr were found in larger amounts. Adjacent to this yellow section is the orange region which represents the end of the shaft where a heavier deposition was observed as well as an increase in the composition of several of the major element. Chromium no longer dominated in the orange region. The final area that was

examined with the XRF analyzer is part of the flight control system hydraulic assembly. This section is located at the end of the hydraulic assembly where the shaft would be able to retract when the elevator position was changed. Three main elements were found on the surface of the hydraulic assembly, Al with roughly 57 wt. %, 17 wt. % Fe, and 9 wt. % Ni. These elements are most likely coming from nearby components surrounding the elevator actuator rod.

Table 3.4 Results of several XRF readings obtained from the starboard-side of the elevator actuator shaft. The position of where they were taken as well as the general area on the shaft with average results for each of these zones are also represented

<i>Element Wt. % Position</i>	<i>Deposit Lines</i>				<i>Deposit Zone (Middle)</i>				<i>Deposit Zone (End)</i>					<i>H.A.</i>	
	1	2	86	Avg.	8	20	92	Avg.	10	11	22	23	94	Avg.	Avg.
<i>Al</i>	44.4	52.9	48.4	48.6	62.4	56.4	43.5	54.1	56.25	46.1	49.5	48.5	43.1	48.7	57.2
<i>Cr</i>	55.5	45.7	50.3	50.3	15.2	16.5	34.2	22.0	5.77	8.64	6.92	8.25	20.3	9.97	5.54
<i>Fe</i>	-----	1.04	0.70	0.58	4.07	4.65	2.76	3.83	16.5	25.8	19.4	21.8	6.96	18.1	16.8
<i>Cu</i>	-----	0.27	----	0.09	3.34	3.10	5.01	3.82	2.01	2.08	2.37	1.6	2.57	2.13	5.88
<i>Ni</i>	-----	0.38	0.44	0.27	3.18	4.57	1.92	3.22	6.88	5.26	6.13	7.80	13.3	7.87	8.92
<i>Ti</i>	-----	-----	-----	-----	0.95	1.05	1.77	1.26	2.70	1.02	4.19	0.61	4.29	2.69	0.67
<i>Si</i>	-----	0.31	-----	0.10	8.67	11.1	8.35	9.37	6.98	7.68	7.69	8.01	6.61	7.39	5.56

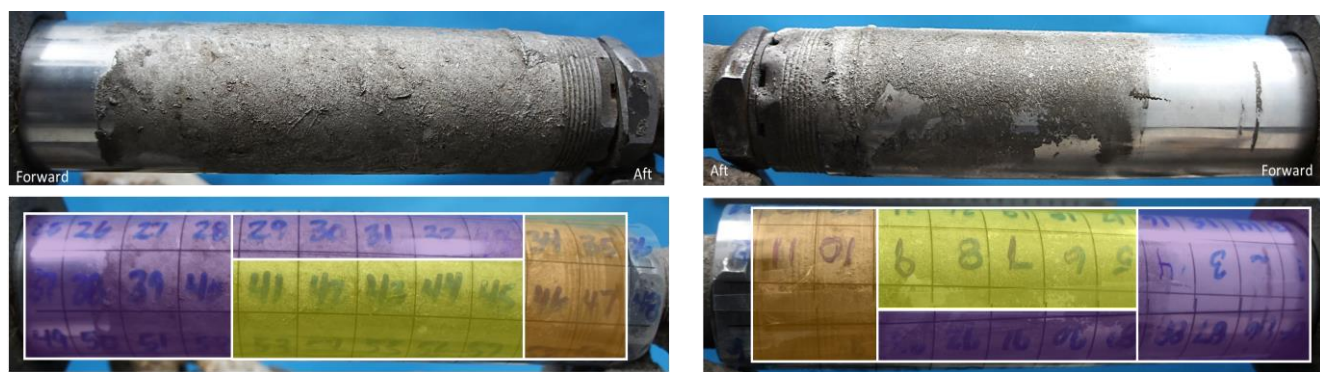


Figure 3.8 Left. Port-side of actuator shaft showing the overlay grid designed to provide exact area where readings were taken. **Right.** Starboard-side of actuator shaft showing the overlay grid. Different colored sections show areas where elemental trends were seen.

3.2 SECTIONING

Three main cuts to the actuator shaft were done using a water jet cutter which would liberate the shaft from the actuator and isolate the starboard-side of the shaft which was the area of interest in this research. The reason for choosing the water jet cutter for primary sectioning of the shaft is that it provides better precision when cutting and will not leave any heat induced changes to the microstructure. Once the three main cuts were done, information on the internal structure of the shaft was known and the overall result is shown in Figure 3.9. Only the starboard-side of the shaft as well as part of the housing are being used for the study and are in Figure 3.9 enclosed by Box D. Letters shown in Figure 3.9 correspond to the nomenclature of the shaft which was used to keep track of all the child pieces of the elevon actuator. All the pieces except for the starboard-side of the shaft in Box D were safely stored back into crates and will not be used for the remainder of this research.

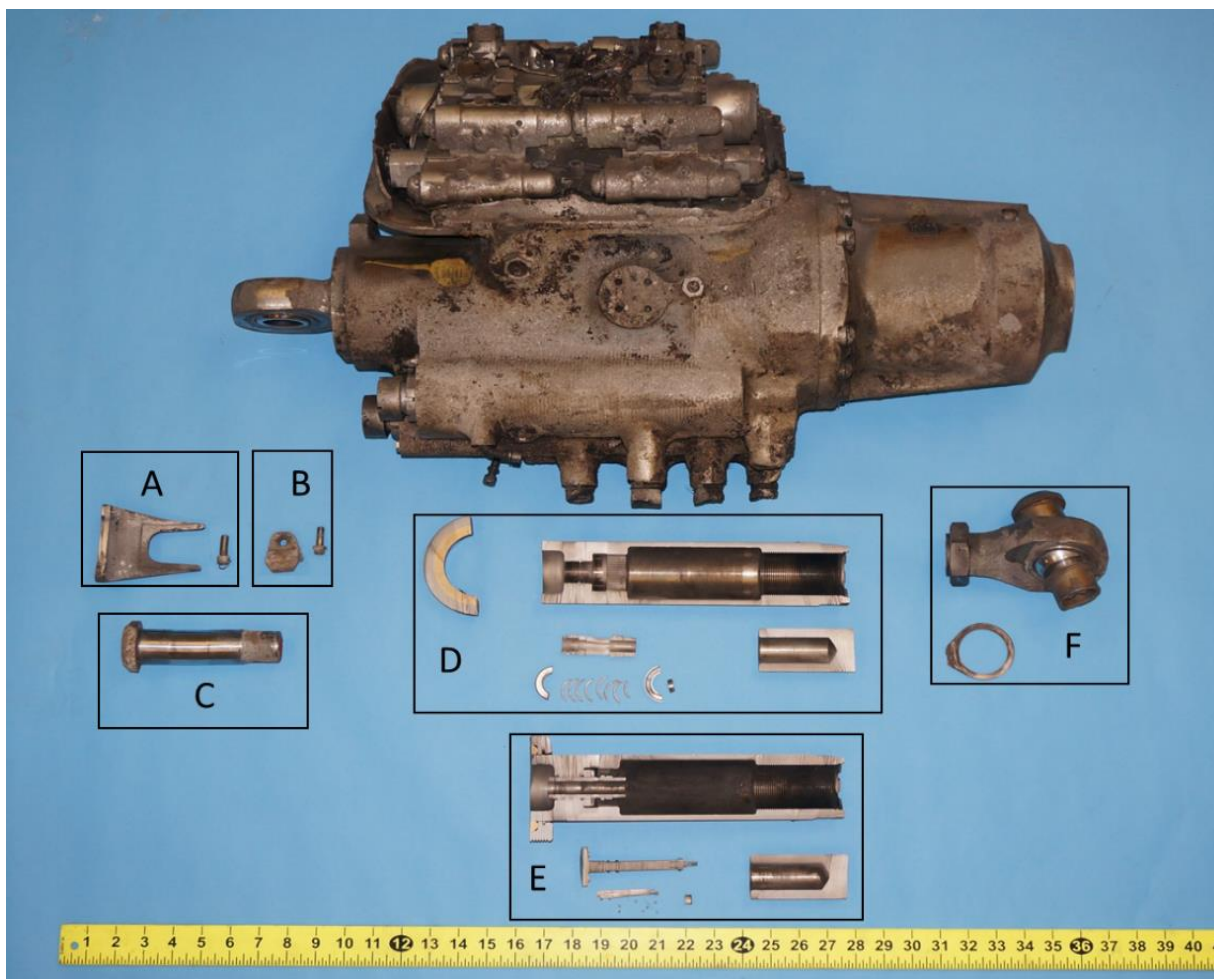


Figure 3.9 Elevon actuator after three primary cuts were executed and airframe was detached from elevon actuator.

Secondary cuts done to the starboard-side of the rod were done with an abrasive cut-off saw because the water jet cutter had the potential of disrupting areas of interest. Sectioning done using the abrasive saw was done in such a way that minimal thermal alterations and contamination occurred. Figure 3.10 shows the sectioned starboard-side of the shaft as well as the resulting areas once secondary sectioning took place. Areas 2, 3, and 4 were chosen based on the position of where the three depositions are believed to have occurred at different times throughout the event. The texture of the deposits in each of these areas were very different from one another making them areas of interest. Also included in Figure 3.10 is part of the housing for the hydraulic assembly which is an area of interest and shows the position where it will be sectioned as well. Additional sectioning of these individual four areas were necessary to obtain specific samples, small enough to be able to use with the analytical equipment.

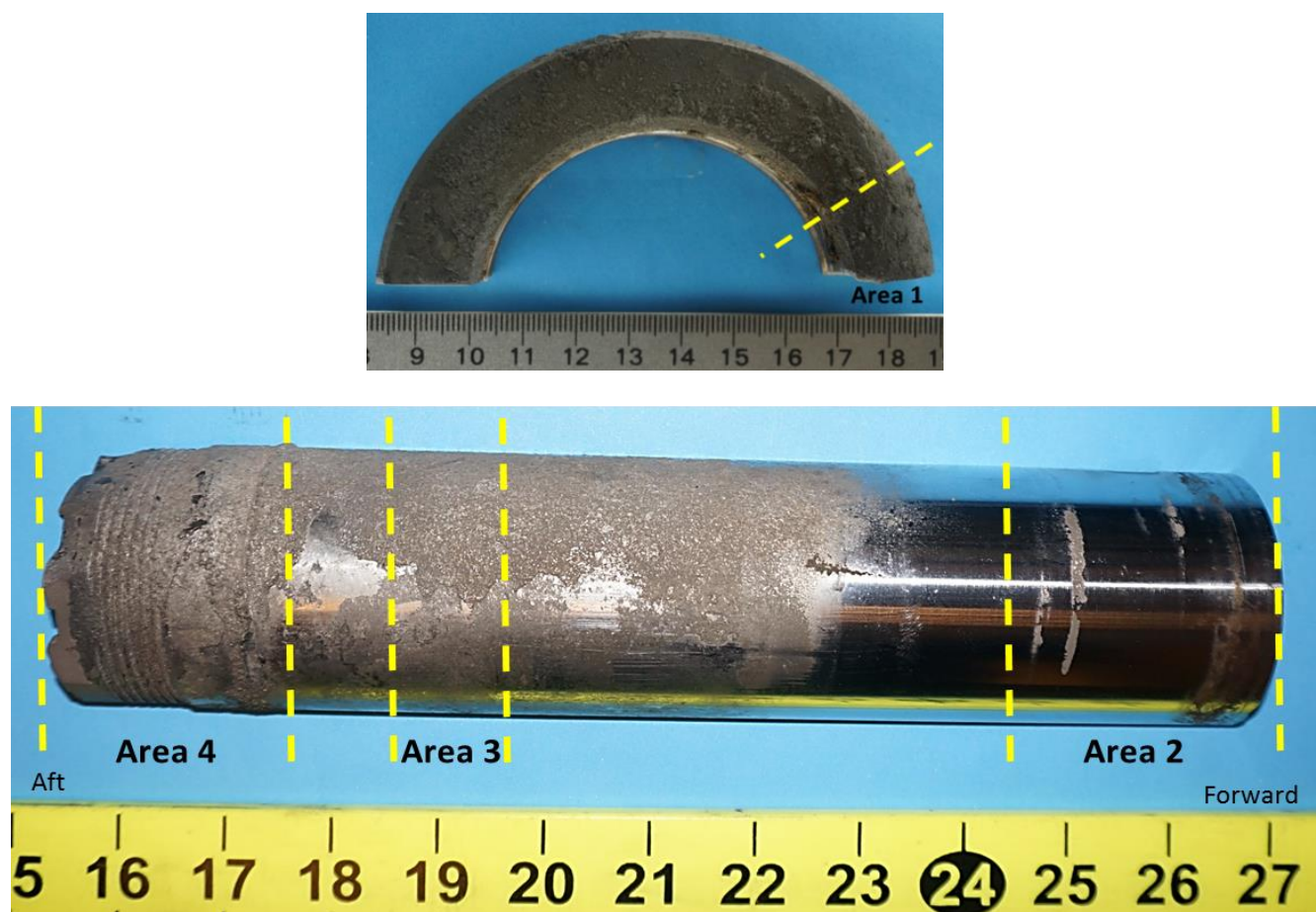


Figure 3.10 Top. Section of the hydraulic assembly housing which will provide sample for Area 1. **Bottom.** Starboard-side of actuator shaft showing areas of interest 2, 3, and 4. Sectioning indicated by yellow dotted lines.

3.2.1 AREA 1

After Cut 2 and Cut 3 were made, the resulting piece was a threaded semicircle as shown in Figure 3.10. To obtain Area 1, an additional transverse cut was made with the abrasive cut-off saw on the location in Figure 3.10 and the resulting piece, Area 1, is shown in Figure 3.11. The sample size is approximately 3.8cm (1.5”) by 3.8cm (1.5”) and was sectioned at the beginning of the threaded area. Sectioning this area is of interest because it can provide information about the housing material as well as identifying deposits that are found on the surface of the sample, which could be the results of the deposits found on the shaft. By further examining this area for thermal alterations and identifying the base metal and deposits, it would verify if deposits found on this sample belonging to the hydraulic system had similar deposits of those deposited onto the shaft.

3.2.2 AREA 2

Area 2 was a resultant of two transverse secondary cuts done on the starboard-side of the shaft. The first cut was done approximately 1cm (0.39”) to the right of the third deposit line and a couple of centimeters to the left of the third deposit line. Reasoning behind choosing this specific area was the fact that Area 2 contains the three deposits lines that were detected by the XRF as mostly being aluminum. The way these deposit lines positioned themselves onto the shaft is very peculiar, so taking a closer look at them will verify what the depositions are and lead to possible answers as to why the depositions were discontinuous line. Additional sectioning of this area was necessary to obtain smaller samples. The abrasive cut-off saw was used to make one transverse cut and one axial cut which resulted in four pieces; only three being used for samples belonging to Area 2 since one of the pieces did not contained any deposits. The transverse cut was done between the first and second deposit lines and the axial cut would split the second and third deposit lines in two. Each sample shown in Figure 3.11, Area 2, measured roughly 3.5cm (1.38”) in length and 2cm (0.79”) wide. Because these three samples all contain part of the three deposition lines and contained the same deposition, each sample was used for a specific technique.

One of the samples was used for XRD analysis while another was used for surface and cross-sectional analysis done with the SEM with EDS capabilities. The final sample in Area 2 was used for metallography and for optical microscopy. Being able to characterize these deposit lines according to their proximity in relation to each other through the techniques mentioned earlier can also offer an explanation as to the position of the elevon at the times during which formation of these deposits occurred.

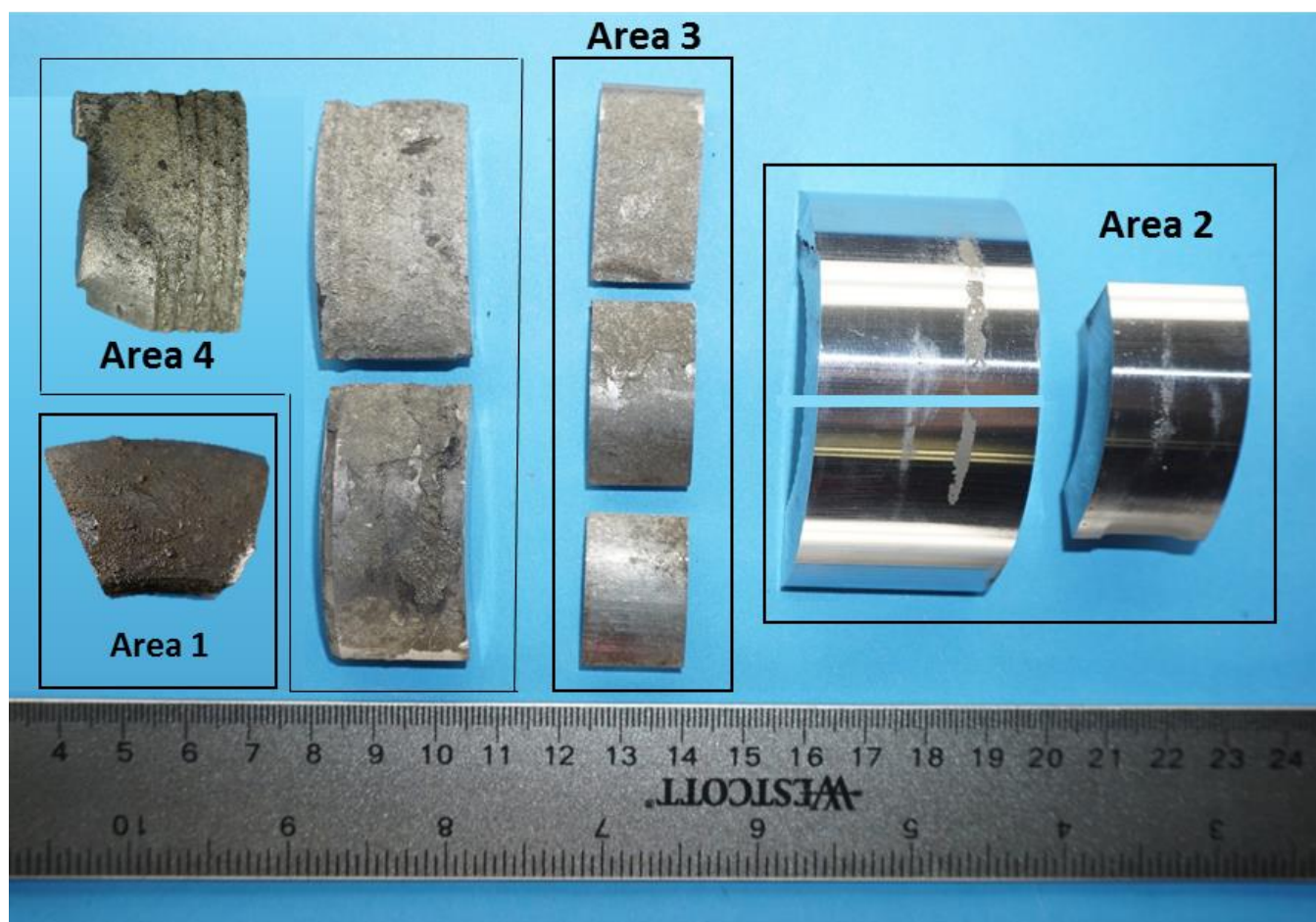


Figure 3.11 Samples obtained after sectioning the starboard-side of the shaft resulting in Areas 1, 2, 3, and 4.

3.2.3 AREA 3

To obtain samples from Area 3, secondary sectioning was done which consisted of two transverse cuts done at approximately 16cm (6.3”) and 17cm (6.7”) away from the housing. Sectioning in Area 3 became of interest since deposits in this area had a uniform, granular texture and also showed evidence that at some point, some of the deposits chipped off and exposed a thinner layer of deposit. XRF analysis

show there are additional elements being detected in this area when compared to Area 2 which is another reason that further examination in this area was conducted. This region was then sectioned once again, now with two axial cuts which resulted in three samples for Area 3. These samples can be seen in Figure 3.11. Area 3 measured around 3cm (1.18”) in length and 2cm (0.79”) wide. One of the samples contained the spray-like deposition and was closely examined under the SEM. Another sample contained parts of the spray-like texture where the deposits had flaked off and part of the thin layer of the deposit that was exposed. The final sample is located at the lower portion of the shaft in the middle section and had a very thin layer of deposit in several regions as well as metallic spatter that was looked at under the SEM as well. There were expectations of finding several depositions on these samples when examining them under the SEM. Any thermal alterations to the base metal of the shaft was also examined and a comparison of the layers found here can be made to those found in the previous areas.

3.2.4 AREA 4

Secondary sectioning for Area 4 consisted of one transverse cut which was about 22cm (8.66”) away from the housing. This last area was of interest since it consisted of a thicker deposit with a much rougher surface than Areas 3. Also in this section, there was an area where thermal erosion was a possibility, since the diameter of the shaft decreased in this area and can clearly be seen with the naked eye. Coming to the end of the shaft, there is also a threaded area which appeared to have reached extremely high temperatures since several of the threads were not as pronounced as the rest. This region also became of interest and a sample was taken from this region as well. Area 4 was then sectioned again, first with one transverse cut which was located at the end of the erosion zone nearly splitting Area 4 in half. Taking the piece that contained the possible thermally eroded area, an axial cut was made in the middle dividing it into two pieces which were used for examination. Another axial cut was then made in the threaded piece so that a sample, which was directly adjacent to the eroded zone, could be used for analysis. The transverse cut and two axial cuts produced four pieces but only three were used for analysis, the extra pieces were

stored away. The samples that were used for this researched can be seen in Figure 3.11, including those in Area 4. With possible signs of thermal erosion showing in one of the samples and heavy deposits adhering tightly to the base metal, investigating this area demonstrated thermal degradation that might have occurred and show again any existing layers that might have developed in denser areas.

3.3 SUMMARY

Several non-destructive techniques were employed to document the as-received condition of the starboard elevon actuator before sectioning occurred. While the visual examination was conducted, several features were pointed out and became areas of interest. Elemental analysis done using the XRF also helped determine elements found on the surface of the shaft. Once the non-destructive evaluation concluded, sectioning of the starboard-side of the actuator shaft proceeded. A total of 10 samples belonging to four distinct areas on the starboard-side of the actuator shaft were obtained. Since the same major elements, Al, Cu, Ni, Cr, Fe and Ti were found in several of these areas, the possibility exists that depositions of these layers might have occurred uniformly throughout the region but it is necessary to thoroughly analyze the samples obtained. Comparing all areas would allow for distinctions to be made in each region, investigate how the molten metal was deposited, and identify the source of where it came from. The thermally eroded area was also be analyzed. Knowledge on how different materials behave in re-entry environments were gained, which helps reduce the risk of materials used in future commercial spaceflight.

CHAPTER 4: MICROSCOPY RESULTS

The four distinct areas identified as areas of interest that make up the starboard-side of the elevon actuator shaft were analyzed in detail with different types of microscopes and x-ray instrumentation. These microscopes included a light microscope, Keyence digital microscope, and a scanning electron microscope (SEM). Analysis of the sample surfaces as well as the cross-sectional views were conducted using these visual aids. Surface morphology differ in several of the samples which was expected and similarities were also found among the areas of interest. The cross-sectional view of the samples also revealed information which included regions of certain elements embedded in a matrix of another.

Elemental analysis was also done on the samples using energy dispersive x-ray spectroscopy which is equipped with the SEM. EDS was essential especially when doing the cross-sectional analysis since there were different colorations and layering found within the deposits. It was necessary to conduct elemental analysis on each section to know if these layers consisted of the same material. Instrumentation such as x-ray diffraction was also used in the investigation to obtain element and compound information belonging to the deposits found on the surface of the actuator shaft. Results showed elements such as aluminum, nickel, iron, copper, chromium, and titanium were all present on the surface and cross-sections of the samples. All four areas seem to have a predominating element besides aluminum which was found in all areas and in large quantities in some locations.

SEM micrographs taken of the surface morphology and cross-section will be presented in this section along with corresponding EDS spectra results conducted on specific areas of each sample. Optical micrographs of the microstructure belonging to the base material as well as the deposits profile view will also be discussed. When looking at the microstructures, a heat affected zone was seen in a few samples and layering was also visible in the micrographs. Results obtained from XRD analysis will be presented in this chapter which show several main compounds that make up the deposits adhered to the surface of the elevon actuator shaft.

4.1 SCANNING ELECTRON MICROSCOPY ANALYSIS

The FEI Quanta 400 and the Hitachi S-4800 scanning electron microscopes with EDS capabilities were used to analyze the surface morphology and do quantitative elemental analysis on the surface and cross-sections of the samples from all four areas. Results showed surface morphology changed from one area to another as well as within the sample. Most deposits had a granular, rough texture to them where some regions were denser than others. In other areas, where deposits were light, the surface was covered in metallic multidirectional spatter or would also be found on top of already deposited debris. On occasion, the molten metal adhering to the surface would have a liquefaction behavior where the deposits would have a smooth liquefied texture. The cross-section of the samples showed similar results for most areas where porous and regions of embedded metal within the matrix of the deposit could be seen. EDS spot analysis conducted showed the presence of all the major elements detected by the XRF survey done on the surface during the non-destructive phase of the project. SEM micrographs along with the corresponding EDS spectra for each area will follow.

4.1.1 AREA 1

A small area belonging to the flight control system hydraulic actuator was taken as a sample piece to be closely examined to obtain information on the base material as well as the deposits on the surface. Since the piece of this sample was located at the position where the shaft extended out, depending on the elevon position, examining the deposits and its base material provided information on whether material from the hydraulic actuator deposited onto the shaft and if the same elements present on the deposits of the shaft are similar to those found on the hydraulic actuator. Deposits were found on a threaded region where a metal sleeve was connected to it and served as a break for the elevons when the shuttle was stationary. The other end of the metal sleeve connected at the end of the shaft where a threaded region was also seen. The deposits found on the threaded region were mostly found on the roots of the threads in the sample shown in Figure 4.1. On the adjacent side where the threads were located, deposits were also

found. Here deposits had a thick uniform layer and contained small chunks of deposits which were intermittently spread throughout that surface. Figure 4.1 depicts the sample obtained from Area 1, both sides are shown, one side showing the threads and the other side, adjacent to the threads which is facing in the aft direction. Note, coloration seen on the sample piece is possibly due to hydraulic fluid that came out of the actuator during the breakup and did not dissolve during the ultrasonication. EDS analysis made it possible to identify these deposits.

4.1.1.1 SURFACE ANALYSIS

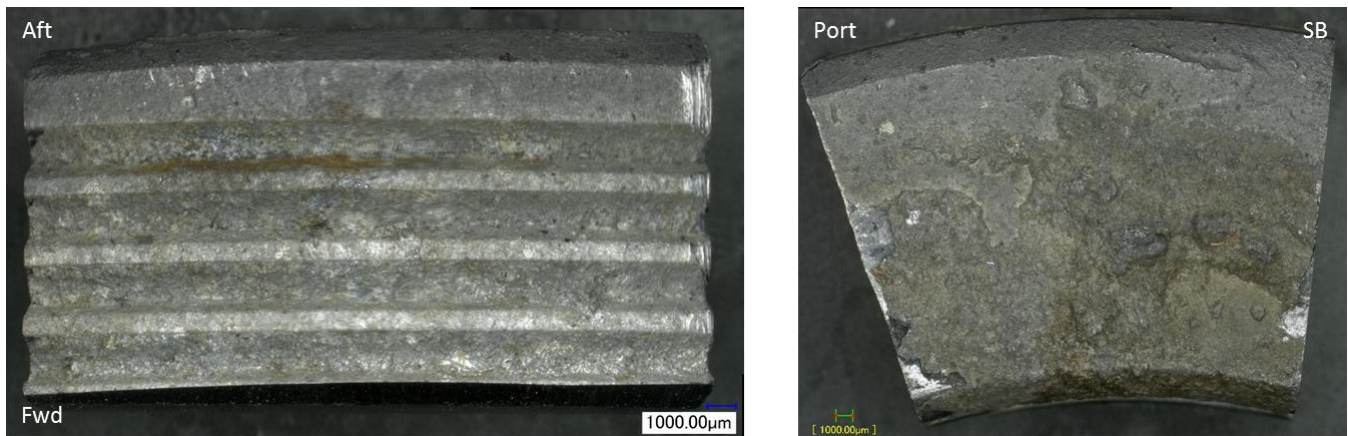


Figure 4.1 Sample used from Area 1 showing deposits on the surface of the threaded region (Left) and on the aft-facing side (Right). 30X.

The surface of the aft-facing side of Area 1 was examined at a higher magnification using the SEM for surface morphology and elemental composition. Analyzing Area 1 showed a variety of surface texture, some regions had a rocky texture, others were flat and granular, and there were also regions with a flat smooth surface. Figure 4.2 shows the different regions that were seen in Area 1. About 15% of the terrain had a coarse surface, and deposits clustered in small piles forming column-like structures (Figure 4.2 A and D). These column-like structures varied in height and width and were accompanied by smaller agglomerated deposits that had a “popcorn texture”. Besides this region having a very rough texture and a denser deposition, cracking was observed, which is an indication of rapid solidification of the molten metal upon contact. Another region that was seen in the sample consisted of smooth hills and valleys which were considerably lower in height when compared to the column-like structures seen in the nearby

region. As in the coarser region, cracks could be distinguished in this region as well. There were also areas where the hills and valleys contained spray-like deposits, which made a patchy but smooth layer in the already solidified deposits. This area covered about half of the sample (Figure 4.2 B and E). A thinner layer of deposit, which is found along the top edge on the port-side of the sample, makes up the remainder of the surface. Figure 4.2 C and F shows how the surface is flatter than other regions and a lot coarser as well. This layer had a flaky texture which also demonstrated that the deposits did not have enough time to adhere to the base metal or debris already deposited onto the shaft. Other features seen in this region were spatters being deposited once again on top of an already deposited re-solidified metal but were not seen much throughout the region.

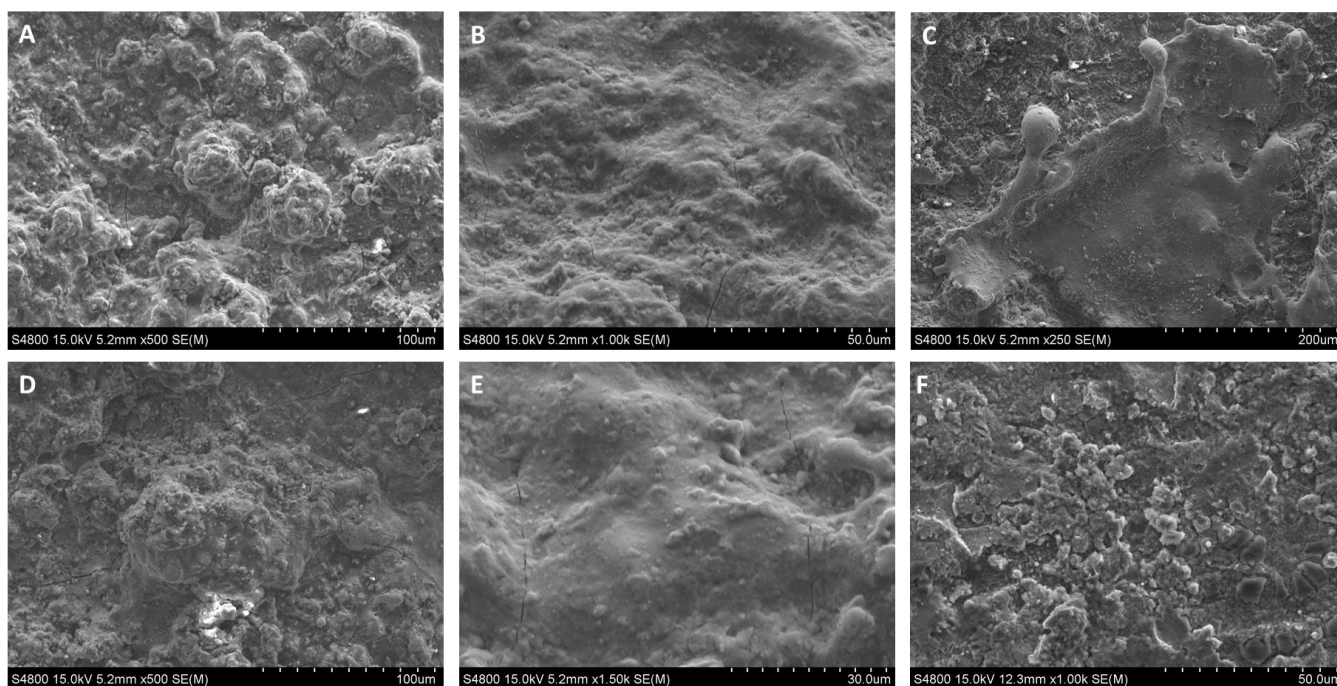


Figure 4.2 SEM micrographs from Area 1 showing different surface morphology seen throughout the sample region. Images are at different magnifications.

Elemental analysis using EDS was conducted on the surface of the sample from Area 1. These results helped confirm the preliminary results obtained from x-ray fluorescence which was also conducted on the surface. With several limitations encountered when using the XRF, verifying those results with the ones obtained from the EDS would provide accurate results of what elements were present in the surface of Area 1. In Area 1, the predominant element found on the surface was aluminum. Aluminum was

detected on the regions containing hills and valleys as well as the coarser terrain where the column-like structures were located, in amounts of about 25 to 30 wt. % Al. Traces of minor elements were found at the surface as well and amounts varied slightly on the three identified areas. On the region where the surface had a rough texture, copper was found in higher amounts than on the bumpier surface where iron was the dominating minor element. The average of several EDS readings was calculated and showed that Cu and Fe were present in amounts of about 8 wt. %. Elements such as nickel and chromium were also detected but at smaller concentrations of 7 wt. % and 3 wt. %, respectively. Smaller traces of titanium were also identified on the surface but in amounts of less than 2 wt. %. In the spatter that was found on the port-side corner of the sample, the same elements were detected with the exception that composition varied dramatically. These spats were mostly composed of Fe and Ni with concentrations of about 30 wt. % Fe and 20 wt. % Ni. Other elements that were found in the spatter were Cr and Al with 8 to 10 wt. % of each and smaller amounts of Cu and Ti were also detected. Figure 4.3 shows EDS spectra of readings taken from areas shown in Figure 4.2. SEM micrographs A, B, and C on Figure 4.2 correspond to the EDS spectra 1, 2, and 3 respectively. For SEM images A and B, the whole area was surveyed. As for image C, only a part of the spatter was analyzed since the bottom layer had similar results to the ones found in micrographs A and B.

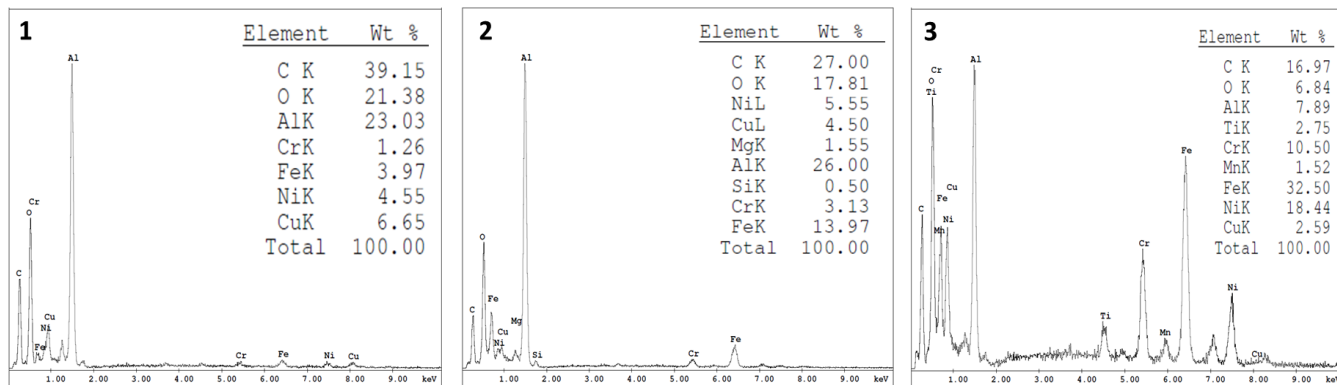


Figure 4.3 EDS spectra from regions taken from Area 1. Spectra 1, 2 and 3 correspond to reading taken from micrographs A, B, and C shown in Figure 4.2.

Looking at the surface of the threaded side of Area 1, there were high expectations of finding a different morphology but some regions had similar features to the ones found in the adjacent side. One of the noticeable differences in the deposits found in between the threads was that the surface was a lot rougher. This type of morphology was mostly found on the threaded angle walls where tiny molten metal droplets seemed to agglomerate and form a “popcorn-like” structures with many nooks and crannies. Deposits were found to adhere uniformly against the first three thread angled walls which were located closest to the forward direction of the shuttle. This uniform deposition happening on both threaded faces, the forward and aft-sides, had the same amount of deposits and the root of the threads was where most the debris accumulated. As the threaded region advanced in the aft direction, which is closest to the adjacent side, the amount of deposits adhering to the thread faces decreased and it was observed that they mostly adhered to the aft-side of the threaded face. The morphology found on these thread faces were where the main differences were seen when comparing to the morphology from the adjacent side. The roots and crests by contrast, had similar morphology and also had similarities to the morphology found on the adjacent side. On the root of the threads, for the most part, the surface was even though rough, but did however, have some particle agglomeration occurring. This accumulation of molten metal droplets and splats were found evenly dispersed throughout the surface. Spatter was also detected in the roots of the threads covering a larger area, making the layer thicker than the ones found on the aft-facing side. The morphology found on the crests of the threads had a smoother surface than the one seen at the roots, which might be due to the fact that it was located at the top of the threads where deposits would not encounter problematic geometry unlike depositing into the roots of the threads. One of the major things that was observed in this area was “mudcracks,” which are molten metal that quickly solidified producing to contraction which lead to cracking. Due to these cracks and poor adherence of the deposits, residual cavities within the solidified metal were left behind in several of the mudcracks. Even though there were indications of metal flaking, the already deposited layer below these mudcracks were tightly bonded to

the base metal. Similar to the surface texture found on the adjacent side, hills and valleys of metallic metal were also present. Figure 4.4 show several micrographs taken with the SEM of sample Area 1 where the yellow boxes indicate the spot were EDS readings were taken. Images A and D show the deposit seen accumulating on either sides of the threaded faces, which B and E show micrographs taken at the roots of the threaded regions, and images C and F correspond to the crests of the threads.

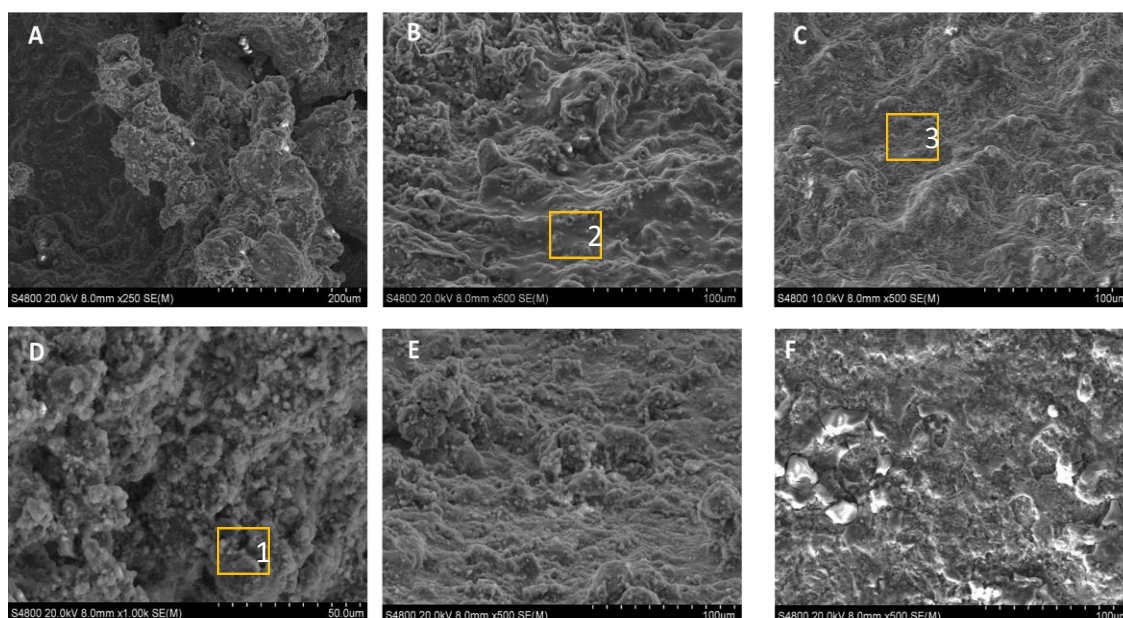


Figure 4.4 SEM micrographs taken from the threaded region belonging to Area 1. Yellow outlined boxes designate the area were EDS analysis was performed and correspond to the results shown in

Chemical analysis done on the surface of the threaded region revealed that the major composition of the deposits were aluminum, iron, and oxygen. Due to the angular nature of the thread faces and the surfaces having a granular texture, EDS analysis was difficult, but these areas were mostly composed of aluminum and oxygen. Noting that this area had large clusters of micro-particles agglomerating together, there was a greater surface area which made these particles react at a faster rate and could have led to aluminum oxidation. Figure 4.5 (1) shows the EDS results for this region which are shown on Figure 4.4 D, spot 1. Another element that was detected here but was not present on the EDS spectra in Figure 4.5 was silicon. While examining the thread faces, there were areas where a lot of granular silica particles were occupying space in the cavities seen in these deposits, which created a lot of charging making it difficult to obtain images as well as chemical identify by EDS. The next region that was analyzed by EDS

was the root of the threads. Here, the main elements that were found were once again Al, Fe, and O, but did also contain smaller amounts of Ni and Cu. Within the threaded roots, there was about 30 wt. % Al present, which was the element with the largest concentration in that region. Fe and O were also detected in large quantities with approximately 15 wt. % Fe and 20 wt. % O. Ni was present in concentrations of about 5 wt. % and around 10 wt. % Cu was also detected in this flat, yet patchy deposits. The EDS results for the reading performed at the root of the thread is shown in image 2 of Figure 4.5 and the location of the spot tested is shown by the yellow box in Figure 4.4 B. On the crest of the threads, once again Al, Fe, and O were the major elements except that Fe was the predominate element. Fe was detected in concentrations of approximately 30 wt. % whereas Al only made amount 20 wt. % of the total composition. Aluminum and oxygen were particularly found in areas where there were mudcracks and Fe was mostly present in the flatter surfaces. The chemical composition analyzed by EDS in Figure 4.4 C is shown in Figure 4.5 (3). Note that carbon would appear in most EDS results, but should not be representative of the sample's chemical composition. This high concentration of carbon were due to residue from the hydraulic fluid coming from the hydraulic system or wiring insulation. These artificially high C values would also be due to contamination and the interaction between the E-beam and the sample as well as the surrounding environment in the chamber even with a high vacuum. Carbon can be found in the samples but the amount present should not be very high.

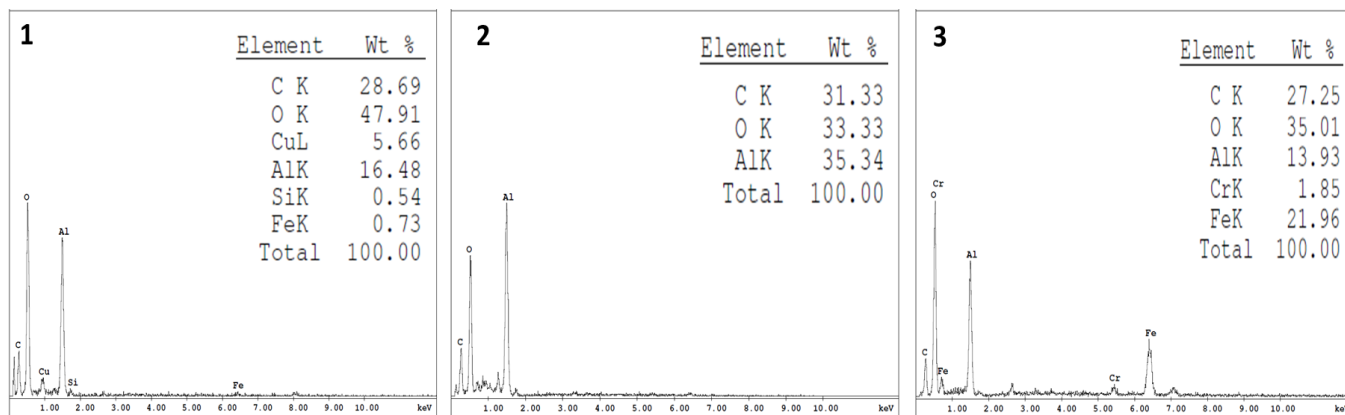


Figure 4.5 EDS analysis conducted on the threaded region of Area 1 in three different sections.

4.1.1.2 CROSS SECTIONAL ANALYSIS

Concluding surface analysis conducted on Area 1, the sample was mounted in an epoxy resin mold in preparation for metallography. The sample was ground and polished to observe the cross-sectional view of the deposits. Images taken of the cross-sectional view of the deposits from both the aft-facing side and the threaded side using the Keyence digital microscope are shown in Figure 4.6 along with the EDS spectrum of the base metal. Note the base metal of Area 1 is a chromium-nickel steel similar to the base metal of the shaft, which contained about 15wt. % Cr, 5wt. % Ni, and Fe making up about three fourths of the composition, comparable to 15-5 PH stainless steel. Results for the cross-section of the aft-facing side of the sample belonging to Area 1 will be discussed first.

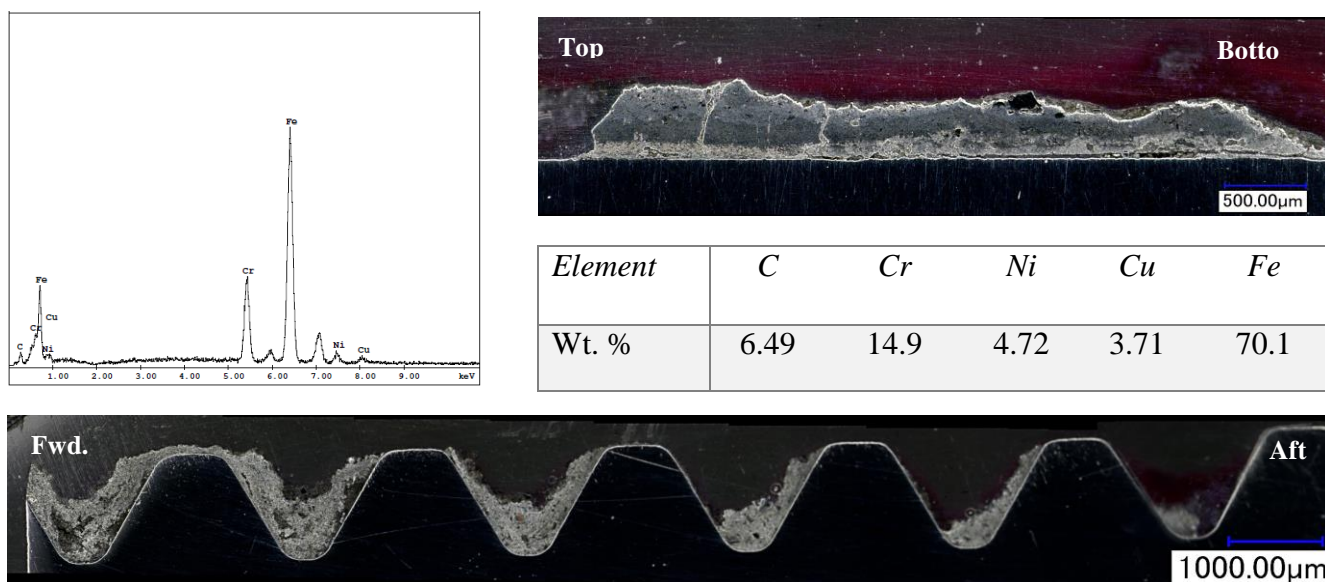


Figure 4.6 Top Left. EDS spectrum of base metal for Area 1 along with the chemical composition shown on middle table. **Top Right.** Keyence micrograph of aft-facing side of Area 1 sample at 200X. **Bottom.** Cross sectional view of threaded region in Area 1 sample taken with Keyence microscope at 150X.

The aft-facing side of the sample consisted of a deposit layer of approximately 460μm in thickness and four distinct layers. The first layer, which is directly above the base metal, is a few micrometers in thickness and contains a combination of the main elements found by XRF in the early stages of the study. A slight deformation at the interface between the base metal and the first layer of deposit was noticeable

and can be seen in Figure 4.7 D. In this thin layer of deposits, there were areas where the deposit had a small discontinuity. Detecting this layer was obvious since it had a darker coloration than the base metal.

The second layer consisted of small patchy areas of agglomerated particles that when examined in the polished cross-section, some of the particles intersected looked as if they are individual particles and would be considered this way from now on. These small solid particles were embedded between the thin layer and the rest of the deposit. Debris varied in size and shape but most of them were polygonal consisting of multiple sides and sharp edges. These multi-faceted particles were discontinuous and were dispersed throughout the cross-section. In some areas there were particles that had a more porous structure but had similar size and shape when compared to other particles seen. In areas where there was discontinuity, a hollow space existed, which can be seen on image C in Figure 4.7 as a black spacing, sandwiched between the first layer and third layer.

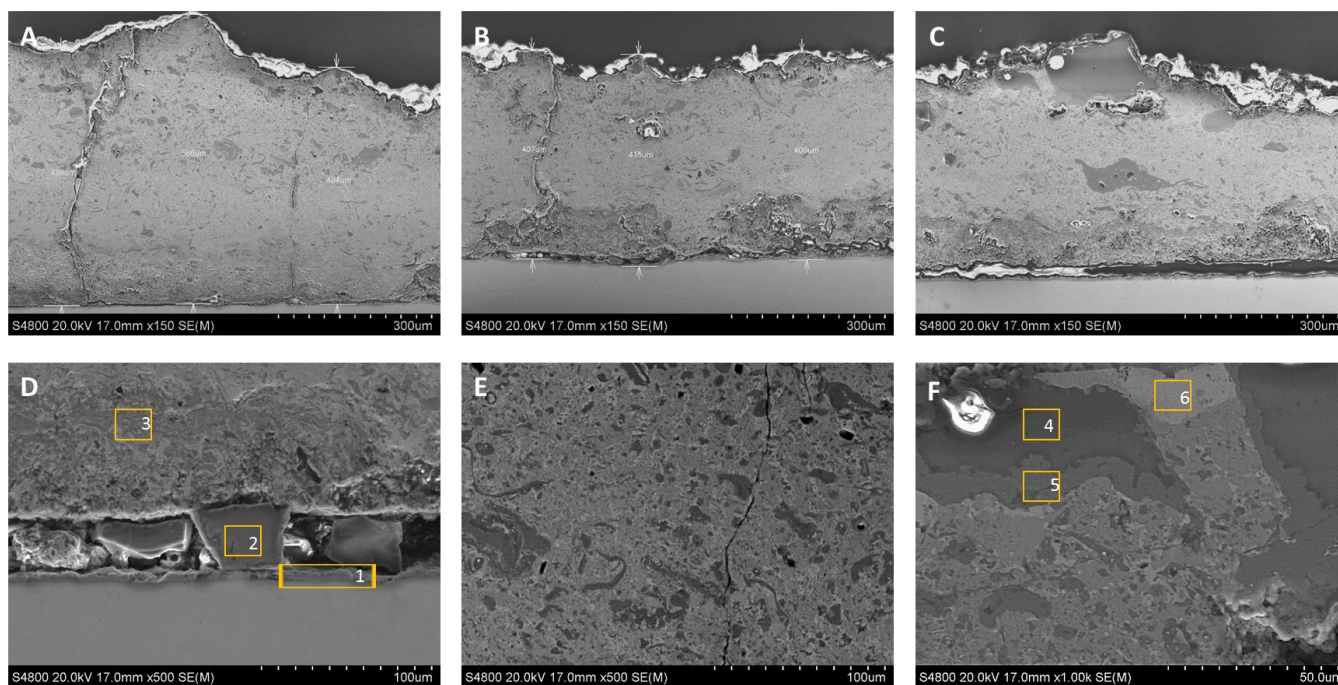


Figure 4.7 SEM images of the cross-sectional view of aft-facing side in Area 1. A through C show deposit as well as some measurements of the height of the deposit. D through F show magnified images of several regions found throughout the deposit. Yellow boxes show area where EDS spot analysis was conducted. These results are shown in Figure 4.8.

Just above this particles and hollow tunnels, the third layer can be found. This layer is shown as a dark gray area on A, B, C, and D in Figure 4.7 and consists of a light and dark gray matrix where the latter

has the greater amount present especially seen at the top portion of the layer. In this area, cracking can be seen in Figure 4.7 B but the rest of this layer is uniform and has an average thickness of 80 μ m. Present in this layer were also large and smaller porous areas, again these hollow areas appear in the SEM micrographs as a black region.

Also noticeable was the well define interface between the third and fourth layer as well as how at the top of the third layer, in several regions, the flow trajectories that the molten metal took as it solidified, could be distinguished. The final layer is the thickest of all four layers having an average thickness of approximately 310 μ m. The fourth layer is shown in all the images from Figure 4.7, excluding micrograph D, and magnified images of this layer are shown in micrographs E and F. From these images, the fourth layer has a similar matrix as the third layer with the exception that this layer had three different constituents. The matrix consisted of three different shades of gray: a light gray, a gray shade, and a dark shade of gray with the gray shade making up most of the matrix. Irregular shaped regions made of the darker colored material could be found throughout the fourth layer. Most of this darker constituent had a string-like or spherical shape and were mostly small in size. Other larger regions of this same material were present and was evident that surrounding this darker, large, irregular shape was a lighter gray phase (Figure 4.7 F). Mostly making up this fourth layer was the gray phase and was mixed with the light gray phase. Even though the light gray constituent was not present in larger quantities, there were a few large irregular regions where this light gray phase was deposited and is shown on image F in Figure 4.7. As seen in most layers from the cross-sectional view of Area 1 sample, there was a few porous regions especially close to the top of this layer whereas not as much cavities were seen in the third layer. Along with these areas where hollow areas appeared within the deposits, cracks were seen running from the top to the bottom of the deposit only stopping as the base metal was reached. In Figure 4.7, images A through C, charging can be seen outlining the top of the fourth layer and is represented by the white coloration.

Table 4.1 Average chemical composition of the four different layers found on the cross-sectional view of Area1. Gray shades represent the fourth layer found on the sample.

<i>Elements</i>	<i>O</i>	<i>Al</i>	<i>Ti</i>	<i>Cr</i>	<i>Fe</i>	<i>Ni</i>	<i>Cu</i>	<i>Si</i>
<i>1st Layer</i>	2.87	19.4	-----	3.38	16.4	10.2	28.2	-----
<i>2nd Layer</i>	34.0	1.67	-----	-----	-----	-----	-----	52.4
<i>3rd Layer</i>	12.7	29.3	1.4	1.76	8.15	5.19	24.6	-----
<i>Dark Gray Phase</i>	31.9	44.6	1.72	2.28	-----	-----	-----	2.15
<i>Gray Phase</i>	2.12	39.6	3.36	7.54	27.9	11.1	9.17	-----
<i>Light Gray Phase</i>	1.34	20.1	1.05	-----	24.5	34.7	8.61	-----

To identify the chemical composition of the four distinct layers found on the sample for Area 1, EDS spot analysis was performed. Readings taken at different locations throughout the deposit found in Area 1 were averaged to represent the chemical composition of each layer and the results are shown on Table 4.1. Note, the fourth layer in Table 4.1 is the combination of dark gray, gray, and light gray which represent the different constituents that made up the fourth layer. The first layer, as described previously, consist of a thin solid layer directly above the base metal. The first layer mainly consisted of Cu with approximately 30 wt. % Cu. The minor elements that were also detected in the areas were Al, Fe, and Ni, which ranged from 10 to 20 wt. % of each of these elements. Because the hydraulic actuator had several connections attached to it, there was copper wiring, which could explain copper making up the first layer of the deposit. Even though copper has a higher melting temperature than aluminum, copper is found at a closer proximity than surrounding Al airframe and deposited first on to the hydraulic actuator. The second layer which contains irregular shaped particles were mostly composed of silicon and oxygen enrichments. These crystalline silicate particles make up one of the most abundant dust grains in outer space and finding silicates on the deposit was expected [42]. Silica can also be coming from the TPS tiles and Cerachrom insulation blanket in the area. The silicon particles were located at completely random places just above the copper layer and is possible it occurred at a time when the first layer was close to completing

solidification, since there was no evidence that mixing of these two layers occurred. Being that these are particles in the micron scale and are exposed to oxygen, a reaction between the silicates and oxygen would quickly occur, which might be the reason why much silicon and oxygen were detected on the second layer.

The third layer belonging to the light and dark matrix where mixing of these two materials was merely apparent at higher magnifications, was composed of 30 wt. % Al and 25 wt. % Cu. Again, Al and Cu were the dominating elements found on the layers of Area 1. The presence of Al however did jump from 20 wt. % to 30 wt. % and is possible that this was due to the airframe's temperature increasing dramatically, leading to a higher melting rate and quicker deposition of Al on the hydraulic actuator housing. Copper was still detected in similar amounts than it was detected in the first layer. Nickel and iron were detected in this third layer as well, but were not as high as the amounts found in the first layer. Unlike the first two layers, Ti was detected but only in a small amounts. In the fourth layer, there were three different constituents as they are displayed by a variety of shades of gray. The same dark and light shades of gray found in the third layer were also present here. The dark gray color seen here as well as in the previous layer belonged to aluminum and oxygen enrichments. In this layer traces of Ti, Cr, and Si were also detected by the EDS in concentrations of 2 to 3 wt. % of each of these elements. These areas of aluminum and oxygen were found all over the layer, but do not compose most of the fourth layer, while it does dominate the content in the third layer. The most abundant constituent in the fourth layer consists of 40 wt. % Al. Again, the main element in this layer is Al with the exception that these gray areas contain less than 2 wt. % O. Another major element found in the gray areas of the fourth layer was Fe, which made up approximately 30 wt. % of the elemental composition. There was a sudden decrease in copper composition in this layer, which dropped from about 20 wt. % Cu to 10 wt. % Cu. This drop might be due to wiring and surrounding copper components completely being consumed at this point during the re-entry. Nickel and chromium had similar amounts present in this gray shaded region. Lastly, large light gray areas were seen throughout the fourth layer. These light gray regions were mostly seen at the top of

the fourth layer and correspond to Ni, Fe and Al depositions. Though these three elements were detected in the fourth layer, Ni made up the greatest amount of the chemical composition with about 35 wt. %. Iron then followed with 25 wt. % and Al was present in concentrations of about 20 wt. %. Overall, the second layer was the layer which had the most distinct elemental composition whereas the other three contained the same elements but the concentrations present in each layer differ. Figure 4.8 shows several EDS spectra coming from different regions of the deposit layers found on Area 1. These selected spots are represented in Figure 4.7 by yellow boxes where the numbers correspond to the numbered EDS spectra in Figure 4.8.

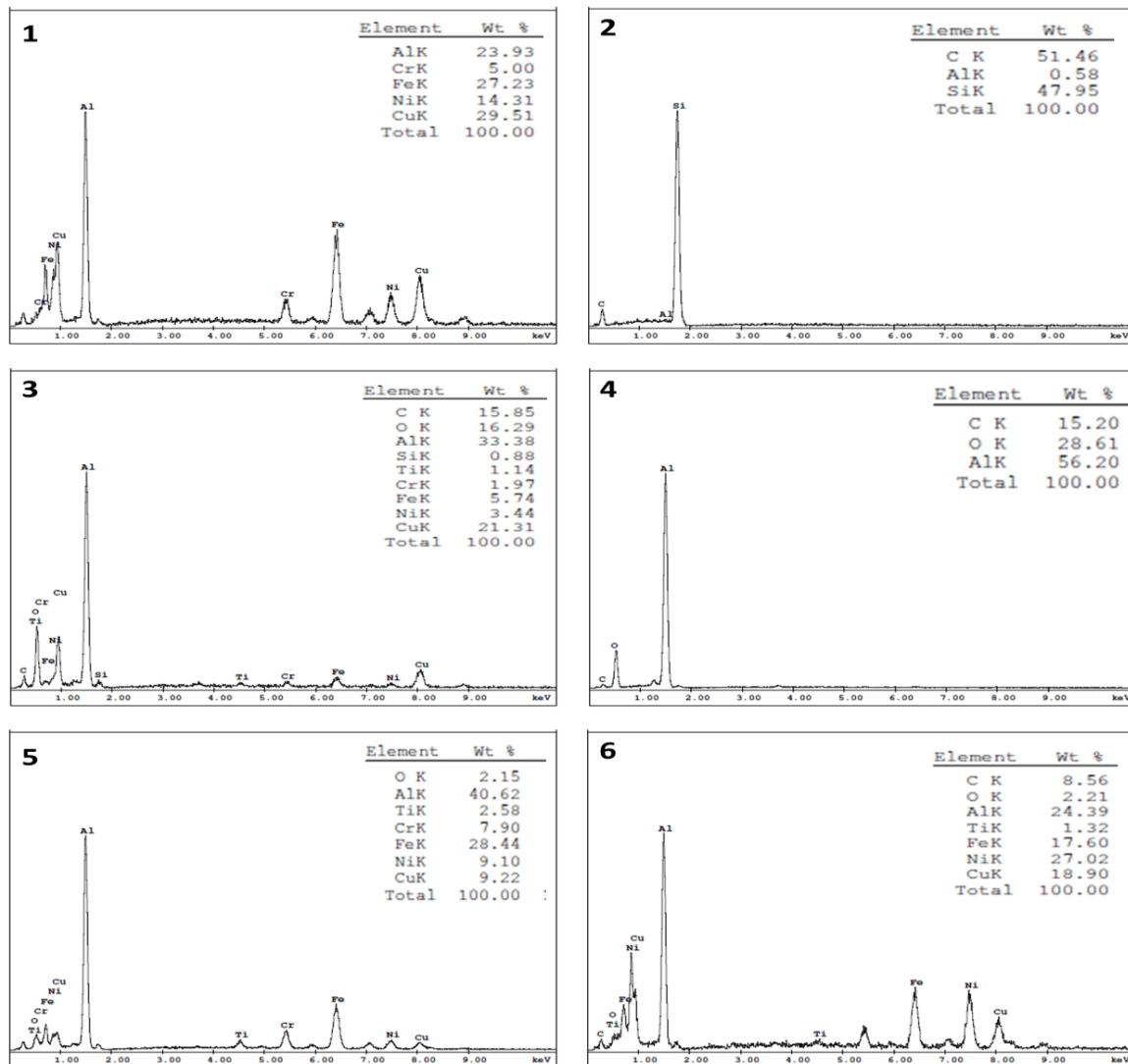


Figure 4.8 EDS spectra corresponding to the cross-sectional view of the aft-facing side in Area 1 sample. (1) 1st layer. (2) 2nd layer. (3) 3rd layer. (4-6) 4th layer.

The cross-sectional view of the threaded side of the sample was also analyzed under the SEM with EDS capabilities. SEM micrographs corresponding to this side of Area 1 sample are shown in Figure 4.9. Images A, B, and C show the root and thread faces with deposits on the first, second and fourth threads, which show the topography of the deposit and display areas in the deposits that contained large shrinkage voids, depicted by black areas. The base metal of the hydraulic actuator housing is represented in Figure 4.9 as the smooth and light colored area, whereas the dark colored region on the top corresponds to the epoxy mount of the sample. Along with large voids, the deposit contained spots where it was acquiring a charge build up, which made it difficult to obtain a good image. Charging was shown in Figure 4.9 as bright white regions.

On the threads inspected, it was noticed that deposit decreased from forward to aft which would indicate a directional flow occurring from forward to aft which is expected. Debris first started to deposit uniformly in the first three thread roots but as it advanced further back into the shuttle, the amount of deposits started to decrease and the deposit itself on the right side of the thread faces only. The morphology in this part of the sample was unlike in all the threads, which could correspond to a single material being deposited into the threaded region of the hydraulic actuator housing surface. Images D, E, and F in Figure 4.9, are magnified areas of the morphology found in the threaded region. The morphology seen in the threads consisted of a gray and dark gray matrix where the two constituents were seen in a 1:1 ratio. Though the ratio of these two constituents was similar, the lighter phase had a dendritic morphology and can be seen in Figure 4.9 F. In contrast, the darker phase present in the deposit had a globular morphology.

At a larger magnification, large cavities were observed more often and in most cases, white spherical micro particles would occupy the voids. These granular particles caused the sample to charge, which was readily seen in the magnified images as white specks. Another observation that was noticed while looking at the morphology of the threaded region was sintering of small granular particles, specifically occurring within the thread roots and are shown in Figure 4.9 D. This behavior was not noticed

on the remainder of the deposit. In this same region, embedded debris with irregular shapes was commonly seen as well. Also, observed occasionally throughout the deposit were large regions of a smooth light gray phase, irregularly shaped as well (Figure 4.9 E).

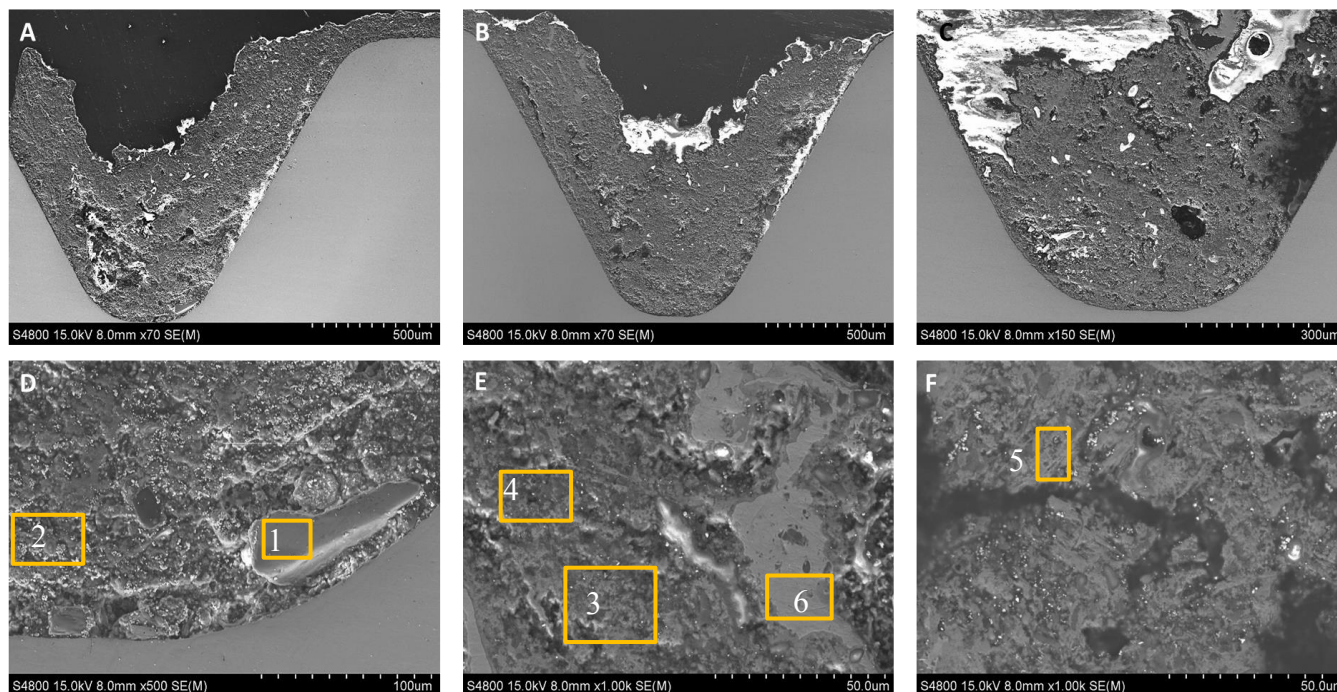


Figure 4.9 SEM images of threaded side of Area 1 sample. (A-C) Lower magnification images showing base metal and deposit as well as portion of epoxy mount. (D-F) Higher magnification images of deposit showing the different morphology found throughout in detail. Yellow numbered boxes correspond to EDS results in Figure 4.10.

The chemical analysis conducted on the threaded side of Area 1 varied in composition from the other regions that were chosen for analysis from that same sample. The same elements at different concentrations were seen in this area and there were no distinct layers as there were in the aft-facing side. These elements were Al, O, Cu, Cr, Fe, and Ni. Figure 4.10 shows EDS results for several spots that were tested. The particles found on the bottom of the roots of the threads corresponded to either silica particles or in the case of larger debris, it was mostly composed of Fe. The bigger irregular chunks contained approximately 25 wt. % Fe, 20 wt. % Al, and lesser amounts of O, Ni, and Cr, all between 3 wt. % and 8 wt. %. Because these types of debris were a lot bigger in size, had sharp and irregular edges, and were mostly composed of Fe and Al, it is probable that these little pieces of debris suddenly broke off from

nearby components before the component reached its melting temperature and deposit themselves in the thread roots. These deposits contained some differences of what was found within the rest of the deposits as pointed out earlier. In this area, close to the root, the deposit had high concentrations of Al and O.

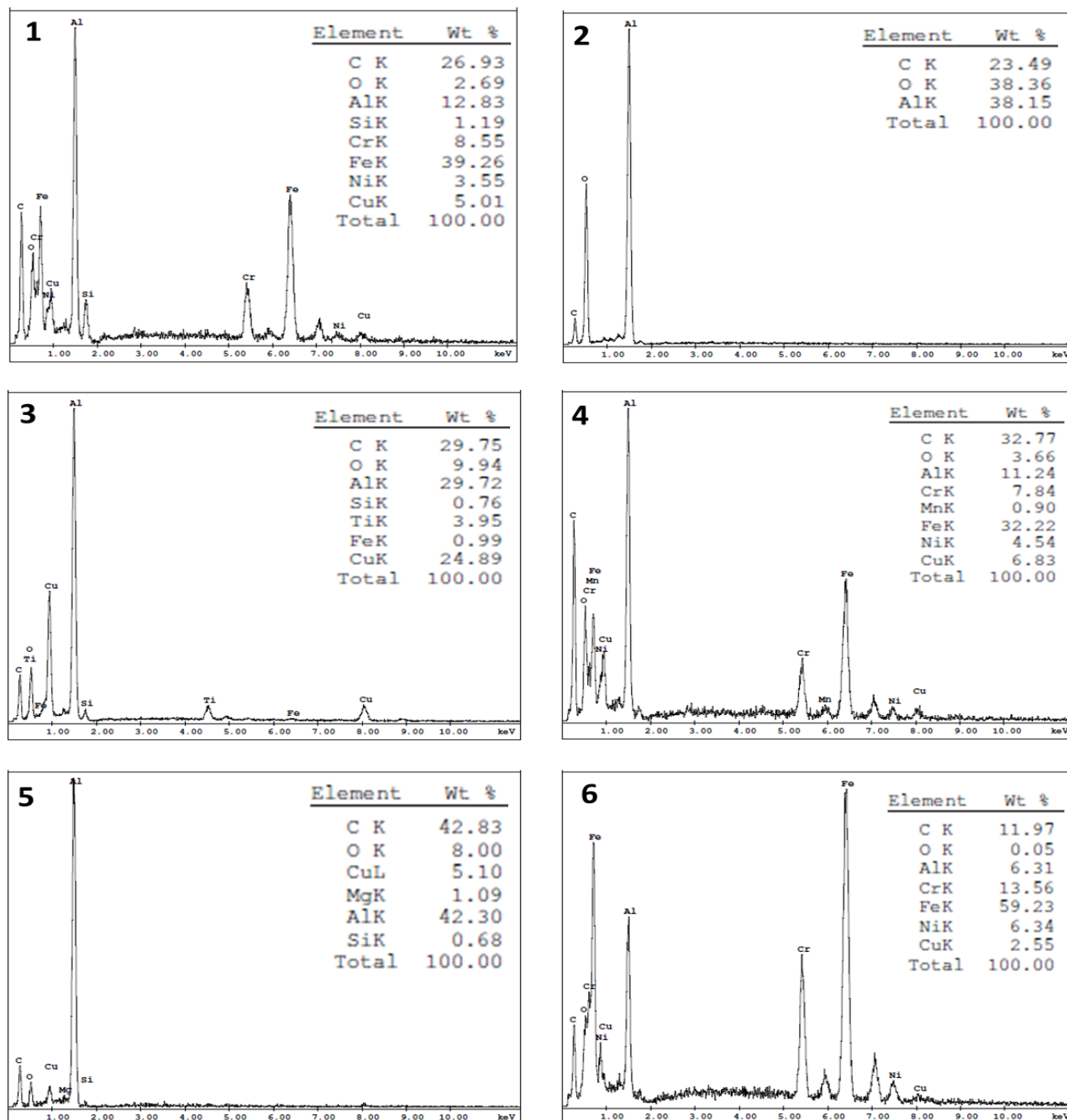


Figure 4.10 EDS spectra corresponding to the cross-sectional view of the threaded region in Area 1 sample. (1) Particle (2) Granular deposit found close to root (3) Matrix (4) Dark Phase (5) Gray Phase (6) Light regions found on top layer of deposit. Exact locations of were EDS readings were taken area shown in Figure 4.9, with corresponding numbers.

Other features seen in these deposits was the matrix composed of a gray and dark gray deposits. EDS results coming from the matrix were similar to the ones found on the aft-facing side. This matrix structure was seen in the third layer of the aft-facing side and here in the threaded region of the sample. EDS results showed that besides aluminum and oxygen being the predominant compound, Cu was also present in high concentrations. EDS results for a single spot analyzed are shown in Figure 4.10 (3). About 30 wt. % Cu was found on the aft-facing side were less than 20 wt. % Cu was found in this part of the sample. Even though there was a 10 wt. % Cu difference, Cu was the element found in greater amounts besides Al in the matrix on both areas that were analyzed in Area 1. Within the matrix, the dark phase was mostly composed of Fe, followed by 15 wt. % Al, and around 7 wt. % of Cu and Fe. This was unexpected since the dark phase in the aft-facing side was mostly Al and oxygen and is exactly what was thought would be present in this dark phase. Instead, Fe became the dominant element in the deposit and was probably coming from a steel component since it does contain other elements like Cu, Cr, and Ni. As for the lighter shade of gray detected, EDS results showed an average composition of 47 wt. % Al and 6 wt. % Cu. Again, differences can be seen from results found here and the ones found on the aft-facing side. One thing that was noticed about the composition if these two phases when compared to the two phases seen in the third layer of the aft-facing side was the fact that the composition of the dark phase found here was more similar the lighter phase in the aft-facing side and vice versa. Lighter colored regions that were also found on the matrix were also analyzed for their elemental composition and it was determined that these larger deposits were about 60 wt. % Fe (Figure 4.10 (6)), finding another main difference from that of the aft-facing side where these areas were mostly made up of Ni.

It is evident that the composition of the deposits found in these two side of the sample vary in composition which could be because the sides are at a 90° angle from each other. This could explain the fact that different materials from different components were depositing on adjacent sides of each other at the same time, again, each coming from a different angle. Table 4.2 shows the average composition of

each of the features seen in the deposits coming from the cross-sectional view of the threaded side of Area 1.

Table 4.2 Average chemical composition of deposit found on the cross-sectional view of the threaded side in Area1.

<i>Element</i>	<i>O</i>	<i>Al</i>	<i>Si</i>	<i>Fe</i>	<i>Cu</i>	<i>Ti</i>	<i>Cr</i>	<i>Ni</i>
<i>Matrix</i>	15.3	24.0	2.25	7.25	17.2	2.84	-----	-----
<i>Dark Phase</i>	5.63	15.1	-----	28.9	7.19	-----	6.9	4.11
<i>Gray Phase</i>	6.55	47.0	-----	-----	5.54	-----	-----	-----
<i>Deposit at Surface</i>	36.1	36.3	-----	-----	-----	-----	-----	-----
<i>Particles at Surface</i>	5.30	19.6	1.00	24.3	7.58	-----	5.76	3.89
<i>Light Phase</i>	4.63	15.0	-----	61.68	2.35	-----	-----	6.19

4.1.2 AREA 2

Concluding the surface and cross-sectional analysis done on the hydraulic actuator housing, the examination of the shaft which was connected to the hydraulic actuator proceeded. Area 2 corresponds to the first of three areas of the shaft that were analyzed by the SEM with EDS capabilities. In Area 2, the presence of three thin deposit lines were of interest and three samples from this same area were obtained for analysis. Only one of the samples was used for SEM and EDS analysis since these three deposit lines were composed of the same material and had similar texture. In the earlier stages of the project, XRF analysis conducted on the surface detected mostly aluminum and chromium, as explained earlier, the chromium was being detected from the base metal coating which was applied to it for wear and corrosion resistance. Analyzing Area 2 under the SEM and being able to conduct a second chemical analysis would verify the XRF results and micrographs of the surface and cross-sectional view of the deposit line would be taken as well. A micrograph taken with the use of the Keyence microscope is shown in Figure 4.11 of the sample that was analyzed under the SEM and its chemical composition obtained by EDS analysis. As

seen in this image, the deposit line seems to be very thin and uniform throughout. The base material of the shaft was also analyzed by EDS, since it was a separate component of the hydraulic actuator housing. The EDS results of the shaft's base material and coating is seen in Figure 4.12 where composition is consistent to that of a 17-4 precipitation hardening stainless steel with approximately 17wt. % Cr and 4wt. % of Ni and Cu each, with most of the remaining balance being Fe. The coating of this material as projected by the XRF results was a Cr (electroplated) coating with about 96wt. % Cr.

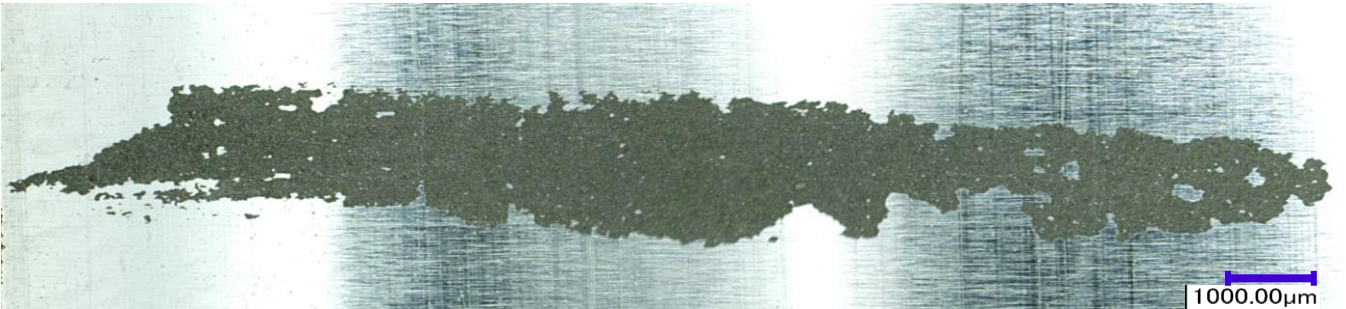


Figure 4.11 Keyence micrograph of sample D_2.1 from Area 2 which will be used for SEM and EDS analysis. 30X.

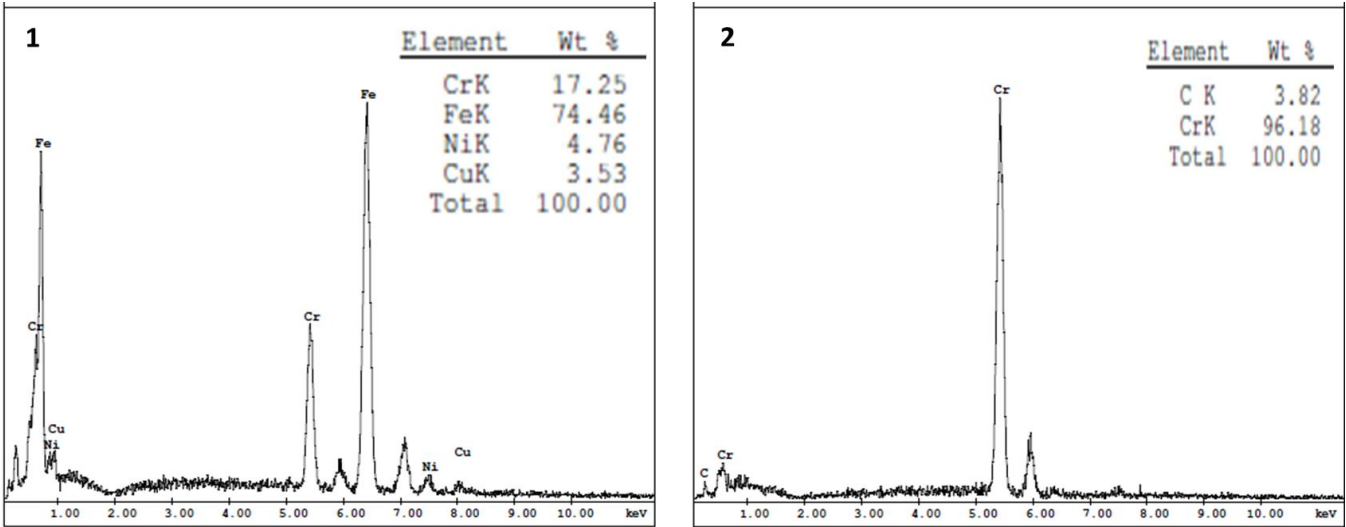


Figure 4.12 EDS spot analysis of (1) base material and (2) coating of actuator shaft.

4.1.2.1 SURFACE ANALYSIS

The surface morphology of sample A2.2 coming from Area 2 and making up part of the 2nd deposit line was examined thoroughly. Overall, the deposits that made up the three deposit lines had smooth and

globular regions along with other sections showing agglomeration of smaller, rougher, globular particles. SEM images showing surface features found in Area 2 are shown in Figure 4.13. Most of the deposit line contained crusty, flat, granular surfaces all throughout the deposit as shown in Figure 4.13 A through C. In this region, agglomeration of particles was apparent and there were regions where some of these particles accumulated enough to make larger masses of deposits; these were usually found in small clusters. This behavior can be seen on Figure 4.13 B as well as in image E at the upper region at a higher magnification. This same image contained a very spherical particle as well, which was commonly seen in this sample. A few areas were found where the deposits had a smoother surface as if liquation occurred and molten metal deposited onto the debris that had already adhered to the base metal (Figure 4.13 F). Here, agglomeration of micro-particles was also evident and along with these particles, there were areas that contained many small cavities. The morphology found on the deposit lines was very similar throughout which should correspond to a uniform elemental composition.

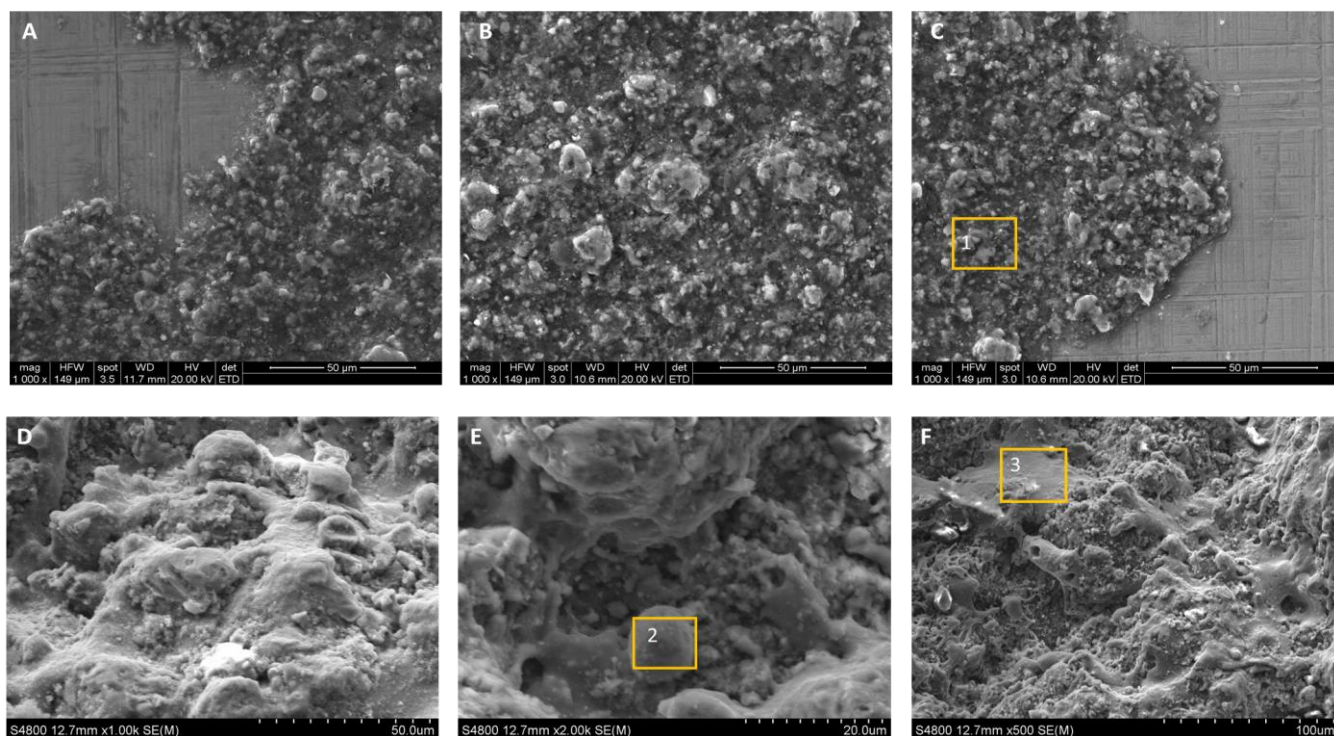


Figure 4.13 SEM micrographs showing the surface morphology of the 2nd deposit line found on Area 2 at different magnifications and locations on throughout the deposit line. Note, images A through C were taken using a FEI Quanta 400 SEM whereas images D through F were taken using the Hitachi S-4800 SEM. Yellow numbered boxes correspond to EDS spectra shown in Figure 4.14.

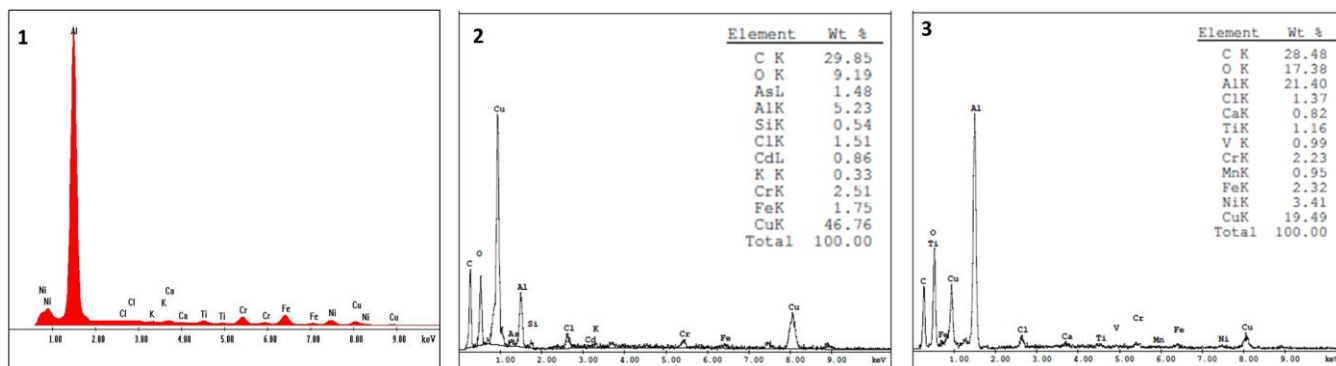


Figure 4.14 EDS spectra for regions located in Area 2 of the actuator shaft. (1) Granular surface [FE Quanta 400 SEM used] (2) Spherical particles (3) Spat [Hitachi S-4800 SEM used on spectra 2 and 3]. Location of EDS spot analyzed can be found on Figure 4.13.

Earlier EDS results showed how the base metal of the shaft is in fact a 17-4 PH stainless steel which was coated with a hard chrome for wear resistance. The deposit lines seen in Area 2 on the shaft were analyzed to identify the elements present. In most of the deposit, which consisted of a granular texture, Al was the element present in higher concentrations. Along with aluminum, there were a lot of tramp elements such as K, Ca, and Cl, which were detected. Since the deposits are very small thin deposits, ultrasonication was done for a shorter amount of time to prevent any of the deposits flaking off while the sample was being clean which led to elements such as Cl and Ca to be detected, most likely coming from residue obtained while the shaft was being sectioned. Besides these tramp elements, small traces of Ni, Ti, Fe, and Cu were detected. Figure 4.14 (1) shows EDS results obtained when the FEI Quanta 400 SEM was used and quantitative results were unavailable for this reading. Other regions on the 2nd deposit line were analyzed with the Hitachi S-4800 SEM and EDS results of two spots are also shown in Figure 4.14. The other regions where chemical composition was obtained from Area 2 were the spherical particles seen in areas where the topography seem to be more rough but smoother in other areas. These particles were mostly composed of copper and oxygen and once again the presence of other contaminants was seen but in negligible quantities. There was about 46wt. % Cu present and 10wt. % O along with 5wt. % Al (Figure 4.14 (2)). Spats being deposited on top of another layer of deposit were also analyzed by EDS and the chemical composition also showed a high presence of Cu. This spats were mostly composed of aluminum

and oxygen but did have approximately 20wt. % Cu which is in greater concentrations than other main elements also present such as Ni, Fe, Ti, and Cr.

Overall, results from the EDS spectra show that the deposit was in mostly aluminum with a minimal amount of iron and nickel. The results from the chemical analysis conducted on the lines of deposit found in the deposit-free zone go along with the XRF data, corroborating that they were aluminum. Because more than 25% of the entire space shuttle structure is structural aluminum, deposits found in this area are most likely coming from the surrounding airframe [7]. As for the presence of Cu found areas of the deposit line and in Area 1, which is found in close proximity to Area 2, it is possible that Cu is coming from the same source. Most likely, Cu is coming from electrical wiring from the hydraulic actuator.

4.1.2.2 CROSS-SECTIONAL ANALYSIS

Looking at the cross-sectional view of the 2nd deposit line under the SEM was accomplished by mounting the sample once all surface analysis was completed. Images obtained from the cross-section of the deposit line are presented in Figure 4.15. Over all, the morphology was very similar throughout and consisted of two layers. The bottom layer contained a discontinuous segment of polygon-shaped particles. These particles sat on top of the chromium layer, which can also be seen in the SEM images in the lower portion of the micrograph, in Figure 4.15. Most of these particles were solid and multi-faceted measuring from 10 to 15 μ m in height and twice as much in length. In areas where particles were discontinuous, there was micro-particles that had clustered together to form a small mass of deposit. The second layer and last one found on the deposit line mostly consisted of a solid single phase layer with some areas containing small cavities, especially seen near the surface of the deposit. The topography was coarse all along the cross-section but generally maintained the same thickness throughout. There were some occasions where the deposit accumulated a lot more, making it a lot thicker but did not make a significant difference when averaging the thickness. This deposit had an average thickness of approximately 23 μ m from the surface of the chromium coating to the surface of the thin deposit. Note that from Figure 4.15, a darker shade of

gray appears to be a layer in the middle between the particles and the top layer. Obtaining images from the SEM in this area were particularly difficult since deposits were so thin and the cross section of this deposit line only covered a couple of millimeters. Due to this, small particles were continuously charging as well as part of the epoxy mold. Charging of the mold is evident in all images along the top, just above the deposit, seen as a bright glossy glare and charging of the particles is displayed by white regions in the bottom layer of the deposit.

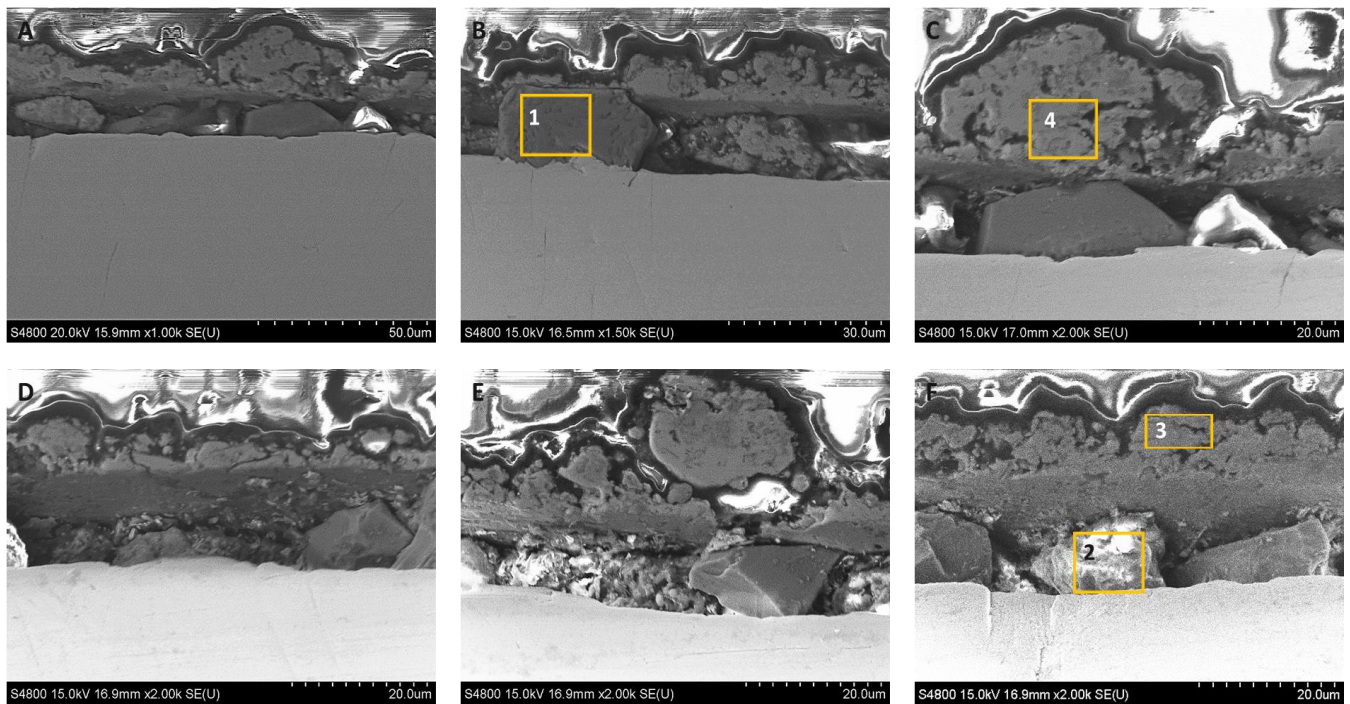


Figure 4.15 SEM images of cross sectional view of 2nd deposit line found on the free-deposit zone of the actuator shaft.

The first layer of this deposit line which consisted of the multi-faceted particles was analyzed with the EDS capabilities provided by the SEM and two different chemical compositions were detected for these particles. When conducting spot analysis on different embedded debris, silicon and carbon were the main elements found to make up most of the particles. The EDS spectra for the particle analyzed in Figure 4.15 F, which is shown in a yellow box with a number 2, can be seen in Figure 4.16 (2). Results show a high presence of Si and O. Other particles that were analyzed were mostly composed of aluminum and chromium. About 5 wt. % Cu was also detected on these particles, which is an element that was commonly

detected at the surface of the deposit line. The second layer also had two distinctive compositions. When obtaining EDS reading from the top surfaces, aluminum and oxygen were the elements that was detected whereas for regions tested closer in the center of the second layer, other element made up the composition. Besides aluminum found in lower areas of the second layer found on the deposit line, Cu, Fe, and Ni were present in amounts as high as 10 wt. %, though aluminum was present in amounts as high as 60 wt. %. Titanium was also detected in most the readings taken in this area but only constituted less than 2 wt. % of the total. Figure 4.16 (3) and (4) show EDS spectra of two areas where readings were taken on the second layer of the deposit line.

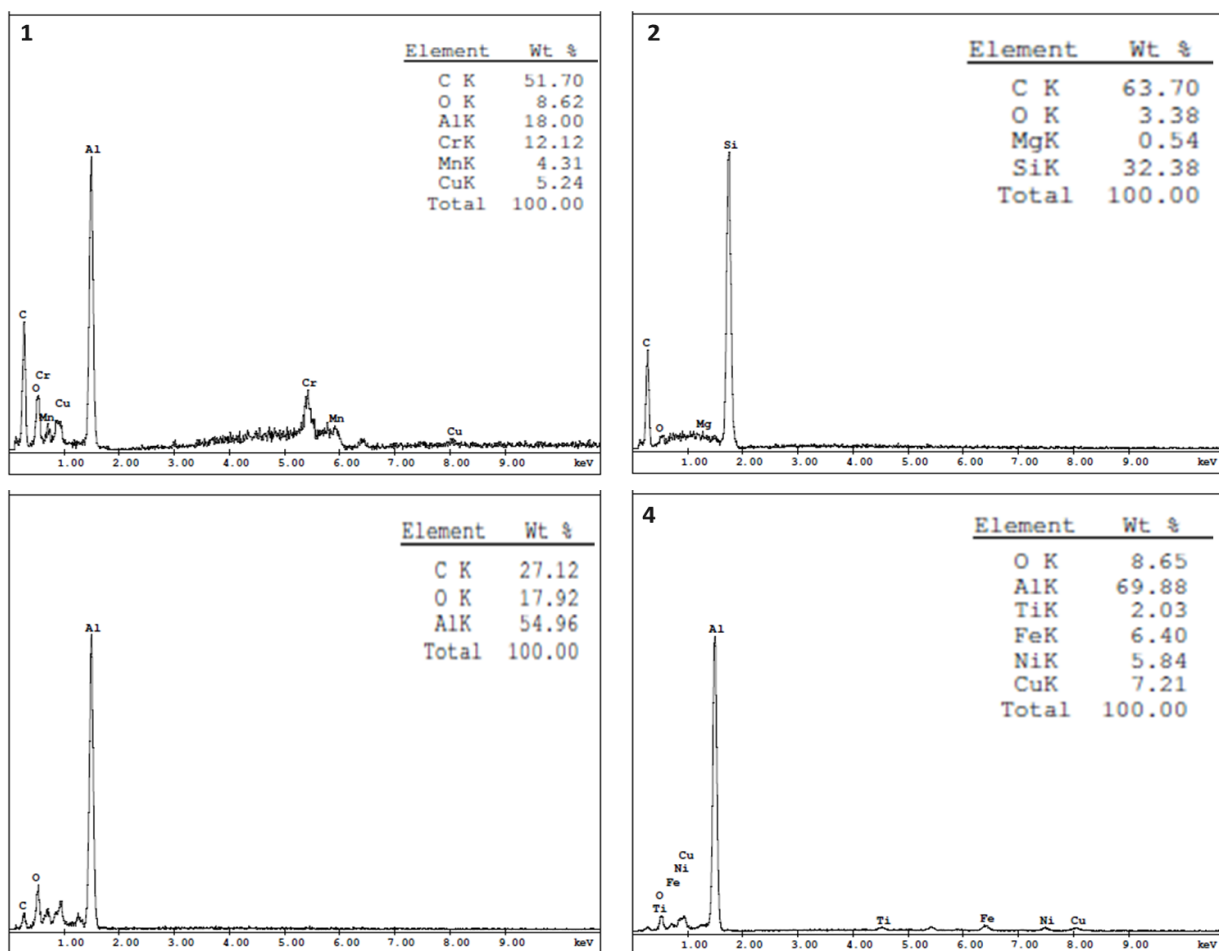


Figure 4.16 EDS spectra of the cross sectional view of 2nd deposit line. (1) and (2) show EDS results for the bottom layer. (3) and (4) show results found on the top layer. Exact location of area analyzed can be found on Figure 4.15.

4.1.3 AREA 3

Three samples from Area 3 were selected for analysis in this study. Samples from this area came from the middle section of the shaft where deposits had adhered to the base metal in a spray-like manner and some areas appeared to have cracked or flaked off due to impact. In the area where deposits had broken off, a thinner layer of deposit in the lower section of the area was observed. The first sample A3.1 shown in Figure 4.17 was located near the lowest point on the starboard side of the shaft in Area 3. Sample A3.2 is the second sample from Area 3 and contained areas of the shaft where the thin layer of deposits were present as well as the thicker spray-like deposit (sample A3.2 is shown in Figure 4.18). The final sample that was analyzed was sample A3.3, which contained the spray-like deposits as well as a large splat, which lays on top of the spray-like deposits (Figure 4.19). These three samples were analyzed under the SEM and elemental analysis conducted with the use of the EDS. Elements such as Al and Cr were detected in large quantities by the XRF and less of Fe, Cu, and Ni. Such elements were expected to be found on the surface and cross-sections of these samples.



Figure 4.17 Sample A3.1 belonging to Area 3 where metallic streaks and heavier deposits can be seen at the starboard-side of the sample. (30X)



Figure 4.18 Sample A3.2 belonging to Area 3 where metallic steaks and heavier deposits can be seen at the starboard-side of the sample. (30X)

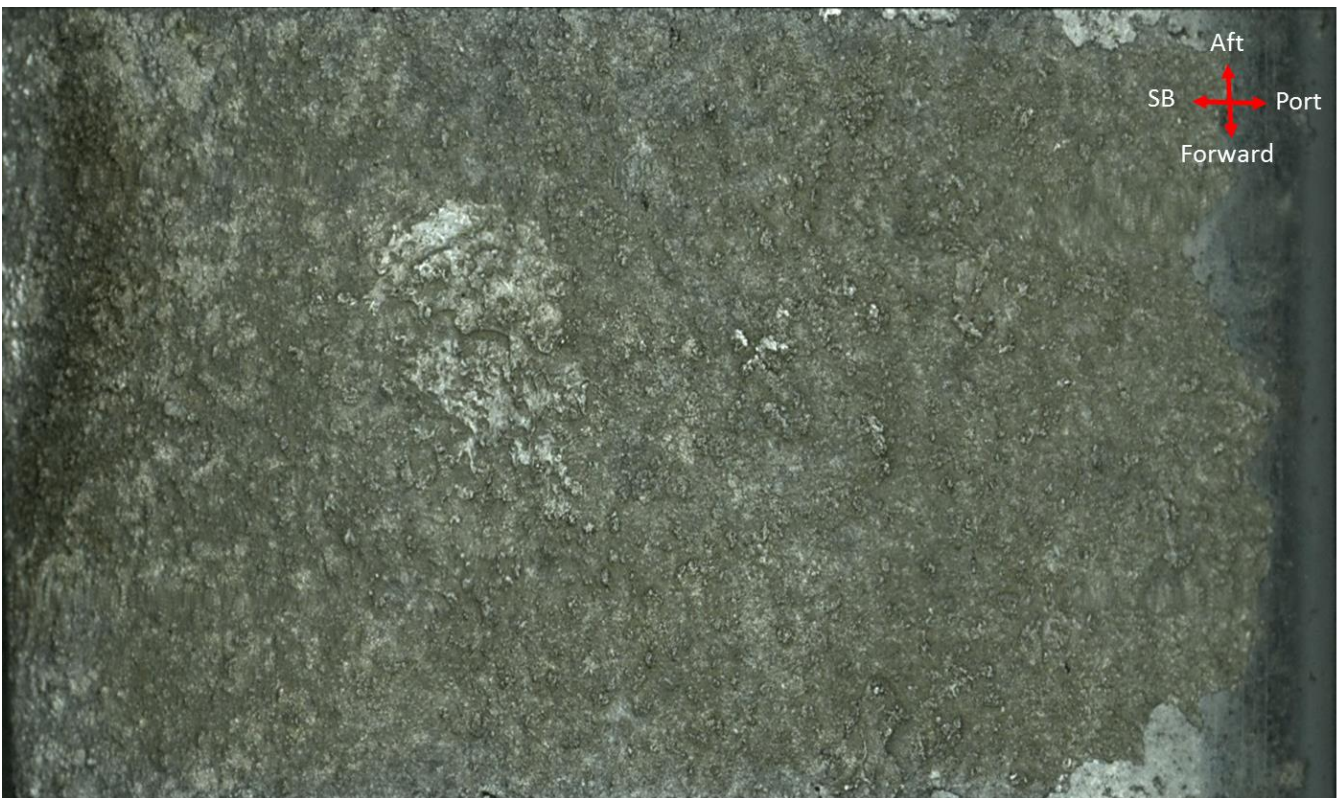


Figure 4.19 Sample A3.3 belonging to Area 3 where heavier deposits can be seen covering the whole sample with a large metallic splat deposited on top of the heavy deposit layer. (30X)

4.1.3.1 SURFACE ANALYSIS

The sample A3.1 contained narrow, silver colored, metallic, streaks where the majority had a directionality going from forward to port with respect to the position of the elevon actuator in the space shuttle. Other streaks were deposited in the opposite directions, from aft to starboard which can indicate that the *Columbia* rotated 180° at a point in time during the breakup. The streaks were seen in the forward-starboard corner of the sample. Along with these very thin metallic streaks, heavier deposit splats were observed in the aft-starboard corner. These bulkier deposits appeared to have been covered in hydraulic fluid or oil since they had a dark coloration and the solid heavy substance did not clean easily. Due to the fact that this sample was located at the bottom region of the shaft, no continuous deposit layer was observed. Approximately 25% of the sample surface was covered by light splat deposits.

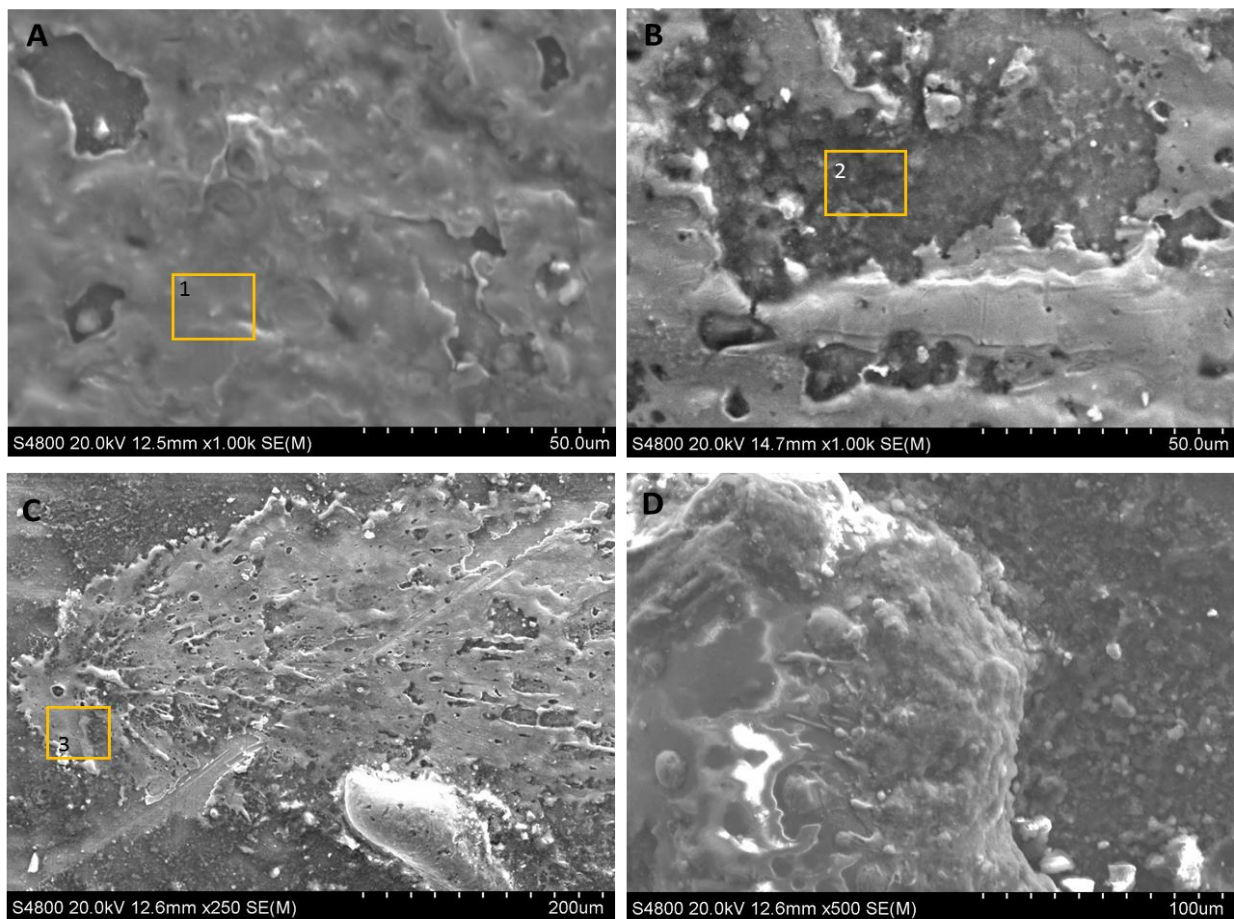


Figure 4.20 SEM images of surface deposits found on sample A3.1. EDS spot analysis is indicated by yellow squares in images A through C.

Analyzing the sample under the SEM, it was observed that the sample contained two layers. The first layer had a very granular texture where agglomeration of small particles was seen. This bottom layer was mostly seen on the starboard side of the sample. The second layer, which was observed to be deposited on top of the thin granular layer, was a lot thicker than the first layer and consisted of splats and thicker granular deposits. Several of the surface features seen in this sample are shown in Figure 4.20 and consist of the agglomeration of small particles along with large metallic splats. Splats observed in Figure 4.20 A and B were smooth and flat as if the molten metal flowed freely as it was being deposited; before it solidified completely. These splats were located on the forward-starboard side of the sample. In Figure 4.20 C and D deposits, which were coming from the upper corner, starboard-aft location with respect to the shuttle, showed the presence of large, thick deposits, the thinner layer of deposits, and a splat deposited in a direction going from starboard to port. Splats in this area were thinner than the ones seen in the upper region of the sample and had a rougher texture and porous areas due to entrapped gas bubbles (Figure 2.20 C). The thick, bulky deposits seen in the area had mostly a globular shape and did not appear to be deposited in a particular direction.

EDS spot analysis in this area revealed that the splats seen in the area were composed of what appeared to be two different material systems. Figure 4.21 1 shows the EDS results for one of the splats analyzed in the sample and are shown in Figure 4.20 A. Splats deposited in the surrounding areas consisted of approximately 85 wt. % Ti as EDS results showed. On areas in the starboard-aft corner, splats differ in chemical composition and were mostly composed of Fe and lesser amounts of Cr (Figure 4.21 2). Similar chemical composition from the upper and lower starboard-side of the sample was seen on the first layer that was observed in sample A3.1. The thin spray-like layer, where large splats of Ti, Cu, and Fe were deposited on top of it, was composed of Fe, Cu, and Al. This composition was similar to the thinner splats seen in the sample at the upper starboard corner. Around 60 wt. % Fe was present in the thin layer with about 15 wt. % Cr and 5 wt. % Al as indicated by the EDS results in Figure 4.21 3 taken from the

area indicated by a 3 in Figure 4.20 C. Due to results showing Ti splats and the Fe deposits, it can be concluded that two material systems were being deposited in this area during the break up. It also suggests that splats were deposited at a later time after the first thin layer that was observed.

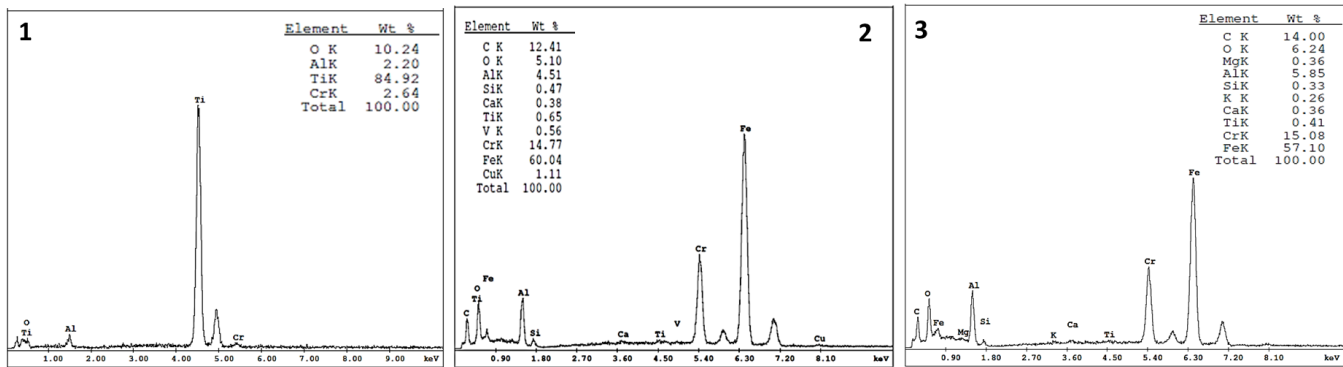


Figure 4.21 EDS spectra from sample A3.1 of first and second layer of deposits found at the surface. EDS 1 and 2 show chemical composition of splats and EDS spectrum 3 is the composition of the thin layer of deposit observed in the sample.

Sample A3.2 located directly above sample A3.1 also had the thin layer present, taking up about two thirds of the samples’ area. In this area, circular splats could be seen without the aid of an instrument. This splats differ from the ones seen on sample A3.1 since they had a more circular shape instead of an elongated strikes and were found in closer proximity to each other and covered most of the area where the thin layer was present. Though most of this area was covered by splats and a thin layer of deposits, there were small deposit-free zones. The rest of the sample which made up about a third of the sample and was located on the port side, had a thick layer of deposit which also contained the metallic circular splats.

First analyzing the area belonging to the thin layer of deposits, the same granular, spray-like texture on deposits that was seen in sample A3.1 was observed on this sample as expected since it was adjacent to sample A3.1. Figure 4.22 A and B show SEM images of this thinner layer of deposit. Along with this thin layers the splats could be observed as well and cracking of these splats was also noticed. In some locations, the splats had chipped off, suggesting spallation and most probably due to impact or handling after recovery (Figure 4.22 B). The flaking of the splats revealed the chromium coating of the base metal and is probably why bare areas on the sample were observed during the visual examination. When

analyzing the deposit layer on the other area of the sample, smoother surface textures were seen. Flat regions of continuous heavy deposits were observed and cracks were still seen in several regions of the sample close to where chipping of this layer occurred. Agglomeration of globular metallic droplets shown in Figure 4.22 E and F were also seen deposited directly on top of the thick deposit layer and once again cracking was present and noticed on these droplets. The thick deposits though smooth, had areas where deposits were chunky.

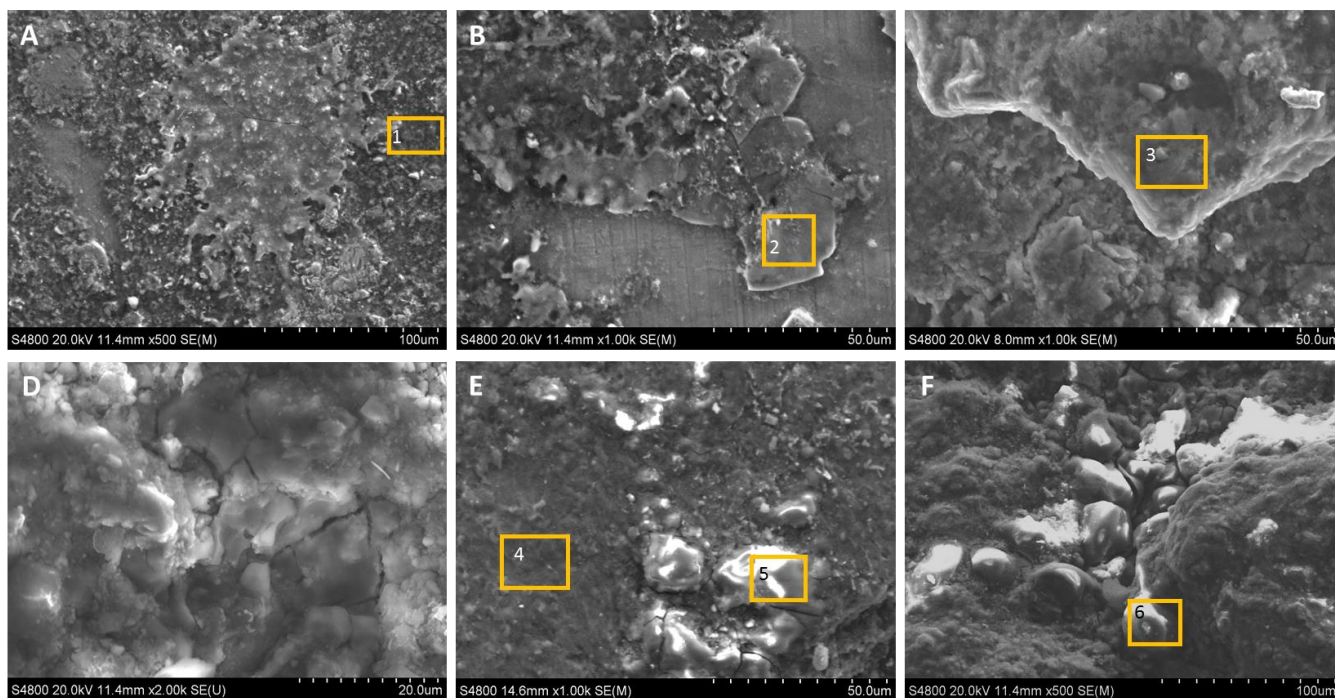


Figure 4.22 SEM surface analysis of sample A3.2 showing different regions throughout the sample including splats, cracking of deposits, and globular metallic droplets. Yellow squares indicated EDS spot analysis shown on Figure 4.23.

Examining these same areas for their chemical composition indicated that the thin layer of deposits was different from the one identified on sample A3.1. The areas analyzed for the thin layer showed that the layer was mostly composed of Al and O. In addition to Al and O, about 5 to 9 wt. % of elements such as Cr, Fe, Ti, Cu, and Ni were detected (Figure 4.23 1). The splats in these areas were composed of Ti and had similar composition to the splats found on sample A3.1. Smaller amounts of V, Al, and Fe were found in these splats as well. EDS results belonging to the splats area shown in Figure 4.23 2. On the heavier deposits seen, EDS spectra showed that the main composition of this layer was composed of Al and O with smaller amounts of Cu as seen in Figure 4.23 3 and 4. EDS results on Figure 4.23 5 and 6

belong to spot analysis done on the metallic droplets seen in sample A3.2. Two major elements in different locations that were analyzed were detected, Al and Fe. These solidified droplets were located all throughout the thicker layer of deposit and there was no particular location where Al and O or Fe droplets dominated. The globular droplets of Fe made up about 70 wt. % of the total composition followed by approximately 20 wt. % Cr. Results for these Fe droplets are shown in Figure 4.23 5. As for EDS results of the aluminum droplets, about 50 wt. % of O was present meaning these aluminum droplets could have rapidly and heavily oxidized.

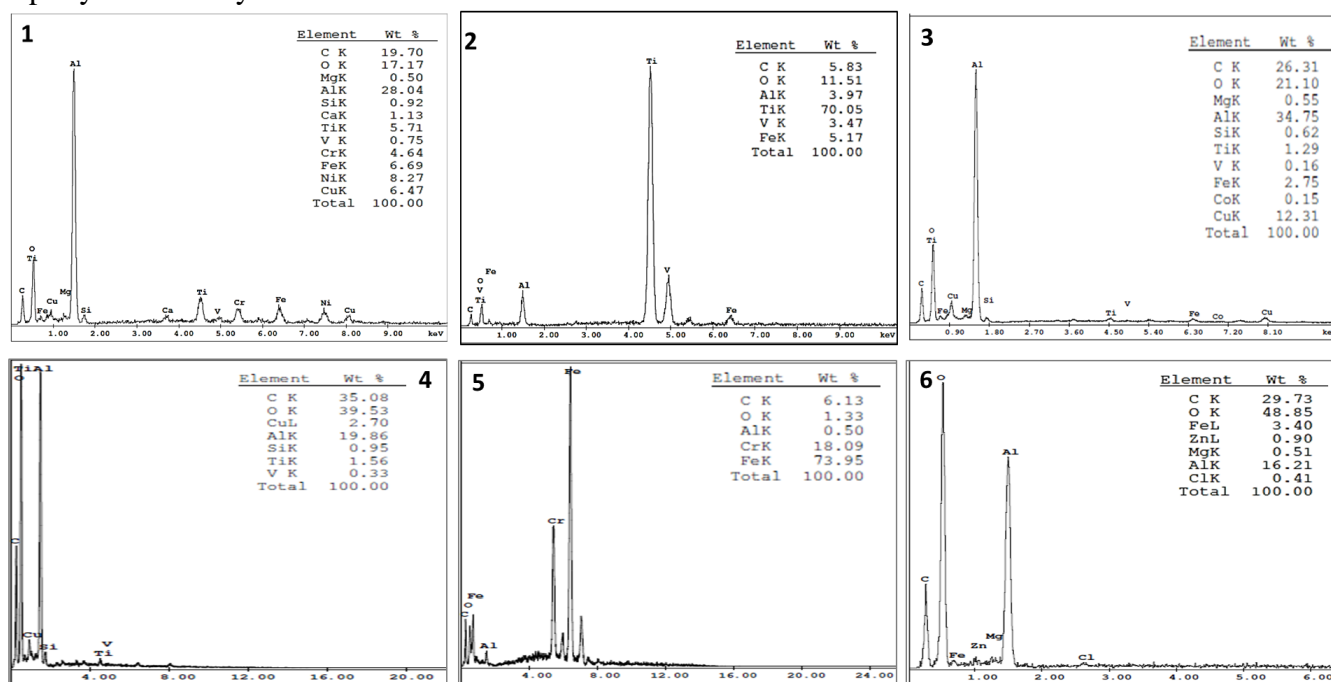


Figure 4.23 EDS results for surface analysis belonging to the heavily deposit area on sample A3.1. Exact location of where readings were taken in sample are shown in Figure 4.22.

The final sample in this area, A3.3, was completely covered in heavy deposits and was also directly above sample A3.2. It was expected to see the same morphology and chemical composition of this thicker layer of deposit as the ones detected in the second sample analyzed from Area 3. Looking at the surface under the SEM, the large splat visible in the center of the sample was analyzed first (Figure 4.24 A and B). It was evident that the material that got deposited in this area was in a liquid phase due to the morphology observed under the SEM. A smooth, flow texture was seen through the whole area that consisted of the splat and was noted that silicon particles were embedded in this deposit as well. The

silicon particles can be seen in images A and B on Figure 4.24. The morphology in other regions was similar to sample A3.2 with bumpy rough surfaces. There were areas where the surface textured changed and different particle sizes clustered together forming larger particles or the particles stayed as one and deposited on the top surfaces of the deposits. SEM images of the behavior seen in sample A3.3 are shown in Figure 4.24 E and F.

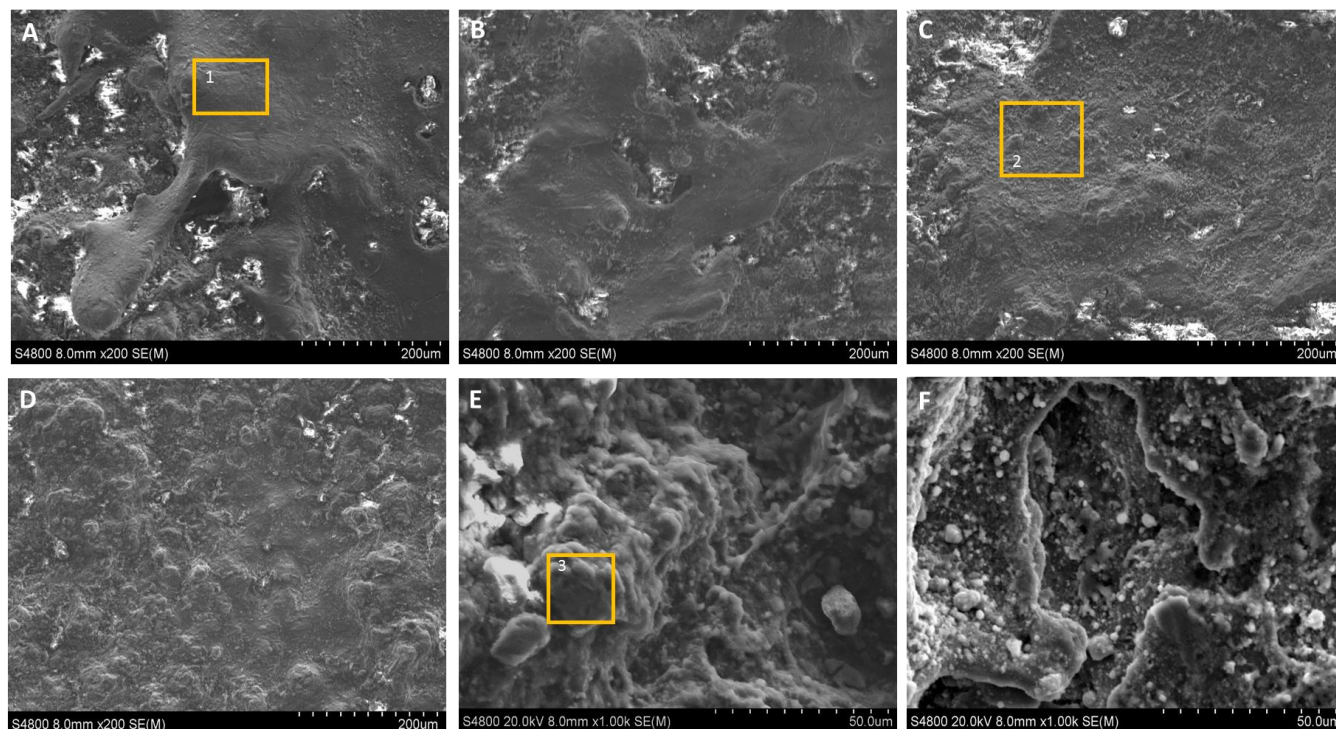


Figure 4.24 SEM images of sample A3.3 surface analysis where a smooth surface was found on a large metallic splat. Rougher surfaces and clustering of particles were also detected.

Much of the chemical composition of the deposits found on this sample were Al and O. This is expected due to the Al airframe surrounding the hydraulic system. EDS spot analysis in areas shown in Figure 4.24 detected approximately 40 wt. % Al in deposits and around 60 wt. % Al in the large metallic splat that was found on the sample. Minor elements that were detected by the EDS were Fe and Cu. Cu was found to be present in concentrations as high as 11 wt. % and Fe was detected in quantities of 9 wt. % when different readings were taken around the sample (Figure 4.25). Less than 3 wt. % Mg was also found to compose the heavy deposit found on the sample. Comparing the composition of samples A3.2 and A3.3, Al and O enriched areas dominated the deposits and both samples also had lesser amounts of

Fe and Cu which was expected since the deposit is coming from the same area. The only difference in composition was that Ti was not detected in sample A3.3, which might be because this sample was located at the upper region of the shaft, whereas A3.2 was located on the side of the shaft and was where most the Ti splats and streaks were found.

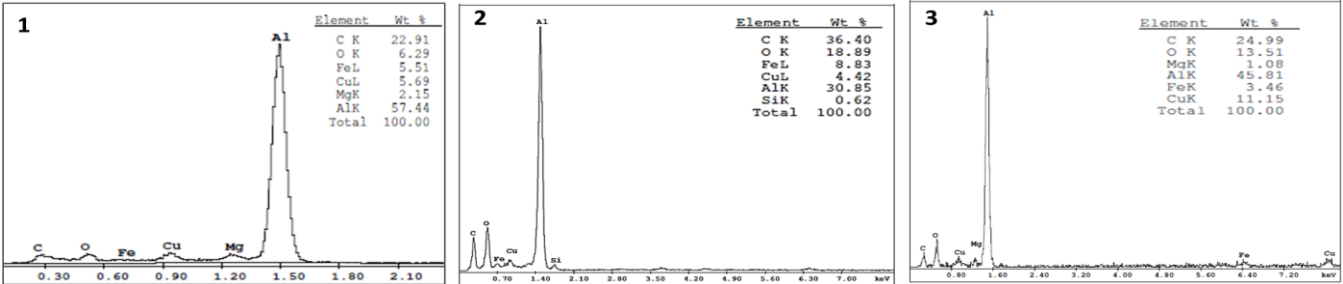


Figure 4.25 EDS results from surface of sample A3.3 of Area 3 showing the majority of the deposit were AlO. Area of spot analysis is shown in Figure 4.24.

4.1.3.2 CROSS-SECTIONAL ANALYSIS

All three samples analyzed from Area 3 were mounted in a transverse direction to examine the cross-sectional view of the deposits morphology and elemental composition. Sample A3.1 did not have many features and mainly consisted of a flat thin layer that ranged from approximately 50μm to 88μm in thickness. This layer was mostly Al and O enriched deposits and about 20 wt. % Cr was also detected in the deposit, but is mostly likely due to the Cr layer that is found directly below the deposits. Note that Ti deposits were detected in this area as well. Due to the deposits being very thin, charging of the sample was occurring and was difficult to focus on thinner deposits which most probably belonged to the Ti streaks observed during surface analysis. Results of EDS analysis done on this thin layer and particles found on the sample are shown in Figure 4.26 1 and 2.

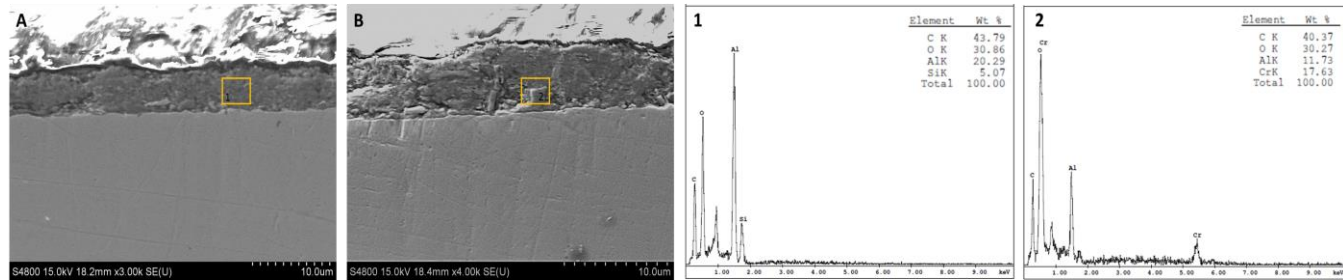


Figure 4.26 SEM cross-sectional view of sample A3.1 from Area 3 area shown in A and B. EDS spectra of areas shown in A and B area shown in 1 and 2, respectively.

Sample A3.2 which consisted of the same thin layer shown in Figure 4.26 and a thicker layer of continuous deposits was examined for any layers or particles embedded under the top surface of the deposits. The average thickness of deposits found on the area where chipping was occurring was 230 μ m compared to 88 μ m for the thinner layer exposed due to spallation. The chromium coating applied to the shaft for additional protection was also measured and had an average thickness of 103 μ m. The coating did not show any indications of thermal alterations. Seen throughout the entire length of the deposits was a porous area located just above the chromium coating. In some regions, the discontinuous cavity contained individual particles about 20 μ m wide which was approximately the same width as the cavity. The particles seen in the hollow region were identified as Al and O enriched particles. Above this region, a compacted solid deposit with few porous areas was observed. Figure 4.27 show SEM micrographs of the cross-sectional view of the deposits found on A3.2.

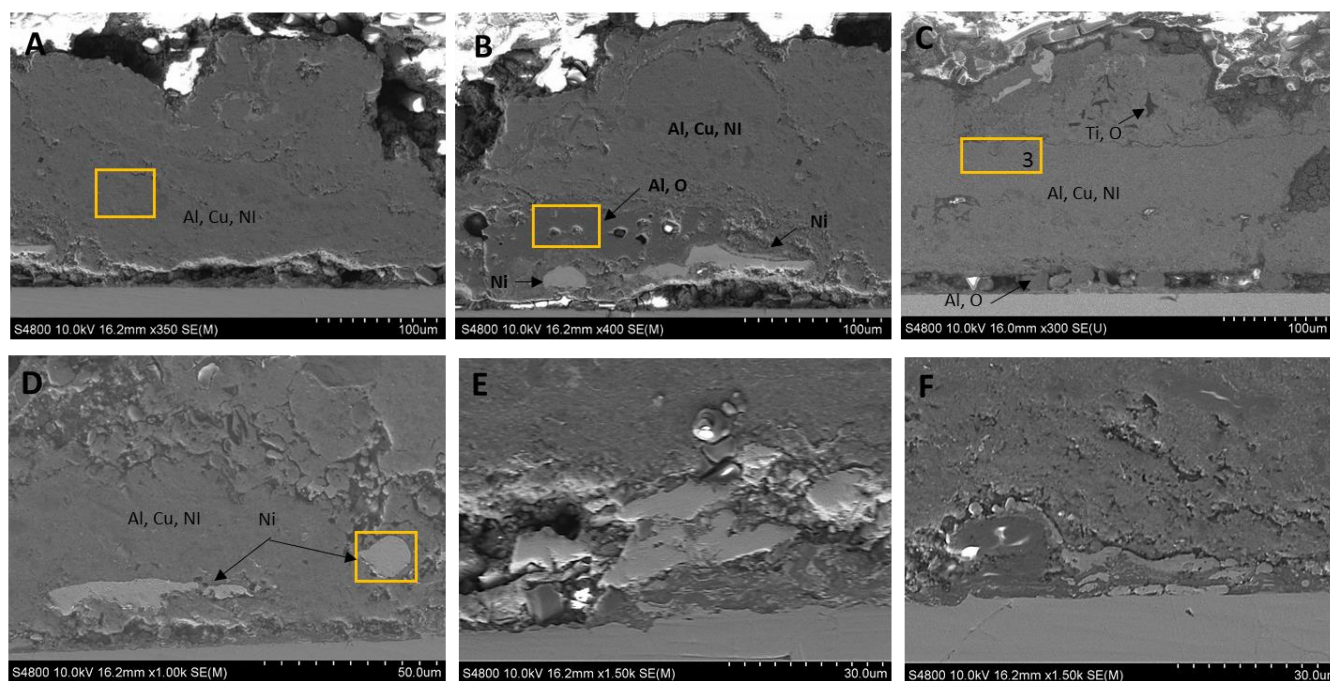


Figure 4.27 SEM cross-sectional view of sample A3.2 from Area 3 area showing dark and light deposits surrounded by dark gray matrix which makes most the deposits.

Three distinct deposits were analyzed. The first deposits, which made up most of the thick layer and is depicted in a gray color by the SEM images, were analyzed by EDS showing that they were mostly

consisted of Al, Ni, and Cu (Figure 4.27). The second deposits were observed at the bottom and top surfaces of the deposits. These dark color deposits were found usually larger in size but were present in fewer quantities when compared to lighter deposits seen in the cross-section. The dark areas as shown in Figure 4.27 B, E, and F consisted of Al and O. EDS results can be seen in Figure 4.28 2. Other darker regions found in the deposits were analyzed by EDS and corresponded to Ti being dispersed throughout the entire area of the deposit (Figure 4.27 C). The final embedded deposits analyzed were light deposits that were usually seen also embedded at the bottom or top surfaces of the deposits. EDS spot analysis conducted on the light deposits demonstrated that they were composed of Ni with smaller amounts of Fe (Figure 4.28 4).

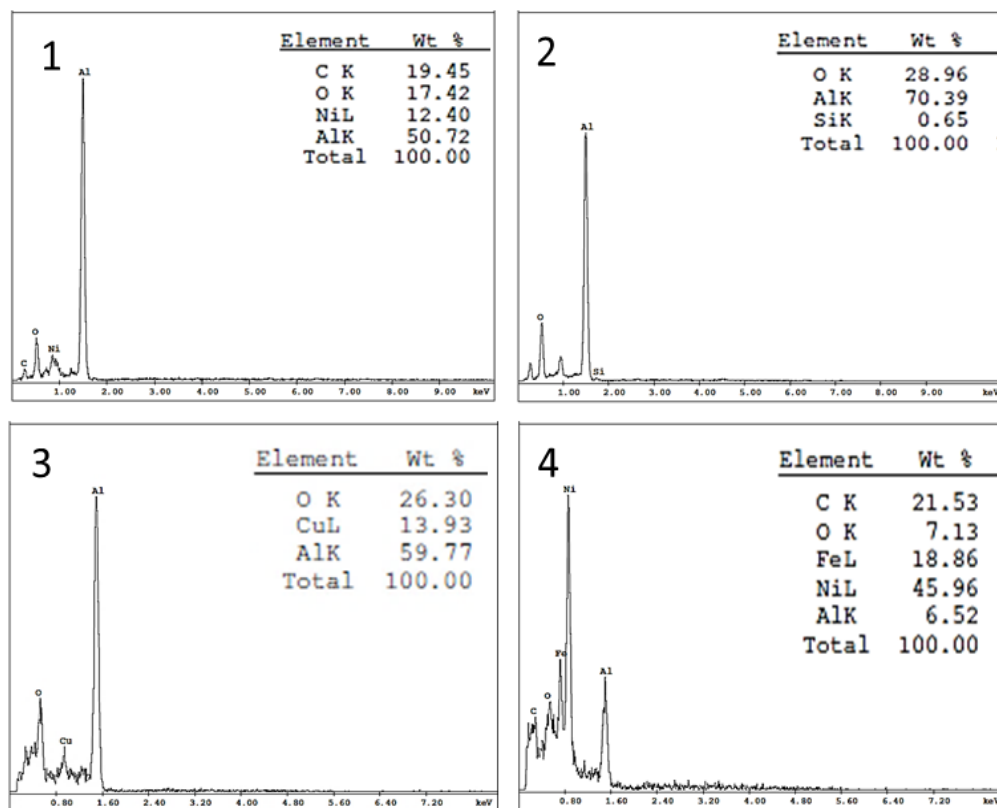


Figure 4.28 EDS results for the three distinct layers observed in sample A3.2. Location of where reading was taken is shown in Figure 4.27

The third and final sample of Area 3 was analyzed and showed similar light deposits being present in this area. These lighter deposits were found in larger quantities in sample A3.3 and were seen mixing with the darker gray matrix as shown in Figure 4.29 A and C. The light deposits had a swirling flow

texture while mixing with the rest of the deposit and might be due to molten metal being deposited in a more dynamic manner. This type of behavior was observed in the port-side of the sample, whereas on the starboard side, closer to the location of sample A3.2, larger irregular areas of the light deposits embedded themselves in the matrix as in sample A3.2. An EDS reading for the light deposits seen in this sample is shown in Figure 4.29 1. Also, noticed in this sample was the amount of porosity present as compared to the porosity seen in A3.2. This increase in porosity, again, could be due to the more violent way the deposits adhered to the shaft with more rapid solidification expected. The elements found in the deposit were Al and a smaller amount of Cu than the ones detected in sample A3.2. Overall, the thin layer of deposits seen in sample A3.1 and portions of A3.2 were Al and O and the thicker layers of deposits contained major amounts of Al, Ni, and Cu.

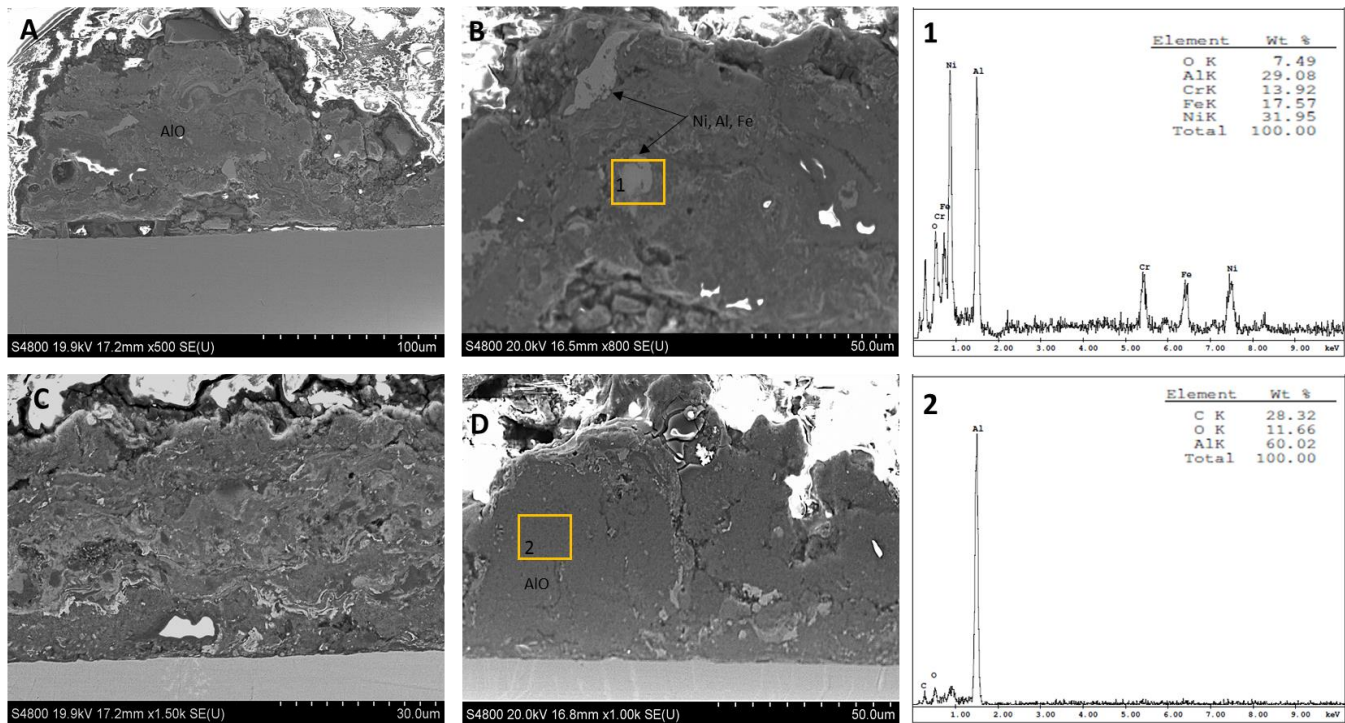


Figure 4.29 SEM images of cross-sectional view of sample A3.3 A through D showing areas where EDS spot analysis was conducted, depicted by the yellow boxes. EDS spectra of readings taken in sample A3.3 area shown in 1 and 2.

4.1.4 AREA 4

The final area investigated in this research was Area 4, which was located at the end of the actuator shaft near the clevis and locking nut, connecting directly to the shaft. This area was selected for analysis

due to the distinct eroded area seen in the shaft, which also contained very heavy amounts of deposits and were tightly adherent to the shaft. Some areas were solidified as molten metal ran down the circumference of the shaft and a thicker layer of deposits was seen surrounding this area. Three deposits were sectioned and analyzed. Two of these samples, A4.1 and A4.2, were located on the area where a significant valley in the shaft was noticed and was assumed to have experienced localized melting. Sample A4.1 and A4.2 are shown in Figures 4.30 and 4.31, respectively. The third sample A4.3 was located at the end of the shaft where a threaded area was present. This threaded area was where a safety break was connected when the shuttle was not in use and prevented the movement of hydraulic system, hence the shaft. This sample piece had light deposits present and the threaded region appeared to have experienced minimal uniform erosion as well. This last sample is shown in Figure 4.32. The surface of these samples as well as their cross-section will be analyzed under the SEM and their chemical composition was made known by utilizing EDS.



Figure 4.30 Sample A4.1 belonging to Area 4 showing heavy rough deposits in the port side of the sample where thermal erosion is also observed. Cracked deposits can also be seen in the forward bottom portion of the sample. (30X).



Figure 4.31 Sample A4.2 belonging to Area 4 where metallic splats can be seen throughout the sample as well as black spots that correspond to oil stains. Seen in the lower forward edge is the dent where possible thermal erosion of base metal might have occurred. (30X).

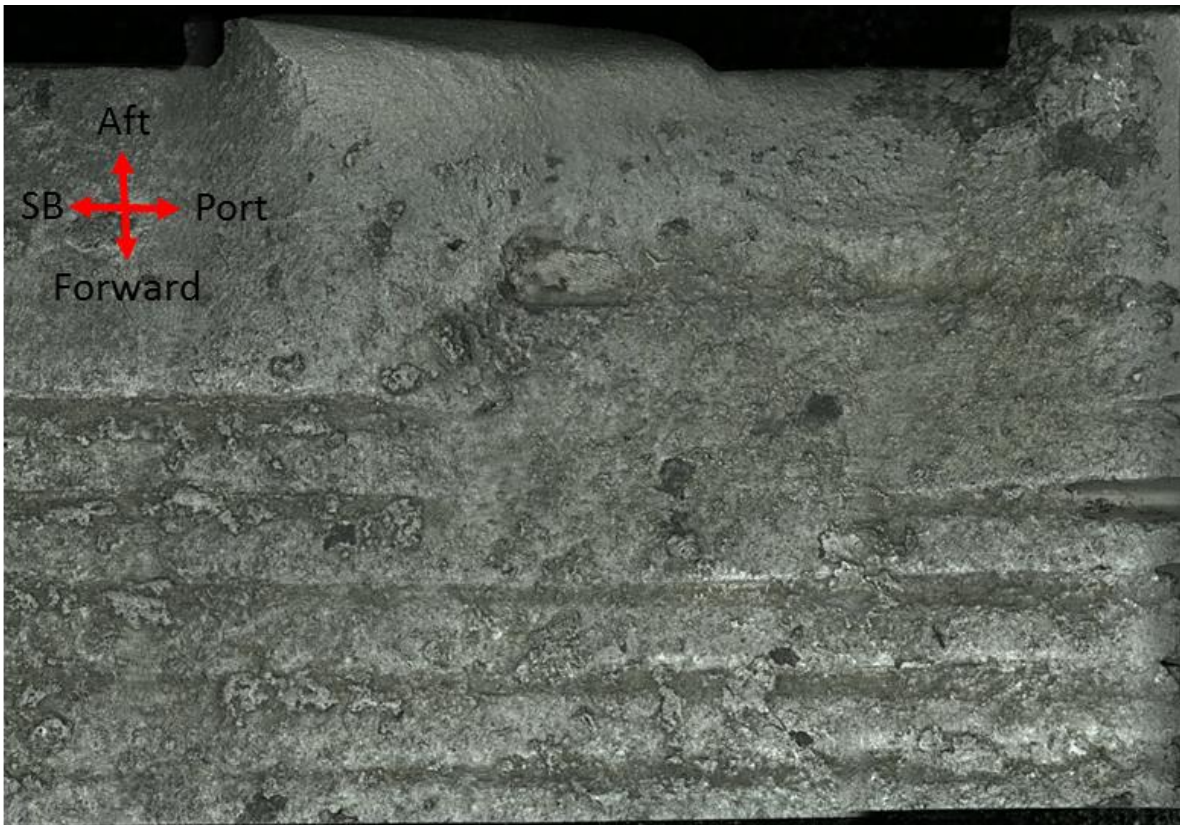


Figure 4.32 Sample A4.3 belonging to Area 4 showing threaded area which has multiple metallic deposits, black oil stains, and thermal damage. (30X).

4.1.4.1 SURFACE ANALYSIS

While analyzing A4.1, particle agglomeration and re-solidification were seen in several regions where popcorn-like texture, with many crevices, was observed and is shown by the SEM images in Figure 4.33 A and B. In this same region, faceted surfaces were also noticed but were most likely caused by mechanical damage to the deposits after they had solidified. This surface morphology is shown in Figure 4.33 C. Deep cracks in the deposits were observed as well as in the region where the accumulation of deposits was the greatest and tiny silica particles were seen throughout the sample. These silicon and oxygen enriched particles were mostly detected in the crevices where rough surface textures were observed. Other regions such as those seen in Figure 4.33 E and F consisted of bumpy surfaces but much smoother than regions observed earlier. Deposits appeared to adhere tightly to the shaft's base metal and small particles were also noticed on top surfaces of the deposits but were found in a smaller amount than in areas where porosity and crevices were seen. These deposits were observed in the starboard-side of the sample where a thinner layer of deposits was present. The final surface feature that was detected when analyzing sample A4.1 was splats, which were also present in Area 3. The splats found in sample A4.1 were also very like the splats seen in Area 3 and were deposited on to sections where flatter surfaces were present. SEM images in Figure 4.33 G through I show several splats found on the sample. These splats were deposited on the surface when they were in a state of liquation since the texture was smooth and appeared to have liquefied quickly. Splats seen in this sample appeared to have deposited in smaller amounts since they were thinner than splats on Area 3. Cracking of these splats was also noticed and is most likely due to the splats oxidizing rapidly making them very brittle and susceptible to cracking upon impact.

EDS spot analysis on deposits as those shown in Figure 4.33 A through C revealed that they consisted of approximately 40 wt. % Al and 20 wt. % Ni. Smaller quantities less than 10 wt. % of Fe and Cr were also detected in these popcorn-like surfaces and about 3 wt. % Ti was present as well. The EDS

spectrum of this area, where higher quantities of deposits accumulated, is shown in Figure 4.34 1. In areas where a thinner and smoother layer of deposits were found, a similar elemental composition as the one found on the rougher surfaces was detected. Al was present in quantities of about 40 wt. % and Fe, Ni, and Cr were all detected but were in quantities of approximately 5 wt. % (Figure 4.34 2). Metallic splats like those observed in Area 3 were analyzed by EDS and several splats indicated that these were also coming from a titanium component just as those in Area 3. Deposits consisted of an average of 68 wt. % Ti, 15 wt. % O, and 13 wt. % Al. EDS spectra of deposits and splats found in A4.1 are shown in Figure 4.34 3 and 4.

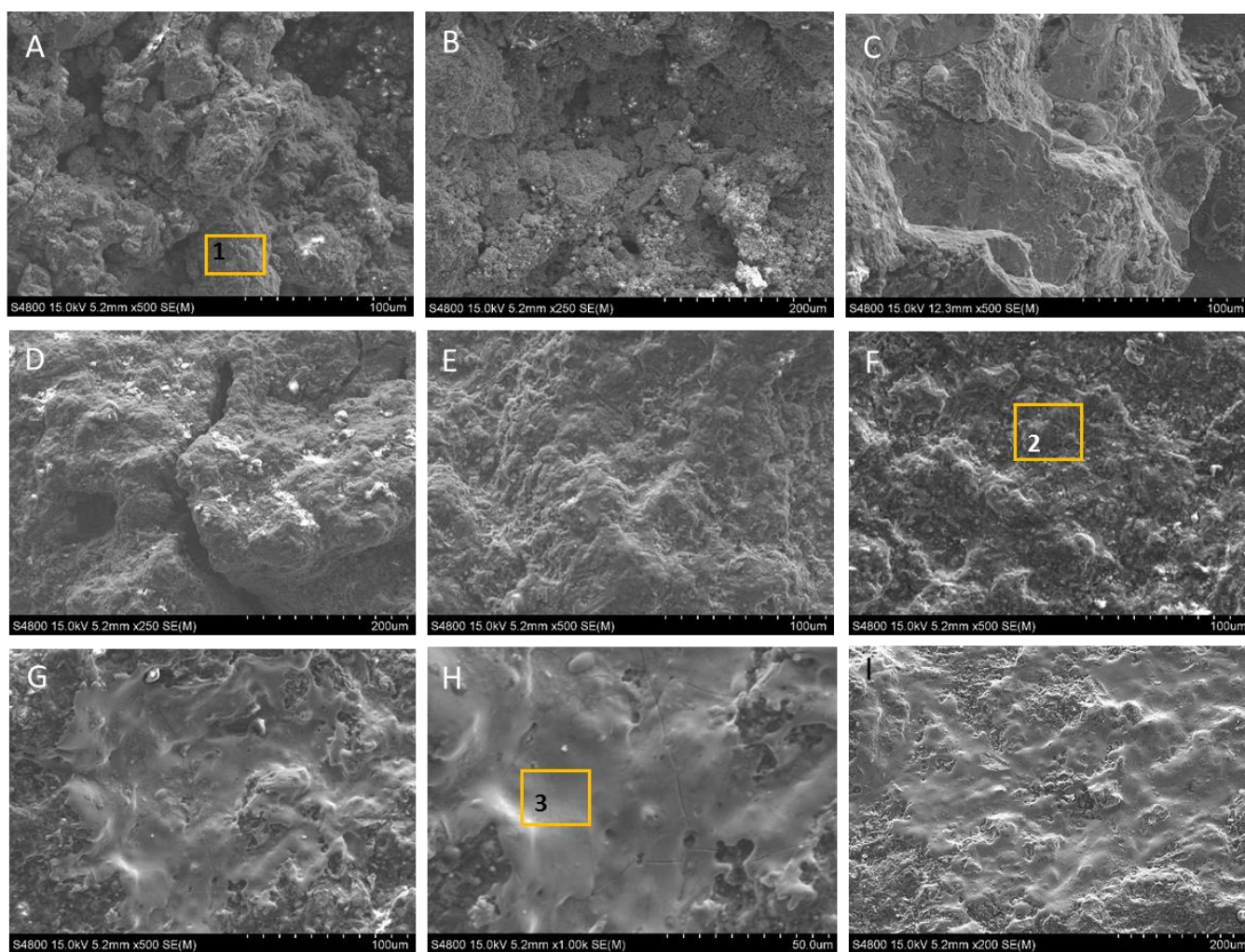


Figure 4.33 SEM surfaces analysis conducted on sample A4.1. (A-C) Popcorn-like texture with small Si particles present found on area where the heaviest deposits were present. (C-F) Thinner deposits present where a bumpy surface can be observed. (G-I) Splats seen deposited on top of re-solidified deposit.

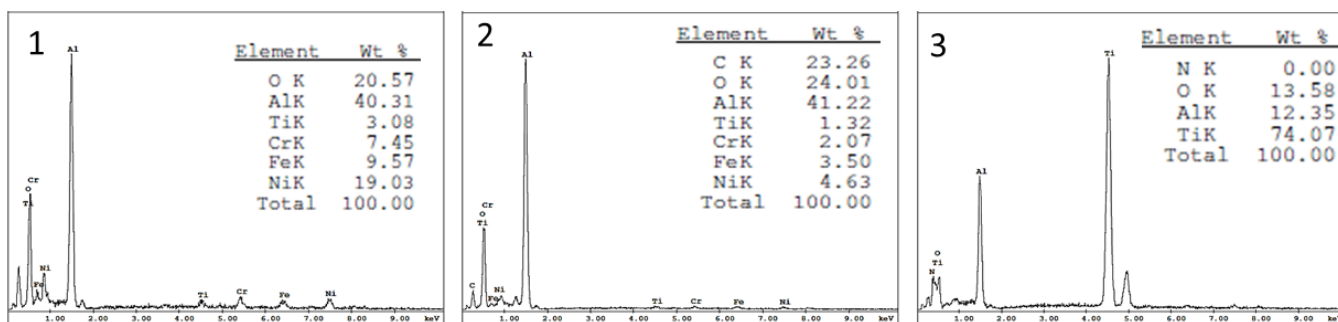


Figure 4.34 Elemental analysis of sample A4.1 conducted by EDS. Results for spot analysis done on areas in Figure 4.33 are shown 1 through 3.

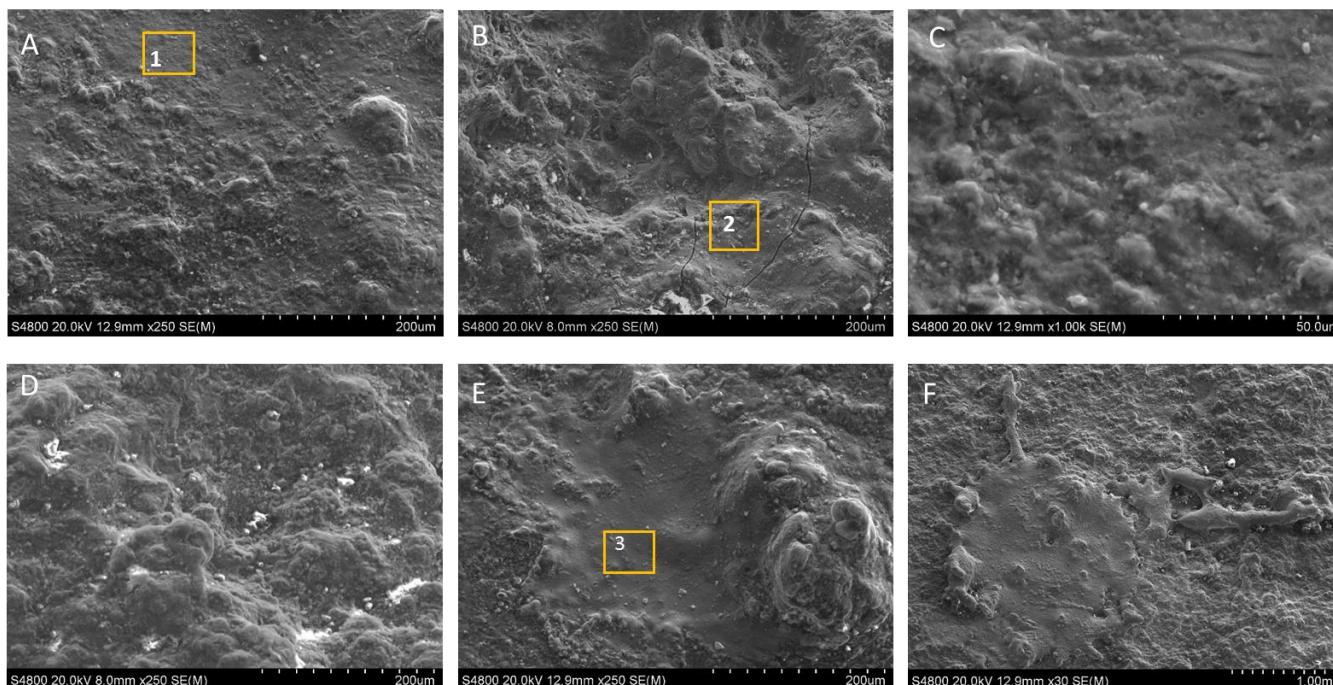


Figure 4.35 SEM images of sample A4.2 surface analysis. Large clusters of deposits can be seen throughout the sample along with Si and O enriched particle and splats.

Sample A4.2 which was found directly above sample A4.1 was analyzed for surface morphology and elemental composition was analyzed in this area. The presence of Si and O enriched particles was more apparent than other areas. Small particles that deposited on to the shaft's surface seemed to have clustered together and formed larger clusters, which protruded from the deposits. These protrusions were observed in different sizes and covered most of the surface of the sample (Figure 4.35). In the area where the change in diameter occurs at the shaft, the texture of these deposit becomes a lot smoother but agglomeration of particles was still present and the clusters were smaller in size (Figure 4.35 A). As seen in deposits from the adjacent sample, cracking occurred in the area as well but on this occasion, cracking

was observed in the deposit itself as shown in Figure 4.35 B and not on splats like seen in other samples. The silica particles can be visible in Figure 4.35 C and splats again were seen on this sample as well. Some of the splats seen on the sample are shown in Figure 4.35 E and F.

The elemental analysis conducted in this area showed that the deposits consisted of a large mixture of elements with Al having the largest content in the deposit. Al was found to make up as much as 60 wt. % of the deposits (Figure 4.36 1). Ni, which is also found in large quantities in other samples was present here in concentrations of about 30 wt. %. EDS results for deposits, which contained large amounts of Ni, are shown in Figure 4.36. One major difference seen in the splats on Area 4 was that the major element found to compose the splats was Ni. In these splats, approximately 40 wt. % Ni was present in these deposits and the EDS spectrum of a splat analyzed in sample A4.2 is shown in Figure 4.36 3. Other elements in the splats were Fe and Cr which made up about 12 wt. % each. Al and O regions were present but again, Ni was the major element found in the splats on this sample.

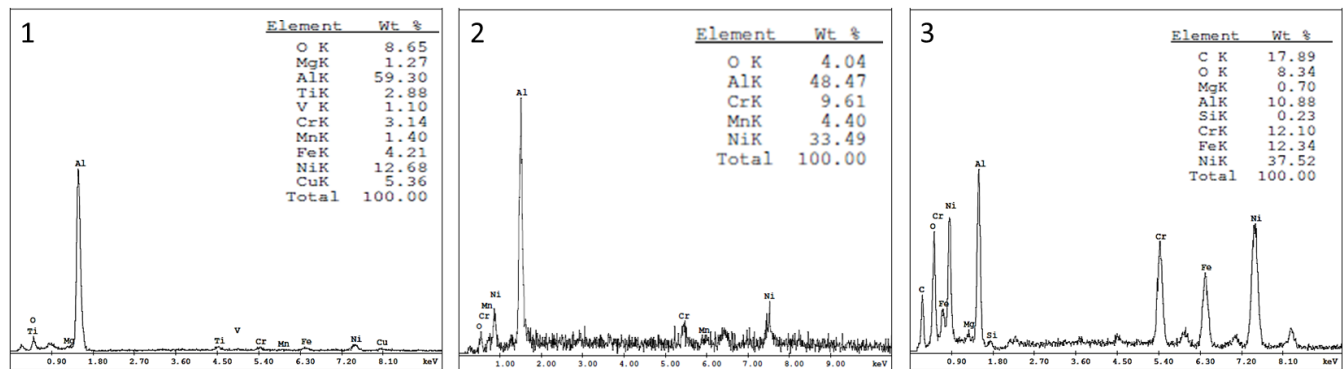


Figure 4.36 Elemental analysis of sample A4.2 conducted by EDS. Results for spot analysis done on areas in Figure 4.35 are shown 1 through 3.

The final sample analyzed was sample A4.3 and was located directly next to sample A4.2. This sample contained many metallic spats and very rough surfaces. SEM images belonging to this area are shown in Figure 4.37. The surface texture in the threaded region was observed to be a lot rougher than any other sample analyzed. As molten metal and small metallic particles deposited onto the shaft, agglomeration occurred all throughout the sample. Images in Figure 4.37 A and B show many particles that came together to make clusters. Loose small particles were also seen in these deposits and most likely

solidified in a quick manner, preventing further agglomeration with the bigger clusters present. Other regions had smoother surfaces but small hills and valleys of deposits could still be observed in these large smoother surfaces on the sample. Figure 4.37 C shows these textures seen in the sample as well as deep cracks. Cracks that were not as deep as others in the area were also present in deposits that appeared to be tightly adhered to the base metal and are shown in Figure 4.37 D. In the threaded regions, a different type of texture was observed which had a very granular and rough surface. Along with the granular surfaces, Figure 4.37 F shows cavities and splats present in the threaded areas. The deposits found in this area were Al with small amounts of Ni, Fe and Cr. EDS spot analysis conducted on several areas in sample A4.3 are shown in Figure 4.38 1 through 3. In this sample, not much Ti was detected and reduced amounts of Ni or Fe were present in the sample.

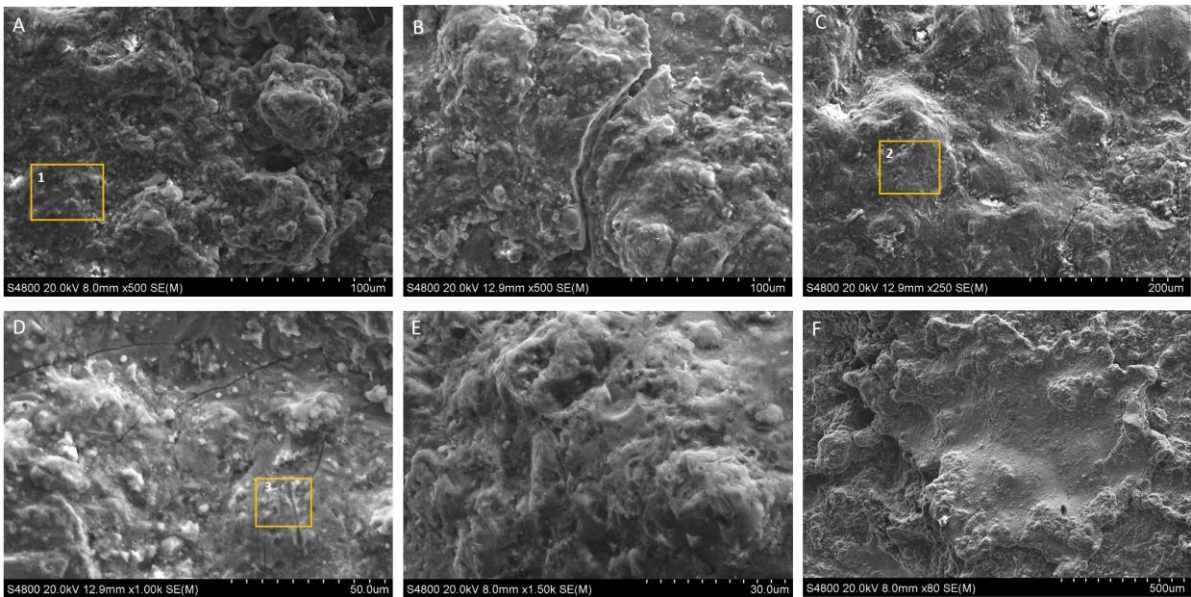


Figure 4.37 SEM surface analysis of sample A4.3 which shows particles clustering along with loose smaller particles in images A through F. Cracks can also be seen in C and D. Splats also seen in the sample are shown in image F.

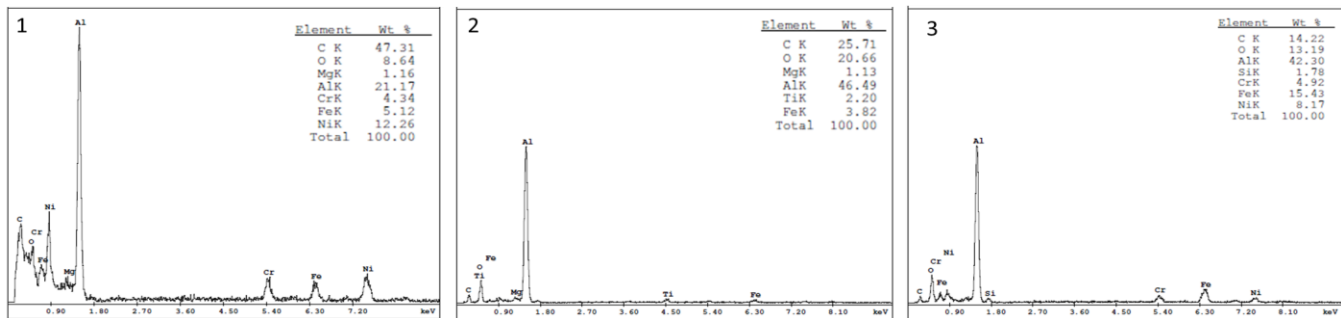


Figure 4.38 EDS spectra of sample A4.3 of areas shown in Figure 4.37.

4.1.4.2 CROSS-SECTIONAL ANALYSIS

The cross-sectional analysis performed in Area 4 where signs of thermal erosion were expected to be seen, will be discussed in this section. Different layers of deposits and embedded debris were expected to be present when the cross-sectional view of the samples was analyzed under the SEM, like ones observed in Area 3. The chemical composition of these different layers should also be similar to the ones found in Area 3 since these two areas are in close proximity to each other. The only difference might be finding higher concentrations of certain elements in the deposits since this was noticed when XRF was conducted in these two areas. Due to a greater amount of deposits found on Area 4, a greater amount of Cr, Ni, and Fe was expected since the base metal appears to have melted and mixed with molten metal coming from nearby components. When analyzing the cross-section of the samples, the morphology of any mixing that might have occurred with the molten base metal and the deposits from other components should be seen as well. The cross-section of samples A4.1, A4.2, and A4.3 were examined by SEM and EDS where detail of layering of the deposits and their chemical composition were closely examined.

While analyzing the cross-sectional view of sample A4.1, alterations suffered by the shaft due to the extreme temperatures were observed. It was evident that erosion in this area occurred since the loss of material and a change in diameter on the shaft were observed. SEM images from sample A4.1 showing the deposits as well as a downward slope due to erosion are shown in Figure 4.39. The first alteration noticed was on the chromium coating. The thickness of the coating decreased from crest to trough, from an average of 76 μ m to 42 μ m as seen in Figure 4.39 A and B. In the lowest point of the erosion, deposits accumulated and exhibited similar layering to Area 3. The average thickness at this point was approximately 890 μ m and was the largest amount of deposits found in all four areas examine. The depth of material that was removed by erosion in this sample was approximately to 1 millimeter.

A light-colored deposit was seen at the bottom region of the deposits and extended itself through most of the eroded region. The light gray deposits are shown in the SEM images in Figure 4.39 A, B and D sandwiched between the gray matrix. A dark gray deposit was also observed in the cross-sectional view of the deposits and was found to be mixed with a gray colored deposit mostly at the bottom of the deposits. When this dark deposit was found embedded in the deposit, it enclosed the material that surrounded it and resulted in circular shapes of different diameters as shown in Figure 4.39 C. Besides the mixing observed with these two deposits, the light and dark deposits, particles of different shapes and sizes were also seen embedded in a gray colored deposit which made up most of the deposits. SEM images in Figure 4.39 D and E show some of these dark particles which embedded at the bottom region of the deposits as well. The final layer that was observed in the deposits was much of what made up the deposit which is depicted by gray deposits in Figure 4.39 A, B, D, and F. This layer contained small mixtures of the dark gray deposits and was present in all areas of sample A4.1.

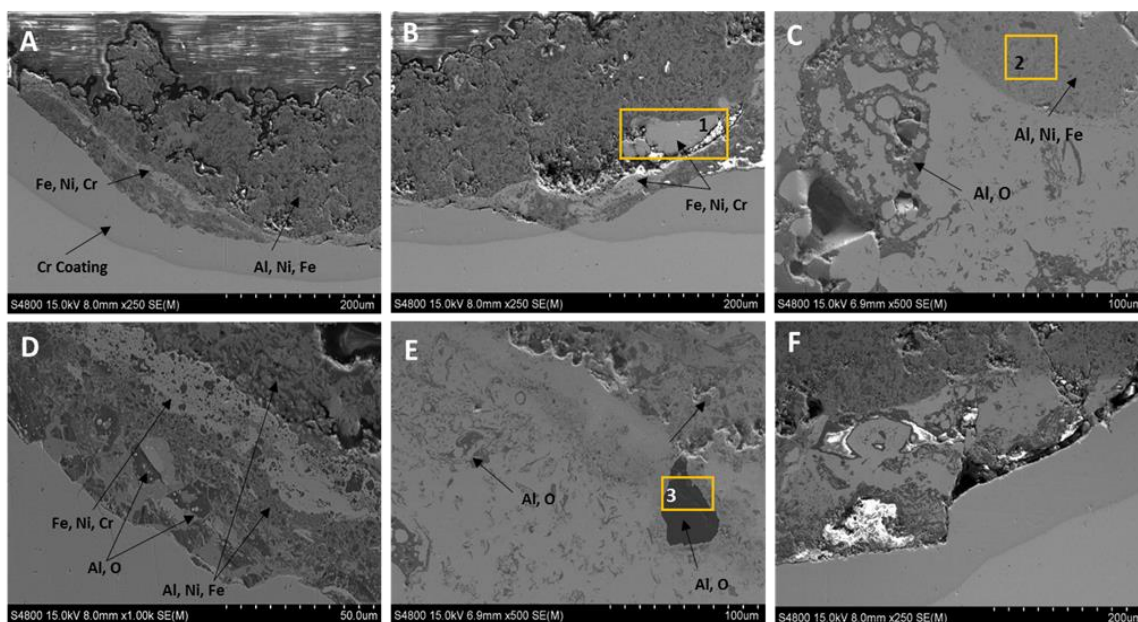


Figure 4.39 SEM images of the cross-sectional view of sample A4.1 on Area 4. (A-B) Slugging of chromium coating can be seen along with deposits. (C-D) Deposits present in the thermal eroded area.

For the chemical analysis performed in sample A4.1 on the light deposits observed in the lower areas of the deposits, EDS results detected large amounts of Fe as well as Cr and Ni in the light deposits (Figure 4.40 1). Approximately half of the composition of these light deposits was Fe and about 15 wt. %

of Cr and Ni each, was detected in this sample's cross-sectional view. In other areas, Fe deposits were mixed with the darker colored deposit. EDS reading of the gray deposit, which can be seen at a higher magnification in Figure 4.39 C and D showed that it was composed of approximately 26 wt. % Al with about 12 wt. % of Fe and 11 wt. %Ni. Other elements detected in this deposit were Ti and Cr but were only in concentrations of 5 wt. %. One of several EDS readings taken from this area of the deposits is shown in Figure 4.40 2. The dark colored deposit seen in sample A4.1 was identified as Al and O. The chemical composition of the dark colored deposits is shown by the EDS spectrum in Figure 4.40 3.

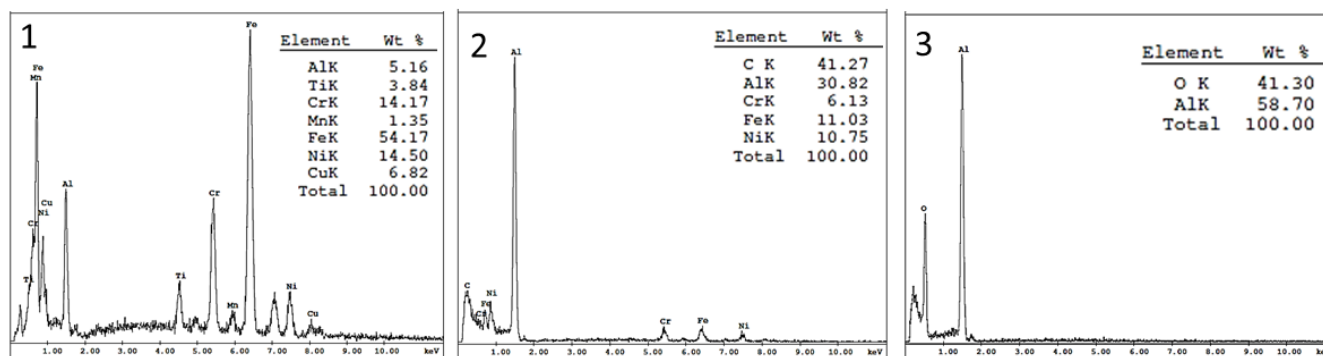


Figure 4.40 EDS spectra of the cross-sectional view of sample A4.1 are shown. Spectrum 1 corresponding to the light layers of deposit seen in the sample. Spectrum 2 indicates the chemical composition of the matrix deposit which have a gray coloration. The final spectrum belongs to the dark colored deposits.

Sample A4.2, where a more visible change in diameter was observed in the base metal, had similar features as sample A4.1 when the cross-sectional view was analyzed under the SEM. Examining the cross-section of this sample in areas where there was no evidence of thermal erosion led to finding deposits as thick as 407 μ m. This area showed the presence of the chromium coating and the base metal intact with no signs that this area was damaged by intense temperatures. A thin layer of light deposits could be seen throughout most of this part of the sample and was located at the bottom of the deposits as shown in Figure 4.41 A. SEM images at a higher magnification of the light deposits can be seen in Figure 4.41 B and C. Below this thin layer, as shown in the aforementioned images, consists of a mixture of gray and dark gray deposits. These deposits contained artifacts of what appeared to be turbulent flow during deposition. A detailed image of this turbulent flow can be seen in Figure 4.41 B and E. In Figure 4.41 D and E, signs of

thermal erosion occurring to the base metal were noticed. Erosion was confirmed in this sample as the chromium layer disappeared when the depression in the shaft was approached. The chromium layer, which originally measured about 103 μ m decreased to 45 μ m in thickness, due to the high temperatures that the molten metal reached as it was deposited on to the shaft which caused the melting of the chromium coating and the shaft itself (Figure 4.41 D). In this area, as the deposits start to flow where localized melting occurred, accumulation of deposits at the bottom were noted. Figure 4.41 E also shows how the chromium layer was compromised and started mixing with the deposits. In this area of the sample, which would be located facing the forward-side as opposed to Figure 4.41 D, while the aft-side deposits were a lot thinner and averaged a thickness of approximately 60 μ m.

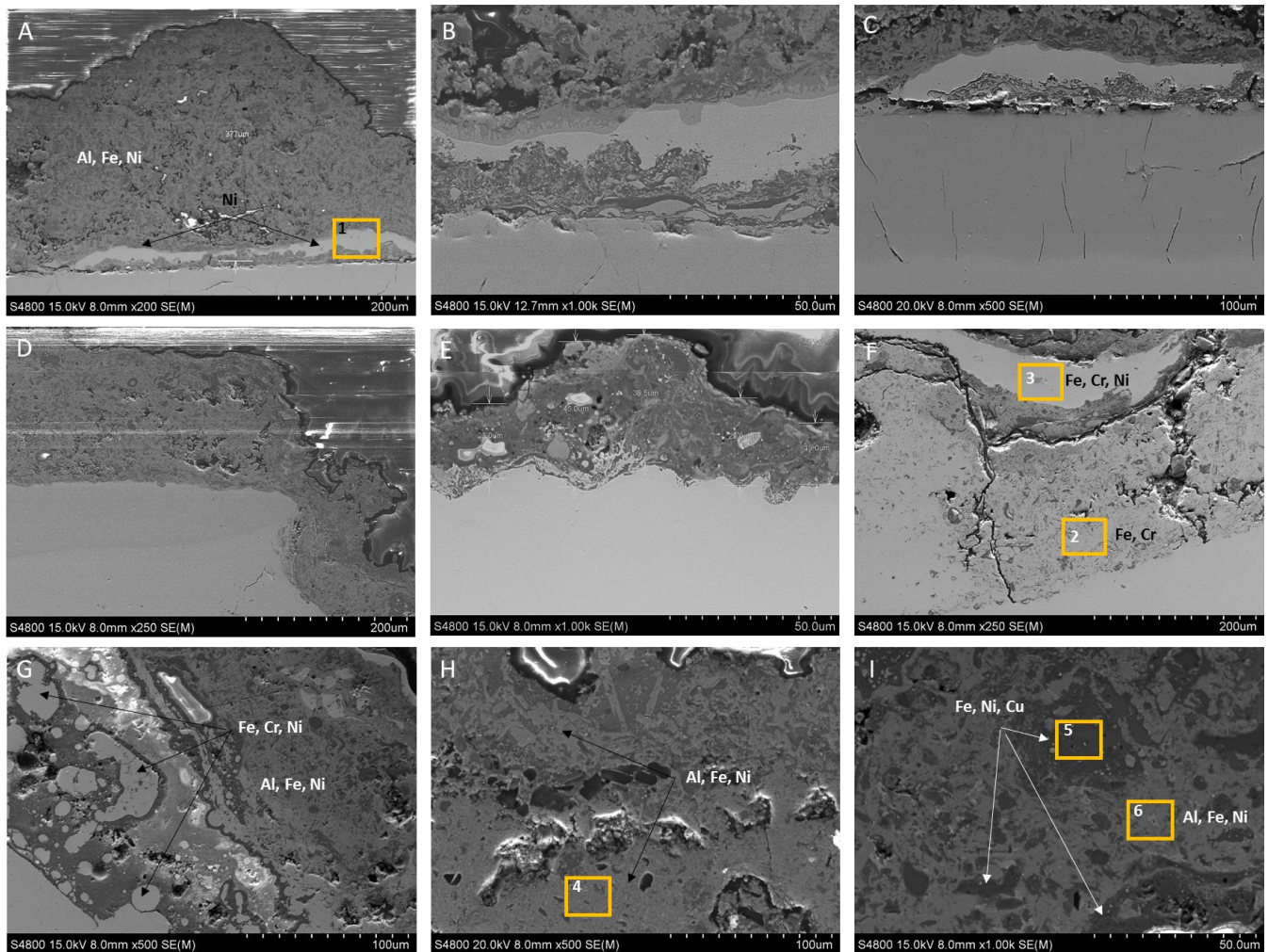


Figure 4.41 SEM images of the cross-sectional view of sample A4.2 on Area 4. (A-C) Area showing deposits as well as chromium coating indicating not thermal erosion in this section. (D-I) Deposits found in the thermal eroded area.

As the thermal eroded area was analyzed, the same light deposits were noticed again along with gray and dark gray deposits. The deposits in the eroded area measured approximately 550 μ m and the total depth of the localized melting that occurred to the shaft was about 1 millimeter. In this area, a lot of cracking within the deposits was seen (Figure 4.41 F). At the interface between the base metal and deposits, the same circular entrappings by the dark gray deposits of the gray deposits was observed and is shown in Figure 4.41 G. This type of behavior was only seen at the interface of where the 17-4 PH stainless steel and the deposits met and was only observed with the interaction of the stainless steel and the dark gray deposits. These dark deposits were also found embedded in the bulk of the deposits in small circular and elongated shapes as seen in Figure G and I. The gray deposits also seemed to have a dendritic texture to them when they interacted with the darker deposits at the top surfaces of the deposits. In this area, a lot of porosity likely due to gas entrapment, was seen as well. These features, which were mostly noticed at the top surface of the deposits, are shown in Figure 4.41 H.

To know if the chemical composition of these three different deposits was similar to the ones found in the first sample, EDS spot analysis was conducted. Areas that were analyzed are shown in Figure 4.41, where the exact location of the reading was shown by the yellow squares. The light deposits seen, located in large narrow strips at the bottom of the deposits that were not altered by the high temperatures of the deposits, were composed of approximately 80 wt. % Ni and less than 5 wt. % of each element of Al, Cr, and Fe (Figure 4.42 1). There were areas where the dark gray deposits would start to interact with the base material as shown in Figure 4.41 F. This area was analyzed to see if the small dark deposits mixing with the base metal made a difference in composition but EDS results in Figure 4. 42 2 showed that not much difference was noticed. Other light deposits seen in sample A4.2 were not Ni but Fe and had a similar composition to the base metal which indicated that large amounts of the base metal started to flow higher in the pool of molten metal deposits as shown in Figure 4.41 F. These same light deposits are similar to those that were entrapped by the dark gray deposits, which were also found at the bottom of the deposits.

The EDS spectra for these light deposits is shown in Figure 4.42 3. Analyzing the gray deposits, which made up the bulk, revealed that about 40 wt. % Fe was present along with 15 wt. % of Al and Ni, each. Chromium was also detected but only consisted of about 10 wt. %. EDS results for these gray deposits are shown in Figure 4.42 4. Titanium in this sample was found in quantities less than 3 wt. % at the subsurface of the deposit. Lastly, the dark gray deposits were identified as a mixture of Fe, Ni, and Cu (Figure 4.42 5).

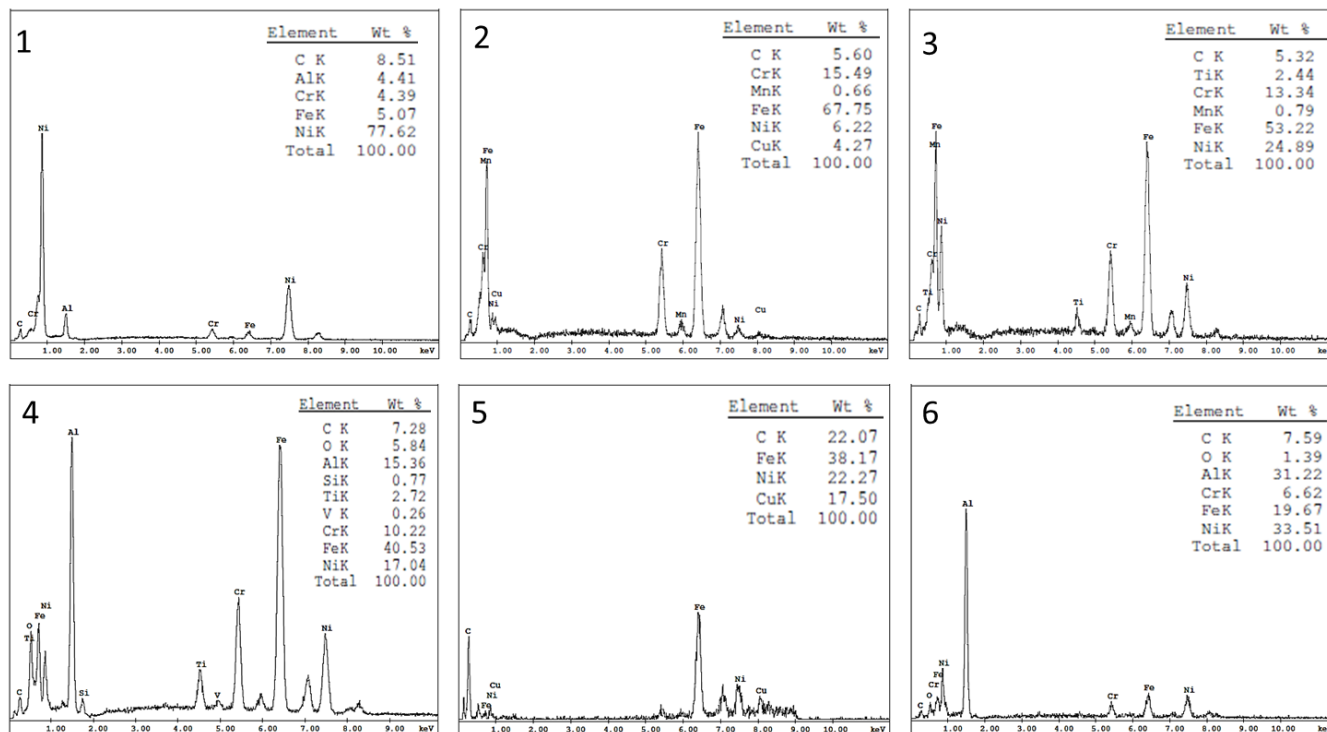


Figure 4.42 EDS spectra of the cross-sectional view of sample A4.2 are shown. Location of where readings were taken are shown in Figure 4.41 by the yellow squares.

In sample A4.3, no chromium layer was detected and in the threaded region, most of the thread crests had eroded. When examining the threads, only three of the five threads that were examined had a defined crest and root, the other two were not as deep within the root as others were. In Figure 4.43 A, deposits located at the crest of the thread can be seen and show again a mixture of a light deposits found at the top surfaces, which are surrounded by a gray deposit. Below these two layers, the base metal mixed with dark gray deposits which was similar to the behavior that was seen in sample A4.2. Measurements of these deposits were approximately 130µm. These deposits then moved toward the roots of the threads

and their morphology changed to a more turbulent flow of light gray deposits mixing with the dark gray deposits as seen in Figure 4.43 B. Light gray circular deposits were seen in the thread roots. These circular deposits had different shapes and sizes. This behavior is shown in Figure 4.43 C at a higher magnification and large cavities with granular textured walls can be observed. On the threaded edges, a very thin narrow strip of chromium coating can be seen but is only present over the threaded length and not on areas where threads have been damaged by high temperatures of deposits that adhered to their surface. Deposits found on the rooted parts of the threads were around 480 μ m in thickness.

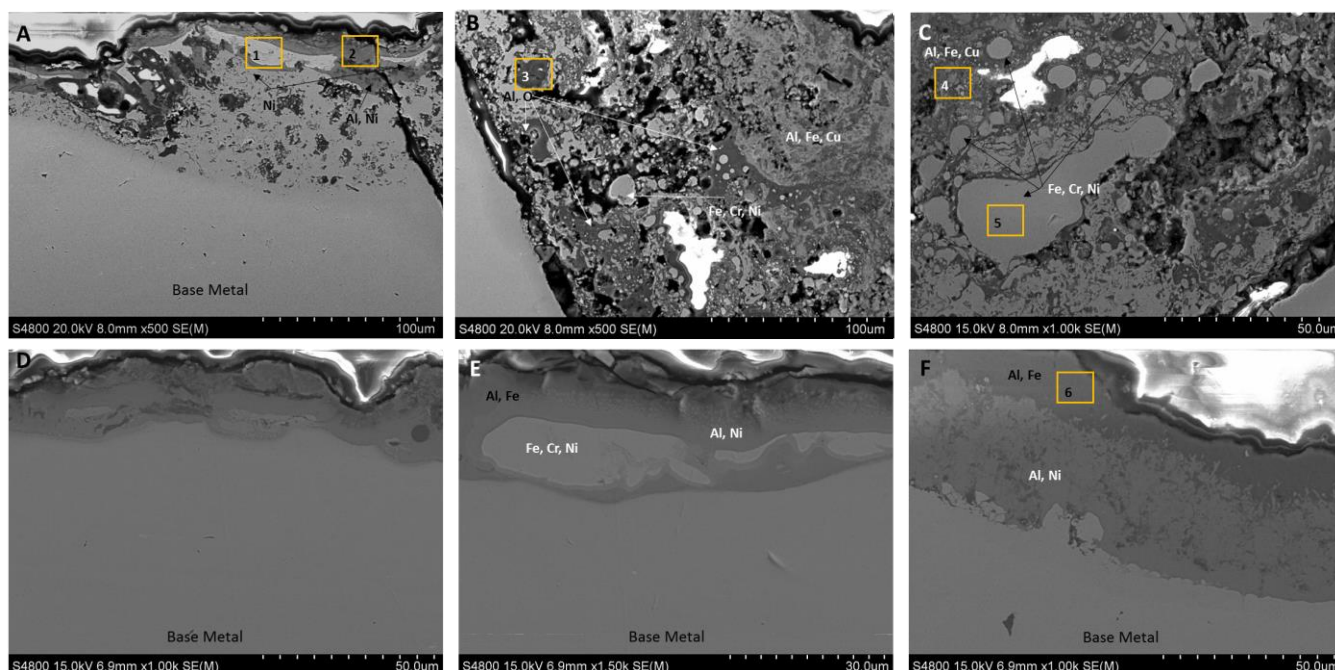


Figure 4.43 SEM images of the cross-sectional view of sample A4.3 on Area 4. (A-C) Area showing deposits found on the threaded length of the sample. (D-F) Deposits found in non-threaded area of sample A4.3.

In the areas where the threads were no longer noticeable, differences were observed in how the deposits solidified. The chromium coating that was applied to the shaft was not present and large globular masses of light deposits were seen throughout this narrow strip of deposits, which measured about 20 μ m in thickness (Figure 4.43 E). It was evident that the undelay base metal at a certain point in the event was in a nearly liquidus state by the way the interface between the deposits and base metal solidified. In this area, porosity was not observed and interfaces between deposits were clear as seen in Figure 4.43. The light deposits were surrounded by a gray deposit, which as it expanded towards the top surfaces of the

deposit, and as it reached the surface, a dendritic formation was noticed. The nucleation of dendrites is observed in Figure 4.43 F as this layer advances towards a darker layer at the surface.

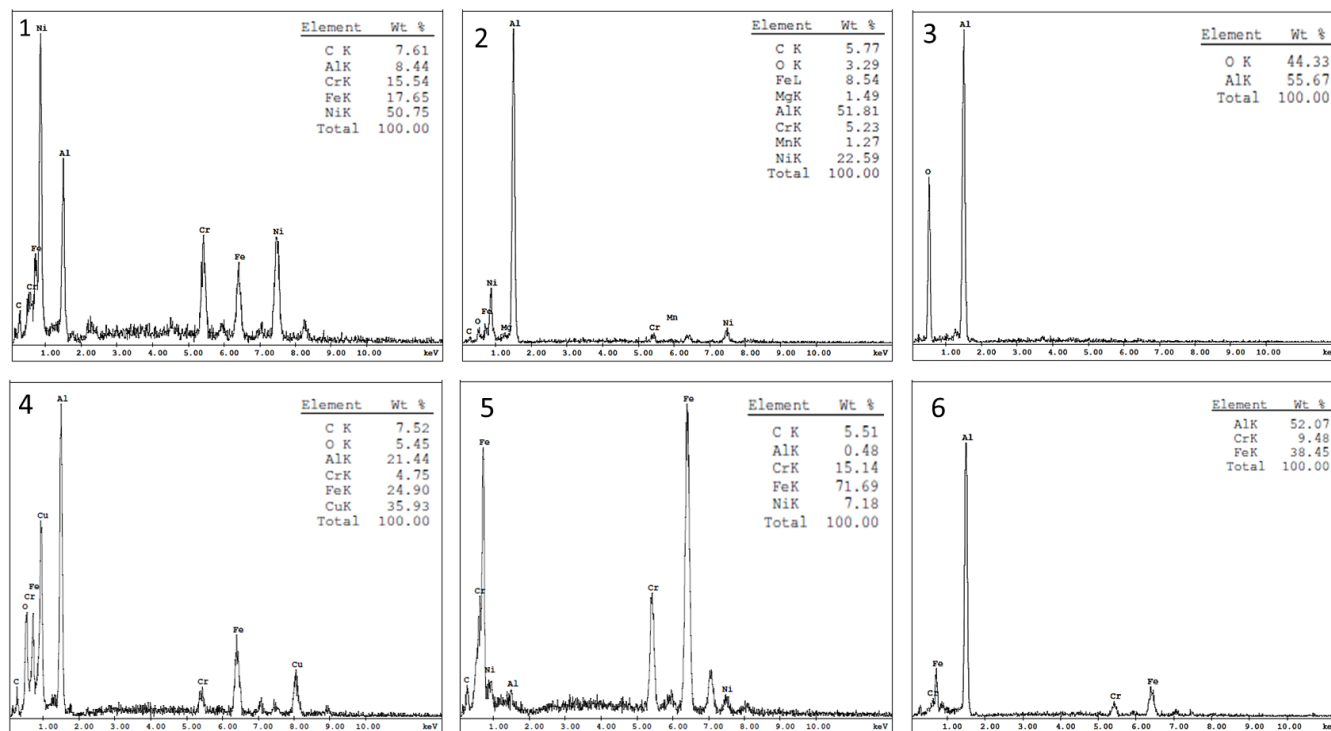


Figure 4.44 EDS spectra of the cross-sectional view of sample A4.3 are shown. Location of where readings were taken are shown in Figure 4.43 by the yellow squares.

As seen in most of the samples that were analyzed from Areas 3 and 4, the light deposits which have been found mostly on the bottom surfaces of the deposits and in this case at the top surfaces, have been identified as Ni deposits as seen by the EDS spectrum in Figure 4.44 1. Nickel deposits were making up nearly half of the light deposit and Cr and Fe make up about 30 wt. % together. Identification of the chemical composition of the gray deposit that surrounded the light deposits was the conducted by using EDS. The results showed in Figure 4.44 2 that these gray deposits that encapsulated the light deposits were mostly aluminum but also contained about 20 wt. % of Ni. These deposits can be seen in the SEM images in Figure 4.43 A, D, E, and F. The dark gray deposits, which were seen in Figure 4.43 A through C were identified as being Al and O as the EDS spectrum in Figure 4.44 3 shows. The matrix of the deposit, which has a mixture of gray and dark gray deposits, had a mixed composition of Al, Fe, and Cu as presented in Figure 4.44 4. Other gray deposits, this time having a circular morphology, were composed

mostly of the base metal which contained about 70 wt. % Fe, 15 wt. % Cr, and around 7 wt. % Ni (Figure 4.44 5). The last layer of the deposit that was analyzed in A4.2 was another dark layer that was only seen at the top surfaces of the non-threaded area. This layer was analyzed by the EDS and showed that it was mostly Al with about 50 wt. % present and 40 wt. % Fe. Chromium was also detected and made up 10 wt. % of this dark gray layer found in the non-threaded region.

4.2 X-RAY DIFFRACTION

The final method used for the identification of the chemical composition of the deposits was x-ray diffraction. A single sample from Area 1 and Area 2 were used to perform the analysis and three samples from Area 3 and Area 4 were also examined. Special sample preparation was not necessary to conduct the analysis and only required readings in areas that had a flat surface which did limit the areas that were analyzed in samples like in Area 4 since this is where rougher surfaces were found on the shaft. This analysis was also spot analysis and has a depth of penetration of a few micrometers to a few hundred micrometers which is mostly known to accurately detect surface information such as phases and crystal orientation. A total of five readings from each sample were taken but only a couple of these readings will be discussed since similar results were seen on different areas of the samples.

4.2.1 AREA 1

In Area 1, two surfaces were analyzed under the SEM, the top surface and the threaded region, due to the XRD requiring a flat surface for better results, only the readings on the top surfaces will be discussed. In this area, XRD detected compounds such as Al_4Cu_9 , Al_2O_3 , and CuO .⁸⁷ The XRD spectrum for one of the areas that was analyzed in this sample is shown in Figure 4.45 and the location of where the analysis was conducted can be seen in this same figure as well. EDS analysis that was conducted on the surface of this sample showed the presence of mostly aluminum and oxygen, which were identified by the XRD as being Al_2O_3 or alumina. This aluminum oxide compound is the most common one of all of them. Another phase that was detected in the deposits was Al_4Cu_9 , and even though not much Cu was detected

at the surfaces of this sample. When it was analyzed with EDS, the spectra from the cross-section analysis showed Cu was present in quantities as high as 30 wt. % compared to only 6 wt. % found on the surface. EDS results show similar elemental composition as the one found when XRD was conducted, confirms the accuracy of the XRD results obtained from this sample.

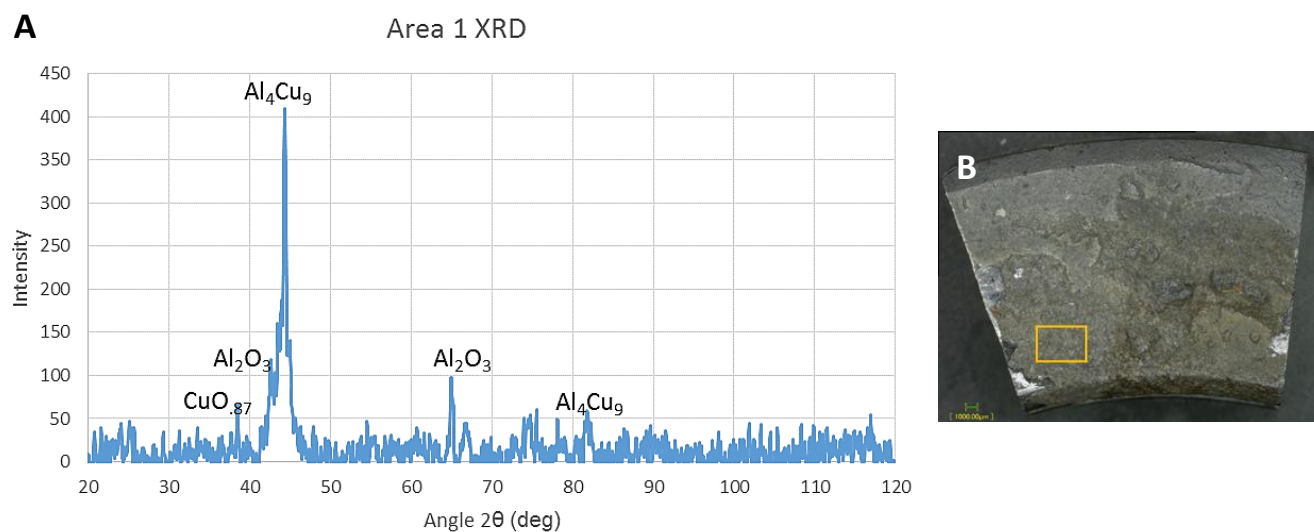


Figure 4.45 XRD spectrum in (A) of spot shown in (B) of Area 1 sample's top surface.

4.2.2 AREA 2

Area 2, which only contained a narrow strip of deposits that were identified by EDS and XRF to be mostly composed of Al and Cu, was analyzed by XRD to verify the deposits on the surface. The deposit-free area of the base metal was first examined and confirmed once again that the coating found on the shaft was Cr since CrNi peaks were the only ones showing in the XRD reading of the deposit-free area of the sample (Figure 4.46 A). When analyzing the narrow deposits, AlFe_3 and $\text{Al}_{.99}\text{Cu}_{.01}$ were detected and became evident that Cu was being deposited in different areas throughout the re-entry. In this area, the XRF spectrum, which were preliminary results, showed that these deposits were about 98 wt. % Al. Once the EDS was performed on the sample, Cu was detected in the deposits with as much as 46 wt. % Cu and about 30 wt. % Al at the surface, which support the XRD results. EDS results changed once the cross-section was analyzed with Al now making up most the deposits with about 70 wt. % and only 6 wt. % Cu was detected underneath the surface. This difference in composition points out that XRD analysis only

has a certain depth of penetration and is greatly dependent on the density of the materials. AlFe_3 was also detected in the deposit for this sample and small concentrations of Fe also appeared in the EDS spectra. The spectra for the second reading (R2) done on this sample is shown in Figure 4.47.

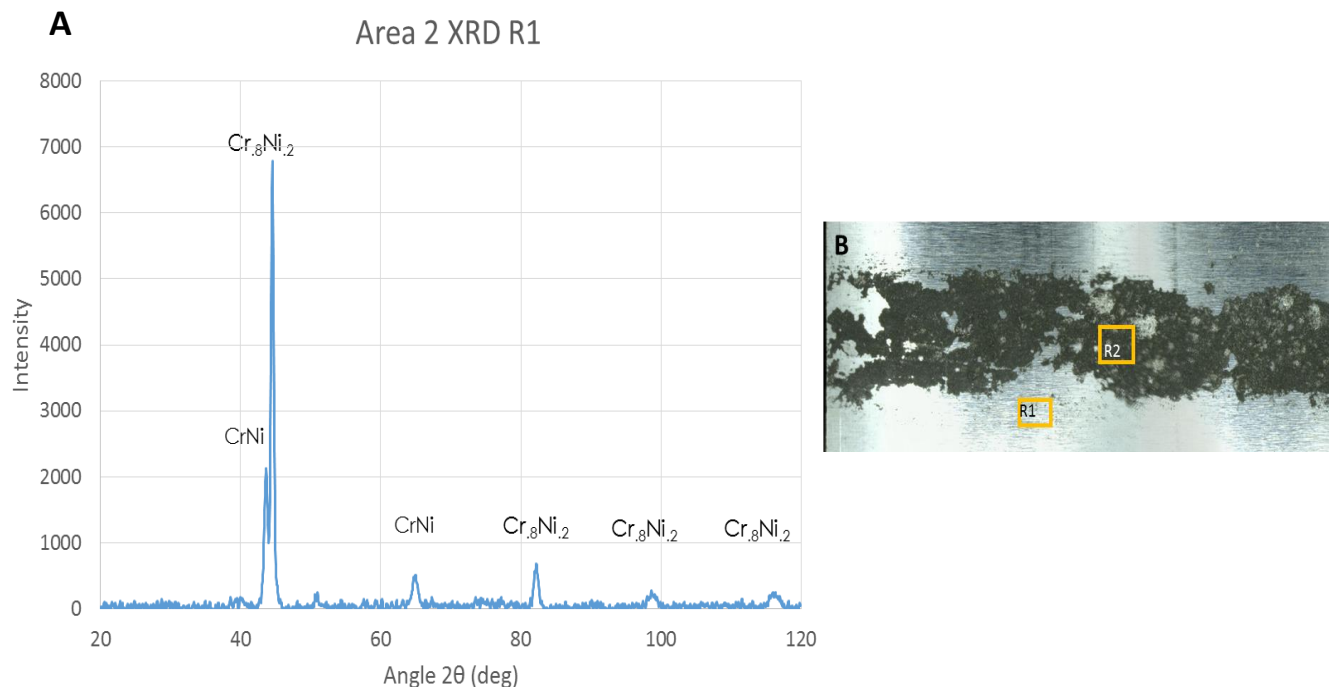


Figure 4.46 XRD spectrum in (A) belonging to deposit-free area shown in (B). Image B shows location of where reading 1 (R1) and reading 2 (R2) were taken.

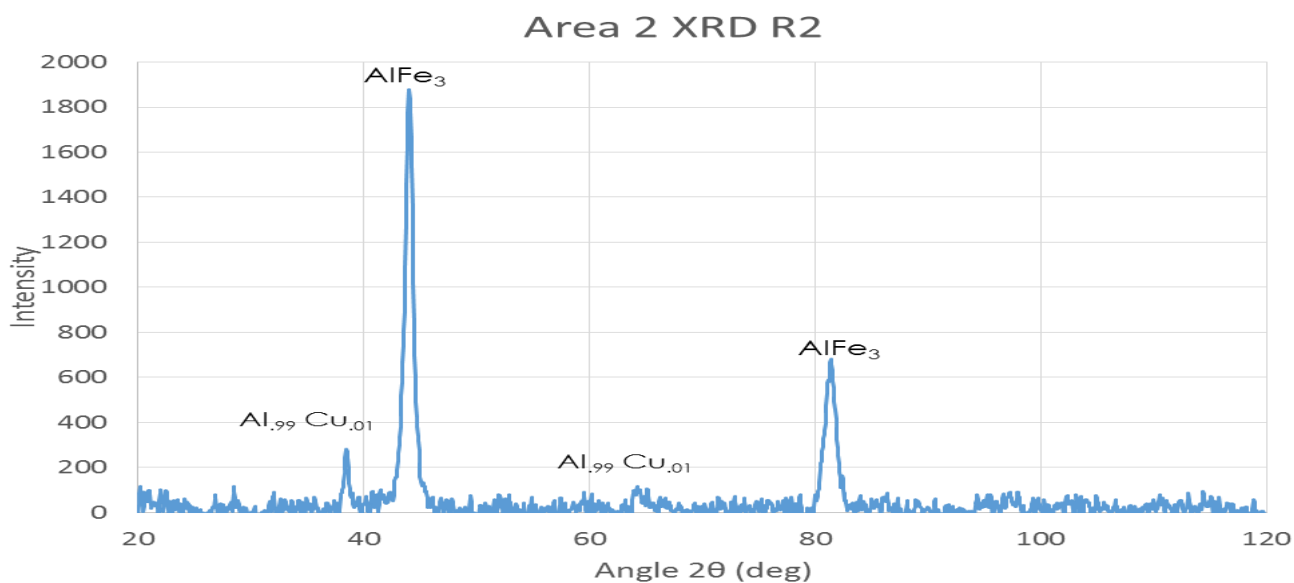


Figure 4.47 XRD spectrum of deposits found in Area 2. Location of where reading was taken can be found in Figure 4.46 B, R2.

4.2.3 AREA 3

For Area 4, samples A3.1, A3.2, and A3.3 were analyzed for their surface chemical composition. Two readings for sample A3.1 were performed, which included an area where visible streaks were present in the sample. The second reading was taken from the uniformly thin layer of the deposit also for this sample. Location of these two areas that were examined are shown in Figure 4.48 A. For the first reading, R1, which is where the streaks were seen, the XRD spectrum detected several compounds such as $(\text{Al}_{0.5}\text{Cr}_{0.5})\text{Fe}$, TiO_2 , and $\text{CrO}_{0.87}$. These results are shown in Figure 4.48 B. Due to TiO_2 being detected in this sample, the streaks that were being analyzed by the XRD were most likely the same Ti streaks that were identified by EDS. Since these streaks were seen to deposit on top of a thin layer of deposit and in other occasions on the base metal itself, the detection of the $(\text{Al}_{0.5}\text{Cr}_{0.5})\text{Fe}$ and $\text{CrO}_{0.87}$ are most likely coming from the deposits and the chromium coating.

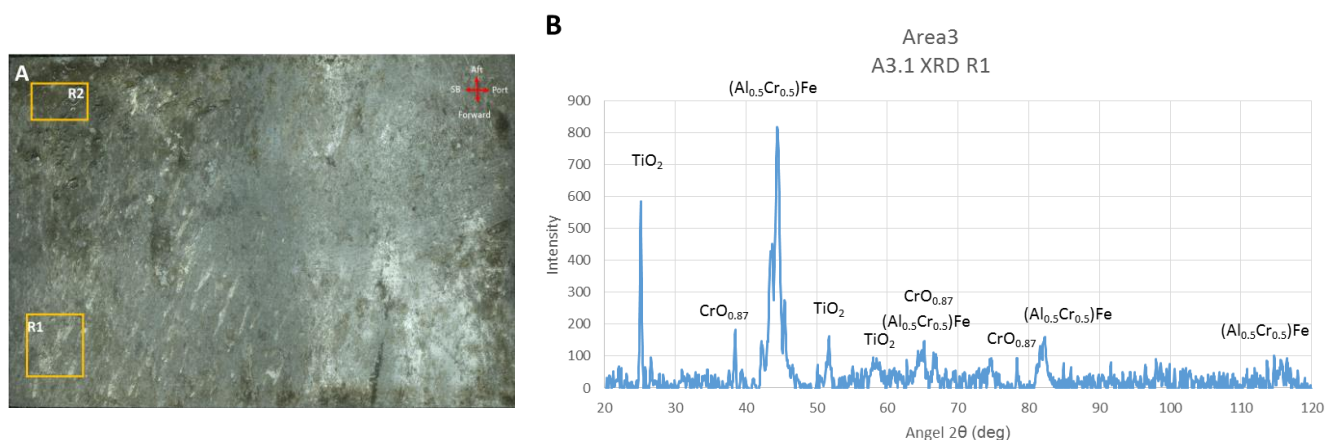


Figure 4.48 Location of where the two reading of sample A3.1 from Area 3 are shown in A. XRD spectrum of compounds identified in the deposits of sample A3.1 are shown in B.

The second reading, which belongs to the thin layer of deposits, had compounds that were not very common but included elements which were also detected by EDS. Compounds such as $\text{Fe}_{0.23}(\text{Fe}_{1.95}\text{Ti}_{1.42})\text{O}_4$, $\text{Al}_{14}\text{Ni}_{86}$, $\text{Al}_{25}\text{Fe}_{75}$, and $\text{Cr}_{1.07}\text{Fe}_{18.93}$ were some of the compounds that were detected in sample A3.1 for the thin layer of deposit. Results for this area are shown in Figure 4.49. Even though these phases are non-stoichiometric, they were coming from AlNi , and AlFe compounds as well as TiO . It is probable that the

different Fe compounds detected by the XRD came from some of the Fe streaks that were also detected on this sample. SiO_2 and $\text{CrO}_{0.87}$ were also present and are most likely coming from all the tiny loose particles seen on the deposit surfaces and chromium coating, respectively.

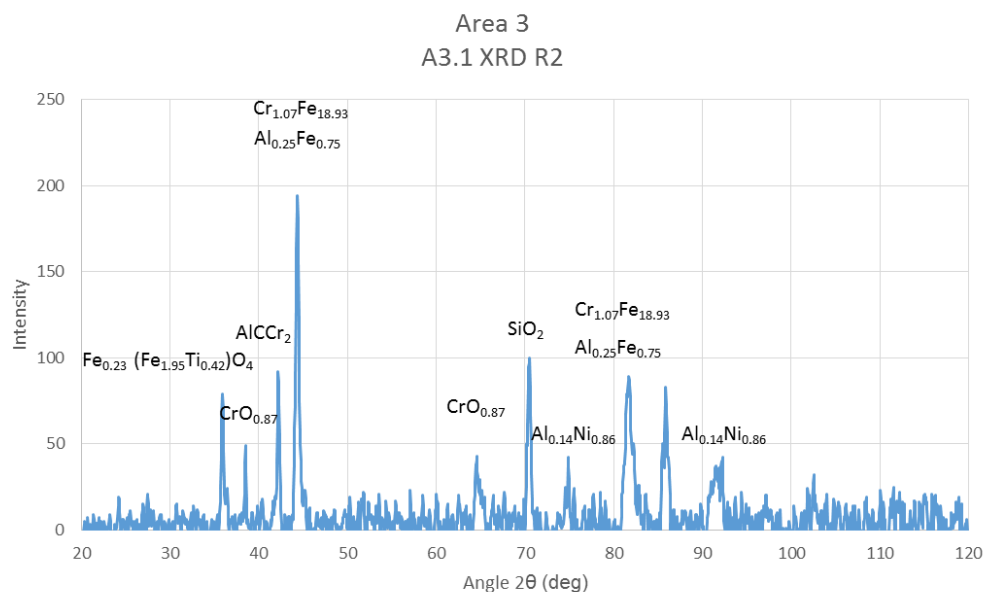


Figure 4.49 XRD spectrum of thin layer of deposits found in Area 3. Location of where reading was taken can be found in Figure 4.48 A, R2.

Sample A3.2 had two layers of deposits, a thin layer and a thicker uniform layer. The thin layer, which was analyzed in the previous sample of Area 3, had very similar peaks as the ones found in sample A3.1 and were not be presented for sample A3.2. The thicker layer of uniform deposits had peaks such as Al_2Fe , FeNi , and AlFe_3 which were detected when XRD analysis was conducted (Figure 4.50 A). These compounds are coming from an AlFe component. EDS results for this area were mostly composed of an Al, O, and Cu but did have splats that were mostly Fe, which is why Fe was being detected here. Unlike the EDS results for the thicker layer of deposits in A3.1, Cu peaks were not present in the area tested by the XRD. The second reading in this sample came from a big splat that could be seen in the sample. This splat like the one found in sample A3.1 was a Ti splat. AlNi and AlFe_3 compounds were also seen in the XRD spectrum in Figure 4.51. About 70 wt. % Ti was present along with 4 wt. % Al and V which confirms

that this splat was coming from a Ti-6Al-4V component. XRD results for these two readings went along with EDS results from surface analysis of sample A3.2.

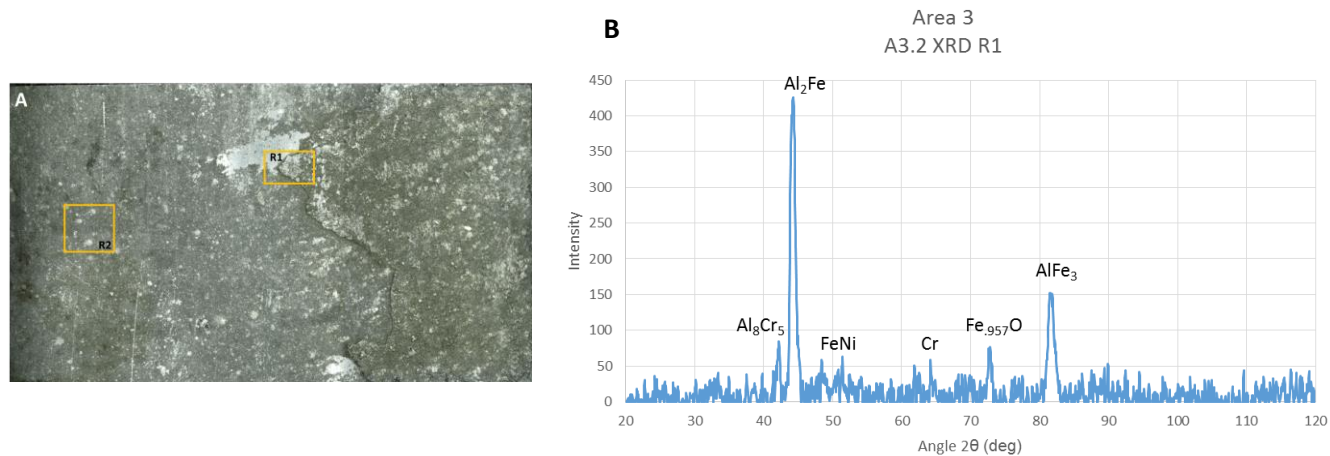


Figure 4.50 Location of where the two reading of sample A3.2 from Area 3 are shown in A. XRD spectrum of compounds identified in the uniform deposits of sample A3.2 is shown in B.

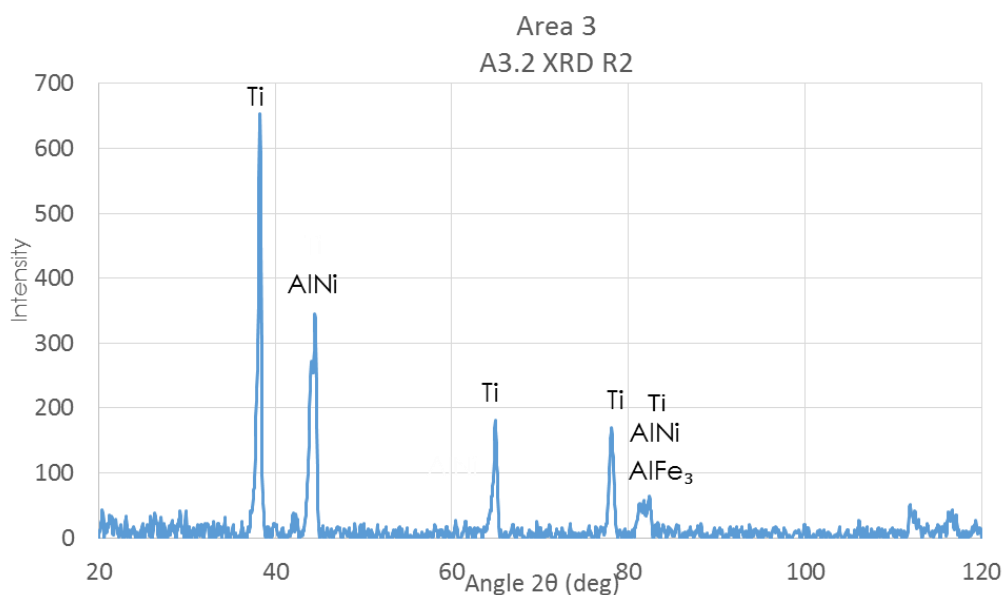


Figure 4.51 XRD spectrum for second reading done on splats seen in sample A3.2.

The last sample analyzed for the Area 3 was sample A3.3, which had a uniform deposition of metallic materials. Analyzing areas in this sample showed that mostly pure Al with compounds seen in other samples, such as AlFe_3 and AlCu along with Si, were present at the surface (Figure 4.52 A). When this sample was examined under the SEM, globular silicate particles were observed in the sample and was the reason why a Si peak was detected in the XRD spectrum. As for the presence of AlFe_3 and AlCu , EDS

detected large amounts of Al in the deposits. Approximately 60 wt. % Al was in the deposits for sample A3.3. Copper and Fe also made up about 12 wt. % and 5 wt. % of the deposits in the sample, respectively which once again confirms the XRD results match with EDS results. Note that a lot of Ni deposits were present in Area 3 but were mostly found at the bottom region of the samples which were not detected by the XRD due to limitations on the depth of penetration.

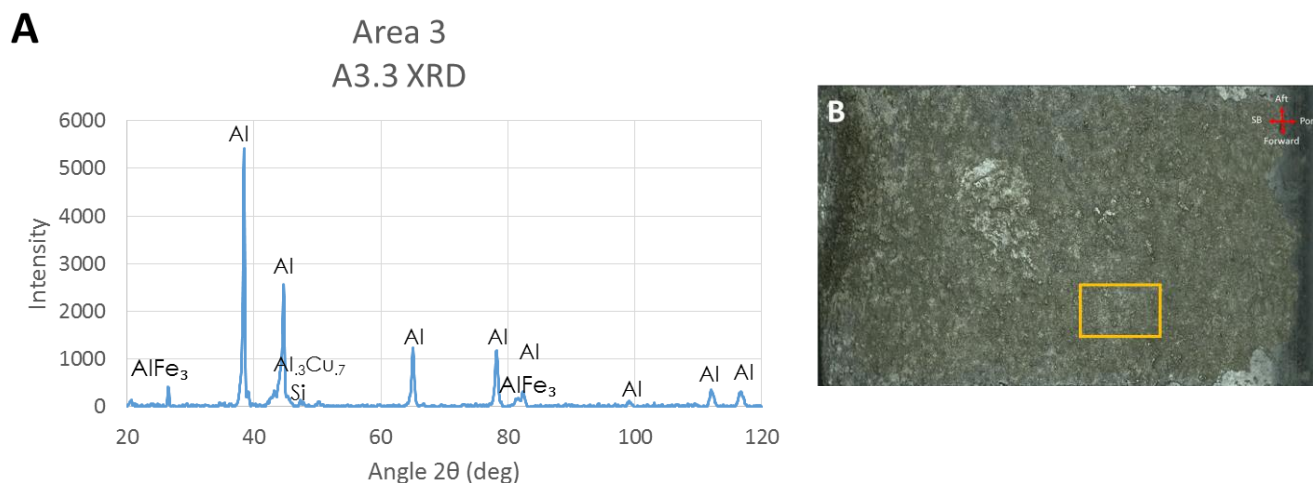


Figure 4.52 XRD spectrum of sample A3.3 is shown in A. Location of reading taken in sample A3.3 from Area 3 is shown in B.

4.2.4 AREA 4

Samples for Area 4 had heavier amounts of deposits and rougher surfaces which made it difficult to get a good XRD readings. Several good readings were obtained, but did include a lot of background noise in the spectrum. For sample A4.1, XRD results in Figure 4.53 A showed a AlFe_2Ni phase present and Al metal, which matches with the EDS surface results for this area. EDS results showed A4.1 deposits consisted of about 40 wt. % Al, 20 wt. % Ni, and around 10 wt. % of Fe and Cr, each. Only one reading from sample A4.1 was taken since there were a lot of rough surfaces present and accurate results were difficult to obtain. In sample A4.2, two areas were analyzed, one included the adherent thick deposits and another was an area where a splat was deposited. Results for the first reading can be seen in Figure 5.54 A which belong to the deposits in close proximity to where the erosion damage was observed. The area

for the first reading, R1, is shown in image B of Figure 4.54. The spectra showed that compounds such as AlCu and Fe₃Ni were detected. In this area when analyzed under the SEM and EDS was conducted, approximately 60 wt. % Al was present and smaller amounts between 12 wt. % and 6 wt. % of Ni, Cu, and Fe were detected. The accuracy of the XRD results in this area are very accurate since peaks were readily identified and coincided with the EDS results as well. Several splats were visible in the sample but results for only the splats shown by R2 in Figure 4.54 B were discussed. XRD spectrum confirmed that the splat was coming from a Ni rich component since most the peaks were NiO and ESD results showed 40 wt. % Ni present in the same area. Other compounds that were detected in sample A4.2 were SiC, Fe₄Al₁₃, and Al(CrNi) and the spectra are shown in Figure 5.55. Elements that make up these compounds were also present in the EDS spectra.

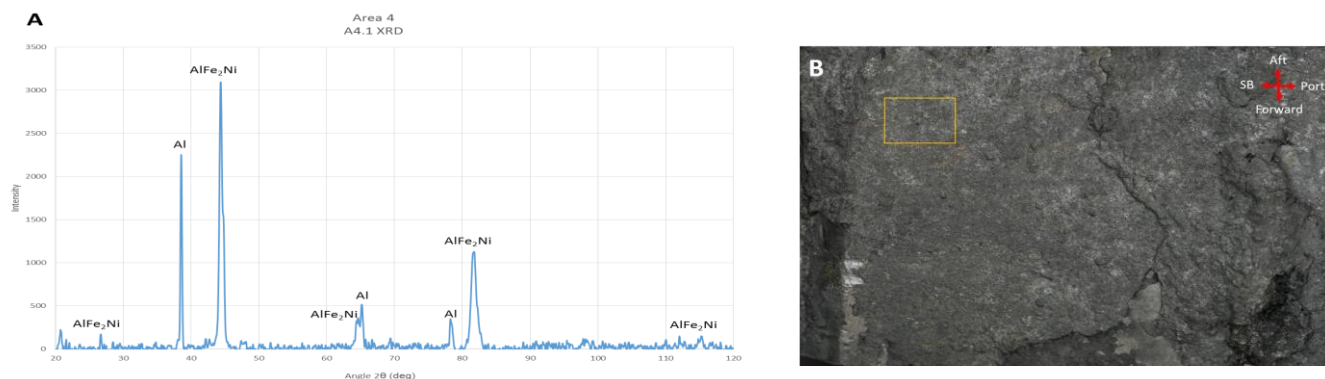


Figure 4.53 XRD spectrum of sample A4.1 is shown in A and location of where reading was take is shown in image B.

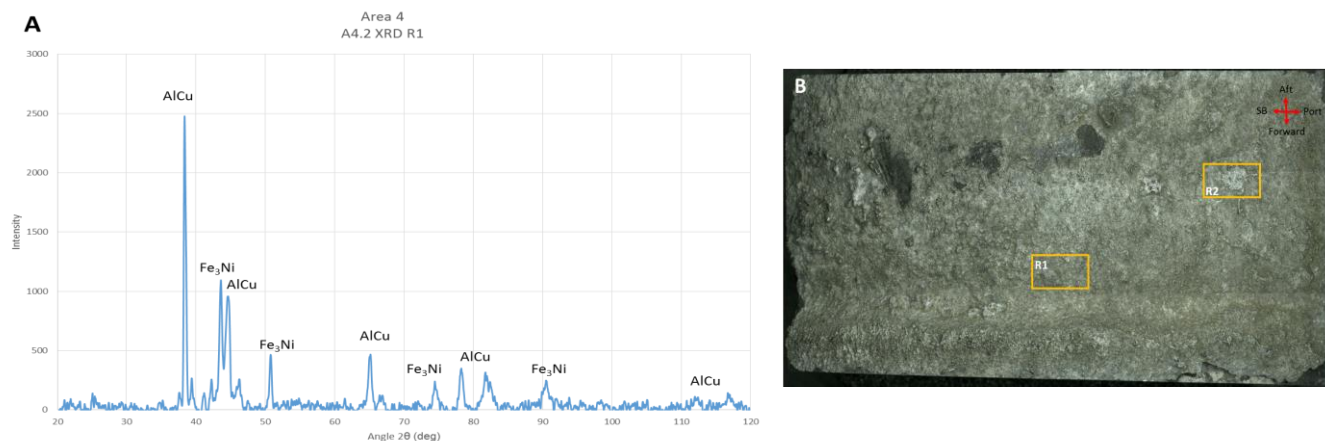


Figure 4.54 XRD spectrum of the first reading in sample A4.2 is shown in A and location of where reading was take is shown in image B.

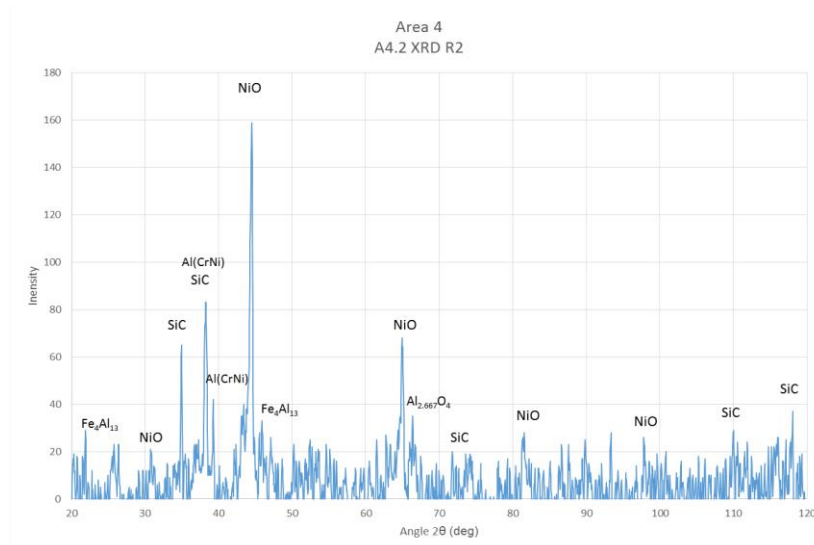


Figure 4.55 XRD spectrum of second reading in sample A4.2. Location of R2 is shown in image B.

Conducting XRD analysis on Sample A4.3 was difficult, so since this sample had a threaded area but a region where erosion of the threads had occurred was selected for analysis. The XRD peaks were identified to be AlFe_2Ni , $(\text{AlCu})\text{Ti}$, Ni_3Ti , and FeNi compounds that were present in the deposits for sample A4.3 (Figure 4.56 A). In this area, EDS detected mostly Al and O but did contain approximately 12 wt. % Ni and less than 5 wt. % Ti, Cr, and Fe, which go along with XRD results. EDS was unable to detect any presence of Cu but a $(\text{AlCu})\text{Ti}$ peak was detected by the XRD. Overall, XRD served to verify the chemical composition with results found while performing EDS surface analysis on all the samples and identification of phases was also accomplished by obtaining the XRD spectra.

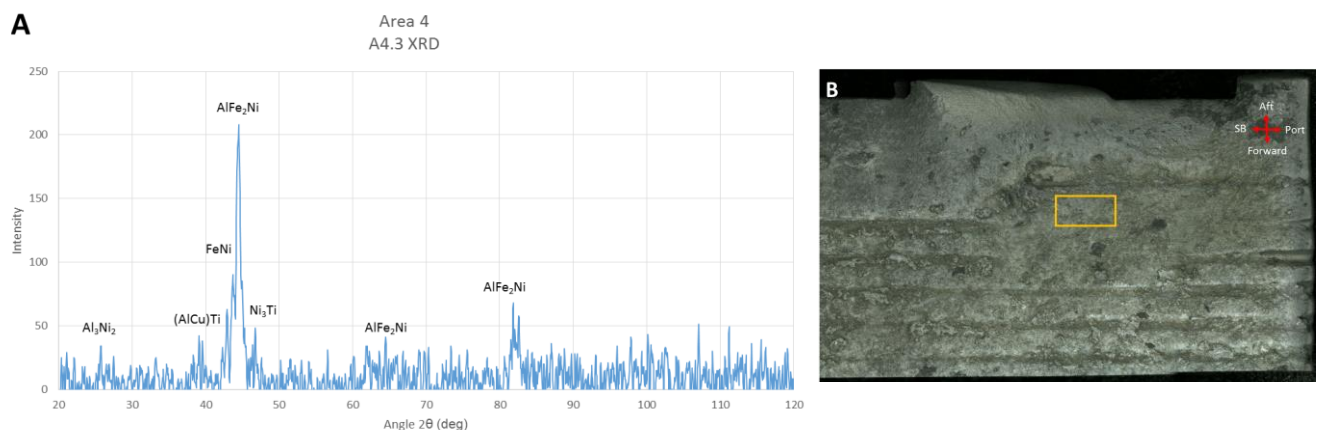


Figure 4.56 XRD spectrum of sample A4.3 is shown in A and location of where reading was take is shown in image B.

4.3 OPTICAL MICROSCOPY

The final analysis that was conducted in this research was optical microscopy to examine the microstructure of the four areas of interest and deposits as seen by the cross-sectional view. This analysis revealed a detailed view of the morphology found in the deposits as well as microstructural changes that occurred to the base metal due to excessively high temperatures. The sample from Area 1, which belongs to the hydraulic system as identified before, was of a 15-5 PH stainless steel which differ from the shaft material which was a 17-4 PH stainless steel. Any microstructural differences will be discussed as well as any differences in behavior to the extreme temperatures for each of the materials. The sample taken from the housing of the hydraulic system, a single sample from Area 2, and three samples from Areas 3 and 4, each, will be examined under the optical microscope.

4.3.1 AREA 1

The 15-5 PH stainless steel sample from Area 1 is a variant of the 17-4 PH stainless steel shaft. Area 1 sample is a chromium-nickel-copper precipitation hardening stainless steel just like the shaft's base material and is expected to have the same martensitic microstructure. It also has similar properties as the 17-4 PH stainless steel such as high strength and corrosion resistance but does exhibit a much higher toughness than that of the 17-4 due to a reduction in delta-ferrite [43]. The processing on this stainless steel is well controlled in order to reduce the content of delta ferrite which is present in the 17-4 PH stainless steel. Besides the way this material is processed, the composition is also controlled to lower the number of inclusions and their size. The heat treatment is done at a low temperature and will also precipitate a copper phase as will the 17-4 PH stainless steel. When the analyzing Area 1 sample under the optical microscope, a martensitic microstructure was revealed and did not appear to have any type of heat alterations at the surface where deposits could be seen. Figure 4.57 A shows the microstructure of Area 1 sample along with micrographs from the cross-sectional view of deposits found on the sample. Note that the cross-sectional micrographs are not etched while the micrograph of the microstructure has

been etched using Kalling's No. 2 reagent. Etching the deposits with the same etchant used for the base material lead to the deposits getting burnt and the etchant not being compatible with the mixture of materials that were present within the deposits. This procedure was also used for the rest of the samples.

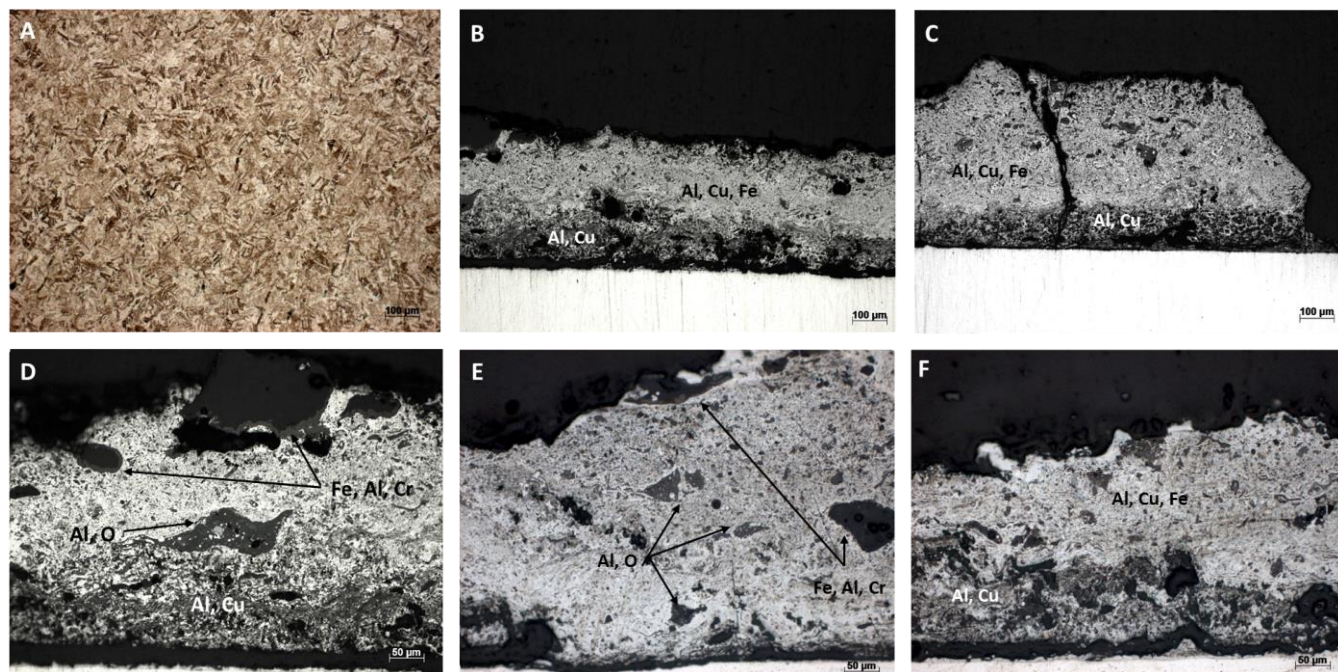


Figure 4.57 A) 15-5 PH stainless steel microstructure for Area 1 sample. Magnification for (A) is 150X. (B-F) Optical micrographs of Area 1 aft-facing side sample showing several inclusions in the deposits as well as shrinkage and oxidation layer. Magnification for (B-C) is 150X and (D-F) is 200X.

Examining the aft-facing side under the optical microscope revealed more detail on how the inclusions and layers of the deposits. Figure 4.57 B and C shows two distinct layers, a darker layer at the bottom and a lighter layer at the top surface. Though they appear as two distinct layers, the composition was not very dissimilar. EDS results showed that the top layer contained higher concentrations of Fe while the bottom layer was mostly Al with a combination of Cu in both layers of the deposits. The small irregularly shaped islands of Al and O enrichments and bilayer deposits seen at the surface of the deposits are also more visible with the optical micrographs and are shown in Figure 4.57 D and E. The cavity between the chromium layer and deposits was another feature that was clearly defined. In Figure 4.57 C, a deep crack can be seen running down the deposits until it hits the base metal. Cracking was seen throughout the deposits. In many cases, cracks lead to the surface of the base metal forming a long

continuous hollow space between the base metal surface and deposits as described in earlier sections. These tunnels are shown in Figure 4.57 D through F. On the threaded side of the Area 1 sample, similar deposit morphology could be seen (Figure 4.58). The main difference that was noticed in these deposits was more porosity most likely due to trapped gas. Deposits that were embedded in the matrix and were identified as being mostly Fe deposits are shown in Figure 4.58 A and B. Optical microscopy on Area 1 verified that there were no thermal alterations on the aft-facing side as well as the threaded side of the sample belonging to the housing material of the elevon's hydraulic system.



Figure 4.58 Optical micrographs of threaded side of Area 1 sample showing deposits and porosity. Magnification of (A-C) is 500X.

4.3.2 AREA 2

Area 2 is the first area of the shaft that was examined and contained very thin and narrow deposit lines. One sample from this area was used to obtain the microstructure of the base metal, which would serve as a control to detect any microstructural changes on Areas 3 and 4 since most of the sample in Area 2 was unaffected by deposits. Part of this area was covered for most of the event which led to deposit-free areas that were thought to be free of thermal damage. Due to the deposits being very narrow and thin, capturing good micrographs was difficult. Figure 4.59 A through C show how irregular and thin deposits were. Copper colored inclusions were seen in Figure 4.59 A but were not detected by the EDS, instead Cr was found in the deposits along with Al, which comprising most of the deposit. The same gap along the base metal surface was also seen in the deposit with Al and O concentrated particles dispersed discontinuously throughout (Figure 4.59 B and C). The chroming coating was also detected and no

damages seemed to have occurred. As mentioned before, the base metal of the shaft is a 17-4 PH stainless steel which would have a martensitic microstructure. Figure 4.59 D through F shows several micrographs that were taken of Area 2 sample once it was etched with Kalling's No. 2 reagent. A martensitic microstructure with long delta-ferrite stringers is seen in Figure D and E, where image E shows delta-ferrite stringers with clusters of Cu precipitates enclosed within them. At a higher magnification, Cu precipitates can be seen throughout the whole martensitic microstructure. A uniform martensitic microstructure with approximately 5% delta-ferrite stringers was seen in the sample and verified that the microstructure could be used as a control when identifying microstructural changes due to excessive heat.

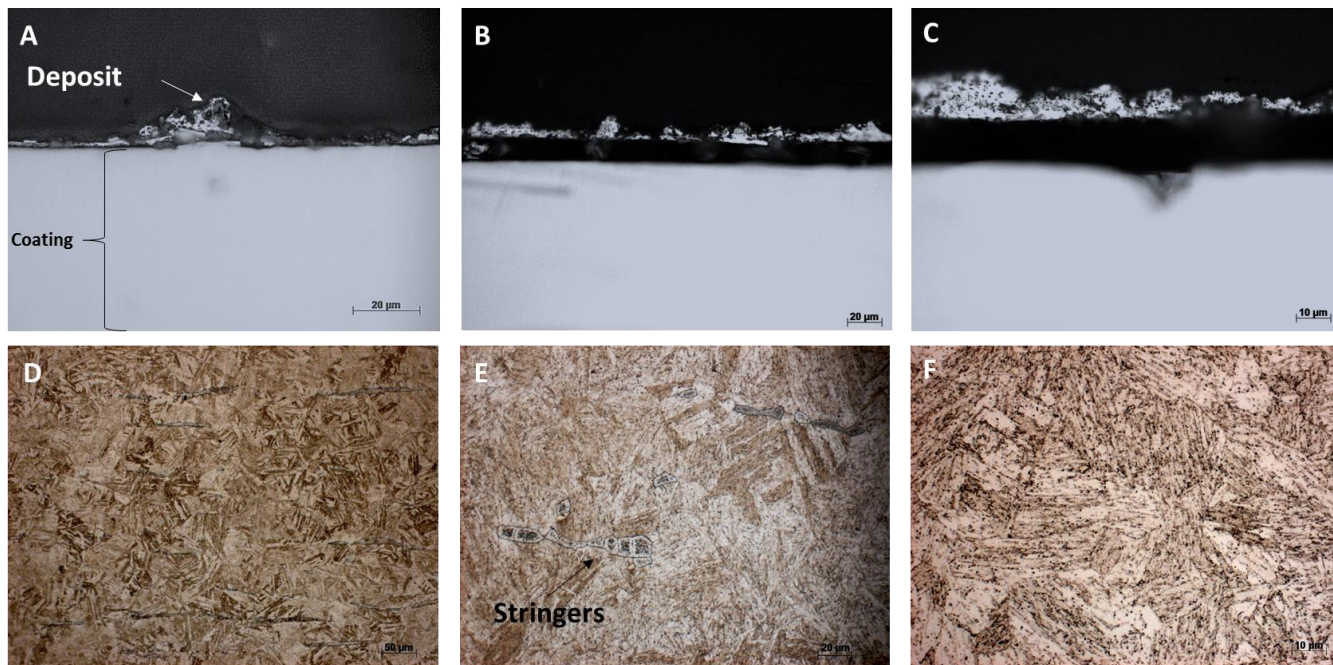


Figure 4.59 (A-C) Optical micrographs of Area 2 sample deposits as well as Cr coating. Magnification at 500X for (A) and (B) and 1000X for image (C). (D-F) 17-4 PH stainless steel microstructure which will be used as a control since no heat damaged was caused in Area 2. Magnification for image D is 200X, for E is 500X, and image F is 1000X.

4.3.3 AREA 3

The same three samples that were used for surface and cross-sectional analysis were used for optical microscopy. Figure 4.60 shows optical micrographs of the deposits of sample A3.1 as well as the microstructure of the 17-4 PH stainless steel in Area 3. While examining sample A3.1, only small discontinuous deposits were observed and seemed to have oxidize very quickly due to the dark color of

the deposits. Embedded in this Al deposits were shiny metallic copper colored deposits. EDS showed that these deposits were rich in Al and Cr only and no Cu was found in this sample, which leads to these metallic particles being Cr (Figure 4.60 A and B). Chromium could be coming from the coating in the nearby eroded area since the Cr coating in Area 3 was intact. Along with these deposits, shown in Figure 4.60 C, Si particles with high concentrations of C were seen deposited on the chromium coating surface but was probable that some of these particle adhered to the sample during metallography and did not detached during the ultrasonic cleaning done afterwards. The microstructures of Area 3 seen in Figure 4.60 D through F showed the same martensitic microstructure as the control seen in Area 2 with not damage to the coating or the undelaying base material due to high temperatures.

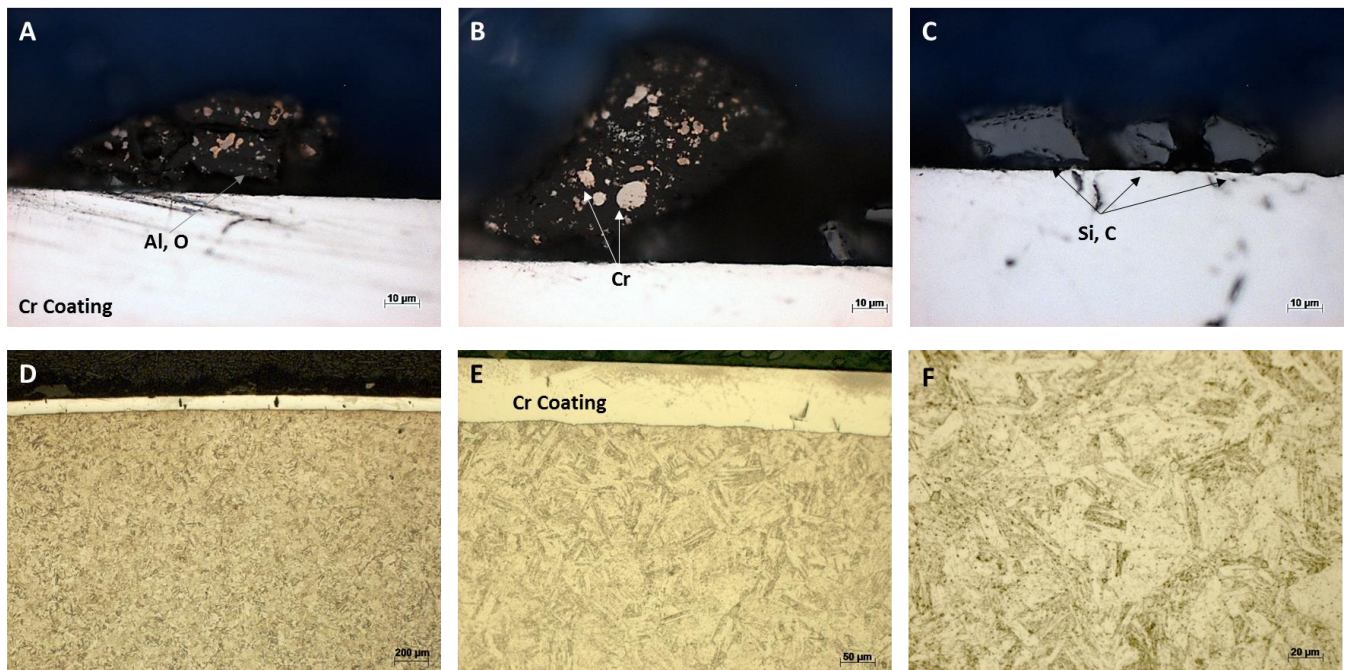


Figure 4.60 (A-C) Optical micrographs of sample A3.1 on Area 3 showing oxidized deposits with metallic particles. Magnification for images (A-C) is 1000X. (D-F) Microstructure as seen in Area 3 with an unaffected chromium layer and martensitic structure. Magnification of (D) is 50X, for (E) magnification is 200X, and for (F) is 500X.

In sample A3.2, the presence of the a darker colored layer at the bottom surface of the deposits and cavity at the surface of the base metal that was seen on Area 1 were detected on the deposits for this sample and can be seen in Figure 4.61 A through C. In the Al and O enriched layer, a lot of porosity was seen and particles laying on the top surface of the chromium coating that were seen in sample A3.1 were

also present but differ in composition with the majority of these particles being Al and O. Cracking was particularly seen in the top layer of the deposits and helped define a flow pattern in some areas of the deposits (Figure 4.61). The top layer which can be seen in Figure 4.61 D through F at higher magnification show how thin, narrow streams of Ni deposits were found mixed with the matrix of the deposits, which was composed of Al and Cu or were also seen as small embedded islands. When looking at the metal matrix of the deposit, a webbed texture was observed with porosity throughout this top layer and is shown in Figure 4.61 E and F.

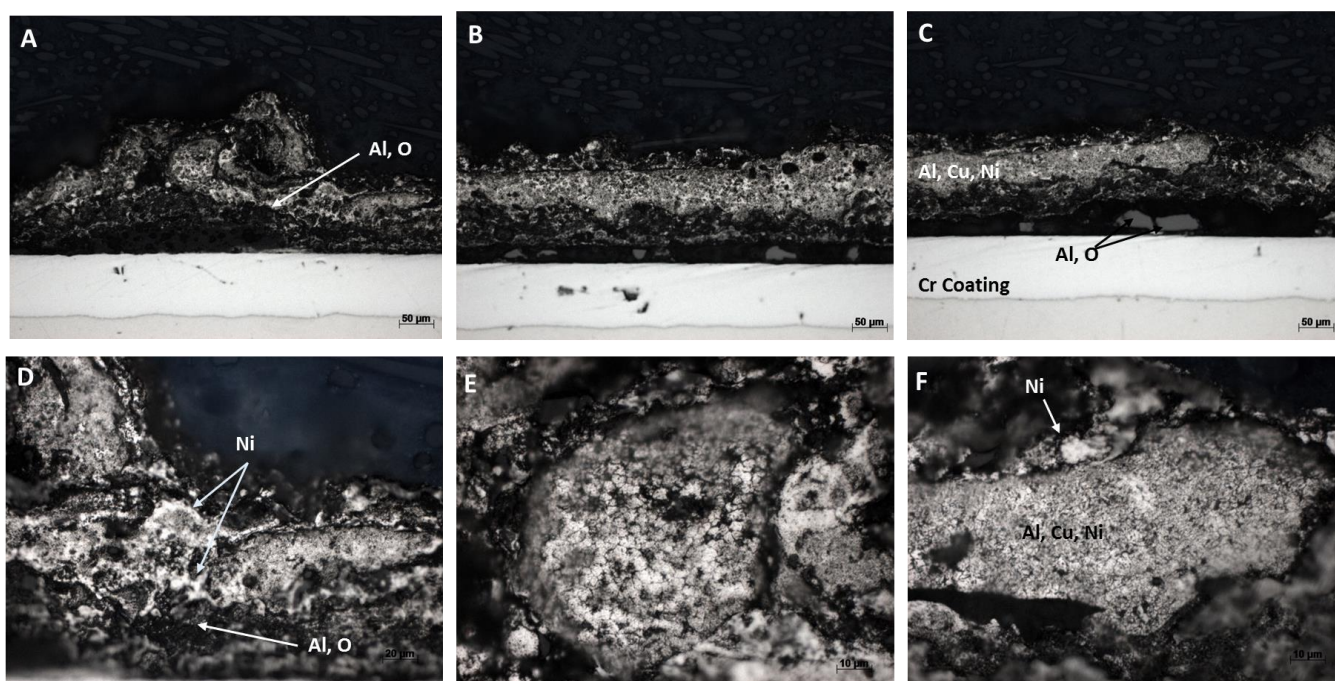


Figure 4.61 (A-C) Optical micrographs of sample A3.2 on Area 3 showing oxidized deposits with metallic particles close to the surface of the base metal. Magnification of (A-C) is 200X. (D-F) Higher magnification of deposits where embedded nickel deposits can be seen and the morphology that the metal matrix of the deposits took as it solidified. Magnification for (D) it is at 500X, and for (E-F) it is 1000X.

Sample A3.3 had the same features as sample A3.2 which was expected since they were coming from the same area and texture did not appear to change. On difference that was noticed in sample A3.3 was that there were a lot more cavities found in this area, which made it difficult to focus on deposits. Once again, Ni deposits were found mixing with the matrix (Figure 4.62 A to C). In Figure 4.62 B, Ni deposits were found in the bottom of the deposits in large quantities and appeared to have a discontinuous flow pattern as well. In other areas, large islands of both Al and Ni deposits, which did not mix as much

as deposits in the lower layers of the sample where turbulence was more aggressive were observed (Figure 4.63 C). Area 3, which made up the area where spray-like deposits were found on the elevon actuator shaft was analyzed for thermal damage and was confirmed that not alterations occurred to the chromium coating and the base material.

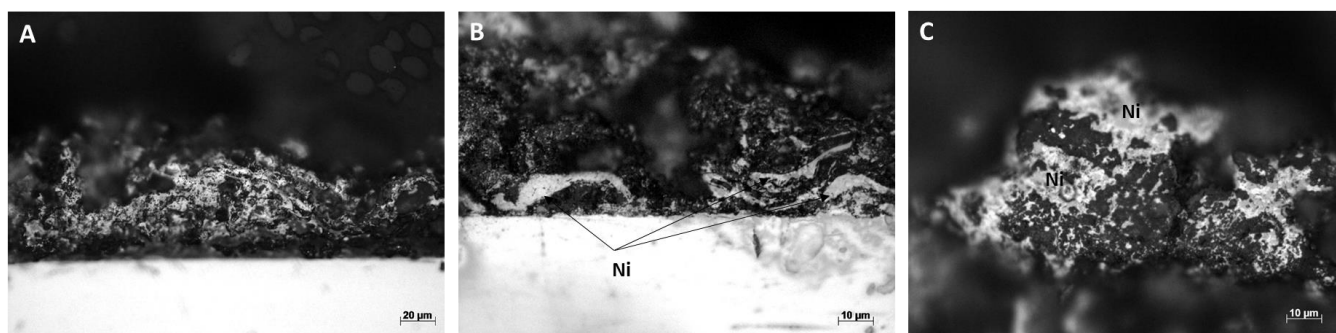


Figure 4.62 (A-C) Optical micrographs of sample A3.3 on Area 3 showing oxidized deposits with Ni deposits embedded between the Al and O concentrated deposits. Magnification of (A-C) is 500X.

4.3.4 AREA 4

As discussed earlier, there was evidence that erosion of the shaft's base metal occurred. Optical microscopy revealed thermal alterations that occurred to the microstructure. Sample A4.1 was the first sample analyzed under the optical microscope and the lighter colored deposits seen on the SEM micrographs were seen in Figure 4.63 A through C as a lighter off-white color. These were composed of Fe, Ni, and Cr and again were mostly seen at the bottom layers of the deposit. In this islands of mostly Fe deposits, small regions of Al were embedded in them. The Al, Ni, and Fe matrix was also identified and contained a larger quantity of embedded Al and O deposits in it. In this sample, not much porosity was seen and the damaged caused to the chromium layer was also clearly observed. The depth of the eroded area where loss of material occurred was about 1 millimeters and was not as thermally eroded as sample A4.2 since this sample was located at the end of the eroded area which was not as damaged as the area on top, that being sample A4.2. The microstructure of the base metal was then analyzed and in fact did show several microstructural changes occurred to the base metal. Figure 4.63 D shows the chromium layer and the position of where the lowest point in the thermal eroded area was located and just below this area, not

much microstructure can be seen. This area appears to be mostly ferrite as if decarburization occurred. Further down on the sample, delta-ferrite stringers appeared as well as austenite. At this depth in the sample, the formation of martensite started to become apparent and so did ferrite grain boundaries on the prior austenite grains (Figure 4.63 E). A transition occurred again as the ferrite grain boundaries started to disappear and narrow needle like martensite started to nucleate as shown in Figure 4.63 F. This tempered martensite then lead to the martensitic microstructure of an unaffected 17-4 PH stainless steel metal like the one found on Area 2.

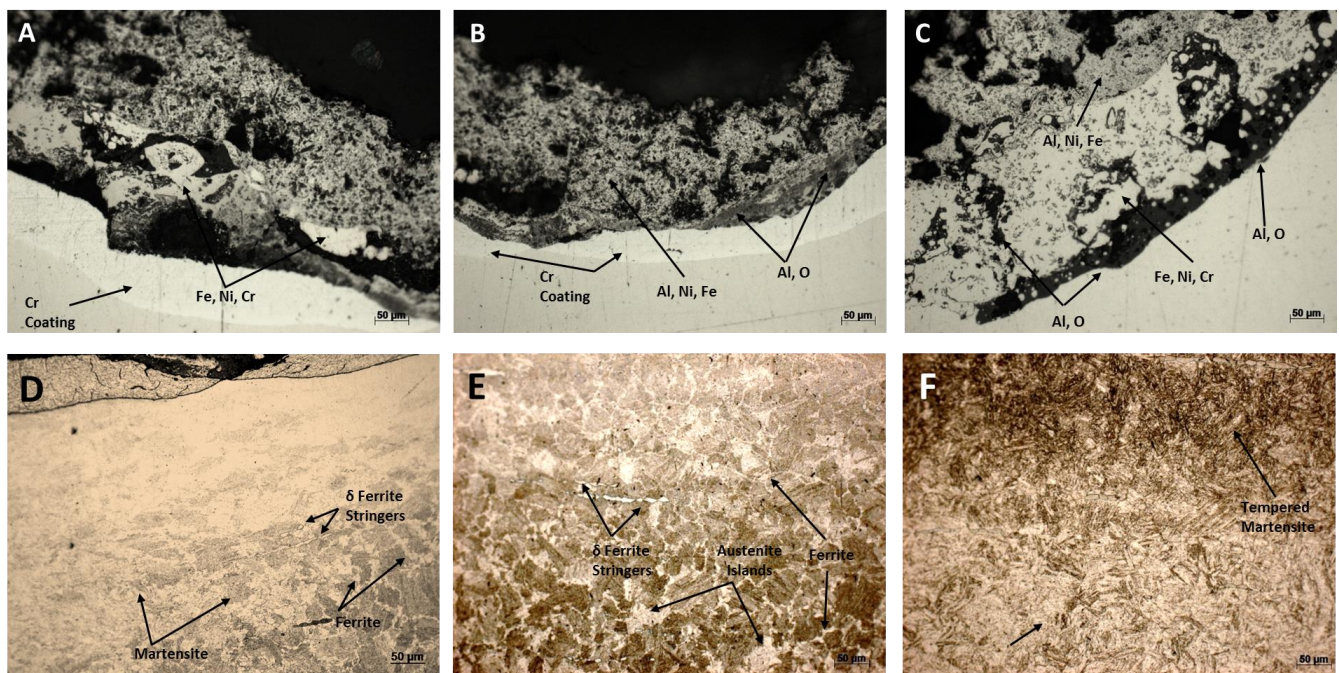


Figure 4.63 (A-C) Optical micrographs of sample A4.1 on Area 4 showing compromised Cr coating along with Ni deposits and an Al, Fe, and Ni matrix. (D-F) Microstructural changes seen in sample A4.1. Magnification of (A-F) is 200X.

Figure 4.64 shows a magnified micrograph of the profile view of sample A4.2 taken with the Keyence digital microscope at a magnification of 300X. As seen in Figure 4.64, the loss of shaft material was significant and unlike sample A4.2, no chromium coating could be seen along the walls of the eroded area. Only a small portion of the Cr coating can be appreciated on Figure 4.64 in the forward direction where the beginning of localized melting occurred. Cracking in varies places throughout the deposit's

length can be seen as well as embedded light and dark deposits in the matrix. In this sample, depth of loss of material was almost double that of sample A4.1, with this area approximately 2 millimeters in depth.

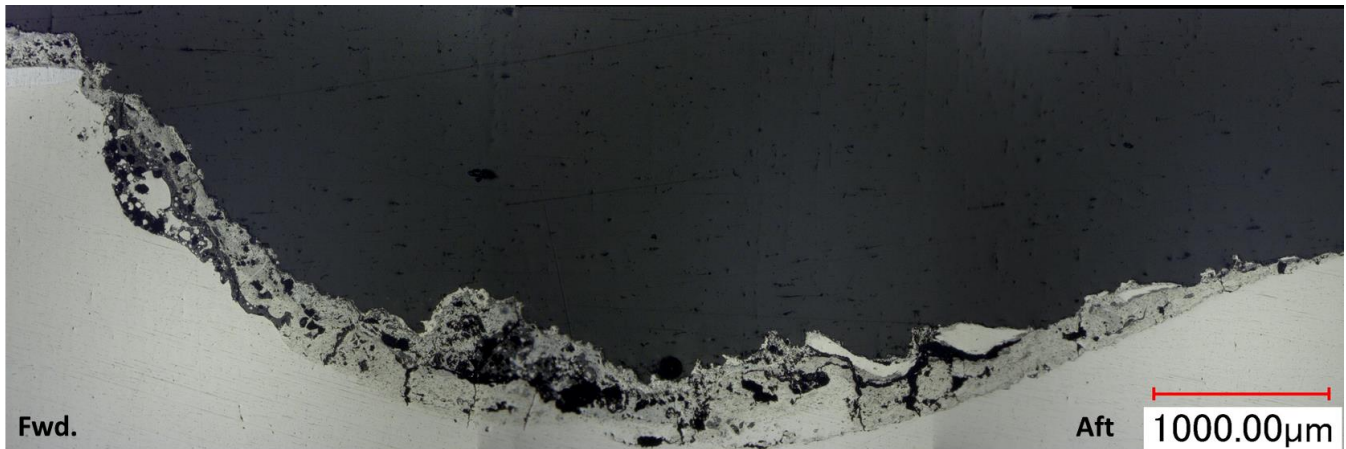


Figure 4.64 Profile view of sample A4.2 of Area 4 taken with the Keyence microscope showing different features found in the deposits.

With the optical micrographs obtained from sample A4.2, which are shown in Figure 4.65, a better look at the features mentioned can be seen. Images A through C in Figure 4.65 showed areas on the sample where erosion of the shaft occurred but was not as severe as the adjacent area and not much deposits accumulated. Most of these deposits were identified as Al and Fe deposits. In Figure 4.65 D through F, magnified micrographs of the deposits found on the eroded area are shown and a better look at cracks parting into different directions can be seen. The light color deposits which were mostly Fe are also shown and can be seen outlining the top surface of the deposits in Figure 4.65 E. In Figure 4.65 F, the dark colored Al and O deposits embedded on the shaft material are shown as well as how the base material started to mix with the deposits coming from nearby components. Microstructural evaluation determined a change in microstructure while analyzing sample A4.2. At the interface between the deposited debris and base material, melting of the base material was evident by the change in diameter of the shaft as seen also in the profile view. At the surface, a decarburized microstructure could be seen and is shown in Figure 4.66 A. The total depth of partial carbon loss was measured to be around 135 μ m. Decarburization occurred along the affected area, which measured approximately 10 millimeters wide and 2 millimeters in height. This mechanism was unnoticeable in the surrounding region.

Following the decarburization zone, a mixed microstructure of austenite with ferrite nucleating from the grain boundaries was observed as well as the beginning stages of the austenite to martensite transformation just as in sample A4.2 This mixed microstructure is demonstrated in Figure 4.66 A and B. Advancing further down the heat affected zone, the delta-ferrite grain boundaries were still present but martensite become more prominent. Austenite islands also existed in the area along with delta-ferrite stringers and can be seen in Figure 4.66 C. The microstructure transitioned to tempered martensite in Figure 4.66 D where ferrite grain boundaries were no longer present. As the lower surface of the sample was analyzed, a final microstructural change was observed before reaching the unaffected area on the sample. Figure 4.66 E shows a mixed microstructure of tempered martensite and the complete transformation of martensite along with delta-ferrite stringers, which were observed throughout the whole heat affected zone. Delta-ferrite stringers made up around 5% of volume of the microstructure of the base material. Following the tempered martensite, Figure 4. 66 F shows the unaffected microstructure, which was similar to the one shown in Figure 4.59 from Area 2.

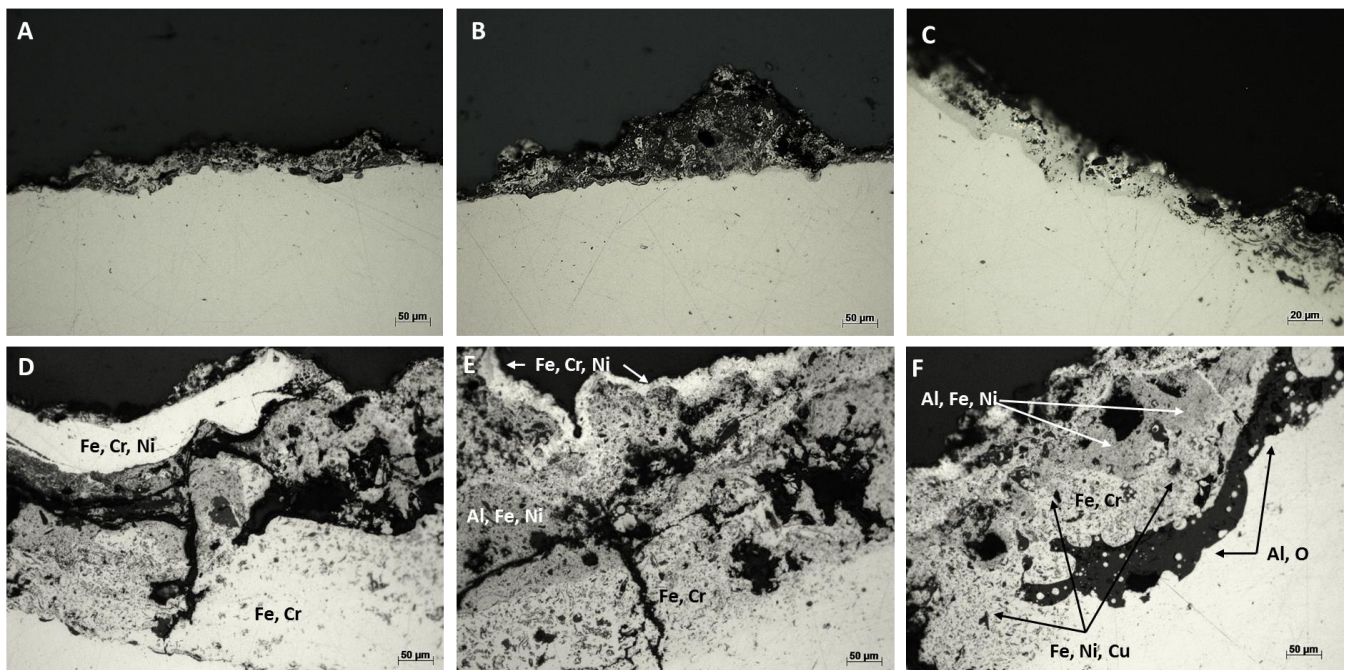


Figure 4.65 (A-C) Optical micrographs of sample A4.2 on Area 4 showing areas in the sample where not much deposits accumulated but erosion did occur. Magnification of (A-B) is at 200X and (C) is at 500X. (D-F) Magnified images of deposits found in eroded area. Magnification of (D-F) is 200X.

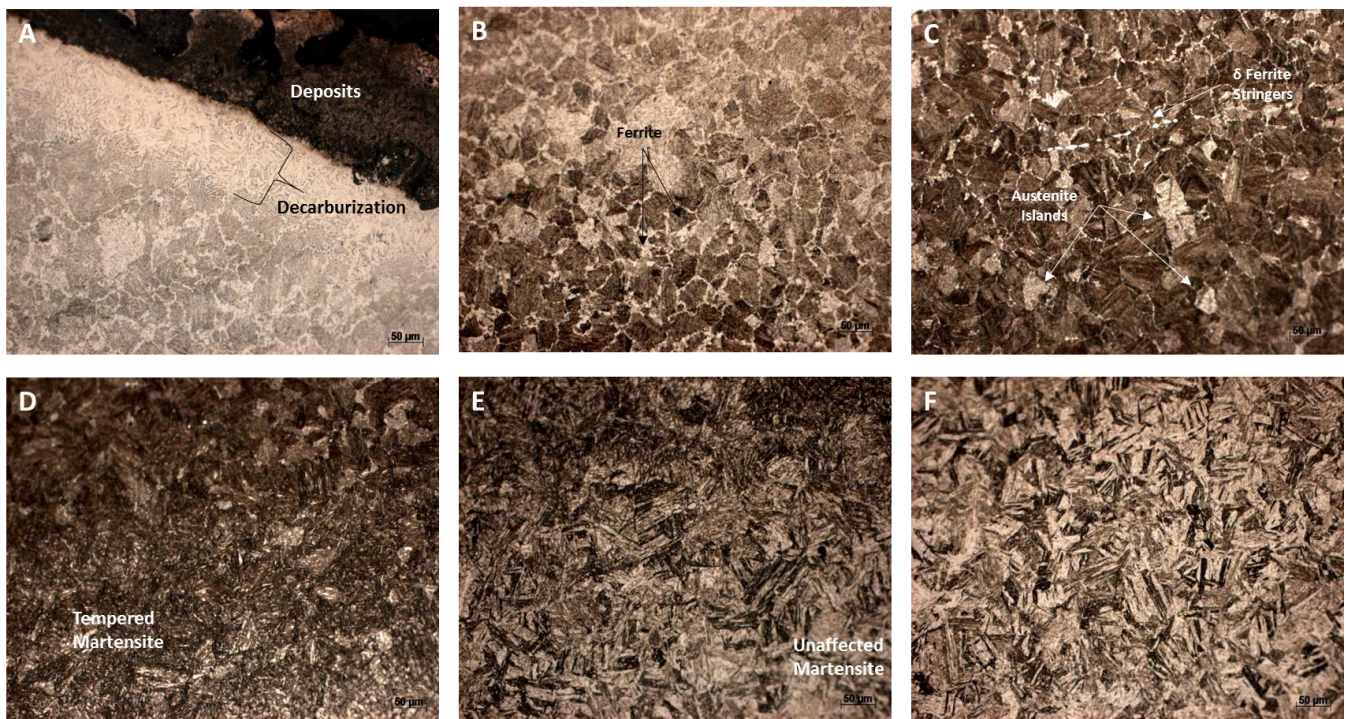


Figure 4.66 Microstructural changes occurring in the radial orientation of the base material. A) Decarburization proceeding deposit layer B) Mixed microstructure of austenite, delta-ferrite, and martensite C) Austenite patches with delta-ferrite stringers D) Tempered martensite E) Mixed microstructure of tempered and complete transformation of martensite F) Unaffected microstructure

For the last sample in Area 4, the first three threads were analyzed under the optical microscope and the micrographs are shown in Figure 4.67. Images A through C show how the threads suffered material loss from the extremely hot temperatures that the deposits exhibited when they adhered to the shaft. The thread seen in Figure 4.67 A showed how the thread crests had several deposits on its surface and as it descended to the root, where deposits start to accumulate and not much signs of thermal erosion were evident. In Figure 4.67 B, both ends of the thread crests appear to have suffered erosion. Both threads showed similar deposit morphology and a separation along deposits and the base metal interface was seen running down to the root. In the third thread, the crests and roots of the thread were severely damaged by heat (Figure 4.67 C). The loss of material can be seen in this area as the depth of the thread decreased from an average of 480µm to approximately 320µm. The amount of deposits that accumulated in the thread were also less and had different features than the other two threads analyzed. In this thread, instead of seeing the matrix with Al with O enrichment and deposits embedded on them, a gray colored deposit

was seen which was identified as a mixture of Al and Ni (Figure 4.67 C and E). In Figure 4.67, D and F, micrographs at higher magnification were shown with an Al and O concentrated layer present. Iron, Ni, and Cr deposits were also found in the same area of the sample, mostly in the bottom layer. As for the microstructural changes that were seen in this area, the microstructures consisted of alterations that also occurred in samples A4.1 and A4.2. The microstructures of sample A4.3 are shown in Figure 4.68. All three samples, having similar microstructures, indicates that intense temperatures were experienced in and around Area 4 only, since other areas examined did not show any thermal alterations.

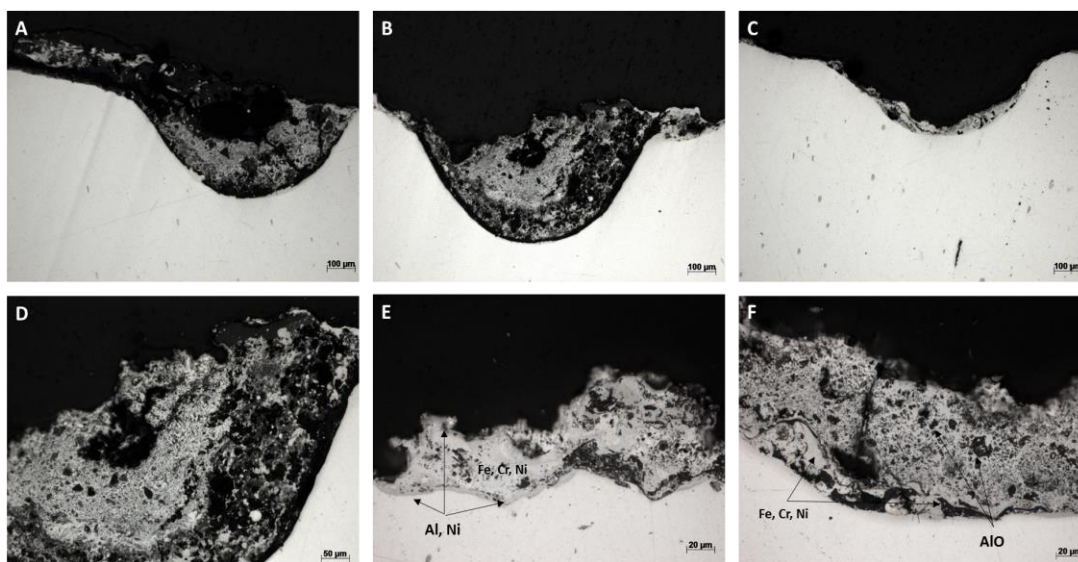


Figure 4.67 (A-C) Optical micrographs of sample A4.3 on Area 4 showing how the threads suffered from thermal erosion. Magnification of (A-C) is at 50X. (D-F) Magnified images of deposits found on the crests and roots of the threads. Magnification of (D) is 200X and (E-F) is 500X.

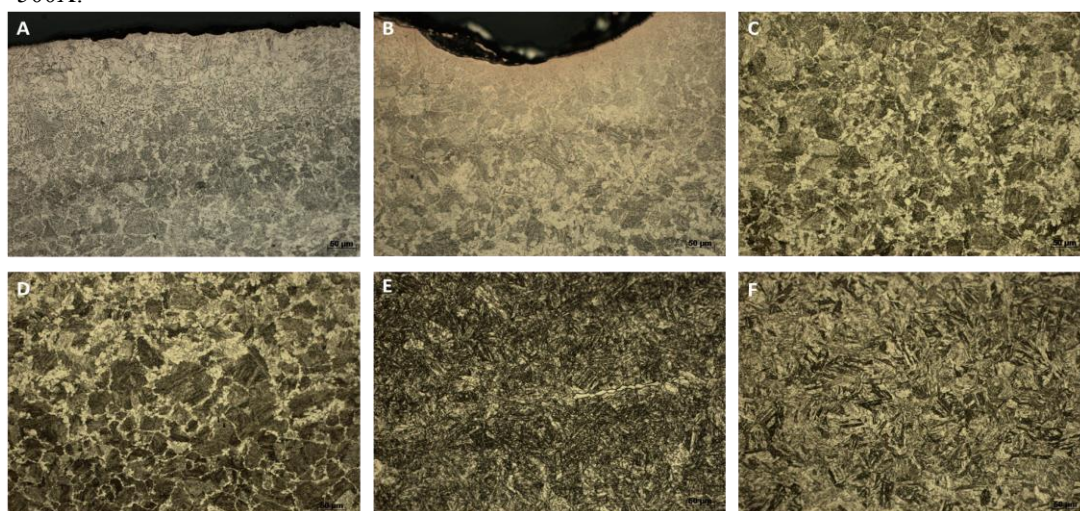


Figure 4.68 (A-F) Microstructural changes seen on sample A4.3 from Area 4 due to excessively high temperatures.

4.4 SUMMARY

Chapter 4 included results on microscopy which included SEM with EDS capabilities to identify the chemical composition of deposits and their morphology on the surface as well as the sub-surfaces when examining their cross-sectional views. EDS results obtained from the samples were then compared with XRD spectra that were obtained from performing XRD on the surface deposit of samples from all four areas belonging to the elevon actuator shaft and housing material of the elevon's hydraulic system. Optical microscopy was also performed on all samples to reveal any microstructural changes occurred to the shaft's base metal due to extremely high temperatures. SEM images taken at the surface for all four areas had different textures that consisted of rough surfaces especially seen in Areas 1 and 4. Granular, "popcorn-like" topography was also observed in Areas 2 and 3. In Areas 3 and 4, a lot of splats were seen at the surface of the already solidified deposits which appeared to have solidified while in a liquidus state. These splats were mostly coming from a Ti or Ni components. EDS along with the XRD spectra revealed that deposits in Area 1 had Al_4Cu_9 , Al_2O_3 , and CuO compounds present. On Area 2, deposits were mostly composed of AlFe_3 and AlCu as XRD results showed and EDS result did identify small quantities of Cu as well. For Area 3, Al, Fe, and Ni enrichments with occasional Cu detections were seen in this area. Ti splats were also detected by EDS and XRD on Area 3. Similar results to those seen on Area 3 were obtained for Area 4 with the exception that Ni was detected more readily on Area 4 than it was for Area 3.

When examining the cross-sectional views of all four areas under the SEM, deposits in Areas 1, 3, and 4 had very similar morphology which included a gap at the interface between the base metal and deposits where either Al or Si particles enriched in O could be seen embedded in a discontinuous manner inside the gap. Above this void space, an Al and O concentrated layer was observed and a combination of Al, Fe, Ni, Cu, and Cr deposits were found directly above the Al and O layer. Higher concentrations of Cu were found on Areas 1 and 3 besides Al, which made up most of the deposits. In Areas 3 and 4,

embedded in the deposits were also Ni and Fe deposits where Ni deposits were mostly found at the bottom layers of the deposits whereas Fe deposits were seen both at the bottom and top surfaces of the deposits. Fe was also present as one of the main constituents in the matrix of the deposits in Area 4 where thermal erosion occurred.

Optical microscopy allowed for the microstructures of both the housing of the hydraulic system and actuator shaft to be analyzed. Both the 15-5 PH and 17-4 PH stainless steel had martensitic microstructure with the only difference being that the 15-5 PH stainless steel had a reduction in delta-ferrite. Delta-ferrite stringers were absent from the 15-5 PH stainless steel sample from Area 1. Areas 1, 2, and 3 were areas where no thermal alterations were seen and the chromium coating would be seen intact in Areas 2 and 3 since Area 1 did not have a chromium coating. For Area 4, where the eroded area was present, damaged to the chromium coating was noticed in sample A4.1 and completely vanished in samples A4.2 and A4.3 which indicated that the top surfaces of the shaft experienced high temperatures for longer periods of time as compared to the sides where sample A4.1 would be located. Microstructural changes could be seen in all three samples from Area 4 where decarburization occurred in two of the samples and the microstructure at some point reverted to austenite and ferrite grain boundaries started to nucleate from the austenite grains before the martensitic transformation occurred once again. Tempered martensite was the last microstructural change noticed before reaching an unaffected area in the sample where the same martensite structure seen in the unaffected areas was observed. Overall, the same main elements, Al, Ni, Fe, Cr, and Cu were present in the deposits with the only difference being the quantity of each element in each sample.

CHAPTER 5: DISCUSSION

Characterization of the four areas of interest selected from the actuator shaft and housing material belonging to the hydraulic system of the elevons was performed by using different instrumentation. The SEM with EDS capabilities, XRD analysis, and optical microscopy were all instrumentation used to help determine chemical composition and the materials behavior of the surrounding materials system found around the elevon actuator shaft. Results of these different studies were presented in the previous chapter and will be discussed in this chapter. Similarities and discrepancies between results coming from different sources of analysis will be presented. Identification of the sources where the deposits were coming from as well as temperatures that were experienced by the shaft and its surrounding components will be discussed as well. The events that occurred to the shaft and the elevon's movement during the event will also be discussed. The fact that the shaft contained three different indications of movement which most likely happened when the hydraulic system was functional or had completely loss of control of the shuttle's aerosurfaces gave insight to what these elevons were trying to do to keep the shuttle in flight. Even though not much information was known on the exact course the shuttle took while entering the Earth's atmosphere, the three depositions provided new information on how the elevons behaved during re-entry.

5.1 SURFACE ANALYSIS DISCUSSION

The surface analysis done on all the samples revealed several similarities in the topography. Area 1 and Area 2 had very similar surface morphology which showed a lot of granular deposits where agglomeration of these deposits was visible. Due to this agglomeration of the deposits, a lot of nooks and crannies were observed in these deposits. The deposits in these two areas were identified as mostly Al and Cu deposits which contained significant amounts of O. Aluminum being present in any of the deposits was expected since the surrounding aluminum actuator rib assembly was constructed out of Al 2024. The surrounding honeycomb construction of the wing's skin was also made from 2000 series aluminum alloys.

XRF analysis in these two areas revealed to have about 6 wt. % Cu present in the deposits, which is not a large amount of Cu but increased to around 40 wt. % when EDS analysis was conducted in these two areas. The finding of Cu in Area 1 and 2 in such large quantities by EDS and identifying phases such as Al_4Cu_9 and CuO by XRD was not expected. While examining the elevon actuator debris and looking at some of the damages in the surrounding areas of the debris, the electrical junction box attached to the hydraulic system, which had damages of melted and burnt components was possible source of Cu since a lot of wiring was located in this area. With Cu having a melting temperature of 1085°C (1984°F) and being the lowest melting temperature known of surrounding materials besides Al, the source of the Cu deposits was coming from surrounding wiring on the electrical junction box of the hydraulic system (Figure 5.1).

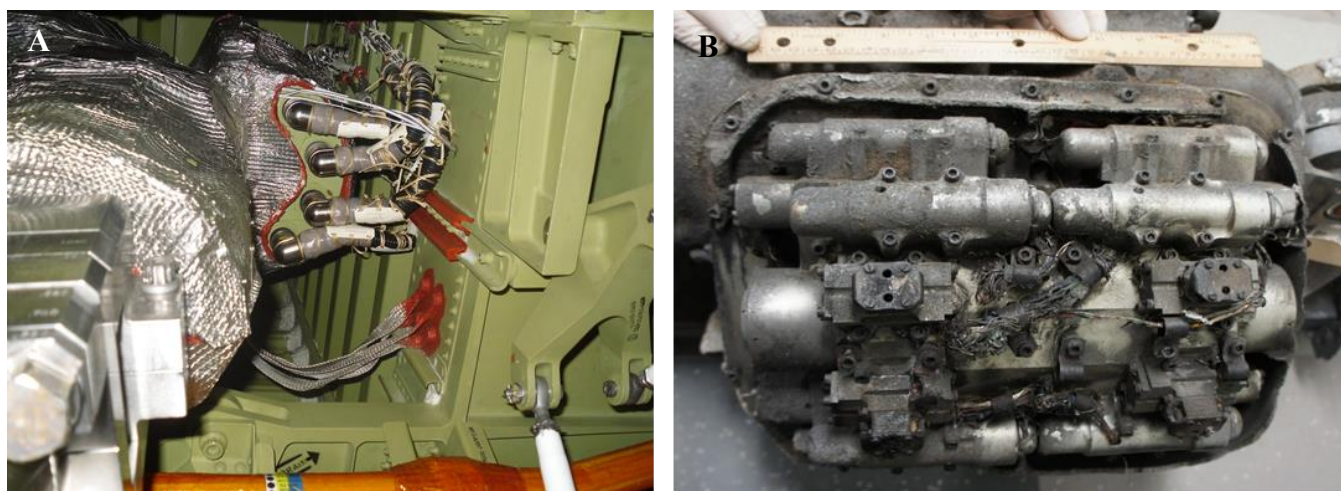


Figure 5.1 A) Side view of electrical junction box of hydraulic system from Space Shuttle *Endeavor*. B) Front view of electrical junction box of hydraulic system from Space Shuttle *Columbia* debris showing damages of wiring and other components.

Area 2 had to be the last area to get deposits on its surface since deposits were narrow strips and discontinuous along the circumference of the shaft. These deposit lines had to be deposited last otherwise, deposits would have covered the whole Area 2 and not have any visible deposit-free zones. Deposits would have had a different texture as if they had been smeared onto the shaft due to the shaft sliding from Area 2 to Area 3 leaving behind traces of deposits between the Area 2 to Area 3 transition if they were to have been deposited first. It could be observed that the shaft had some movement occurring at that point since the deposit lines kept advancing a total of three times. It was unsure if these deposit line made up a

unique deposition event as originally hypothesized. There existed the possibility that these deposits could have deposited during any time in the first or second deposition. The location of these deposit lines and how well defined they were as well as the texture indicated the possibility that they were imprinted by a possible Al alloy pressure seal belonging to the hydraulic system at any time during the event. The hydraulic system became extremely hot on the starboard-side of the shaft since these deposit lines were only detected on the starboard-side. The possible high temperatures the hydraulic housing experienced would cause the heating of the metallic pressure seal, leaving behind the deposit lines. Deposits could have also come from deposits on the housing aft-facing side since chemistry of Area 1 and Area 2 were very similar. The fact that there were several deposit-free zones between Areas 2 and 3 and within Area 2 indicated that movement of the shaft at Area 3 came to a complete stop for a certain amount of time and had “jerk-type” movements occurring throughout Area 2. At this point in time, it was possible that the hydraulic system was not functional. This quick, sudden movements of the shaft sliding in Area 2 would justify the way the narrow strips got deposited onto the shaft and why there were deposit-free zones in the area. This movement would have happened during a time where not much surrounding components were exhibiting high temperatures and transferring of deposits was mostly likely not occurring. The time of this deposition would have occurred at the very end of the break-up, but at a time when deposits were still sufficiently hot enough to adhered to the shaft’s surface. From the calculations made by NASA engineers to determine the angle of the elevon at these three different positions in the shaft, Area 2 shows that the elevon was at a 14.1° , which would indicate the pitch was down. This position was 33.66cm (13.25”) away from the center of the clevis pin to the last deposit line on the shaft.

Area 3 was distinct from other areas when looking at the surface texture of the deposits. Sample A3.2 did not have many continuous deposits and streaks were mostly analyzed. The metallic streaks and smaller splat deposits found in this sample were coming from Ti and Fe components. The Ti streaks that were seen in the deposits which had a directionality of forward to port, were most likely coming from the

Ti panels which provide a closeout of the wing-to-elevon cavity and would be located behind the elevon actuator shaft. (Figure 5.2). Melting or possible combustion of this Ti panels occurred and deposited in to the shaft in a forward to port direction, which is what is expected if the shuttle was flying from forward to aft since the location of the sample was on the side in a 3 o'clock position. Other small deposits found in the area were mostly composed of 60 wt. % Fe and around 15 wt. % Cr, which was possible these deposits were coming from the eroded area of the shaft since they were found in multiple directions and were only seen in a small area in the aft-starboard direction in close proximity to Area 4. For sample A3.2, Ti splats were found deposited on to of a thin layer of deposit and showed signs of cracking or had already cracked and detached from the base metal. This cracking was due to the fact that these thin Ti splats oxidized and became very brittle. For thicker layers of Ti that completely cracked, impact with other components during the break-up or while transferring debris from recovered location to Kennedy Space center could have been the reason why these splats suffered from spallation. The fact that Ti splats were found at the top surfaces of Areas 3 and 4 indicated that the deposits found on the shaft had a lower melting temperature than Ti and had time to solidify before Ti got deposited onto these deposits.



Figure 5.2 Titanium honeycomb sandwich construction panels from Space Shuttle *Endeavor*.

The thinner layer of deposits found in this area had a spray-like texture which make the thin Al deposits readily oxidizable because of the larger surface area of the small particles. This layer being mostly Al with large quantities of O and exposed due to the chipping of deposits in Area 3, meant that Al in this location of the shaft which was midway from the total length of the shaft, was deposited first. In the thicker layer of deposit that chipped off due to impact, to unveil the thin layer, Al, Fe, and Cu were the main compounds that were found in the samples, which differ from Areas 1 and 2 where not much Fe was present. The matrix of these heavy deposits were mostly Al and Cu oxides as detected by XRD. These results also coincide with XRF results showing some concentrations of Cu in Area 3 which were conducted at the beginning of the study. Only about 12 wt. % Cu was present in the deposit, which is reasonable if these Cu deposits were coming from surrounding wiring as well as small concentrations that were present in the alloying metals around the area such as Al 2024 and 2219 and Type 304 stainless steel, which made parts of the hydraulic system and locking nut and clevis pin. The locking nut and clevis showed signs of erosion, which can be seen in Figure 5.3 A when compared to how it should look, which is shown in Figure 5.3 B. Due to the melting of the locking nut and clevis pin, temperatures around this point in the event where surpassing 1455°C (2650°F) since this is the melting temperature for Type 304 stainless steel. Image B from Figure 5.3 B is coming from the retired Space Shuttle *Endeavor* which is on display in the California Science Center. Splats with large concentration of Fe and smaller amount of Cr were seen at the surface deposits of Area 3 as well and with about 75 wt. % Fe and 18 wt. % Cr, the source of these deposits were from Type 304 stainless steel components, most likely the locking nut and clevis pin.

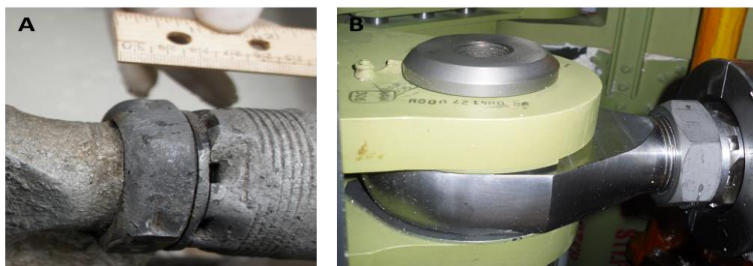


Figure 5.3 A) Locking nut and a portion of clevis from the Space Shuttle *Columbia* debris showing erosion in the locking nut. B) Locking nut and clevis pin from Space Shuttle *Endeavor* without any damages.

For Area 4 only a few similarities on surface topography were comparable to those of Area 3. As seen in Area 3, Ti splats were still visible in Area 4. These Ti splat were mostly likely coming from rub strips and panels, which were located behind the shaft and can be seen in Figure 5.4. Another similar feature that Area 4 exhibited like Area 3 was the texture in some areas of the deposits where for the most part, chunky deposits had a rough but uniform surfaces. This chunks of molten metal that cluster together indicated that at the time of deposition, the debris was solidus enough that it adhered to other debris that were also accumulating in the area. The continuous uniform surface also indicated that the rate of deposition was constant. Even though different textures in Area 4 were seen, the deposits were mostly composed of different combinations of Al, Fe, and Ni compounds. EDS results showed approximately 60 wt. % Al present in the deposits with around 12 wt. % Ni and 6 wt. % Cu, Fe, and Cr, each. The main matrix of this deposits was then coming from the Al airframe. In Area 4, there were also Ni splats, which helped increase the Ni composition found in this area. These Ni splats, which were identified to contain about 40 wt. % Ni, and about 13 wt. % of Cr and Fe, each, indicated that it was coming from Inconel 718 components, which were most likely the Inconel struts found on the sides of the shaft as seen in Figure 5.5 and panels which were on the outboard of the wing.

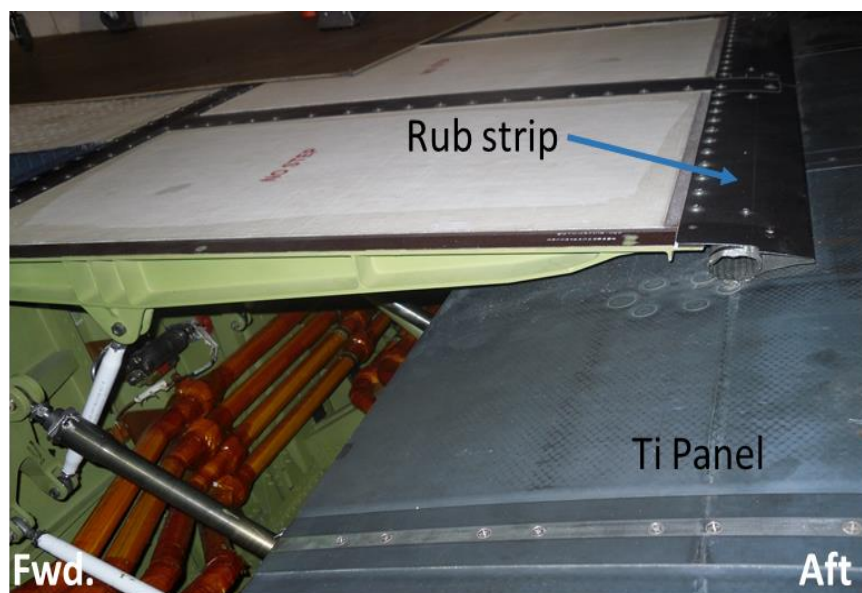


Figure 5.4 Titanium rub strip and elevon panel on the port side of Endeavor's wing.

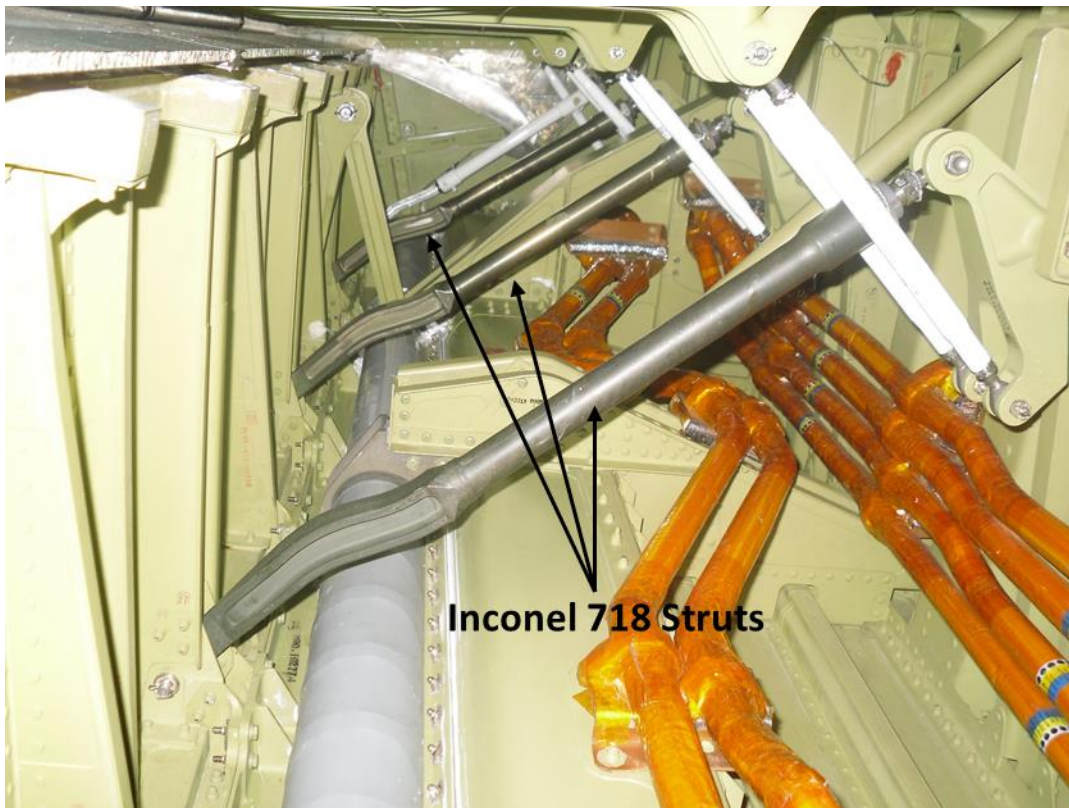


Figure 5.5 Inconel 718 struts on the *Endeavor's* wing/elevon interface.

Other surface topography was seen which showed that deposits adhered onto the shaft in a more aggressive manner which was not observed in any other area. The fact that these deposits adhered to the shaft more violently and in larger amounts showed that at this point in the break-up, temperatures were extremely high which allowed for components to reach their melting point and the velocity of the shuttle must have been at its highest which was recorded at Mach 24.5 during re-entry [2]. Surrounding components were also experiencing combustion or some type of melting due to longer exposure times to elevated temperatures of re-entry, which allowed for these deposits to travel and adhered to the shaft's surface. The deposition of deposits in Area 4 occurred first but not immediately after the disintegration of the left wing. This allowed enough time for surrounding components to exhibit re-entry temperatures, which they were not design to encounter and led to these components being compromised. As mentioned before, this area had the longest duration of all three areas examined on the shaft since thermal alterations to the shaft's base metal occurred and larger amounts of deposits were seen in Area 4. Along with the

longest duration at Area 4, the angle of the elevon at this position, 15.88 cm (6.25”) away from the center of the clevis pin, was at -33.5° which would be nose down with pitch going up. Since the pitch was going up, at this position, there was a possibility that the hydraulic system was still functional and allowed the shuttle to travel in a descending manner but, evidence points to another possibility, which could have occurred when the hydraulic systems were functional. Due to this area being so close to the clevis and locking nut, which exhibited erosion occurring from aft to forward, finding deposits that belong to those components in Area 4, it was possible that deposits adhered to the shaft when the shuttle had rotated 180° so that the deposits were deposited in a aft to forward direction. Area 3 was the second movement that the shaft made and was most likely being automatically controlled by the hydraulic system. The deposits in this area were very uniform, which indicated that there were rarely any drastic movements occurring to the shuttle and since the elevon seal panels were mostly covering the shaft, uniformity of deposits occurred. The angle of the elevon on Area 3, which was 28.58cm (11.25”) away from the center of the clevis pin to the end of the deposits found in Area 3, was 0.5° . At this angle, the elevon was almost be at a standstill and did not affect the pitch and roll of the shuttle.

5.2 CROSS-SECTIONAL ANALYSIS DISCUSSION

By looking at the deposit's cross-sectional views, information on what the chemical composition of the layers was known which provided additional details on the series of events that occurred on the shaft and its surroundings. When the profile view of all four areas were analyzed, similarities were found on Areas 1, 3, and 4. Area 2 was very difficult to analyze due to deposits being so thin and charging of the sample while under the SEM, which did not allow for good quality images to be taken. The few micrographs that were capture showed the presence of loose particles, which were Al and Si particles with high amounts of O present as well. These silicon chunks were most likely coming from the thermal protection system tiles which are composed of silicon and Cerachrom insulation. This thin layer of deposits oxidized very quickly and since the first layer that was found on Area 2 had different size faceted

particle, it was easy for these particles to oxide. The second layer of deposit was a continuous, narrow, and enriched layer of Al and O. Because not much embedded deposits were found in this area and only consisted an Al and O layer, the hypothesis formed in the previous section suggest that these deposits did in fact come from deposits falling off from the aft-facing side of the housing material or from the pressure seal belonging to the hydraulic system as the shaft experienced sudden sliding movements, possibly in the last seconds before landing on Earth. The thin Al layer deposited on top of these particles was also seen in the other three areas, which indicated that Al deposits were constantly being deposited on to the shaft and most likely came from different locations of the shuttle's wing spar which was made of 2000 series Al alloys. Another similar feature that was seen in all areas was the gap between the substrate, chromium layer, and deposits. This gap which sometimes contained chunks of Al or Si particles, may have occurred due to deposits not adhering completely to the chromium layer because it is a protective layer from oxides which deposits at the bottom layer did have large amounts of oxides. Another possibility for seeing these gap between the chromium coating and deposits was metallography. During metallography, the deposits detach at that interface during the harsh process that the sample is subjected to.

One of the most common features that Areas 1, 2, and 3 had was the presence of different size particles at the surface of the shaft, which were mostly Si or Al particles with enriched O or in occasions for Si, there were also C enrichments. Knowing that Cerachrom with Inconel foil were used for insulations on different areas around the wing's leading edge and elevons and was made of an alumina-silica-chromia fiber, it was no surprise that these particles were found at bottom of the deposits. Cerachrom will melt between 1800°C (3272°F) and 1900°C (3452°F) which means these were deposited on the early stages. The presence of Si can also be coming from the thermal protection tiles as mentioned earlier, which are present in the surrounding areas. Also, finding these particles at the surface indicated that these were detaching from surrounding components due to mechanical damage as parts were being hit by others at the beginning stages of the break-up. Note that most of these particles were found on Area 1, 2, and in

Area 3, sample A3.1, which was located at the lowest point on the starboard-side of the shaft and contained a small thin layer of Al and Cr. Not many of these small particles were seen on samples located on the top surface of the shaft where heavier deposits were seen.

In Areas 1, 3, and 4, different layers embedded in the matrix of the deposits were seen. In sample A4.3, which belonged to Area 4 and in Area 1 sample, the same deposits were seen at the top surfaces. These consisted of an Al and Fe mixture with about 10 wt. % Cr. Since there was a very high concentration of Fe in these surface deposits, the Fe and Cr content found here was coming from the Type 304 stainless steel locking nut and clevis pin, which were directly across sample A4.3 and this same material was found in the hydraulic components, which would be close to Area 1. The presence of Ni deposits at the bottom layers on Area 3 suggest that this high concentration of Ni was coming from the Inconel 718 rod assembly found all throughout the elevon construction. Though the melting temperature of Inconel is considerably high at 1360°C (2437°F), it was lower than most of the material systems found on the deposits and would be expected to exhibit localized melting at an earlier time than Ti-6Al-4V or Type 304 stainless steel hence, found at the bottom of the deposits. In Area 4, also found at the bottom layers were Fe, Cr, and Ni deposits, which indicate they belong to the Type 304 CRES stainless steel components since EDS results showed the chemical composition was similar to that of Type 304 stainless steel. The temperature experienced in this area was a little higher than that of Inconel at 1454°C (2650°F). Also in Area 4, seen at the bottom of the thermal eroded area was the mixing of the base metal, 17-4 PH stainless steel, with enriched regions of Al and O. This indicated that at this area, temperatures reached at least 1404°C (2559°F) since the base metal of the shaft had to be in a liquidus state when mixing occurred. The absence of Ti in high quantities on the cross-sectional view confirmed that Ti components were the last ones to deposit onto the shaft due to their high melting temperatures. This also confirmed the possible 180° rotation of the shuttle since Ti sources were found further back behind the shaft. This suggests Ti splats deposited in an aft to forward manner.

The bulk of the deposit or matrix, were mostly composed of Al and Cu for Areas 1 and 2, which again, confirm that the deposits in Area 2 were coming from Area 1 and Al, Ni, and Fe for Areas 3 and 4. Composition of the matrix in Area 3 contain higher amounts of Cu and less of Fe when compared to Area 4, which contained a higher concentration of Fe and not much of Cu. The amounts of Cu found on Area 3 was coming from Al 2024, which contains 4 wt. % Cu and from electric wiring in the area. Cu was detected in smaller amounts in Area 4 and higher amounts of Fe were present since extreme temperatures were sustained for longer periods then on Area 3. These Fe deposits were likely coming from both Al 2024 and Type 304 stainless steel components as well as the 17-4 PH stainless steel whose condition showed signs of erosion. Ni and Al were found in both areas in similar quantities.

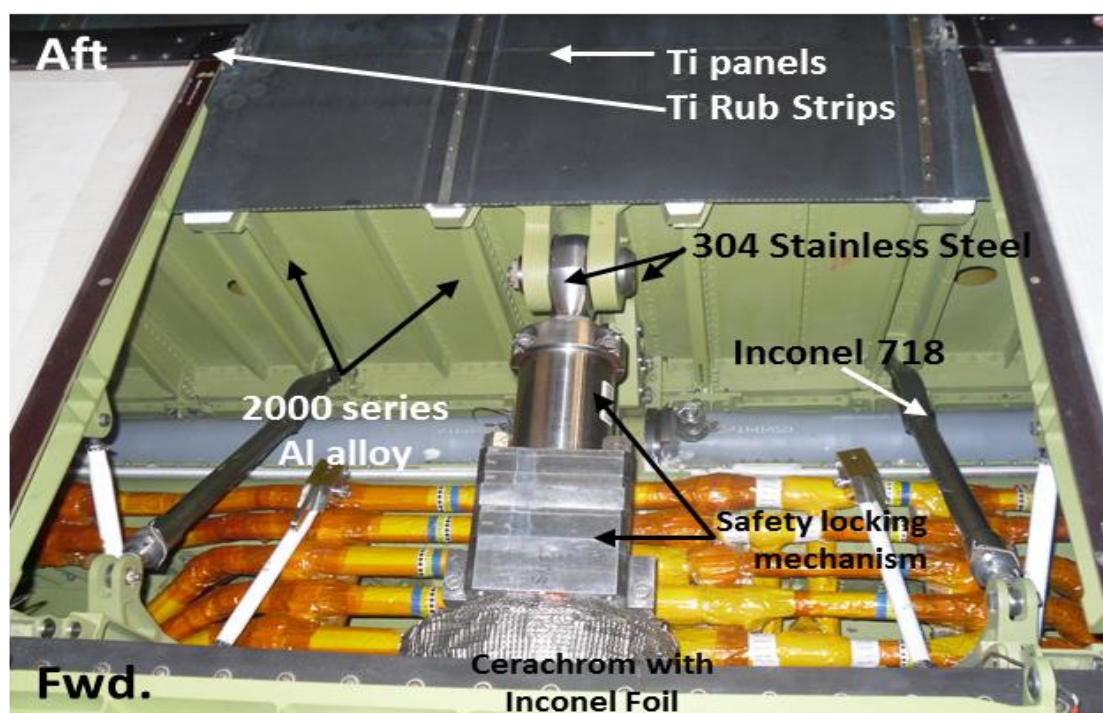


Figure 5.6 Surrounding components and material systems of the elevon actuator shaft of *Endeavor* which has the same construction as *Columbia*. Note actuator shaft is being covered by a safety locking mechanism which comes off during use of the Space Shuttle.

Because the matrix of the deposits in all four areas was a mixture of elements with no closely related composition to any alloy known in the surrounding areas, it was appropriate to assume that this matrix was a result of the different material systems mixing with each other during the event as they solidified. The matrix would include the Al alloys such as 2024, Type 304 stainless steel, Inconel 718,

and Ti-6Al-4V along with copper wiring. The components where these material systems were found and their proximity to the elevon actuator shaft is shown in Figure 5.6. In Figure 5. 6, the Inconel struts can be seen as well as the Type 304 stainless steel locking nut and clevis pin. Shown in Figure 5.6, is the Ti-6Al-4V rub strips and the aluminum honeycomb skin. From the information obtained from these studies, the surrounding regions saw temperatures that ranged from 638°C (1180°F) to above 1660°C (3020°F) since deposits ranging from Al to Ti were seen deposited onto the shaft.

5.3 OPTICAL MICROSCOPY DISCUSSION

Optical microscopy was conducted mainly to detect any microstructural changes that occurred to the shaft due to intense temperatures and deposits adhering to the base metal. As seen in the results, only Area 4 sustained thermal damages to the chromium layer and undelaying base metal while the other three areas investigated had the chromium coating intact and no microstructural changes to the 17-4 PH stainless steel were detected. Deposits seen on the cross-section by optical microscopy had the same profile views as the SEM images and will not be discussed in this section. By examining the microstructural changes that Area 4 went through, temperatures that were experienced by the shaft were predicted and the alterations to the microstructure discussed. The erosive damage observed where a noticeable change in shaft diameter occurred indicated that temperatures higher than the melting point of the base material were reached. The shaft was manufactured by using a 17-4 PH stainless steel which has a melting temperature starting at 1404°C (2560°F) and corresponds to the minimum known temperature that was experienced on samples in Area 4 since melting of the base metal occurred. Since not much information was given about the shaft material and its condition, relying on XRF along with EDS results was crucial in identifying the base material. With optical microscopy, examining microstructures of different heat treatments done on 17-4 PH stainless steel, the condition of the stainless steel was predicted.

The microstructure from Area 2, which was used as a control when analyzing samples for microstructural changes, did not encounter any thermal alterations and had a similar microstructure to that

of a H925 condition for a 17-4 PH stainless steel (Figure 5.7 A). The microstructure in Figure 5.7 B had a mixture of plate and lath martensite with several delta-ferrite stringers present and was coming from Area 2. These delta-ferrite stringers were shown in the micrograph at the lower right hand corner and were not present in the H925 condition image shown in Figure 5.7 A but, can be found in the microstructure with this heat treatment. Retained austenite was also present which is shown as the light-colored islands in the microstructure whereas martensite was depicted in a darker shade. At higher magnifications of the microstructures, copper precipitates were seen all through the microstructure. Not shown in Figure 5.7 B was the chromium coating, approximately 103 μm in thickness, which coats the base material. Due to the high temperatures that were sustained at the surface of the shaft on Area 4, the protective chromium layer was completely eroded in two of the samples and exhibited degradation in one of the samples. A typical microstructure for a 17- 4 PH stainless steel H925 condition will show a martensitic microstructure with minimal fine copper precipitates, delta-ferrite stringers, and retained austenite as shown in Figure 5.7 A [13]. With features closely resembling those of the unaffected microstructure belonging to the elevon actuator shaft, it was very likely the stainless steel went through a H925 heat treatment. In a H925 heat treatment, the steel is solution treated at 1038°C (1900°F), air cooled, aged at 496°C (925°F), and air cooled once again [44].

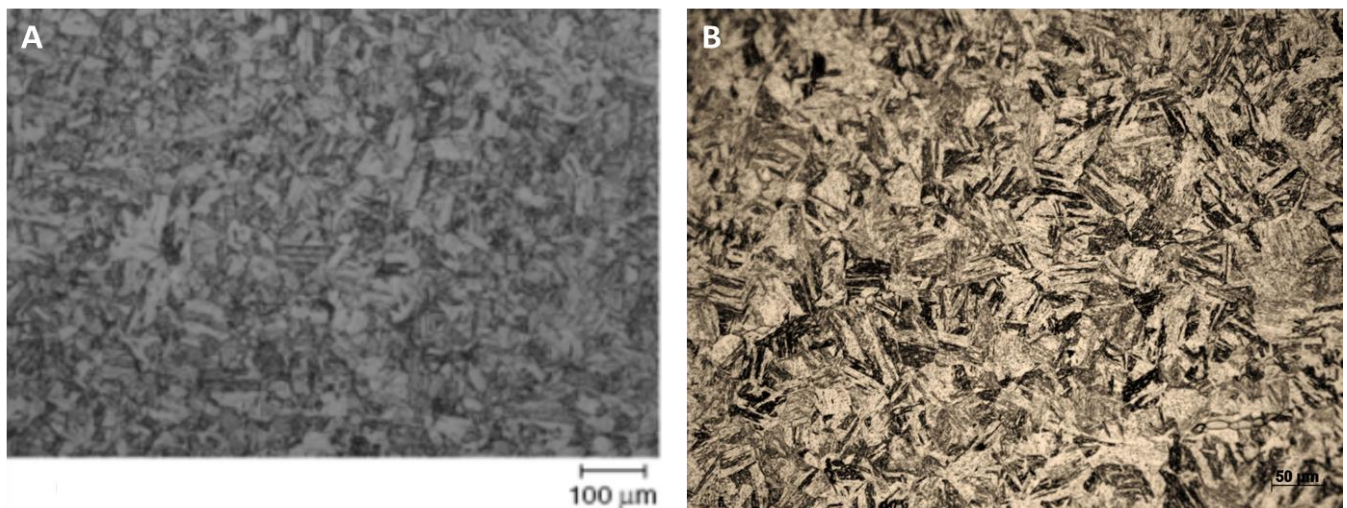


Figure 5.7 A) General microstructure of 17-4 PH stainless steel in a H925 condition showing a martensitic structure [13]. B) Martensitic structure of the shaft's base metal, 17-4 PH stainless steel with no thermal alterations. Magnification at 200X.

While analyzing the three samples that were coming from Area 4, all of the samples showed the same type of microstructural alterations to them with the exception of sample A4.1, which showed slugging of the chromium coating. Samples A4.2 and A4.3 did not show any signs of the chromium coating in the eroded area of the shaft. Sample A4.2 however, showed the chromium coating in areas where no erosion occurred and showed sign of the chromium layer thinning as it approached the thermal eroded region. Even though the coating was still present in sample A4.1, the microstructural changes that occurred in this sample were similar to those seen in the other two sample and the microstructural alterations seen in all three samples will be discusses as one. The presence of the chromium coating in sample A4.1 was due to the position of the sample on the shaft. This sample would be located on the 3 o'clock position of the shaft whereas, samples A4.2 and A4.3 were located directly next to each other in the 12 o'clock positon of the shaft. At the 3 o'clock positon on the shaft, adhesion of molten metal to the shaft was more difficult. While visually inspecting the heavy deposits in Area 4, it was noted that at the 12 o'clock positon, molten metal deposits were running down the circumference of the shaft, along the 3 o'clock positon while solidification was in progress. This indicated that at the 3 o'clock position, the molten metal had already traveled a certain distance and had time to solidify. At this point, sample A4.1 was not experiencing temperatures as high as the top surfaces of the shaft in Area 4, hence, a thinning chromium coating could still be seen while at the top, no chromium coating was detected.

Microstructural evaluation determined a change in microstructure in the samples. The observation of several microstructures in the radial direction of the shaft suggested a temperature gradient occurred from the top surface of the shaft in the eroded area to the bulk of the material where an unaffected microstructure was visible. The first alteration that was seen below the deposits was decarburization. The micrographs for Area 4 showed free-ferrite regions at the surface just below the deposits where no austenite and only the single phase of ferrite was present in some area. In other areas, partial carbon-loss was seen where small traces of austenite were present. This mechanism is particularly common in steels

and occurs when the metal is exposed to temperatures above 700°C (1292°F). At or above this temperature, carbon atoms at the steel surface react with gases which contain oxygen or dry hydrogen, in the case of stainless steels. Decarburization in stainless steels will only decarburize if it reacts with dry hydrogen which does not contain any water [45]. Atoms will then start to diffuse interstitially until they dissolve into a gaseous phase [46]. The total depth of partial carbon loss was measured to be around 135µm. This mechanism was unnoticeable in Areas 1, 2, and 3. Since decarburization occurs above 700°C and this mechanism was observed below the eroded base metal and re-solidified deposits, it indicated that the decarburized area experienced double the temperature at which this mechanism occurs. Due to the loss of carbon atoms, the only microconstituent present at the decarburized zone was ferrite which led to a reduction in fatigue and wear resistance since ferrite is a soft phase. With lower hardness values in this area, the tensile strength of the shaft would have also been compromised since hardness values correlate directly to the ultimate tensile strength. These are several of the mechanical properties that were affected due to the removal of carbon at the surface caused by sustained elevated temperatures. The duration of heating at temperatures above 1404°C (2560°F) would be the longest since melting of the shaft happened just above this region.

As temperatures decreased quickly and the microstructure continued to change, allotriomorphic ferrite close to the surface of the eroded zone as well as the beginning transformation of austenite to ferrite indicated temperatures above or around 1220°C (2228°F). At this temperature, delta-ferrite is known to nucleate in a continuous grain boundary morphology from retain austenite grains which was seen occurring just below the decarburized zone [47]. In this area, a reduction in hardness would also occur but would not be as low as the decarburized area since austenite was present at this point in the microstructure. The reduction in hardness and changes in mechanical properties are due to delta-ferrite being a soft phase when found in the presence of a martensitic matrix [47]. Even though delta-ferrite is a soft phase, the tensile strength may not be affected since the percentage of delta-ferrite in this metal is not

large enough [47]. Delta-ferrite stringers can also be seen in the microstructure and made up around 5% of the microstructure. Having 5 to 10% of stringers in this type of steel is acceptable and would not be detrimental to the mechanical properties and form due to an imbalance of Cr- Ni ratios. Increasing the Cr content will decrease the temperature of formation for the delta-ferrite [11].

As the formation of tempered martensite started to dominate the region, less delta ferrite at the boundaries was observed. When taking a look at aging conditions performed on a 17-4 PH stainless steel, an H1150 temper was comparable to what was seen in Area 4 micrographs. An H1150 heat treatment will have martensite and retained austenite. Having a microstructure similar to that of an H1150 age treatment suggests that at this midsection of the sample, temperatures reached around 621°C (1150°F). The heat treatment to obtain an H1150 condition on the 17-4 PH stainless steel consists of the material experiencing temperatures around 621°C (1150°F) before it is air cooled which suggests this area of the shaft also experienced this temperature since similarities in microstructure were found [44]. Tempering the martensite will allow the trapped carbon to be released and in turn reduces the hardness and strength of the base material which is probable that this area of the shaft experienced this changes as well [48]. Figure 5.8 A shows the general microstructure that is expected from an H1150 age treatment and Figure 5.8 B shows a micrograph from sample A4.2 in Area 4 which has a similar microstructure to that of the H1150 condition found on a 17-4 PH stainless steel.

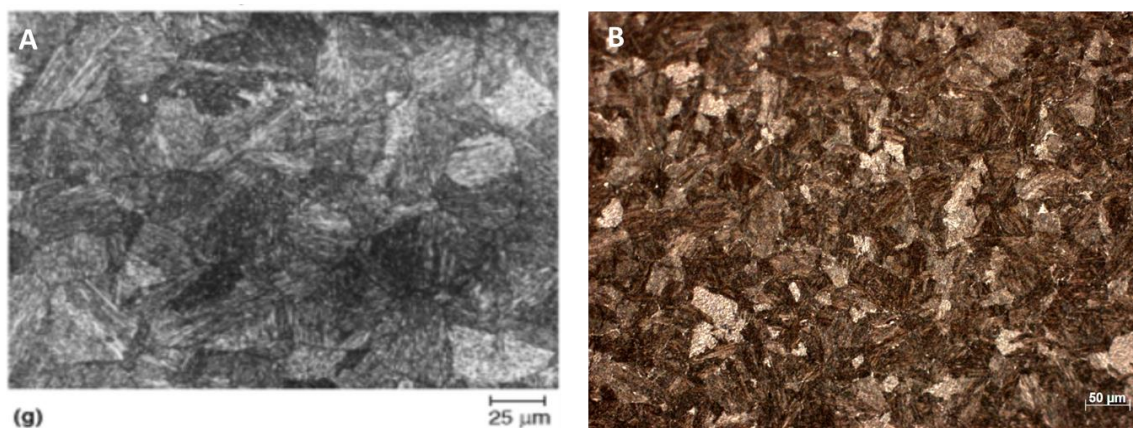


Figure 5.8 A) General microstructure of 17-4 PH stainless steel in a H1150 condition showing martensite and reversed austenite [13]. B) Microstructure of sample A4.2 from Area 4 showing similarities to that of an H1150 condition. Magnification at 200X.

Since there was a rapid decrease in temperatures from 1220°C (2228°F) to 621°C (1150°F), rapid cooling occurred and the higher temperatures were not sustained for long periods of time. Toward the bulk material, lath martensite microstructure was seen just below the tempered martensite. The martensite now appeared to have a lath morphology which is due to the lower carbon content this material contains. Banding in this area was also present and occurs when alloying elements segregate during solidification and appear as darker sections or bands on the martensitic matrix [49]. This microstructure is typical of a H1075 temper for a 17-4 PH stainless steel and approximates the temperatures of this area to be around 580°C (1075°F) since comparable microstructures were seen in Area4. The typical microstructure of an H1075 condition as well as a similar microstructure belong to Area 4 of the 17-4 PH stainless steel shaft are shown in Figure 5.9. At this depth, less heat was being transferred to this region and microstructural alterations were less noticeable as the unaffected microstructure was reached.

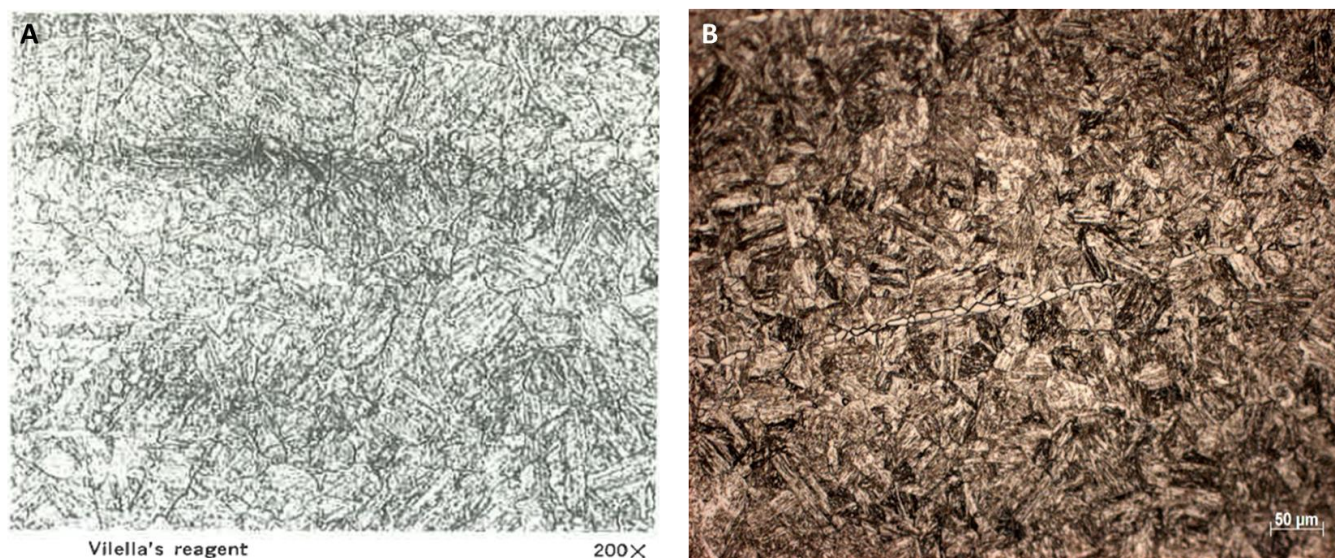


Figure 5.9 A) Typical microstructure of 17-4 PH stainless steel in a H1075 condition showing martensitic microstructure with banding [45]. B) Last microstructural change seen on Area 4 showing martensite along with banding. Magnification at 200X.

5.4 SUMMARY

Materials characterization was conducted on the four areas belonging to the starboard elevon actuator shaft of debris recovered from *Columbia*. Analysis provided information such as identification of

deposits adhered to the shaft, thermal alterations, and an approximation of temperatures experienced by the shaft. Area 1 and 2 deposits were mostly composed of Al and Cu oxides and was concluded that deposits may or might not be coming from a distinct deposition. There exists the possibility that the debris lines were deposited from deposits belonging to Area 1 onto the shaft in a manner that lead to the deposits in Area 2. It could also be that these deposits happened due to an inprint caused by the hot hydraulic pressure seal. Area 3 deposits were identified as Al, Ni, and Cu which belonged to Al 2024 and Inconel 718 components as well as electrical wiring. Area 4 with most of the deposits composed of Al, Ni, and Fe indicated that these were coming from Type 304 CRES stainless steel as well as Al 2024. Deposits in Area 4 were also found mixing with the base metal, 17-4 PH stainless steel. The differences in composition and thickness of deposits suggests that Area 4 was exposed for longer periods of time then the other three areas. Titanium splats were also present at the surfaces of Areas 3 and 4 and indicated these were the last to deposits onto the shaft. This also confirm temperatures as high as 1660°C (3020°F) were seen in surrounding areas during re-entry since re-solidified Ti was found on the deposits.

Optical microscopy provided micrographs where decarburization was observed proceeding the deposition layers. Significant microstructural alterations in the radial orientation of the base material were also documented. By visually analyzing these micrographs and their microstructures, an approximation of the temperatures that were experienced by the shaft in that area were obtained by comparing their microstructure to different heat treatment 17-4 PH stainless steel is subjected to. Temperatures ranging from 580°C to above 1404°C (1075°F- 2560°F) were predicted to have caused the microstructural changes seen on the thermally eroded area of the elevon actuator shaft. Rapid cooling was also suspected to have occurred since the temperatures decreased quickly from the top surface to the midsection of the samples in Area 4 where alterations were observed.

CHAPTER 6: CONCLUSIONS

The debris recovered after the Space Shuttle *Columbia* breakup has been examined to better understand how materials behave at extreme temperatures encountered during re-entry. Debris recovered after the Space Shuttle *Columbia* disintegrated while entering Earth's atmosphere included the starboard (inboard) elevon actuator shaft. The actuator shaft was covered in metallic deposits, indicating thermal degradation of material systems from other regions of the vehicle occurred throughout the duration of the event. The identification of these deposits and the physical aspects of the eroded areas have been characterized to include the microstructural changes of the shaft material, which is a 17-4 precipitation hardening stainless steel. Scanning electron microscopy with energy-dispersive x-ray spectroscopy as well as x-ray diffraction results were utilized to identify the chemical composition of the metallic deposits. Microstructural changes were observed by means of optical microscopy and knowledge gained from this analysis provided data on temperatures reached by the shaft as well as components surrounding it. The forensic examination of the actuator shaft will expand our understanding of material behavior during the degradation events sustained by *Columbia*.

6.1 OVERVIEW

The unexpected loss of Space Shuttle *Columbia* on February 1, 2003 led to the re-evaluation of the Space Program itself. The Orbiter which had carried 160 crew members safely into space for 22 years and made 28 successful missions, saw its final flight when entering the Earth's atmosphere due to a breach in the TPS that occurred seconds after liftoff. The break made by a piece of foam that was removed from the external tank was the size of a suitcase and allowed for plasma to infiltrate through the structural components in the left wing, which led to the loss of control of the Space Shuttle and its inevitable disintegration over east Texas and western Louisiana. After the accident, the thought that the Space Shuttle might not be the safest and most reliable way for space exploration set in. The shuttle, even though it served its purpose and enabled on-orbit operations as well as repairs and assemblies of the ISS, there was

much more that it could not do. Some capabilities that it could not do were launching on demand and the payloads that it could carry were also very restricted making it no longer cost-effective. Though safety was of the foremost importance, the harsh unpredictable environments encountered during flight made this task very complex to accomplish which makes space exploration always a risky mission. With this in mind, the government decided to end the Space Shuttle Program in 2011.

With the loss of *Columbia*, even though devastating, NASA approved a loan to the university to uncover untold stories of the shuttle and its events during the breakup. The starboard (inboard) elevon actuator shaft, debris from the shuttle, was analyzed and a thorough materials characterization on four areas of interest were conducted. The selection process of these four areas of interest started by conduction non-destructive evaluation. Non-destructive evaluation consisted of visually examining the surface deposits of the shaft and their surroundings as well as documenting this in writing and digitally by high definition photography. Photography allowed for evidence of the original state of the shaft as it was received to be captured permanently. While visually inspecting the shaft, the way the deposits were presented on the actuator shaft suggest three deposition events. These depositions were based on the relative movement of the elevon during re-entry to Earth's atmosphere. One of these depositions on the shaft exhibited an area of possible thermal erosion, since metal loss on the shaft was detected. If the shaft sustained localized melting, a heat affected zone would be observed. Another feature that was noticed but was not directly seen on the shaft was evidence of reverse flow. Surrounding components belonging to the elevon's hydraulic system had erosion signs that indicated the flow of plasma was going in the opposite direction where the nose of the shuttle would have rotated 180°. X-ray fluorescence was then conducted to obtain possible elemental composition of the surface deposits. The main elements found were Al, Cu, Ni, and Fe where a specific element would be found in larger concentrations then in other areas. With observations made and additional data obtained from these preliminary analysis, four areas were chosen for analysis. These included the three areas that were related to three different depositions and an

additional area belonging to the housing of the hydraulic system. These three areas had very distinct textures to them which is why the possibility existed that they were deposited onto the shaft at different times when the elevon was at a certain position, meaning, the shuttle had a certain roll and pitch at those positions.

As the non-destructive evaluation phase of the project concluded, sectioning of the shaft followed, which was done by using a water jet cutter as well as an abrasive cut-off saw. Once the samples were obtained, the second phase of the project included analysis by SEM with EDS capabilities, XRD, and optical microscopy. The SEM with EDS analysis would allow for both surface and subsurface morphology to be characterized and identification of elemental composition for deposits to be known. XRD was done to verify EDS results and know the compounds present in the surface deposits. Results showed that deposits on the surface were mostly composed of the same elements detected by the XRF, Al, Fe, Ni, and Cu. Areas 1 and 2 had similar compositions and was demonstrated similar quantities of Al, Cu, and O found on these surfaces. The deposition zones verified movement of the elevon and showed that Area 2 was caused by sudden “jerk” movements. The way that the three deposit lines in Area 2 were observed also indicated that these features were the last deposits onto the shaft and the duration of deposition was in a matter of seconds when temperatures were below the maximum temperatures reached, above 500°C (932°F). When the angle of the elevon at this position in Area 2 was calculated, the pitch of the shuttle was down. It is almost certain that the hydraulic system was not functional during the deposition of the debris on the shaft by the way the deposits solidified. Loss of the actuators happened only after the disintegration of the shuttle over the Dallas area where it went into an uncontrollable spin. At this point, it is possible the elevons on the starboard (inboard) side of the wing had lost complete control of the shuttle.

In samples analyzed for Areas 3 and 4, while the composition only differed in the concentration of Cu and Ni, with Cu having a greater amount present in Area 3 and more Ni in Area 4. Titanium splats

at the surfaces of these two areas were also detected throughout by EDS and XRD. In Area 4, where a change in shaft diameter was observed and heavier, rougher deposits were present, indicated that this region had to be the first to deposit onto the shaft and the duration at this probably was the longest as well. The fact that at this position where the shaft is at an -33.5° , indicates that the shuttle would have been a pitch up. The shuttle could have been in an uncontrolled spin or due to the angle of the elevon at this position, there is a possibility that the shuttle was most likely still in the right path and in control since it had a pitch up and descending as it would be expected. This could confirm that the duration at this position was the longest due to it descending and temperatures reaching higher than the melting point of pure Ti which is 1660°C (3020°F), since splats composed of 80 wt. % Ti were seen in these region. Area 3 was the second movement that the hydraulic system made where the elevons were at an almost still position with an angle of 0.5° . Area 3 was the largest area that was covered by deposits and had a very uniform deposition. The deposits had a very flat surface compared to Area 4. Due to the flaps of the elevons almost at a 0° angle meant that not much air flow was seen and could have contributed to the flat, uniform deposition seen in Area 3. Since deposits in this area did not show any thermal alterations and signs of cracking and rapid solidification was observed, lower temperatures, below 1404°C (2559°F) were sustained in Area 3. No melting of the chromium coating or base metal was observed.

Optical microscopy of the cross-sectional areas showed a separation gap between the substrate and deposits as well as porosity in most of the samples. This gap between the chromium layer and deposits could have happened due to deposits not adhering to the chroming coating well. Also, because there were debris chunks found most of the time in these void spaces, there were times when no direct contact with the base metal was made and this gap occurred. Another possible explanation for seeing this deposit lift-off in the metallographic samples was due to the metallographic preparation, when the deposits got detached from the base metal but were contained within the mount. Deposits found in all areas, with the exception of Area 2, had similar layering morphology. In Areas 1 and 3, the fact that Cu was detected in

larger amounts at the subsurface of each area indicated that surrounding copper wiring from the hydraulic system was one of the first metals to deteriorate and deposit onto the shaft. Not much Cu was found on Area 4 which was located further away from the Cu source. The matrix of the deposits in all four areas was mostly Al which is what was predicted since much of what makes up the wing is from a 2000 series aluminum alloy. Area 3 had Ni deposits embedded mostly at the bottom layers and were coming from Inconel 718 components and for Area 4, the presence of mostly Fe in the embedded deposits of the matrix indicated that these deposits were coming from the Type 304 CRES stainless steel component. The clevis pin and locking nut that attached to the shaft were of Type 304 stainless steel and were likely the source of the deposits in Area 4.

Looking at the microstructure of the 17-4 PH stainless steel, a martensitic microstructure with delta-ferrite stringers and fine precipitates was observed and was comparable to an H925 conditioned microstructure. This same microstructure was constant throughout Areas 2 and 3 where no thermal alterations were observed. A similar microstructure to that of 17-4 PH stainless steel was detected for the 15-4 PH stainless steel of Area 1 except for the delta-ferrite stringers. Area 4 did show thermal alterations to the base material where loss of material was observed. Microstructural changes were seen starting just below the deposits and progressed in a radial direction until an unaffected microstructure was reached midway through the sample. The alterations in the microstructures were compared to different heat treatments that can be performed on the stainless steel and the temperatures that the shaft experienced were approximated. With the microstructural changes observed, the approximate temperature range that the base material reached in the thermally eroded area was from 580°C to above 1404°C (1075°F- 2560°F).

6.2 FOLLOW ON WORK

Further work can be done to obtain additional information of the event that occurred in its surrounding areas. It is of great importance to understand how the microstructural changes affected the mechanical properties of the 17-4 PH stainless steel. Hardness testing can be conducted which will reveal

how severely the damage to the shaft was due to excessive temperatures. With the hardness values, an estimate to the ultimate tensile strength of the material can be performed. Comparison of the values obtained from the eroded area to standard values would be of value when material selection is in question for future space components. Transmission electron microscopy (TEM) would be an additional way to characterize the samples from the starboard-side of the shaft. The TEM is a very powerful instrument that could provide information at the submicron level. A lot of the data that can characterize the behavior of these materials can be obtained by using the TEM. Morphology and topographical information can be obtained which would be relevant to this study, since three distinct depositions occurred. Looking at the morphology and topography can show the way these different depositions layered one after the other. Crystallographic analysis could be included and identification of phases present would be seen at greater magnifications and give a more accurate estimate of temperatures the shaft experienced.

The port-side of the actuator shaft can be another piece to understanding the events that occurred to the shaft since the texture of deposits differ from those found on the starboard side which were analyzed in this study. Contrary to the starboard-side, the shaft on the port-side had heavier splats and had more directionality to the way they deposited and adhered to the metal. It was expected that analyzing samples from the starboard-side of the shaft would provide flow patterns within the deposits and provide information of this sort but not much evidence of reverse flow was seen. Only a few splats depositing in the opposing direction were seen in Area 3, but that was not enough to conclude that reverse flow definitely occurred. Analyzing these splats along with the eroded locking nut could reveal information on the possible 180° rotation that is believed the *Columbia* made. The hydraulic system was attached to the wing's rib assembly and was documented during visual examination as having eroded areas as well as hot tearing and multiple debris depositions. Analyzing different areas where these features were seen provide information on how the disintegration of the starboard wing occurred. In the case that any of the surrounding components were recovered, characterization of this component would also be beneficial,

which could provide information of how much material of the surrounding components was lost and how much of it traveled and adhered to the shaft and the other surfaces.

Materials characterization of the deposits found on elevon actuator shaft provided information such as surface and subsurface morphology, elemental composition, and microstructural alterations. Identifying the source of the deposits and their relative position on the shuttle and the approximation of temperatures reached by the shaft and its surrounding components was also accomplished. Additional work done on the samples could reveal new data that can be key in determining the sequence of events that occurred to the shaft and its surroundings. Certainly, the original designers of the shuttles did not envision that majority of the underlying material systems would be exposed to the rigors associated with orbital re-entry. In view of the spectrum of different material systems used to build a spacecraft, recognizing the subtleties of what conditions will result in catastrophic failure is useful. Furthermore, the data obtained in this research can be of tremendous value to designers of the next generation of orbital vehicles and other spacecraft.

REFERENCES

- [1] "Space Research and You: STS-107 Overview," pp.1-4, PDF file.
<<http://spaceflight.nasa.gov/shuttle/archives/sts-107/mm-sts-107.pdf>>
- [2] "Columbia Accident Investigation Board," vol.1, pp.9-12, D.C., Washington: National Aeronautics and Space Administration and the Government Printing Office, 2003.
- [3] "STS-107 Columbia Reconstruction Report," pp. 1-2, *National Aeronautics and Space Administration*, NSTS-60501, 2003.
- [4] G. Alexander, "Space Shuttle Columbia Foam Impact," *Aerospace Web*, 2003.
<<http://www.aerospaceweb.org/question/investigations/q0131.shtml>>
- [5] M. Bykowski, A. Hudgins, R.M. Deacon, and A.R. Marder, "Failure Analysis of the Space Shuttle Columbia RCC Leading Edge," *Journal of Failure Analysis and Prevention*, vol.1, no.1, pp.39-45, 2006.
- [6] J.D. Olivas, M.C. Wright, R. Christofferson, D.M. Cone, S.J. McDanel, "Crystallographic Oxide Phase Identification of Char Deposits Obtained from Space Shuttle Columbia Window Debris," *Acta Astronautica*, vol.67, pp. 553-560, 2010.
- [7] J.D. Olivas, B. Mayeaux, P. Melory, "Study of Ti Alloy Combustion Susceptibility in Simulated Entry Environments," *AIAA Space 2009 Conference & Exposition*, Pasadena, California, 2009.
- [8] "Human Space Flight- The Shuttle: Wing," *National Aeronautics and Space Administration*, 2002.
<<http://spaceflight.nasa.gov/shuttle/reference/shutref/structure/wing.html>>
- [9] "Chapter 2- Vehicle Failure Assessment," *Columbia Crew Survival Investigation Report*, National Aeronautics and Space Administration, pp.2-1 to 2-7, 2008.
- [10] STS-107 News: Shuttle Left Wing Cutaway Diagrams- View3 and View 5, *National Aeronautics and Space Administration*, 2006.
<http://www.nasa.gov/columbia/home/COL_wing_diagrams.html>
- [11] J.R. Davis, "Stainless Steels," pp. 517-520, Materials Park, Ohio: *ASM International*, 1994
- [12] AK Steel 17-4 PH® Precipitation Hardening Stainless Steel, Condition A, *MatWeb*,
<<http://www.matweb.com/search/DataSheet.aspx?MatGUID=20362bbf0a7f45b8ae59b19a9425239e&ckck=1>>
- [13] "Metallography and Microstructures," *ASM Handbook*, vol. 9, Materials Park, Ohio: *ASM International*, 2004. pp. 130-134, 1585- 1654.
- [14] "What is hard chrome plating?" The Welding Institute. 2016. TWI Global. <<http://www.twi-global.com/technical-knowledge/faqs/process-faqs/faq-what-is-hard-chrome-plating/>>

- [15] “Hard Chrome for High Temperatures,” *Finishing*, 2007,
<<http://www.finishing.com/455/62.shtml>>
- [16] “Hardchrome Plating,” *Hardchrome Engineering*,
<<http://www.hardchrome.com.au/technologies/hardchrome-plating/>>
- [17] I.Hemmati, V. Ocelik, J. Th. M. De Hosson, “Microstructural Characterization of AISI 413 Martensitic Stainless Steel Laser-Deposited Coatings,” *Journal of Materials Science*, vol. 46, pp. 3405-3414, 2006
- [18] G.F. Vander, “Applied Metallography,” pp. 56-59, New York, New York: *Van Nostrand Reinhold Company*, 1986.
- [19] V.J. Colangelo, “The Effect of Ferrite on the Mechanical Properties of the Precipitation Hardening Stainless Steel,” pg.8, *Benet R&E Laboratories*, Watervliet, New York: Watervliet
- [20] “Aluminum Alloy,” *Wikipedia, The Free Encyclopedia*,
<https://en.wikipedia.org/wiki/2024_aluminium_alloy>
- [21] “Aluminum 2024- T6,” *ASM Aerospace Specification Metals*.
<<http://asm.matweb.com/search/SpecificMaterial.asp?bassnum=MA2024t>>
- [22] “How and Why Alloying Elements are Added to Aluminum,” ESAB, 2014,
<<http://www.esabna.com/us/en/education/blog/how-and-why-alloying-elements-are-added-to-aluminum.cfm>>
- [23] “What is Anodizing?” *Aluminum Anodizers Council*.
<http://www.anodizing.org/?page=what_is_anodizing>
- [24] P.V. Petroyiannis, Sp. G. Pantelakis, G.N. Haidemenopoulos. “Protective Role of Local Al Cladding Against Corrosion Damage and Hydrogen Embrittlement of 2024 Aluminum Alloy Specimens.” *Theoretical and Applied Fracture Mechanics* 44, No. 1 (2005). 70-81.
- [25] “Aluminum Tempers, Specifications and Designations,” Engineers Edge.
<https://www.engineersedge.com/aluminum_tempers.htm>
- [26] A.E. Hughes, N. Birbilis, M.C. Johannes, S.J. Garcia, Z. Zhou, G.E. Thompson. “High Strength Al-Alloys: Microstructure, Corrosion and Principles of Protection.” In *Recent Trends in Processing and Degradation of Aluminum Alloys 2011*, edited by Zaki Ahmad, 223-262. In Tech, 2011.
- [27] “304/304L Stainless Steel,” AK Steel Corporation, 2007,
<http://www.aksteel.com/pdf/markets_products/stainless/austenitic/304_304l_data_sheet.pdf>
- [28] D. Samantaray, V. Kumar, A.K. Bhaduri, P. Dutta. “Microstructural Evaluation and Mechanical Properties of Type 304L Stainless Steel Processed in Semi-Solid State.” *International Journal of Metallurgical Engineering* 2, no.2 (2013): 149-153.

- [29] McGuire, Michael. "Austenitic Stainless Steels." In *Stainless Steels for Design Engineers*. Materials Park, OH: ASM International. 2008. 69-78.
- [30] D.N. French. "Austenitic Stainless Steel." *National Board Bulletin*. The National Board of Boiler and Pressure Vessel Inspectors. 1992. 69-78
- [31] "Nickel Chrome Alloys," *Nickel Alloys.Net*, <http://www.nickel-alloys.net/nickel_chrome_alloys.html>
- [32] "Inconel® alloy 718," *Special Metals*, 2007, <<http://www.specialmetals.com/documents/Inconel%20alloy%20718.pdf>>
- [33] M.C. Maguire, J.R. Michael. "Weldability of Alloy 718, 625 and Variants." pp. 881-892, *The Minerals, Metals & Materials Society*, 1994.
- [34] S.C. Ernst, W.A. Baeslack III, J.C. Lippold. "Weldability of High-Strength, Low-Expansion Superalloys." 68th Annual American Welding Society Meeting, Chicago, IL, March 22-27, 1987.
- [35] Pederson, Robert. "Microstructure and Phase Transformation of Ti-6Al-4V." Licentiate Thesis, Luleå University of Technology, 2002.
- [36] "ATI Ti-6Al-4V, Grade 5," *Allegheny Technologies Inc.*, 2012, <https://www.atimetals.com/Documents/ati_6-4_tds_en_v1.pdf>
- [37] "Titanium Ti-6Al-4V (Grade 5), Annealed," *ASM Aerospace Specification Metals Inc.*, <<http://asm.matweb.com/search/SpecificMaterial.asp?bassnum=MTP641>>
- [38] "Titanium Alloy Ti 6Al-4V," *Dynamet Holdings Inc*, 2000, <<https://cartech.ides.com/datasheet.aspx?i=101&E=269>>
- [39] J.L. Buckner, S.W. Stafford, D.M. Cone, "Materials Characterization of the Oxidation and Combustion Behavior of Ti-6Al-4V X-Links from the Space Shuttle Columbia," *Materials Science and Technology Conference and Exhibition*, (2015).
- [40] J.M. Guthrine, "Overview of X-ray Fluorescence," *Archaeometry Laboratory*, University of Missouri Research Reactor, 2012, <http://archaeometry.missouri.edu/xrf_overview.html>
- [41] "DELTA Alloys and Metals handheld XRF Analyzer," *Olympus*, 2016 <<http://www.olympus-ims.com/en/xrf-xrd/delta-handheld/delta-alloy/>>
- [42] "Workshop: Silicates in Space," *Kirchhoff-Institute for Physics (KIP) Building*, 2015 <<http://www.kip.uni-heidelberg.de/spp1385/>>
- [43] "ATI 15-5," *Allegheny Technologies Inc.*, 2012, <https://www.atimetals.com/Documents/ati_15-5_tds_en_v2.pdf>
- [44] "Atlas of Microstructures of Industrial Alloys," *Metals Handbook*, 8th ed., vol. 7, Metals Park, Ohio: *American Society for Metals*, 1972, pp. 146-147.

- [45] “Decarburization,” *Wikipedia, The Free Encyclopedia*
<<https://en.wikipedia.org/wiki/decarburization>>
- [46] Vander, George. “Understanding and Measuring Decarburization.” *Advanced Materials and Processes* (2015): 23- 27.
- [47] Mayr, Peter. “Evolution of Microstructure and Mechanical Properties of the Heat affected Zone in B-containing 9% Chromium Steels.” PHD diss., Graz University of Technology, 2007.
- [48] “The Metallurgy of Carbon Steel.” Go Welding. <<http://www.gowelding.com/met/carbon.htm>>
- [49] Ghena, P.F. “Materials 4340 Steel Stress Corrosion and Effects of Banding Literature Survey Part II Effects of Banding.” Fort Worth: General Dynamics, 1964.

VITA

In May 2012 Ms. Contreras received a Bachelor of Science in Metallurgical and Materials Engineering from The University of Texas at El Paso (UTEP). In the fall of 2012, Mayra enrolled in the graduate program of Materials Science and Engineering at UTEP. While attending graduate school, Mayra worked as a teacher assistant for the Department of Metallurgical and Materials Engineering and as an academic tutor for El Paso Community College at the Northwest Campus. Later on, she was appointed as a research assistant for the Center for the Advancement of Space Safety and Mission Assurance.

Ms. Contreras has submitted several first author manuscripts to scientific journals which awaits publication. The title of her work are “Microstructural Alterations on a 17-4 Precipitation Hardening Stainless Steel Caused by Deposits Coming from Space Shuttle *Columbia*” and “Materials Characterization of Metallic Deposits Adhered to Elevon Actuator Shaft Recovered from Space Shuttle *Columbia*”. These research papers are awaiting publications on The Journal of Space Safety Engineering and Materials Characterization, respectively. She has also presented her work at the Great Minds in STEM HENAAC Conference.

Ms. Contreras’s dissertation is entitled, “Materials Characterization of Deposits on Starboard (Inboard) Elevon Actuator Shaft Recovered from Space Shuttle *Columbia*” and was supervised by Dr. Stephen Stafford. Mayra has accepted a position with Raytheon Company, Space and Airborne Systems in El Segundo, California where she will work as a Mechanical Engineer in the materials department.

Permanent address: 805 Southwood Rd.
Canutillo, Texas, 79835

This dissertation was typed by Mayra J. Contreras